Universidade do Minho
Escola de Engenharia

Eduardo Gil Ferraz Soares Mendes

Optimizing Spatio-Temporal Feedback for Automotive Ultrasonic Mid-Air Haptics

Julho de 2026

Optimizing Spatio-Temporal Feedback for Automotive Ultrasonic Mid-Air Haptics
Eduardo G. F. S. Mendes
UMinho | 2026

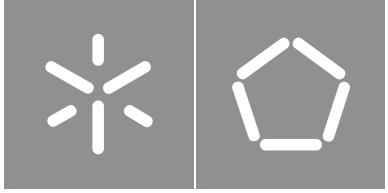

Universidade do Minho
Escola de Engenharia

Eduardo Gil Ferraz Soares Mendes

Optimizing Spatio-Temporal Feedback for Automotive Ultrasonic Mid-Air Haptics

Tese de Doutoramento
Programa Doutoral em Sistemas Avançados de Engenharia para a Indústria (AESI)

Trabalho efetuado sob a orientação de:
Professor Doutor Jorge Miguel Nunes dos Santos Cabral

Julho de 2026

COPYRIGHT AND TERMS OF USE OF THIS WORK BY A THIRD PARTY

This is academic work that can be used by third parties as long as internationally accepted rules and good practices regarding copyright and related rights are respected.

Accordingly, this work may be used under the license provided below.

If the user needs permission to make use of the work under conditions not provided for in the indicated licensing, they should contact the author through the RepositoriUM of Universidade do Minho.

Licença concedida aos utilizadores deste trabalho

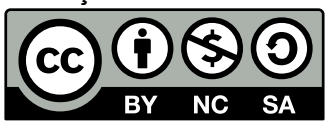

Creative Commons Attribution-NonCommercial-ShareAlike 4.0 International

CC BY-NC-SA 4.0

https://creativecommons.org/licenses/by-nc-sa/4.0/deed.en

This document was created with the (pdf/Xe/Lua)LaTeX processor and the NOVAthesis template (v7.1.19) .

Acknowledgments

In the first place, I would like to thank my advisor, Professor Jorge Cabral, for the opportunity to pursue this PhD in a field of research that I love. Thank you for all the support and guidance throughout this journey. Without you, the research that was developed would not have been possible.

I would like to deeply thank my dearest friends, Paulo Santos, Pedro Guimarães and João Cerquido. Paulo Santos, thank you for your inspiration, strength, patience, support, and guidance every moment I needed it. Words just cannot describe what you mean to me. To my friend Pedro Guimarães, thank you for all the adventures and conversations about life, science, relationships, and guitar. Your professionalism, intelligence, and humility inspire me. Love you as well, bro. João Cerquido, it is hard to explain all the support you gave me. We were together almost every days, playing, laughing, lunching, chilling. I am very proud to have you as a friend and we will keep supporting each other craziness.

I would like to thank all the people who directly and indirectly contributed to the success of this PhD: staff from the University of Minho, the Embedded Systems Research Group, the AESI PhD program, and INL. To name a few: João Novais, Mário Mesquita, Rui Ferreira, Abílio Camelo, Jorge Oliveira, João Carvalho, Edoardo Sotgiu, and many others. Thank you, Cláudia Ribeiro, for pushing me forward a few months ago and encouraging me not to give up.

A special thanks to all the employees of the University campus (Braga and Guimarães) who do excellent work at the bars, cafeterias, and canteens. They know who they are. Thank you, Ana Antunes (aka. Cabeceiras), for all the positive vibes.

I would like to sincerely thank my beloved girlfriend and greatest friend, Catarina Matos. Without your support, I would not be here writing these final words. Thank you for pointing me in the right direction, for encouraging me to never give up, and for being my Polar Star. Thank you for all our projects, our adventures, and our dreams together.

Finally, I would like to deeply thank my family for supporting me, for making me feel comfortable with my personal decisions and not stressing over them, and for allowing me to fly and pursue my dream. Here I am, after this long journey, as a very different person. It was not easy, but with my family, it was possible. Love you very much, Mom, Dad, Sister, and twin brother. My family, my special bonds in life. I miss you

all very much.

The work received financial support from FCT and Bosch Car Multimedia Portugal through the PhD scholarship PD/BDE/150499/2019.

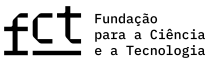





Universidade do Minho



July 24, 2026

STATEMENT OF INTEGRITY

I hereby declare having conducted this academic work with integrity. I confirm that I have not used plagiarism or any form of undue use of information or falsification of results along the process leading to its elaboration.

I further declare that I have fully acknowledged the Code of Ethical Conduct of the Universidade do Minho.

(Eduardo Gil Ferraz Soares Mendes)

Resumo

O presente trabalho de doutoramento aborda uma metodologia para a otimização de estímulos Ultrasonic Mid-Air Haptics (UMAH), baseada na compreensão das sensações que estes produzem e, posteriormente, na sua otimização ao nível fisiológico. Uma das principais limitações da tecnologia UMAH é o facto de o estímulo háptico produzido por estes sistemas ser ténue (ou pouco percetível). Neste contexto, sensações UMAH mais otimizadas do ponto de vista percetual e energético são altamente desejáveis para o setor, contribuindo para o sucesso global da tecnologia, incluindo no setor automóvel.

O caminho escolhido para a otimização da sensação háptica baseou-se no estudo e na utilização da Spatio Temporal Modulation (STM), uma técnica promissora utilizada para criar estímulos e padrões hápticos mais percetíveis. Neste sentido, o trabalho desenvolvido neste doutoramento organiza-se em duas partes principais.

A primeira parte da investigação consistiu em demonstrar que a STM é capaz de gerar sensações hápticas percetualmente distintas. Para tal, foram realizados dois estudos subjetivos. O primeiro teve como objetivo a especificação de três sensações hápticas (dinâmica, vibratória e uniforme), em função de dois parâmetros relevantes para a perceção da STM: a velocidade do Focal Point (FP) e o número de pontos que compõem o padrão haptico. O segundo estudo subjetivo validou, de forma preliminar, que estas sensações hápticas apresentam origens percetualmente distintas, sugerindo a existência de mecanismos fisiológicos diferenciados.

Na segunda parte do trabalho de doutoramento, foi desenvolvida uma ferramenta para a geração de sensações hápticas através da modulação STM. A ferramenta é pioneira pois gera automaticamente o estímulo háptico correspondente á sensação pretendida. A ferramenta permitiu gerar sensações (ou padrões) hápticas com elevado controlo das características espaciais (forma, tamanho e resolução espacial) e temporais (frequência e forma de onda), tendo a ferramenta sido validada em simulação. Através da ferramenta foram também implementadas otimizações para a sensação háptica dinâmica, desenvolvidas com base no conhecimento percetual adquirido ao longo deste trabalho de doutoramento. O trabalho desenvolvido neste documento representa a base para o desenvolvimento de novos estímulos hápticos e sensações hápticas mais otimizadas.

Palavras-chave: Modulação Espaço-Temporal, Optimização Sensações Hapticas, Perceção Tátil, Ultrasonic Mid-Air Haptics

Abstract

This Doctor of Philosophy (PhD) work addresses a methodology for optimizing Ultrasonic Mid-Air Haptics (UMAH) stimuli, based on understanding the sensations they produce and subsequently optimizing them at a physiological level. One of the main limitations of UMAH technology is the low intensity (or low perceptibility) of the haptic stimuli produced by these systems. In this context, perceptually and energetically optimized mid-air haptic sensations are highly desirable for the field, contributing to the overall success of the technology, including in the automotive sector.

The approach adopted for optimizing haptic sensations is based on the study and use of Spatio Temporal Modulation (STM), a promising technique used to create more perceptible haptic stimuli and patterns. Accordingly, the work developed in this PhD is organized into two main parts.

The first part of the research focused on demonstrating that STM is capable of generating perceptually distinct haptic sensations. To this end, two subjective studies were conducted. The first aimed to specify three haptic sensations (dynamic, vibratory, and uniform) as a function of two parameters relevant to STM perception: the Focal Point (FP) velocity and the number of points composing the haptic pattern. The second study provided a preliminary validation that these haptic sensations have distinct perceptual origins, suggesting the existence of different physiological mechanisms.

In the second part of the PhD work, a tool for generating haptic sensations through STM was developed. The tool differentiates from the state-of-the-art in that it automatically generates the haptic stimulus corresponding to the desired sensation. It enables the generation of haptic sensations (or patterns) with a high control over spatial characteristics (shape, size, and spatial resolution) and temporal characteristics (frequency and waveform), and was validated through simulation. The tool also enabled the implementation of optimization strategies for the dynamic haptic sensation, developed based on the perceptual knowledge acquired throughout this PhD work. The work presented in this document provides a foundation for the development of new haptic stimuli and more optimized haptic sensations.

Keywords: Haptic Sensation Optimization, Spatio-Temporal Modulation, Tactile Perception, Ultrasonic Mid-Air Haptics

Contents

List of Figures xii

List of Tables xvi

Acronyms xviii

1 Introduction 1

1.1 Contextualization . . . 2

1.1.1 Research Challenges . . . 3

1.1.2 Taxonomy . . . 7

1.1.3 Spatio-Temporal Modulation . . . 9

1.2 Motivation . . . 10

1.3 Research Questions . . . 11

1.4 Methodology . . . 12

1.5 Main Contributions . . . 13

1.6 Organization of the Thesis . . . 14

2 Fundamentals of Ultrasonic Haptics 15

2.1 Focal Point's principles . . . 16

2.1.1 Physical Principles . . . 17

2.1.2 Modelling Radiation Force . . . 18

2.1.3 Technical trade-offs . . . 21

2.2 Touch Perception . . . 21

2.2.1 Skin Mechanoreceptors . . . 22

2.2.2 Other Psychophysiological Factors . . . 23

2.3 Perception of Ultrasonic Stimuli . . . 26

2.3.1 The cause of the stimulus - Radiation Force . . . 26

2.3.2 Ultrasonic Pulse . . . 27

2.3.3 Amplitude Modulation . . . 32

2.3.4 Spatial-Temporal Modulation . . . 35

2.4 Conclusions 35

3 Spatio-Temporal Modulation **36**

3.1 Introduction 37
3.2 Technical operation of the modulation 37
3.3 Research on mid-air haptic perception 41
3.3.1 Short path stimuli 42
3.3.2 Bigger patterns 46
3.4 Considerations about the modulation's sensations 49
3.4.1 Fast speed motion 49
3.4.2 Slow speed motion 49
3.4.3 Intermediary speed motion 50
3.4.4 Types of sensations 50
3.5 Conclusions 51

4 Ultrasonic Mid-Air Haptic Demonstrator **52**

4.1 Introduction 53
4.2 Acoustic Field Simulator 53
4.2.1 Results 56
4.3 Ultrasonic Mid-Air Haptic prototype 58
4.3.1 Ultrasonic Phased Array 58
4.3.2 System on Module 59
4.3.3 Carrier Board 61
4.4 System's Architecture 63
4.4.1 Overview 64
4.4.2 Software – Processing System 65
4.4.3 Hardware – Programmable Logic 66
4.5 Experimental Measurements 69
4.5.1 Measurement Equipment 69
4.5.2 Acoustic Field Scanning 71
4.5.3 Focal Point force measurement 74
4.5.4 Experimental versus Simulated results 76
4.6 Conclusions 77

5 Specification of Spatio-temporal's Haptic Sensations **78**

5.1 Introduction 79
5.2 User study 1 – Sensation's specification 80
5.2.1 Methodology 80

5.2.2 Results . . . 82
5.2.3 Specification of the Boundaries . . . 87
5.3 User study 2 - Preliminary Validation of the Sensations . . . 88
5.3.1 Combined Mid-Air Haptic Sensation . . . 89
5.3.2 Experiment Overview and Methodology . . . 92
5.3.3 Results . . . 95
5.4 Discussion . . . 97
5.4.1 Results of the User Studies . . . 97
5.4.2 Psychophysical Explanation of the haptic sensations . . . 98
5.5 Conclusions . . . 99
5.6 Next Steps . . . 100

6 Dynamic Haptic Sensations 101
6.1 Context . . . 102
6.2 Maximum focal point's speed . . . 102
6.3 Maximum number of shape points . . . 104
6.4 Rough and smooth pressure sensations . . . 105
6.5 Pressure and vibrotactile dynamic sensations . . . 106
6.6 Overview of the dynamic sensation's specification . . . 107
6.7 Possibilities of optimization for dynamic haptic sensations . . . 109
6.7.1 Optimization Strategy 1 . . . 109
6.7.2 Optimization Strategy 2 . . . 112
6.8 Conclusions . . . 115

7 Haptic Stimulus Generation Module 116
7.1 Context . . . 117
7.1.1 Tool Overview . . . 117
7.2 State-of-the-art . . . 117
7.3 Algorithm . . . 119
7.3.1 Spatiotemporal signal's components . . . 119
7.3.2 Analytical description . . . 124
7.3.3 Temporal component . . . 125
7.3.4 Spatial component . . . 126
7.4 Technical challenges . . . 129
7.4.1 Resolution of the Focal Point's movement . . . 130
7.4.2 Convolution computational shortcoming . . . 131
7.5 Combined haptic patterns . . . 132
7.6 Approach to suppressing noise due to phase discontinuity . . . 133

7.7 Conclusions 137

8 Simulation Results **138**

8.1 Introduction 139
8.2 Pressure field computation 139
8.3 Pattern size 140
8.4 Pattern spatial resolution 140
8.5 Pattern shape 141
8.6 Temporal modulation of the Focal Point's amplitude 142
8.7 Spatial and temporal modulation of the Focal Point 144
8.8 Multiple Focal Points 144
8.8.1 Circle and Square shapes (non-overlapping shapes) 145
8.8.2 Two crossing lines (one-point overlapping stimuli) 146
8.8.3 Haptic Beats (overlapping stimuli) 147
8.9 Phase smoothing 148
8.10 Optimized dynamic haptic sensations 150
8.10.1 Optimization Strategy 1 151
8.10.2 Optimization Strategy 2 152
8.11 Conclusions 154

9 Conclusions **155**

9.1 Conclusions 156
9.2 Future Work 158

Appendices

A Supplementary Material **159**

A.1 Appendix A 159

Bibliography **160**

List of Figures

1.1 Ultrasonic mid-air haptic system used in a DS concept automobile for the creation of haptic feedback . . . 3
1.2 State-of-the-art UMAH developed by Ultraleap (left image). Ultrasonic transducer developed by Ultraleap compared with the traditionally ultrasonic transducer (right image). . . . 5
1.3 The acoustic field created by the haptic array. The FP (i.e., haptic pixel) is surrounded by the grating lobes. . . . 5
1.4 UMAH demonstrator developed by ESRG team from University of Minho . . . 7
1.5 Schematization of key concepts of the thesis. . . . 8
1.6 A STM circular pattern. The FP is generated by the haptic array and controlled to trace a circular pattern. . . . 9

2.1 The FP generation from the ultrasonic haptic phased-array. . . . 16
2.2 Directivity graphic of the Murata MA40S4S ultrasonic transducer. . . . 18
2.3 Main geometrical characteristics of a parabolic focusing emitter. . . . 19
2.4 Representation of the FP targeting the skin. . . . 19
2.5 The skin mechanoreceptors of glabrous skin. . . . 23
2.6 Two-point tactile discrimination. . . . 24
2.7 Tactile temporal resolution perception. . . . 25
2.8 Ultrasonic pulse signal. (Top) The pulse's carrier frequency. (Center) The pulse's envelope and. (Bottom) The skin displacement when the pulse hits its surface. . . . 28
2.9 Tactile detection threshold as a function of pulse duration, compiled from multiple studies. The dashed line represents the estimated critical duration threshold. . . . 31
2.10 Amplitude modulated signal. . . . 32
2.11 UMAH system used by Hasegawa & Shinoda (2018). (Top) The haptic array unit. (Bottom) The UMAH system, composed by four units. . . . 33
2.12 AM tactile thresholds as a function of modulation frequency. Data obtained from several research works on the field. . . . 34

3.1 Variables representing a circular STM pattern. . . . 39
3.2 Spatial-temporal modulation main parameters. . . . 40

3.3 Shape discretization in positions (or shape points). 40
3.4 Circular pattern *seen* as a train of pulses. 42
3.5 The relation between the N_{SP}, d_{SP} and t_{SP}. 42
3.6 Short path stimuli (i.e., LM) sensitivity thresholds. 44
3.7 The FP's movement over short paths stimulus. 44
3.8 Stimulating signal of a 14 mm length line stimulus (signal measured in the center of the path). 45
3.9 Perceived intensity of circular patterns (with 10 cm and 15 cm) as a function of FP's speed. 47

4.1 The FP field. (Left image) The FP's top view. (Right image) FP's side view. 56
4.2 The UMAH system acoustic field. (Left image) Acoustic field's top view perspective. (Right image) field's side view. 57
4.3 3-D isometric perspective of the UMAH's generated acoustic field. 58
4.4 Ultrasonic phased array. (Left image) haptic array's top view. (Right image) haptic array's bottom view. 59
4.5 System on Module from Trenz electronics used in the UMAH demonstrator. (Left image) The SoM's the top part. (Right image) The SoM bottom part. 60
4.6 Zynq-7000 block diagram. 61
4.7 The carrier board developed for the UMAH system. (Left image) The carrier's bottom view. (Right image) The carrier's top part. 62
4.8 The full UMAH prototype developed by the ESRG team from University of Minho. 63
4.9 Ultasonic Mid-Air Haptic setup used in a demonstration. 63
4.10 System architecture overview. 64
4.11 System architecture implementation. 65
4.12 Phase calculation pipeline implemented on the Phase Calculator Module. 68
4.13 GRAS 46BE free-field microphone set. 70
4.14 One axis-stage used for the positioning system. 71
4.15 The Denver SI2002 scale used for measuring the FP's radiation force. 71
4.16 Experiment setup used for the acoustic field scanning of the FP. 72
4.17 The FP's acoustic field. The dashed line represents the FP's diameter defined by the FWHM. 73
4.18 The UMAH's acoustic field. (Left image) Acoustic field top view. (Right image) field's side view. 74
4.19 Weighting setup used for sensing the FP radiation force. 75
4.20 Radiation force results of the FP. 76

5.1 Illustration of the STM's sensations generated by the circular pattern. 80
5.2 Overview of the specification of the haptic sensations (merely illustrative). 81
5.3 Participant during the specification trials. 83

5.4 Psychometric curve obtained for a participant during the D-V boundary region for a 30 points pattern. . . . 84
5.5 D-V boundary FP speed thresholds per number of pattern points N_{SP}. . . . 84
5.6 V-U boundary FP speed thresholds per number of pattern points N_{SP}. . . . 86
5.7 Example of a boundary region specification (in this case D-V). . . . 87
5.8 Specification of the STM's sensations and boundaries. . . . 88
5.9 Results of the Dynamic sensation (v_{SP} of 0.16 m/s or T_{draw} of 1 Hz) for 10 and 50 N_{SP}. (a) and (d) Temporal signals acquired at a SP; (b) and (e) *zoom* of the temporal signal for pulse observation; and (c) and (f) the acoustic field of the stimulus. . . . 90
5.10 Results of the Uniform sensation (v_{SP} of 7.85 m/s or T_{draw} of 50 Hz) for 10 and 50 N_{SP}. (a) and (d) Temporal signals acquired at a SP; (b) and (e) *zoom* of the temporal signal for pulse observation; and (c) and (f) the acoustic field of the stimulus. . . . 92
5.11 Results of the combined Dynamic sensation (10 points) and the Uniform sensation (50 points). (a) Temporal signal acquired at a shape point's position; (b) *zoom* of the temporal signal for pulse observation; and (c) stimulus's acoustic field. . . . 93
5.12 Creation of a combined sensation. . . . 93

6.1 Stimulus Onset Asynchrony in the context of the dynamic haptic sensation. . . . 103
6.2 Temporal requirement for movement perception of the FP. . . . 104
6.3 Dynamic rough and smooth perception and its association with 2PDT thresholds. . . . 106
6.4 Types of dynamic sensations - moving pressure (top) and moving vibration (bottom). . . . 107
6.5 The types of haptic dynamic sensation regimes. (Top) Parameter defining the dynamic sensation regime. (Bottom) Parameters defining the type of the dynamic sensation. . . . 108
6.6 Perceptually similar pulses. The pulse stimuli A and B evoke similar sensations. . . . 110
6.7 Shape point's signal for a dynamic pressure sensation. (a) Pulse signal of a single SP and (b) signals of *all* SPs of the pattern. . . . 111
6.8 Shape point's signal of optimized dynamic pressure sensation. (a) Pulse signal of a single SP and (b) signals of *all* SPs of the pattern. . . . 111
6.9 Modulation of the pulse signal of the SP. . . . 112
6.10 SP's signals considered in the perceptual analysis. SP's signal for pattern A is 50% pulse-modulated. SP's signal for pattern B is not pulse-modulated but has half the SP duration of A. . . . 113
6.11 Perceptual analysis of stimulus A in the context of the dynamic sensation. . . . 113
6.12 Perceptual analysis of stimulus B in the context of the dynamic sensation. . . . 114
6.13 Comparison of the sensations for the case A and case B. . . . 114

7.1 Spatiotemporal haptic stimulus and the signals involved in its creation. . . . 120
7.2 The spatial and temporal components of the SP's signal. . . . 121

7.3 Discretization of the haptic pattern in time and space dimensions. 121
7.4 Illustration of the spatial signals for the Shape Position (SP)s of the pattern. 122
7.5 Illustration of the temporal signals for the SPs of the pattern. 122
7.6 Creation of the SPs' signals. 123
7.7 Illustration of the haptic pattern spatiotemporal signal, as a summation of the composing SPs' signals. 123
7.8 Amplitude modulation scenarios considered for the temporal reference signal. 125
7.9 Window signal used in the generation of the SP's temporal signals. 125
7.10 Sliding window approach for generating SP's temporal signals. 126
7.11 Occurrence time instants of the SPs of the patterns, encoded by shifted impulses. . . . 126
7.12 Shifted window obtained through convolution. 127
7.13 Time-shifted windows associated with the temporal occurrence of the SPs of the pattern. 127
7.14 SP's temporal signals of the pattern obtained from windowing approach. 128
7.15 Spatial reference signal and corresponding FP generation. 128
7.16 Spatial convolution for generating SP's phases. 129
7.17 SP positions of the pattern represented as spatial shifted impulses. 129
7.18 Spatial component obtained via convolution. 130
7.19 Representation of the 'real' and 'virtual' reference signals. 131
7.20 Illustration of the computational convolution shortcoming. 131
7.21 Convolution limitation overcoming by increasing signal dimensions. 132
7.22 Creation of multiple FPs by means of the linearity property of the UMAH system. 133
7.23 Generation of a combined sensation's spatiotemporal signal obtained by adding individual dynamic sensation spatio-temporal signals. 134
7.24 Phase discontinuity problem in ultrasonic mid-air systems. 135
7.25 Phase discontinuity illustrated in a single transducer STM signal. 135
7.26 Window function used for smoothing phase transitions. 135
7.27 Effect of the smoothing window on consecutive SP's signals and their overlaping. 136

8.1 Circular patterns with different sizes.(Left) is a 10 cm length pattern ($N_{SP} = 7$). (Right) is a 15.7 cm pattern ($N_{SP} = 10$). Both patterns have the same haptic spatial resolution. . . 140
8.2 Patterns with different haptic spatial resolutions. (Left) is a pattern composed of 10 SPs. (Right) a pattern made of 30 SPs. Both patterns have 15.7 cm in length. 141
8.3 Pattern shapes implemented in the haptic stimulus generator module – circle, line, square, triangle, ellipse, spiral, cardioid, rhombus and four-pointed star. Some patterns have constant spatial resolution (e.g., circle, line, square, rhombus), while others exhibit varying spatial resolution (e.g., ellipse, spiral and cardioid). 142

8.4 Temporal modulation of the FP's amplitude. In this case, the amplitude varies sinusoidally at 200 Hz. The images on the left depict the spatial pressure field of the FP, and the images on the right depict the temporal variation of the FP's amplitude. 143
8.5 The FP being spatially and temporally modulated. For visualization purposes, the drawing period (T_{draw}) is highly exaggerated. It is possible to observe that while the position of the FP is being changed, the FP's amplitude is varying as well ($f_{draw} = 200\ Hz$). 145
8.6 Haptic stimulus composed by two FPs. The inner pattern is a circle with 10 cm length. The outer pattern is a square shape with 24 cm in length. The square is drawn about three times faster than the circle. Moreover, the circle is made of 7 SPs (rough texture) and the square is made of 48 SPs (smooth texture). 146
8.7 Haptic stimulus composed by two FPs. Each FP describes a line segment, but with different orientations. The two lines meet at the center and, in that position, the amplitudes add up and a stronger sensation event occurs. 147
8.8 Haptic beat sensation. Two FPs travel at different speeds. Thus, the faster FP crosses the slower FP three times (i.e., three beats) per half drawing cycle (of the slower FP). Every time a beat happens, a stronger and localized tactile event occurs. 149
8.9 Haptics stimulus illustrating the 'noise click' problem. Two SP positions are used for easy explanation. At frame instant $t = 100$ ms, the FP jumps to the new SP and a click noise is created. 150
8.10 Haptic stimulus showing the phase smoothing procedure. In this case, the phase smoothness rate was highly exaggerated for visualization purposes. Two SPs were considered for the demonstration. 151
8.11 Optimization strategy 1 for the dynamic sensation. A long duration pulse (in this case a 100 ms duration SP) is modulated as two short pulses (18 ms each) displayed at the beginning and end of the SP. 152
8.12 Optimization strategy 2 for the dynamic sensation. The FP is kept ON for 50% of the SP's duration and then turned OFF. Only two SPs are represented. 153

List of Tables

1.1 Summary of key concepts of the thesis. 9

2.1 Transducer Attenuation as a function of angle. 18

3.1 Summary of modulation techniques and corresponding parameters. 38

4.1 Comparison between simulation, microphone measurement and scale measurement results. 76

5.1 Description of the haptic sensations produced by STM. 80
5.2 Results of the Shapiro–Wilk normality test for different N_{SP} values (n=18). 85
5.3 Results of the D–V boundary region. 85
5.4 Results of the matched-sample t-test for different N_{SP} combinations. 85
5.5 Results of the Shapiro–Wilk normality test for different N_{SP} values (n = 18). 86
5.6 Results of the V–U boundary region. 87
5.7 Boundary regions specification: D–V and V–U. 88
5.8 STM sensations used in the experiment. 94
5.9 Combined STM sensations used in the experiment. 95
5.10 Sensation identification rates per N_{SP} (confusion matrix). 96
5.11 Sensation identification rates per v_{FP} (confusion matrix). 96
5.12 Confusion matrix for the combined sensations (FP's speed). 97
5.13 Sensation confusion matrix for the combined sensations (averaged per FP's speed). . . 97

Acronyms

2PDT Two-Point Discrimination Threshold

ADC Analog-to-Digital Converter
AESI Advanced Engineering Systems for Industry
AM Amplitude Modulation
AR Augmented Reality
ARM Advanced Risc Machine
AXI Advanced eXtensible Interface

CMUT Capacitive Micromachined Ultrasonic Transducer

ESRG Embedded System Research Group

FP Focal Point
FPGA Field Programmable Gate Array
FTDI Future Technology Devices International
FWHM Full-Width at Half-Maximum

I/O Input/Output
IDE Integrated Development Environment
INL Iberian Nanotechnology Laboratory
IP Intellectual Property
IQR Inter Quartile Range

JTAG Joint Test Action Group

LM Lateral Modulation

PC Pacinian Corpuscles

PCB Printed Circuit Board
PhD Doctor of Philosophy
PIEP Pólo de Inovação em Engenharia de Polímeros
PL Programmable Logic
PMUT Piezoelectric Micromachined Ultrasound Transducers
PPT Printed Polymer Transducer
PS Processing System
PWM Pulse-Width Modulated

RA Rapidly Adapting receptors
RA1 Meissner Corpuscles
RMS Root Mean Square
RQ Research Question

SA Slow Adapting receptors
SA1 Merkel Cells
SOA Stimulus Onset Asynchrony
SoC System-on-Chip
SoM System-on-Module
SP Shape Position
SPL Sound Pressure Level
STM Spatio Temporal Modulation

TOJ Temporal Order Judgment

UART Universal Asynchronous Receiver–Transmitter
UMAH Ultrasonic Mid-Air Haptics
UR Update Rate
UR$_{max}$ Maximum Update Rate
UX User Experience

VR Virtual Reality

Introduction

1.1 Contextualization

Before starting the Doctor of Philosophy (PhD), I worked on a research project titled Cockpit of the Future, a collaboration between Bosch Car Multimedia (Braga) and the University of Minho (Guimarães). I was part of a multidisciplinary team within the Embedded System Research Group (ESRG) at the University of Minho. During this project, the team developed Ultrasonic Mid-Air Haptics (UMAH) prototypes and demonstrators. These were integrated into a final demonstrator for a futuristic automotive cockpit.

Within this team, I was responsible for implementing algorithms (previously developed by the simulation team) on embedded systems. My main tasks included implementing and testing these algorithms in low-level software (C language) as well as on Field Programmable Gate Array (FPGA). The implementations were subsequently deployed on a hardware platform designed by the Printed Circuit Board (PCB) hardware team.

I later enrolled in the Advanced Engineering Systems for Industry (AESI) PhD program which has a strong industrial orientation. It is carried out in partnership between the University of Minho and Bosch Car Multimedia (Braga), and is co-funded by the Portuguese government.

Bosch Car Multimedia is a company involved in the development of infotainment systems for vehicles. My PhD research was focused on UMAH. The technology addressed in this thesis aligns with the research conducted within the company, which was interested in assessing whether this technology could represent a market opportunity.

This thesis focuses on a specific haptic technology known as UMAH. These types of systems create tactile sensations in mid-air, typically on the user's palm. Sensations are notable for their unique character and for challenging sensory intuition, as they are produced invisibly in space.

This technology is used in a variety of applications ranging from Virtual Reality (VR) and Augmented Reality (AR) (Howard et al., 2020; Hwang et al., 2017; Villa et al., 2022), multi-modal interaction (Hirayama et al., 2019) and acoustic levitation (Seah et al., 2014). Moreover, UMAH has also been explored in the automotive domain (Georgiou et al., 2017, 2026; Harrington et al., 2018; Large et al., 2019; Shakeri et al., 2018; Young et al., 2020), particularly for providing haptic feedback to support interaction with vehicle infotainment systems. The technology has more recently been featured in a concept vehicle (DS Automobiles, 2021), such as the one illustrated in Figure 1.1, where passengers could experience a refined interior ambience and interact with the car in an exclusive manner through UMAH technology.

The haptic sensations created through this technology can transform user interaction with the vehicle into a unique experience. For this reason, it is often associated with futuristic cockpits and autonomous vehicles, which are expected to be more spacious, allowing greater freedom of movement for passengers.

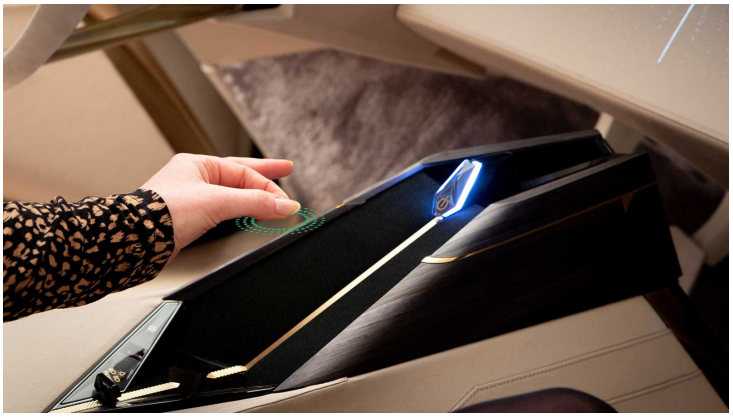

Figure 1.1: Ultrasonic mid-air haptic system used in a DS concept automobile for the creation of haptic feedback

Through a set of multimodal interfaces—including visual, auditory, and tactile modalities—passengers will be able to perform a variety of tasks while being driven.

Due to these associations, the technology has gained popularity. Nonetheless, given the shortcomings of UMAH technology, these systems are not yet implemented in any major application, including the automotive sector.

In summary, UMAH technology was initially driven by the appeal of its unique tactile sensations. However, largely due to current technological limitations, the resulting sensations often fall short of user expectations. Therefore, it is necessary to identify and mitigate these limitations to enable the technology's broader adoption.

1.1.1 Research Challenges

The limitations hindering the adoption of UMAH technology are as follows: To generate tactile sensations, UMAH systems require the emission of (i) high levels of acoustic power. Prolonged exposure to such ultrasonic radiation may pose risks to human hearing (Liebler et al., 2020; Liebler et al., 2019); and, the critical technological shortcoming is that the tactile sensations produced by UMAH systems are (ii) weak or faint (Georgiou et al., 2022; D.-G. Kim & Choi, 2024; Rakkolainen et al., 2019, 2021). This reduces the recognizability of the sensations and can lead to user frustration. The technology is likely to achieve greater market success if these shortcomings are addressed.

Several approaches have been proposed to address the problem of weak stimulus intensity associated with weak tactile sensations. In some studies, authors increased the size of the haptic array (Hasegawa & Shinoda, 2018; Hoshi et al., 2010; Shinoda, 2013), which is the component responsible for delivering the acoustic energy for producing the haptic tactile sensations. However, enlarging the haptic array is unreasonable in many applications. The typical haptic array size is approximately 15 × 15 cm, and, for

instance, in automotive applications, the space available in the centre console—where such devices are usually installed—is limited.

One possible solution involves the development of novel haptic arrays with fundamentally different ultrasonic transducers. Efforts in this direction include transducer's technologies such as: Printed Polymer Transducer (PPT) (Peters et al., 2019; van Neer et al., 2019), Capacitive Micromachined Ultrasonic Transducer (CMUT) (M. C. Kim et al., 2025), Piezoelectric Micromachined Ultrasound Transducers (PMUT) (Billen et al., 2022; Halbach et al., 2019; Liu et al., 2022) among others. Although these represent promising solutions, they still cannot generate acoustic fields with the optimal characteristics for mid-air haptic systems, such as interaction range and stimulus intensity.

The possibility of this thesis pursuing a research path focused on the development of new transducers was limited by lack of fabrication facilities. It is worth noting that shortly after the start of this thesis, a partnership was established with the Iberian Nanotechnology Laboratory (INL) to develop a new type of haptic phased array. This collaboration continues to the present; however, due to reasons beyond the scope of this thesis, no new prototype was provided. Additionally, it is important to highlight that the research group in which this work was conducted (ESRG) had expertise in fabricating the 'traditional' UMAH phased-arrays, which exhibit the key limitations earlier described. Two UMAH prototypes were developed by ESRG team (discussed in Chapter 4) and were used to carry out the research presented in this thesis.

In 2024, Ultraleap (now part of ROLI) (Ultraleap, 2025), one of the leading market players in this technology, presented a promising haptic array. The haptic array is shown in the left side of the Figure 1.2. Few details about its implementation are publicly available due to confidentiality. It can be observed that the system features a modular array approach that can be combined (possibly) to increase the overall power. The transducers in the array (right side of the image) are considerably smaller than the traditional piezoelectric transducers, without compromising power (AudioWell, 2024). This guarantees the haptic stimuli strength and reduces the overall size of the haptic array. Furthermore, this prototype incorporates additional features designed to enhance the performance of the mid-air haptic system. The asymmetric arrangement of the transducers within the array mitigates a classic problem of UMAH systems, namely, the occurrence of grating lobes. To the best of our knowledge, this device represents the most advanced phased array for standard ultrasonic mid-air haptics applications.

To better understand the grating lobe phenomenon, it is necessary to examine how the haptic stimulus is generated. The Focal Point (FP) is the stimulation "agent" (or "haptic pixel"), and corresponds to a small region in space where the acoustic pressure generated by the haptic array is focused. The FP is a localized region where acoustic waves from the multiple ultrasounds combine to produce high acoustic pressure FP. Each transducers' phase is controlled so that the ultrasonic waves arrive in phase at the target FP

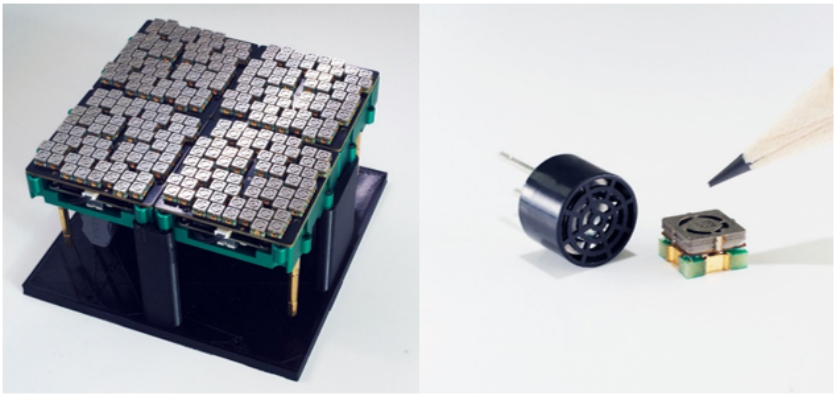

Figure 1.2: State-of-the-art UMAH developed by Ultraleap (left image). Ultrasonic transducer developed by Ultraleap compared with the traditionally ultrasonic transducer (right image).

location. The acoustic field associated with the FP takes the form of a spatial sinc function (Kinsler et al., 1999). As illustrated in the Figure 1.3, the function's shape exhibits a central region of maximum intensity (i.e., the FP) surrounded by four less intense beams (but still perceivable), known as grating lobes.

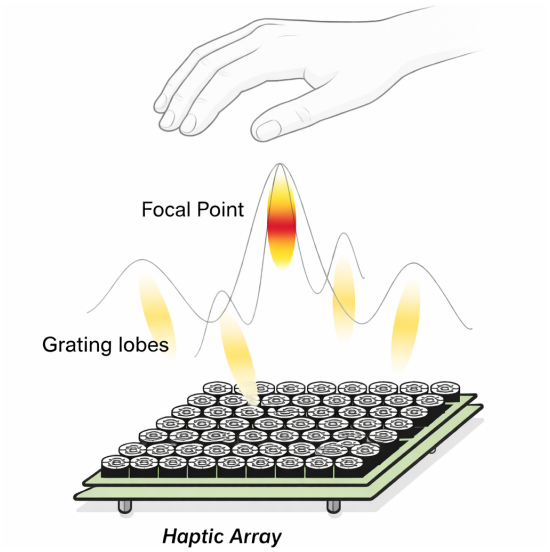

Figure 1.3: The acoustic field created by the haptic array. The FP (i.e., haptic pixel) is surrounded by the grating lobes.

Grating lobes are undesirable for several reasons. They represent acoustic energy that is "wasted" because it is emitted into the interaction space without any haptic utility. Although less intense than the FP, grating lobes can be sensed, and if felt involuntarily, they can distort the perception of the intended haptic sensation (Price & Long, 2018). Therefore, addressing the grating lobe problem constitutes a meaningful research objective.

Grating lobes occur in regions of space where the distance from the transducers corresponds to an integer

multiple of the wavelength. In these regions, the haptic array emitted waves interfere constructively. This issue can be mitigated in two main ways. First, by reducing the size of the transducers so that its diameter is smaller than the emitted wavelength (Price & Long, 2018) (and closely assembled them) the grating lobes are "pushed" to distant regions outside the interaction space, rendering them insignificant. Second, the formation of grating lobes is influenced by the spatial arrangement of the transducers within the array (Gavrilov, 2008; Rakkolainen et al., 2021). For instance, a quadrangular grid—commonly used in UMAH systems—produces four grating lobes due to its axes of symmetry (Camelo, 2020). In contrast, irregular geometries are less prone to grating lobe formation, as the grid symmetry is minimized (Gavrilov, 2008; Price & Long, 2018).

Both aforementioned solutions require the construction of new haptic arrays. At the beginning of this thesis, the research group was developing an array with a quadrangular grid, making it impractical to discard the invested time and resources to build a new one with an irregular arrangement. Furthermore, irregular arrays have an important implication: the spatial arrangement of the transducers is less efficient, meaning that such arrays have lower power output per unit area (Price & Long, 2018). This reduction leads to lower intensity of the haptic stimulus.

There are approaches to reduce grating lobes (Carter et al., 2013; Gavrilov et al., 1997) without modifying the array itself, such as algorithmic methods (Carter et al., 2013; Long et al., 2014) or apodization techniques (Gavrilov et al., 1997; Guo et al., 2013). For instance, apodization techniques consist in decreasing the amplitude of the transducers that contribute the most to the grating lobes formation. However, these approaches share a common drawback: they imply a reduction of the FP's intensity, too. Thus, while attempting to suppress grating lobes, one would simultaneously worsen the other critical limitation of the technology, the stimulus intensity (Price & Long, 2018).

The Figure 1.4 shows the UMAH prototype developed by the ESRG team from the University of Minho. The UMAH system produces a tactile feedback on the user's palm.

Another research question to address was how to improve the haptic stimulus perception, which is considered the main limitation of the technology. During this research, several recent studies were published on a new haptic modulation technique known as Spatio Temporal Modulation (STM) (Frier et al., 2018; Takahashi et al., 2018, 2019). Haptic modulations are techniques that control (or modulate) the FP to create haptic sensations. And the STM is interesting because it creates stronger haptic sensations than traditional haptic modulation techniques.

Motivated by the positive results associated with the STM, the research focused on exploring stimulus perception, particularly those created through STM. Findings from STM research show that modulation techniques can significantly enhance the perceived intensity of the haptic stimulus (Frier et al., 2018, 2019; Takahashi et al., 2018, 2019) without requiring modifications to the system's hardware. Therefore,

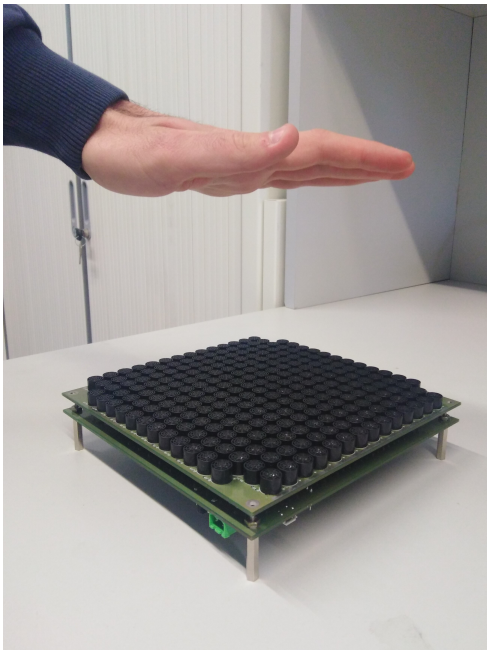

Figure 1.4: UMAH demonstrator developed by ESRG team from University of Minho

through novel modulation techniques (such as STM), it may be possible to improve stimulus perception without modifying the system's hardware. Consequently, limitations in haptic stimulus intensity can be addressed without necessarily increasing the emitted acoustic power levels.

One of the main focuses of the UMAH field should be the improvement of the perceived haptic sensations through perceptual research (and techniques), rather than solely through hardware modifications (such as, e.g., enlarging the haptic array). In other words, the enhancement of the haptic sensations should follow a user-centric approach grounded in perceptual factors, which hardware development should then support and further improve.

1.1.2 Taxonomy

A brief classification (or taxonomy) of several concepts is presented in this section. Although these concepts are generally well known, they appear frequently throughout the thesis and, if not properly understood, may hinder the reading. This taxonomy is therefore intended to clarify these concepts and facilitate a clearer and simpler understanding of the research work presented in this thesis. The concepts addressed are haptic stimulus, sensation, perception and haptics. These are distinct yet strongly related concepts.

In the context of this thesis, a haptic stimulus corresponds to the acoustic energy generated by UMAH system. This mechanical-acoustic energy originates the FP haptic stimulus. The FP is the stimulating agent and may or may not, depending on its characteristics, produce a haptic sensation (typically on the palm of the hand). For instance, a non-modulated FP is not able to generate a haptic sensation in the

user of the system. However, when the FP's amplitude is modulated—for example, at 200 Hz frequency—it becomes capable of eliciting a tactile sensation in the user. In both cases, acoustic energy is generated; however, only in the latter case does the haptic stimulus produce a haptic sensation.

When a stimulus activates sensory tactile receptors of the skin, they generate a response in the form of a tactile sensation (e.g., vibration or pressure). A tactile sensation is a physiological response to the detection of a stimulus by the human skin. For example, a modulated FP can produce a vibration or a pressure sensation on the user's skin.

User perception, in turn, is a more complex process that involves the interpretation of the haptic sensation by the user. It is a cognitive process and entails the subjective interpretation of the sensory input. For example, a vibration may be interpreted as a virtual button or another specific perception.

The term tactile haptics broadly encompasses everything related to the sense of touch (in this case, through the skin). It is the field that studies how we perceive and interact with the world through touch. It is a more comprehensive and holistic concept than those previously described, as it includes the study of tactile interactions and experiences — mediated by stimuli, sensations, and perception—as well as the technologies that enable them. In our context, a UMAH system is capable of generating tactile haptic sensations felt by the user, which can be perceived has a virtual buttons, patterns, etc.

The concepts explained in the section are inter-related and, the relation among them is graphically explained in Figure 1.5. Moreover, on Table 1.1 the referred concepts are summarized. The definition for the tactile detection threshold was also added to the table, as it appears commonly throughout the thesis.

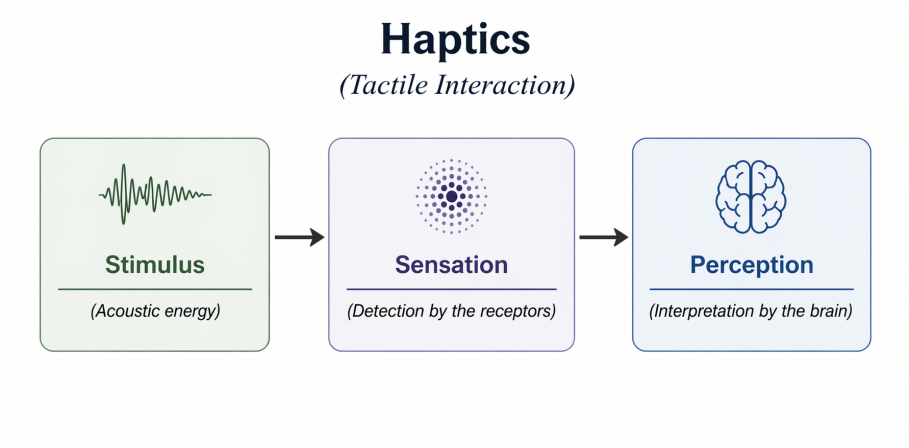

Figure 1.5: Schematization of key concepts of the thesis.

Table 1.1: Summary of key concepts of the thesis.

Concept	Definition
Stimulus	A stimulating agent (energy) generated by the haptic system that may or may not, depending on its characteristics, produce a sensation.
Tactile Threshold	The minimum or lowest amplitude quantity of a stimulus (force, pressure or displacement) causing a sensation.
Sensation	The (physiological) response of sensory receptors upon detection of a stimulus.
Perception	A cognitive and subjective process of interpreting a sensation.
Haptics	A broad concept that encompasses how we perceive and interact with the world through the sense of touch.

1.1.3 Spatio-Temporal Modulation

Spatio-temporal modulation generates stronger haptic sensations (Frier et al., 2018, 2019; Takahashi et al., 2018, 2019). This motivated research focused on the haptic modulation to try to enhance the haptic stimulus perceived by the user.

In practical terms, the STM consists in a moving FP that follows shapes (e.g., lines, circles or squares). In Figure 1.6, the FP moves along a circular pattern. Despite the apparent technical simplicity, from a psychophysiological point of view the STM's perception is complex due to the spatial and temporal dynamics of the haptic stimulus (Mendes et al., 2024).

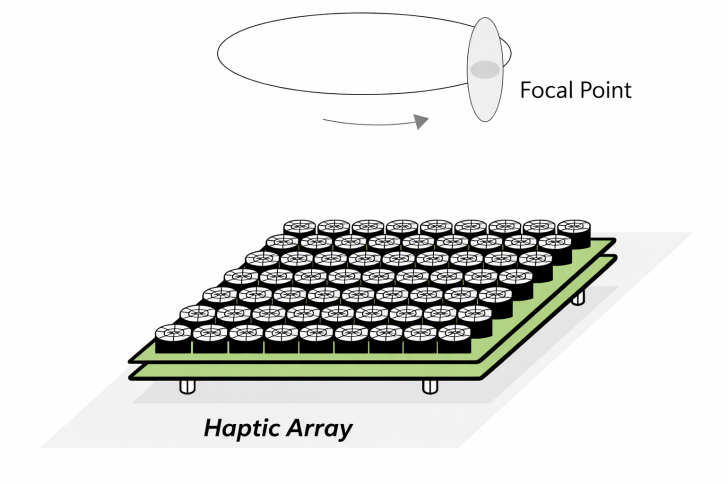

Figure 1.6: A STM circular pattern. The FP is generated by the haptic array and controlled to trace a circular pattern.

Perhaps due to the inherent complexity of STM, several studies describe distinct sensations produced by spatio-temporal haptic stimuli (Ablart et al., 2019; Frier et al., 2019; Mendes et al., 2024; Morisaki et al., 2022). A simple mental exercise helps illustrate this fact. Imagine a ball attached to the tip of a helicopter's blade. During take-off, the rotor initially moves slowly, allowing vision to track the ball's motion. As the helicopter gains lift and the rotor accelerates, the blade rotates so quickly that the motion of the ball can no longer be followed. Instead, what is perceived is the entire area swept by the ball. Similarly, in the tactile perception, when the FP moves slowly, its trajectory can be distinguished, whereas at higher speeds the sensation corresponds to the overall path traced by the FP.

The modulation appears to elicit distinct haptic sensations, each likely governed by a different underlying tactile mechanism. The initial research of this thesis focused on specifying the sensation (also referred to as sensation regimes) created by STM by the parameters affecting STM perception. Such parameterisation can, for instance, serve as a guide for designing haptic sensations. This work is essential for understanding the psychophysiological processes underlying the STM. Ultimately, contributing to the development of novel and optimized haptic sensations, whether from an acoustic or a tactile standpoint.

A second line of research was pursued, also centered on the STM. In the initial research, the haptic sensations used for evaluation required that the User Experience (UX) designer had technical background on the STM (i.e., for designing and implementing the stimulus). This represents a barrier to the use of STM because it entails a learning curve for implementing the haptic modulation (Seifi et al., 2023).

Driven by the goal of enabling broader access to the use of STM, a (proof-of-concept) haptic sensation generation tool was developed. The tool abstracts the UX designer from the complexity involved in creating STM haptic sensations. In practical terms, the UX only needs to specify the desired haptic sensation, and the tool produces the corresponding signals to feed the haptic array. If needed, the tool also allows full stimulus customization. This flexibility is key for those who aim to develop novel and potentially optimized haptic sensations.

Both research efforts carried out in this thesis contribute to advancing perception in UMAH. The research work carried out provides groundwork toward an important goal: the creation of novel and potentially more optimized haptic tactile stimuli.

1.2 Motivation

I have always had the desire to continue studying as part of my personal and scientific development. The opportunity to pursue a PhD research in UMAH technology was also a major source of motivation. I became deeply interested in this technology and remain fascinated by its wide range of potential applications. The haptic sensations it creates, and the way in which it does so, challenge human intuition and inspired me to further explore and haptically advance the technology. This ultimately led me to pursue a PhD in this

field, which is particularly rich, encompassing areas such as haptics, perception, mathematics, physics, embedded systems, and electronics.

1.3 Research Questions

The main goal of this thesis is to improve ultrasonic mid-air haptic sensations, which has been identified as a fundamental challenge in UMAH technology. STM is a haptic modulation technique capable of creating stronger haptic sensations, and for this reason, this modulation technique is the central topic of this thesis.

The research work carried out in this thesis was conducted in two different parts. In the first part, the sensorial regimes produced by STM were specified. This study contributed to the field of UMAH by providing a concrete specification of the haptic sensations created by the STM modulation. Additionally, as an intangible outcome, it created knowledge and understanding regarding the perception of STM. The main Research Question (RQ) of the first study is:

- Can STM elicit distinct tactile sensations?

This primary question can be divided into two research sub-questions that, together, help to answer the main one:

- RQ1: How to establish a specification for the haptic sensations?
- RQ2: How can a preliminary validation of the specification be obtained?

A tool for generating haptic sensations based on STM became a necessity within this thesis research work. Its goal is to assist the haptic UX designer, or perceptual researcher, in creating haptic sensations in a simple, intuitive, and automated manner. Moreover, this type of tool is relevant to the field of UMAH, as it simplifies the creation of haptic tactile stimuli (Seifi et al., 2023) and thus the next research question:

- RQ3: How can a tool capable to generate STM based sensations be developed?

This tool was specifically designed to generate haptic sensations based on the STM. There is a fundamental distinction between what constitutes a sensation and what constitutes a stimulus: a sensation is a stimulus that is perceived through touch, whereas a stimulus by itself may or may not be felt.

The sensation specification layer, developed in Chapter 6, is one of the main contributions of this part of the thesis. It aims to abstract the user of the tool from the haptic stimulus parameterization corresponding to

the specific haptic sensation. Moreover, the haptic stimuli generation algorithm is also a main contribution and constitutes the core of the tool. It was specifically designed for STM modulation and is detailed in Chapter 7. The algorithmic approach enabled the construction of a stimulus-generation module that creates sensations in a simple and efficient manner and that among other things, can be used to generate novel and optimized stimuli.

1.4 Methodology

- *RQ1: How to establish a specification for the haptic sensations?*

Method 1 (M1): The specification for the STM based haptic sensations was carried out for three sensorial regimes of the modulation. First, the three regimes were characterized in terms of perceived sensation by the system's users, based on numerous experiences with the haptic modulation technique. Subsequently, a subjective study was conducted with the involvement of 18 participants. The study's goal was to specify and define the three regimes. The distinct regimes were controlled by two modulation parameters: the focal point speed and the number of points composing the haptic pattern. The boundaries between the sensory regimes were quantified using the method of limits approach and other specific developed approaches. Two boundaries were specified, which was sufficient to define the three haptic sensations of the STM technique. Further methodological details can be found in Chapter 5.

- *RQ2: How can a preliminary validation of the specification be obtained?*

Method 2 (M2): To validate the specification developed in M1, a subjective study was conducted with 10 participants. In this study, participants were asked to identify the STM based haptic sensations present in each stimulus. A set (or palette) of sensations were created, consisting of sensations corresponding to the ones specified in M1. The aim of the study was to measure the identification rates of the haptic sensations. In addition to the "normal" spatio-temporal snesation (i.e., those specified in M1), new combined sensations were also created. A combined sensation is composed of two "normal" sensations presented within the same haptic stimulus. The purpose of including combined sensations was to observe whether participants could identify the sensations composing the combined stimulus. Through this approach, preliminary evidence was provided that STM based sensations indeed have their own distinct perceptual nature.

- *RQ3: How can a tool capable to generate STM based sensations be developed?*

Method 3 (M3): In this context, an algorithm capable of generating STM haptic stimuli was developed. This algorithm, which constitutes the core component of the tool, was specifically designed for the STM. To

enable the generation of haptic stimuli corresponding to STM haptic sensations, an additional *component* was developed to abstract the UX designer from the configuration and parameterization required for haptic sensations creation. As a proof of concept, only haptic sensations corresponding to the dynamic sensory regime (described in Chapter 6) were specified. This *component* was developed based on the knowledge acquired from the study of Chapter 5, and from perceptual literature too. To validate the generated sensations (or any kind of STM stimuli), a simulator (described in Chapter 4) was integrated into the tool. The simulator was adapted to provide visualization of the haptic stimuli generated by the stimuli generator module.

1.5 Main Contributions

During this research work, and with the help of an ESRG team, two UMAH prototypes were developed (details of their implementation can be found in Chapter 4). These prototypes were used in several demonstrators and represent a milestone for UMAH technology in our country. Furthermore, they were extensively used in the research conducted in this thesis.

The research-work developed during this thesis resulted in two main scientific articles. Both Scopus indexed articles focused solely in the research work discussed in Chapter 5 of this thesis. The first publication was a conference article (Mendes et al., 2022) and the second publication was a Q1 journal article (Mendes et al., 2024). In addition, parts of the research work were shared and resulted in another Q1 article as a second author (Santos et al., 2024).

List of Publications:

1. Eduardo Mendes, Paulo Santos, João Carvalho and Jorge Cabral, "Spatiotemporal Modulation for Ultrasonic Mid-Air Haptics: Sensation's Specification and Validation,"*IEEE Transactions on Haptics*, vol. 17, no. 3, pp. 429-440, year. 2024; DOI: 10.1109/TOH.2024.3355187

2. Eduardo Mendes, João Carvalho, Paulo Santos, Edoardo Sotgiu and Jorge Cabral, "Preliminary Assessment of Combined Stimuli with Laterally Modulated Midair Ultrasound Focus,"*2022 International Symposium on Electrical, Electronics and Information Engineering (ISEEIE)*, year. 2022; DOI: 10.1109/ISEEIE55684.2022.00048

3. Paulo Santos, Eduardo Mendes, João Carvalho, Filipe Alves, José Azevedo and João Cabral, "Hardware accelerated Active Noise Cancellation system using Haar wavelets,"*Microprocessors and Microsystems*, vol. 107, year. 2024; DOI: 10.1016/j.micpro.2024.105047

A haptic sensation generation toll was also developed. This tool, which is based on the STM, simplifies the generation of the haptic sensations while offering at the same time, full customization of the sensations.

This tool can be used by UX designers in the development of tactile experiences and by haptic researchers involved in the development of new and/or optimized haptic sensations.

1.6 Organization of the Thesis

This thesis is organized as follows. Chapter 1 provides an introduction and contextualization of the research topic. It also presents the research questions and the methodology adopted to address them. The next chapter, Chapter 2, covers the fundamental principles underlying the physical generation and perception of UMAH stimuli. This chapter aims to provides the necessary background for understanding the work developed throughout the thesis. In Chapter 4, the UMAH system developed at the University of Minho is presented. This haptic system, which was used to conduct the research described in this thesis is described in detail, from its physical structure to the implemented system architecture. Additionally, the simulator developed within the scope of this thesis is introduced, along with selected results obtained using the prototype. Chapter 3 focuses on the main haptic modulation technique researched during the PhD thesis. The STM haptic modulation is presented from both technical and perceptual perspectives. In chapter 5 the research conducted on STM haptic sensation regimes is discussed. Two perceptual studies were carried out: one aimed at specifying these regimes, and another aimed at their preliminary validation. This work can be regarded as the first part of the thesis.

The following three chapters (Chapters 6, 7 and 8) correspond to the second part of the thesis, which focuses on the STM haptic sensation generation tool. Chapter 6 addresses the specification of the dynamic haptic sensation (one of the sensations studied in Chapter 5) and used as an exemplificative use case of the tool. Next, Chapter 7 details the core component of the tool, namely the STM haptic stimulus generation module. The algorithm developed for the system's signal generation is here described in detail. Key features are also presented, including the generation of combined haptic stimuli and phase smoothing. Haptic stimuli simulation results are also provided for the validation of the tool and are described in Chapter 8. Finally, Chapter 9 presents the conclusion of the doctoral research work and outlines directions for future research.

Fundamentals of Ultrasonic Haptics

2.1 Focal Point's principles

The FP is a localized region in space where the acoustic waves emitted by many transducers sum together producing a high-amplitude pressure. The phase (and amplitude) of the transducers is controlled so that the waves arrive in phase to that point in space. If the phase-delay of each transducer compensates its distance to the target point, then all contributions arrive to the target point with the same phase. The Figure 2.1 depicts the creation of the FP. As can be seen the ultrasonic waves emitted by the haptic phased-array are focused in a high-intensity region, the FP.

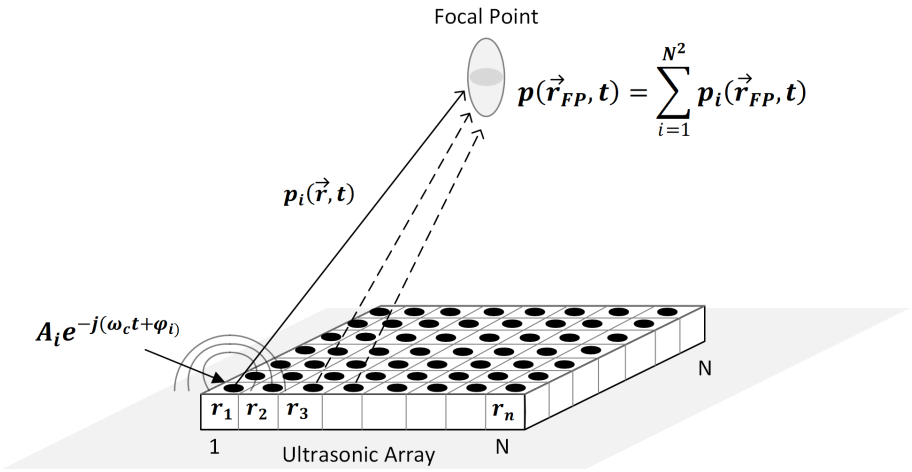

Figure 2.1: The FP generation from the ultrasonic haptic phased-array.

Consider N^2 transducers arranged in a matrix ($N \times N$), where r_i is the position of the i-th transducer in the matrix ($i = 1, 2, \ldots, N^2$). Transducers emit harmonic waves with angular frequency ω_c. ω_c is given by $2\pi f_c$ where f_c is the ultrasonic carrier frequency. The wave number k is defined by $k = \omega_c / c$ (where c is the speed of sound in air) and is the spatial frequency of the wave. The pressure amplitude at the transducer's surface is defined by A_i, and the phase of the pressure wave is set by φ_i.

The pressure (p_i) created by the i-th transducer at the point in space $\vec{r}$ ($r \in \mathbb{R}^3$), is given by (Kinsler et al., 1999):

$$p_i(\vec{r}) = \frac{A_i}{r_i} e^{-j(kr_i + \varphi_i)} \tag{2.1}$$

Where r_i is the distance from the transducer's center ($\vec{r_i}$) to the point in space $\vec{r}$.

The instantaneous pressure at a given point in space can be obtained by *adding* the temporal behavior of the wave into equation 2.1. Moreover, by linear superposition, the total pressure at the point $\vec{r}$ created by the N^2 transducers is calculated by:

$$p(\vec{r},t) = e^{j\omega_c t} \sum_{i=1}^{N^2} p_i(\vec{r}) \tag{2.2}$$

The local acoustic energy depends on $|p(\vec{r},t)|$.

The FP is produced by focusing the wave emission at a position of the FP (i.e., $\vec{r}_{FP}$). In order to maximize $|p(\vec{r},t)|$, the phases of the transducers (φ_i) should be calculated to compensate for the propagation phase.

$$\varphi_i = k\, r_i \Leftrightarrow \varphi_i = k\, ||\vec{r_{FP}} - \vec{r}_i|| \tag{2.3}$$

In simple terms, the goal is that the term in the exponent of Equation 2.1, $(kr_i + \varphi_i)$, remains equal for all transducers (i). Thus, all pressure contributions arrive with the same phase at $\vec{r}_{FP}$ location and add in a constructive manner.

2.1.1 Physical Principles

The acoustic pressure of the FP can be more realistically calculated through the following solution of the linear homogeneous wave equation (Kinsler et al., 1999). Which essentially extends the result developed in Equation 2.1.

$$p_i(\vec{r}) = \rho c U_0 \frac{a}{r_i} e^{-jkr_i}, \quad \text{for } r_i > a \tag{2.4}$$

Where p_i is the pressure [Pa] created by the i-th transducer at the point in space $\vec{r}$. The distance r_i is measured from the center of the transducer ($\vec{r}_i$) to the point $\vec{r}$. The term a is the radius of the transducer's surface (around 5 mm for typical UMAH transducers). ρ is the medium density [kg/m^3] (1.21 kg/m^3 at 23°C), and c is the speed of sound in air [m/s] (343 m/s at 23°C). The term U_0 [m/s] is the amplitude of the radial displacement velocity of the emitter. It is a parameter related to the maximum power of the transducer and can be calculated based on the transducer's datasheet. As explained previously, k is the wave number also defined by $k = 2\pi/\lambda$, where λ is the transducer's wavelength.

As can be seen, Equation 2.4 is defined for distances r_i greater than the transducer's radius ($r_i > a$). Below this limit, this solution of the wave equation no longer holds, because the pressure would tend to infinity.

The directivity of a transducer describes how the emitted acoustic pressure varies with direction of emission. The directivity graphic of the MA40S4S transducer (the typical ultrasonic transducer used in UMAH systems) is shown in Figure 2.2 (adapted from Camelo, 2020; Murata, 2016).

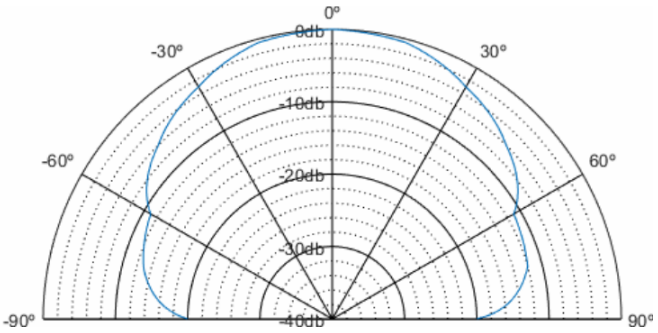

Figure 2.2: Directivity graphic of the Murata MA40S4S ultrasonic transducer.

The directivity depends on the angle θ_i. The θ_i is angle between the normal of the i-th transducer's surface and the imaginary line traced from the transducer's center ($\vec{r}_i$ position) to the observation point ($\vec{r}$). As can be observed through the Figure 2.2, for an angle of 45° the attenuation is around 6 dB. The Table 2.1 resumes the directivity attenuation of the transducer.

Table 2.1: Transducer Attenuation as a function of angle.

Angle (°)	Gain (dB)
0	0
15	-1
30	-3
45	-6
60	-12

By adding the directivity term $D(\theta_i)$ for the transducers and the phase of the pressure wave φ_i, the Equatio 2.4 becomes:

$$p_i(\vec{r}) = \rho c U_0 \, D(\theta_i) \frac{a}{r_i} \, e^{-j\left(kr_i + \varphi_i\right)}, \quad \text{for } r_i > a \tag{2.5}$$

By comparing this expression with the expression from Equation 2.1, the amplitude term A_i (the pressure amplitude at the transducer's surface) is given by:

$$A_i = \rho c U_0 \, D(\theta_i) \, a \tag{2.6}$$

2.1.2 Modelling Radiation Force

Consider an ultrasonic emitting surface modelled as a parabolic radiator (Gavrilov, 2014; Rozenberg, 1969). The radiator in this case is a parabolic surface that emits ultrasonic waves and that, due to its

geometry, naturally focus the energy into a FP. The focal region formed in front of the radiator depends on several geometrical parameters of the surface, like it is represented in Figure 2.3.

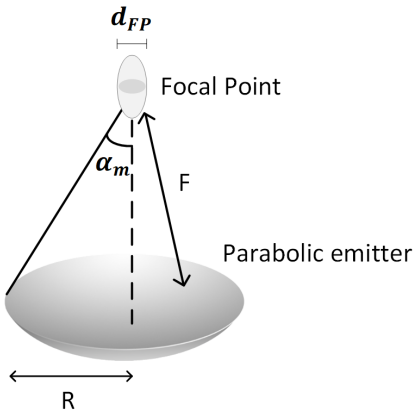

Figure 2.3: Main geometrical characteristics of a parabolic focusing emitter.

The R is the radius of the parabolic surface, α_m is the angle of convergence of the waves, and the focus is created at the focal length (F) distance.

The focal region has an ellipsoidal shape (Gavrilov et al., 1976), as can be seen in Figure 2.4. In the illustration, the FP is being created on the human skin. The intensity of the FP is maximum at its center and the maximum intensity is four times greater than the average intensity (Gavrilov, 1984).

The FP's diameter (d_{FP}) created by the parabolic radiator of Figure 2.3 can be estimated by the Equation 2.7 as stated by (Rozenberg, 1969):

$$d_{\mathrm{FP}} \approx 1.22 \frac{\lambda F}{R} \tag{2.7}$$

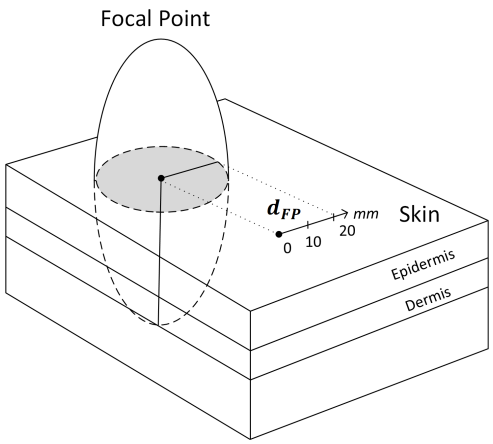

Figure 2.4: Representation of the FP targeting the skin.

As an illustrative scenario, consider a frequency of 40 kHz and the speed of sound in air $c = 343$ m/s. The wavelength is given by the ratio of these quantities ($\lambda = c/f$), which is approximately 8.6 mm. For a radiator with a radious (R) of 10 cm and a focal distance (F) of 20 cm, the diameter of the FP is approximately given by:

$$d_{\mathrm{FP}} \approx 1.22\frac{\lambda F}{R} \approx 1.22\frac{0.0086 \times 0.2}{0.1} \approx 0.021 \text{ m } (21 \text{ mm}) \tag{2.8}$$

The field converges to a region of diffraction maximum (i.e., the FP) and in that region, ultrasonic waves behave as plane waves. Thus, simple equations can be used to relate the physical quantities of ultrasound (Gavrilov, 2014). The acoustic intensity (I) of the FP can be calculated through equations relating to particle displacement amplitude (Δa), particle velocity amplitude (Δu) and amplitude pressure (Δp), as shown in the equation bellow (Gavrilov, 2014).

$$I = \frac{1}{2}\,\rho c\,\omega^2\,\Delta a^2 = \frac{1}{2}\,\rho c\,\Delta u^2 = \frac{\Delta p^2}{2\,\rho c} \tag{2.9}$$

Where I is in [W/m^2], Δa is in [m], Δu is in [m/s], and Δp is in [Pa].

When the FP hits a boundary it creates a steady pressure due to the transfer of momentum from the acoustic wave to the object. This pressure is called acoustic radiation pressure. The radiation pressure (P_r) of a normally incident wave is given by:

$$P_r = \alpha\frac{I}{c} \tag{2.10}$$

Where α is the reflection coefficient. For a perfectly absorbing material, $\alpha = 1$, and for a perfect reflector, $\alpha = 2$ (Hoshi et al., 2010). The skin behaves as a perfect reflector ($\alpha = 2$) for ultrasonic waves propagating through air. By substitution into the expression of Equation 2.9, the equation for P_r is obtained (Hoshi et al., 2010; Liebler et al., 2020):

$$P_r = \alpha\frac{I}{c} = \frac{\alpha\,\Delta p^2}{2\,\rho c^2} = \alpha\frac{p_{\mathrm{rms}}^2}{\rho c^2} \tag{2.11}$$

When the FP hits the hand, it generates a force responsible for the tactile sensation. That force is named radiation force (F_r) and under plane wave conditions is given by (Liebler et al., 2020):

$$F_r = \alpha \iint_S \frac{p_{\mathrm{rms}}^2}{\rho c^2}\,dS \tag{2.12}$$

Where S is the transverse area of the FP in contact with the skin, and $\alpha = 2$ for the UMAH's case.

Moreover, the F_r can be calculated by means of the acoustic power (P), too. The following equation can be used to that end and assumes a normally incident FP (Dalecki et al., 1995).

$$F_r = \alpha \frac{P}{c} \tag{2.13}$$

Where P of the FP is in [W]. In turn, the P is the product of the acoustic intensity (I) by the area of the FP (S). As given by:

$$P = I \cdot S \tag{2.14}$$

S [m^2] is the transversal area of the focal region, approximated by $S = \pi d_{\mathrm{FP}}$ (see Equation 2.8).

2.1.3 Technical trade-offs

A smaller FP is a desirable aspect in UMAHs, as it is synonymous with greater spatial resolution of the "tactile pixel". As can be seen from Equation 2.7, a more localized FP can theoretically be achieved by increasing the emission frequency (f_c recall that $\lambda = c/f_c$) or by enlarging the haptic array size (in this case R). This would create a smaller FP while maintaining an adequate interaction range (F). Nevertheless, there are technical challenges that limit these possibilities.

Increasing the frequency also increases the attenuation of ultrasound in air (Georgiou et al., 2022; Hoshi et al., 2010), which naturally shortens the interaction range for higher-frequency haptic arrays. Moreover, increasing the haptic array size indeed reduces the size of the FP (Hasegawa & Shinoda, 2018), nevertheless bigger arrays are often not practical for most applications. In the same line of though, increasing the radiator density (i.e., number of transducers per array), would also spatially concentrate the FP (Camelo, 2020), but such an approach is not feasible since there are not better (and smaller) commercially available transducers then the already in use today (i.e., Murata MA40S4S).

2.1.3.1 Generation of the Focal Point

The several sections so far discussed aspects related to the creation of the FP from both a physical and mathematical perspective. The generation of the FP (from a practical point of view) is performed by the UMAH system. In Chapter 4 the creation of the FP is discussed in detail.

2.2 Touch Perception

In this section, the human tactile perception is discussed. In the initial part of the section, the topic is addressed in a general perspective. And later in the section, discussion becomes specific to the perception of UMAH stimulus.

2.2.1 Skin Mechanoreceptors

An understanding of the human hand, in particularly its skin, is important for UMAHs. In this section the of the palm skin (glabrous skin) is discussed as well as perceptual mechanisms involved.

Through the skin several types of sensations can be felt, like warm, cold, pain and mechanical sensations (e.g., pressure or vibrations). The mechano-receptive systems (Sekuler & Blake, 1994) in the skin are responsible for transducing all sort of mechanical stimuli (i.e., stimuli that indent the skin surface) into bio-electrical signals. A mechano-receptive system is composed by the mechanoreceptor (responsible for transducing the stimulus) and the afferent nerve fibres (the connecting pathways that transmit the electrical signals from the receptor into the brain) (Johnson & Hsiao, 1992). For convenience, the mechano-receptive system and/or mechanoreceptor are mentioned interchangeably.

Mechanoreceptors are divided into categories that are related to the perception of the stimulus (Pashler, 2002). These can be Slow Adapting receptors (SA) which refers to mechanoreceptors sensitive to the sustained skin indentation (i.e., continuous pressure). Also, there are Rapidly Adapting receptors (RA), which are sensitive to the stimulus transitions (e.g., vibrations or rapid pressure changes). Additionally, there is another classification that considers the receptive field of the receptors (Sekuler & Blake, 1994). These can be divided into punctate or diffuse type of receptors. Punctate-type receptors have a small and well-defined receptive field (i.e., high spatial resolution) and are located near the skin surface. Diffuse receptors have a large and less-defined receptive field (i.e., poorer spatial resolution) and are located more deeply in the dermis (Sekuler & Blake, 1994).

The Figure 2.5 (adapted from Pashler, 2002) illustrates the mechano-receptors present in the glabrous skin of the palm.

The palm's skin is composed by four main types of mechanoreceptors. Each one plays a tactile function and the sense of touch can be understood as the sum of their various roles (Pashler, 2002). Considering their location within the skin (from the most superficial to the most deepest), the mechano-receptors are: Meissner Corpuscles (RA1), Merkel Cells (SA1), Pacinian Corpuscles (PC) and Ruffini Endings (Pashler, 2002; Sekuler & Blake, 1994).

The RA1 is an RA-punctate type receptor and it is located near the skin's surface. It is associated with the perception of grip as it is sensible to sudden and slight movements in the skin (Johansson & Westling, 1987). They also detect light motion and vibrations. In fact, the RA1-system is feels vibrations in the range of 30 Hz to 60 Hz, peaking around 40 Hz to 50 Hz (Pashler, 2002).

The SA1 are of the SA-punctate type and are located near the skin surface. These receptors, associated with the perception of texture, form, and curvature (Pashler, 2002) are particularly sensitive to edges and ledges (Pashler, 2002). Similarly to the RA1 system, SA1 receptors are highly abundant in the skin, and

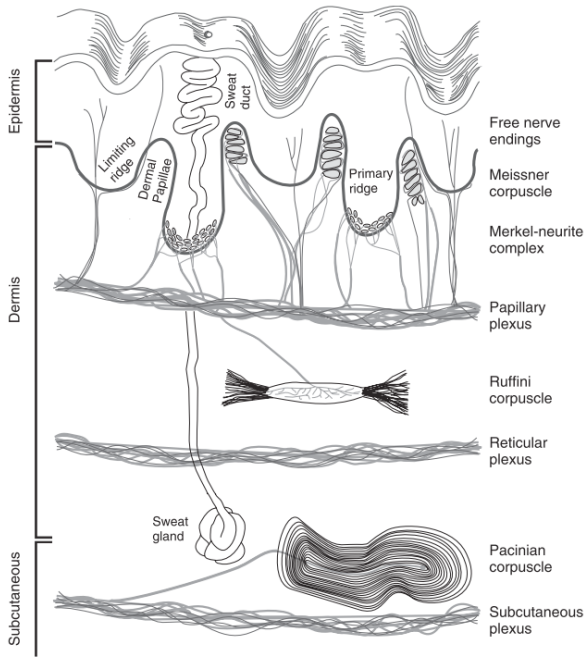

Figure 2.5: The skin mechanoreceptors of glabrous skin.

tactile acuity (i.e., the spatial resolution of touch) is often related to the morphological properties of both mechanoreceptive systems (Johnson & Lamb, 1981).

The PC belong to the RA-diffuse class of mechanoreceptors, and their morphology resembles an onion-like structure. These receptors are associated with the perception of vibrations transmitted through objects, making them essential for tool manipulation (Pashler, 2002). The PC are extremely sensitive to vibrations, particularly at higher frequencies than RA1. They are especially responsive to minute vibrations in the range of 200 Hz to 300 Hz (Pashler, 2002; Verrillo, 1963).

The Ruffini mechanoreceptive system is a RA-diffuse type of receptors (Pashler, 2002). They are related with skin stretch. These types of receptors are unlikely to be activated by the ultrasonic stimuli produced by the technology discussed in this thesis. For this motif they will not be discussed further.

2.2.2 Other Psychophysiological Factors

There are other perceptual concepts that are relevant for the perception of stimuli. It is important to mention that there are very few studies using ultrasound stimulation that specifically address the topics discussed in this section. Therefore, based on existing related studies and on our own experience, perceptual aspects related to spatial resolution, temporal resolution, and selective stimulation are briefly discussed.

2.2.2.1 Two Point Discrimination Threshold

The Two-Point Discrimination Threshold (2PDT) is perhaps the simplest method for measuring the spatial resolution (or spatial acuity) of touch. Although other measures exist—such as the two-point orientation discrimination (Pashler, 2002) — the 2PDT is, in our opinion, an appropriate reference for the purposes of this thesis.

The 2PDT corresponds to the minimum distance at which two points can be distinguished before they merge perceptually into a single point (Loomis, 1981; Pashler, 2002). It is typically measured using a calliper in contact with the skin. An illustration of the 2PDT is shown in Figure 2.6.

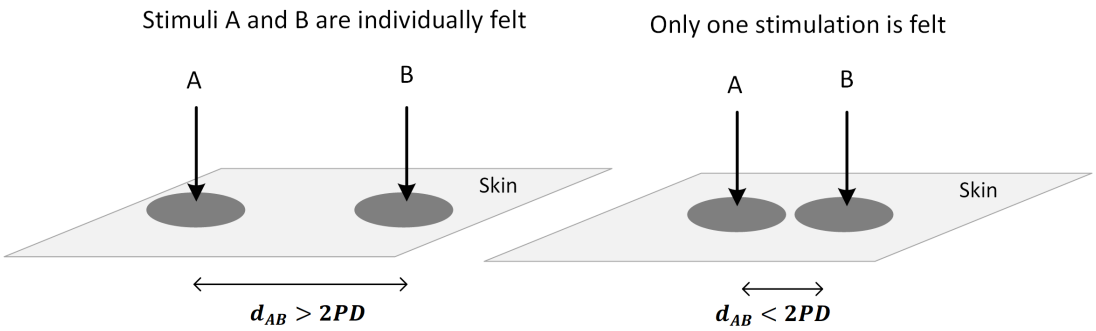

Figure 2.6: Two-point tactile discrimination.

According to Tong et al. (2013), who delivered tactile stimuli using the tip(s) of a digital calliper, the 2PDT ranges from approximately 2 mm to 4 mm for the fingertip and around 8 mm for the palm. Thresholds vary with factors such as the thickness of the skin, age, and the type of stimulus.

Cataldo et al. (2023) measured the 2PDT using ultrasonic stimulation and investigated the threshold for FPs modulated at specific frequencies. The authors used amplitude-modulated FPs and thus minimized the contribution of the SA1 channel, which is typically activated by pressure-based stimuli such as those produced by a caliper tip. Moreover, by selecting specific modulation frequencies, the authors targeted the SA1 channel (50 Hz modulation) and the PC channel (200 Hz modulation). As an illustrative example, the 2PDT on the palm was about 15 mm for 200 Hz modulation amplitude modulated FP.

2.2.2.2 Temporal Resolution of touch

Temporal resolution (or temporal acuity) of touch refers to the human ability to detect two tactile events occurring in rapid succession. The threshold can be defined as the minimum time interval between two brief tactile events that can be detected before they are perceived as a single stimulus (Loomis, 1981).

Temporal thresholds depend on several factors, such as the intensity of the stimulus (Gescheider et al., 2003), the type of stimulus, and the body location (Petrosino & Fucci, 1984). Gescheider (1967) and Gescheider et al. (2003) measured temporal acuity and reported separation delays of about 10 ms. Loomis (1981) mentioned temporal thresholds as high as 40 ms, and Petrosino and Fucci (1984), who measured the fusion threshold of the tactile sense, found values around 20 ms.

In simpler terms, when the delay between two events is greater than around 40 ms, they are perceived as two distinct tactile events. For inter-stimulus delays between 20 ms and 40 ms, the perception of separate events may become ambiguous. If the delay is shorter than about 10 ms to 20 ms, the two events are generally perceived as a single stimulus. The Figure 2.7 illustrates the perception of two successive stimuli according the inter-stimuli duration.

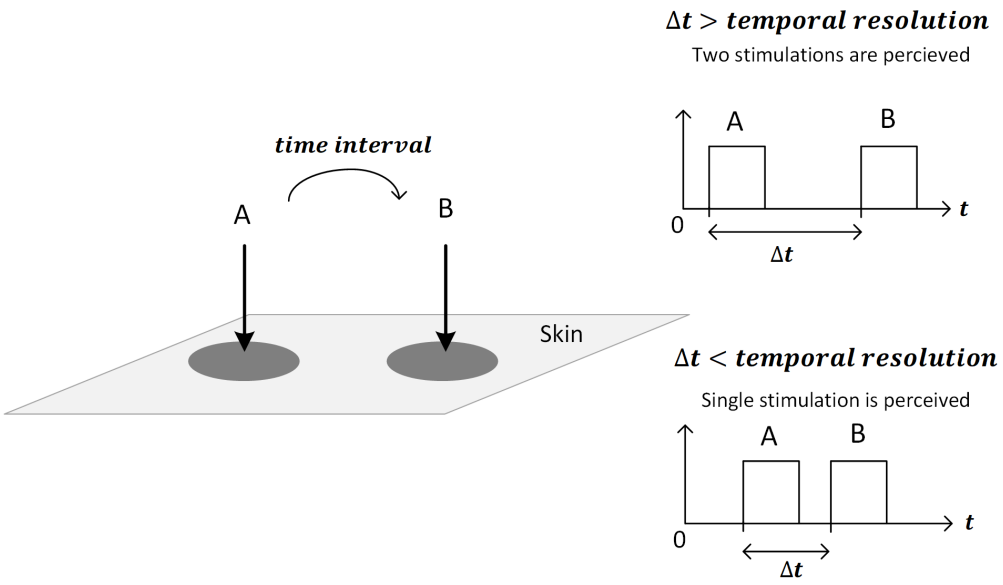

Figure 2.7: Tactile temporal resolution perception.

The temporal acuity sets a boundary between what is referred to a rhythmic sequence of pulses (inter-stimuli duration above temporal threshold) and, what is commonly referred to as a continuous vibration (inter-stimuli duration under the threshold).

In the same line of though, there is another relevant perceptual metric – the Temporal Order Judgment (TOJ). This threshold marks the minimum duration between two pulses needed for its order of occurrence to be judged. According to Loomis (1981) TOJ threshold requires a minimum of 20 ms.

2.2.2.3 Selective Stimulation of Touch

A stimulus with specific attributes activates certain mechanoreceptor types, while other receptors remain inactive. This aspect of selective activation is referred to as the selective stimulation property of touch (Gescheider et al., 2003).

The specific sensitivity of the mechanoreceptor is due to its morphology. The individual study of mechanoreceptors is difficult because often, an activation stimulus ends up triggering several types of receptors. However, through electrical stimulation receptor isolation was achieved by Vallbo et al. (1984) and a qualitative analysis of the produced sensations by each receptor was possible. For the SA1 system, the sensation is perceived as continuous pressure. For the RA1, the sensation was described as tapping or flutter-vibrations and for the PC system, the sensation was described as vibratory (or vibrotactile) sensation.

2.2.2.4 Tactile Summation

When a stimulus lasts longer (up to a certain limit), it becomes easier to detect. Temporal summation is a well known phenomenon related to the integration of energy over time by the sensory system. In technical terms, the detection threshold decreases as the stimulus duration increases. Moreover, if two stimuli occur very close in time (i.e., within the temporal resolution described earlier), they are perceived as a single event, and their combined sensation is enhanced, similarly to the temporal summation effect (Gescheider et al., 2005).

Mechanoreceptors become more sensitive as the size of the stimulated area increases. This phenomenon is known as spatial summation and manifests as a decrease in the detection threshold (or an increase in the perceived magnitude) of the stimulus (Gescheider et al., 2005). In other words, spatial summation refers to the enhanced perception of a stimulus as the stimulated area expands.

Furthermore, if two stimuli occur simultaneously (or within a very small temporal gap) and at close locations (very small distance), their perception can be both temporally and spatially enhanced.

2.3 Perception of Ultrasonic Stimuli

In the previous section, the discussion focused on general aspects of cutaneous perception. In the present section, the ultrasonic stimulus and ways to modulate it to elicit tactile sensations will be addressed.

2.3.1 The cause of the stimulus - Radiation Force

The sense of touch can be elicited by ultrasonic waves through an unidirectional mechanical force known as the acoustic radiation force. Gavrilov et al. (1976) was the first to propose that the physical quantity responsible for the stimulus was mechanical in nature. Later, Dalecki et al. (1995) confirmed that the

tactile thresholds for an ultrasonic beam correspond to the skin's response to the unidirectional action of the radiation force.

The tactile threshold is the minimum intensity or quantity of a stimulus (such as pressure or vibration) required for a person to detect it. Gavrilov published numerous studies on the perception of touch to ultrasound (Gavrilov, 1984; Gavrilov et al., 1976, 1977; Gavrilov, 2014; Vartanyan et al., 1991). He was the first to measure tactile thresholds for ultrasonic pulses (Gavrilov et al., 1976). To achieve this, he employed high-power focused ultrasound transducers with resonance frequencies ranging from 0.5 MHz to 3 MHz. Tactile thresholds were determined for pulse durations between 0.1 ms and 100 ms.

To identify the physical cause underlying the tactile threshold, he calculated several acoustic quantities—such as displacement amplitude, sound pressure, sound intensity, and temperature increment—and examined which varied least across different ultrasonic frequencies at the tactile threshold. The displacement amplitude exhibited the smallest variation with frequency. However, because it is an alternating quantity, it was not considered the causal factor. Nevertheless, the author confirmed that the underlying physical agent was mechanical in nature.

Dalecki et al., 1995 conducted human trials using a 2.2 MHz ultrasonic transducer to determine tactile thresholds for the fingertip and forearm. To prevent direct interaction between the skin and the ultrasonic beam, a rubber disk was attached to the exposed area. Four experiments were performed, designed to identify the cause of the tactile stimulus.

The first experiment measured tactile thresholds for amplitude-modulated ultrasound with modulation frequencies between 50 Hz and 1000 Hz. The second experiment measured thresholds for ultrasonic pulses of 0.1 ms to 100 ms duration (like Gavrilov et al., 1976). The third compared pulse thresholds using two rubber disk sizes, and the fourth measured and compared thresholds on the forearm with and without the rubber disk.

The amplitude-modulated thresholds were consistent with previous studies on the tactile receptor system (Dalecki et al., 1995). Similarly, the pulse thresholds obtained agreed with the results of Gavrilov et al. (1976). Finally, the ratio of thresholds in the fourth experiment was approximately unity. Because no differences were observed when the ultrasonic radiation was blocked by the disk, potential direct interactions between the ultrasound and the skin were ruled out. Since the force thresholds were identical for both direct and isolated exposure, the results confirmed that the acoustic radiation force was the physical factor responsible for the tactile sensation.

2.3.2 Ultrasonic Pulse

The first strategy used to elicit tactile sensations through ultrasound was by creating pulses. The technique was used by Gavrilov in several studies regarding the tactile perception to ultrasound (Gavrilov, 1984;

Gavrilov et al., 1976, 1977; Gavrilov, 2014; Vartanyan et al., 1991).

The type of sensation an isolated pulse produces is described as slight 'tap', 'push' or 'click'. The technique consists in turning ON and OFF the acoustic emission towards the skin, for short periods of time (milliseconds).

The perception of a pulse occurs at the pulse's transitions. The carrier ultrasonic frequencies (i.e., frequencies in the kHz to MHz range) are not perceivable, as skin acts as a natural barrier to such frequencies and thus it is the pulse's envelope that is perceived. Gavrilov, 2014 which isolated Pacinian corpuscles in his studies, pointed these types of mechanoreceptors as the physiological cause of the static single pulse stimulation.

The signal representing the pulse is depicted in Figure 2.8 and it was adapted from Gavrilov, 2014). Moreover, the mathematical definition of the pulse signal is given in Equation 2.15. Where t_p is the duration of the pulse and ω_c is the ultrasound carrier frequency.

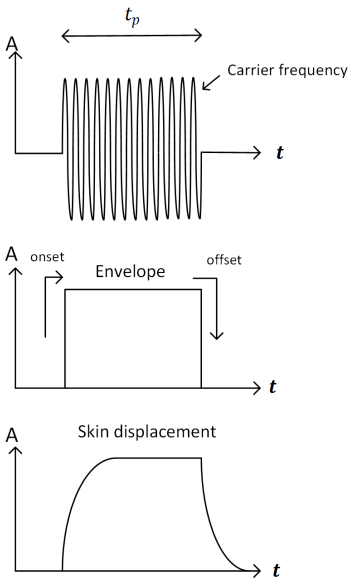

Figure 2.8: Ultrasonic pulse signal. (Top) The pulse's carrier frequency. (Center) The pulse's envelope and. (Bottom) The skin displacement when the pulse hits its surface.

$$A_{\text{pulse}}(t) = \begin{cases} \sin(\omega_c t), & 0 \leq t \leq t_p \\ 0, & \text{otherwise} \end{cases} \tag{2.15}$$

As previously mentioned, an ultrasonic pulse consists in the activation and deactivation of the acoustic emission for short durations. When the pulse duration is "long", for example, equal or greater than 100

ms, the sensation is primarily the response to the onset (beginning) and offset (ending) of the pulse. On the other hand, short pulses (less than, e.g., 15 ms) are perceived as a sole event (Gavrilov, 2014). Accordingly to Gavrilov, the perception to a 400 ms pulse is the response to the beginning and ending of this long pulse. Moreover, a similar perceptual stimulus is the one produced by two short pulses (e.g., 20 ms), separated by 360 ms ('quiet') interval (Gavrilov et al., 1976).

2.3.2.1 Perception to ultrasonic pulses

This type of stimulation strategy was the primary method for studying the tactile perception of ultrasound. It can be used to stimulate the skin surface and deeper tissues, and can evoke tactile sensations and even pain, cold, and warmth sensations. Gavrilov et al. (1976) measured the tactile thresholds for these sensory modalities. Four ultrasonic frequencies were tested, ranging from 0.48 MHz to 2.67 MHz, with pulse durations varying between 1 ms and 100 ms. Tactile perceptual thresholds were obtained for the finger and forearm under controlled subaquatic conditions. It was observed that the lowest thresholds corresponded to the tactile sensations. And that, across all modalities, thresholds increased from the finger to the palm. Moreover, among all modalities, the tactile thresholds were the most reproducible.

In another study, Gavrilov et al. (1977) investigated the influence of environmental temperature and pulse duration on tactile thresholds. Participants were tested using pulses of varying durations (from 1 ms to 100 ms) in water temperatures ranging from 30°C to 40°C. The results showed that tactile thresholds did not vary substantially for pulse durations longer than 1 ms, while an increase in temperature appeared to moderately reduce the thresholds.

It was observed that tactile thresholds do not vary for pulse durations above 1 ms when the stimulated region was the finger (Gavrilov et al., 1976). The study by Vartanyan et al. (1991) further examined this tendency across different regions of the hand and arm. In the study, the duration of ultrasonic pulses was varied between 1 ms to 500 ms, and thresholds were measured on the finger, palm, wrist, and forearm. Like in Gavrilov et al. (1977)'s, results showed that, for the finger and palm, pulse's duration had little effect on the thresholds. However, for the wrist and forearm, thresholds increased substantially with the decrease of pulse's duration.

Like was already mentioned, ultrasonic pulses with durations longer than 1 ms not significantly affected tactile thresholds for the palm (Gavrilov et al., 1977; Vartanyan et al., 1991). Nevertheless, the influence of shorter pulses (less than 1 ms) on the thresholds was investigated by (Gavrilov, 1984). The study examined tactile sensitivity in the context of medical diagnostics and involved a considerable number of participants. Tactile thresholds were measured for pulses with durations ranging from 0.1 ms to 100 ms. The transducer's resonance frequency was 1.95 MHz and the skin of the fingers served as the stimulation site. The results showed that when the pulse duration was shorter than 1 ms, tactile thresholds increased markedly. For example, for a pulse duration of 0.1 ms the threshold was more than four times greater

than for a 1 ms pulse (Gavrilov, 1984).

The same trend was observed in the work of Dalecki (1995). Participants were involved in a study that determined the tactile thresholds for the finger and the forearm for pulses with 0.1 ms to 100 ms duration. The emission frequency was 2.2 MHz and the thresholds were described in terms of acoustic radiation force. Likewise verified in Gavrilov (1984), when the pulse duration was shorter than 1 ms, tactile thresholds increased significantly.

2.3.2.2 Critical pulse duration

In connection with the mentioned phenomenon of the sharp increase in the tactile thresholds for very short pulses, Gavrilov defined the critical pulse duration metric (Gavrilov, 2014). This metric is described as the minimal duration of a pulse causing a sensation with the least threshold (Gavrilov, 2014). The critical pulse duration for the fingertips varies from 1.5 ms to 2.5 ms and it increases from fingers to forearm (Gavrilov, 2014).

In the context of UMAHs, the critical pulse duration is an important metric for the design of the stimulus. As will be explain further in Chapter 6, UMAH patterns can be made of pulses, therefore, critical pulse metric can be used to guide the design of patterns.

Several studies measured the tactile perceptual thresholds to ultrasonic pulses (Dalecki et al., 1995; Gavrilov, 1984; Gavrilov et al., 1977; Vartanyan et al., 1991). The thresholds from those studies were extracted into a graphic, shown in Figure 2.9. The perceptual studies were in the context of high intensity ultrasound, and resonance frequencies ranged from 1.95 MHz (Vartanyan et al., 1991) to 2.67 MHz (Gavrilov et al., 1977). The target of stimulation was the fingers and the measurements were done with the hand and equipment under water. In the studies, the pulse's duration ranged from 0.1 ms to 500 ms. Note that not all durations were tested for all works, and thus the graphic has discontinuities.

Note that, in some works, the thresholds were calculated in terms of acoustic intensity and those thresholds were converted to radiation force (see Equations 2.11 and 2.12). For the conversion the transversal area of the FP was considered, generated at the respective resonance frequency and in sub-aquatic environment.

On the graphic, the horizontal axis is the pulse duration in milliseconds (ms) and in the vertical axis is the radiation force (mN). From the graph, the critical pulse threshold can be estimated. This threshold is obtained by averaging the pulse thresholds for a duration of 1 ms (as noted earlier, Gavrilov defined the critical duration in the range of 1.5 ms to 2.5 ms). Based on this, the critical pulse threshold corresponding to a 1 ms pulse duration is approximately 2.3 mN. The dashed red line represents the critical radiation force threshold associated with this pulse duration. The pulse's thresholds were measured for the fingers. So, the critical duration for the palm is expected to be higher.

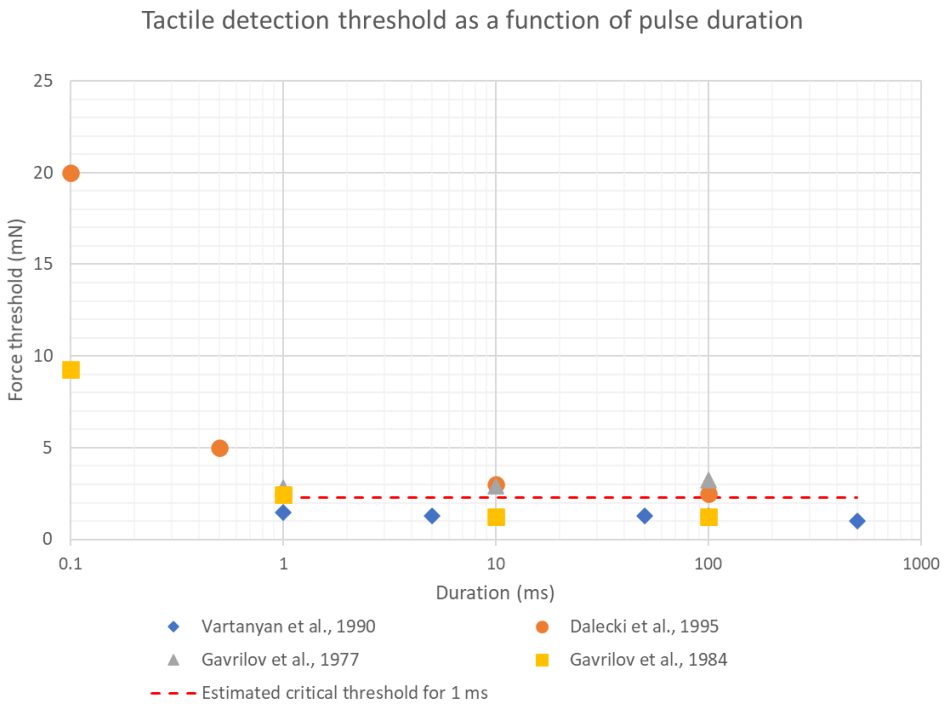

Figure 2.9: Tactile detection threshold as a function of pulse duration, compiled from multiple studies. The dashed line represents the estimated critical duration threshold.

The aim of the graphic of Figure 2.9 is to reiterate the exponential increase of the tactile perceptual thresholds for very short pulses (less than 1 ms). Moreover, since the graphic has thresholds from distinct research works, it provides the typical sensitivity thresholds associated with ultrasonic pulses. There are not concrete measurements for pulse' sensitivity generated by UMAHs, so the thresholds of Figure 2.9 may only be used as a reference in the context of this thesis.

2.3.2.3 Motion Perception of a pulse

The perception of single pulses has been addressed in this section. This surprisingly simple stimulation technique was extensively studied and that allows a deep understanding of various factors affecting its tactile perception.

There is also another aspect related with pulse perception important for the discussion. It is related with the perception of motion of a continuous pulse (or continuous focus). Note that, a continuous static focus targeting the palm, creates a steady force but it is not perceivable.

Nevertheless, by gently moving the hand, the continuous focus will immediately become perceptible. This happens because, the steady force of the focus, when the hand moves, will activate certain types of mechanorecepetors sensitive to motion. Like is the case of the SA1 (Merkel mechanorecptors). And the sensation that is associated with this type of stimulation is described (at least in the context of UMAH) as

moving pressure.

Pulse stimulation is a complex modulation or stimulation technique. As was already explained throughout this section regarding pulse's perception, one could observe the several types of factors the influence the perception of this particular and fundamental type of stimulation.

2.3.3 Amplitude Modulation

The high-frequency vibrations of airborne ultrasound (e.g.„ 40 kHz carrier frequency) can be tailored to produce vivid vibrotactile sensations, beyond the simple "tap" or "push" effects generated by ultrasonic pulsing. By amplitude-modulating or Amplitude Modulation (AM), the carrier at lower frequencies (typically between 200 Hz and 300 Hz), the mechanoreceptors responsible for vibration perception (namely, the PC) are effectively stimulated (Iwamoto et al., 2008). The carrier frequency is rectified by the skin (Lamoré et al., 1986), generating a static force that helps bypass the skin's natural attenuation. As a result, the modulated vibrations are efficiently transmitted to the deeper tactile receptors.

The AM signal is represented in Figure 2.10. This figure was adapted from Hasegawa and Shinoda (2018). The mathematical definition of the AM signal is given in Equation 2.16.

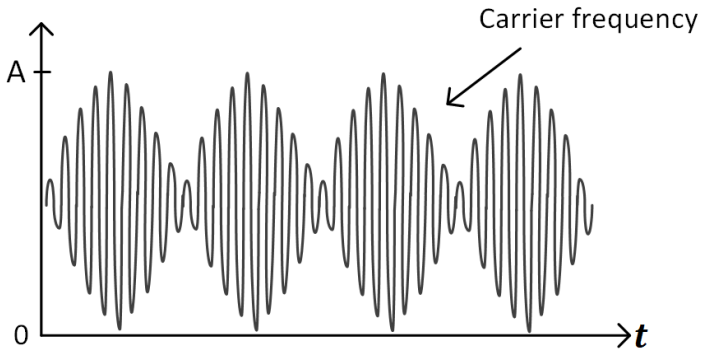

Figure 2.10: Amplitude modulated signal.

$$A_{\mathrm{am}}(t) = \frac{A}{2}(1 + \sin(\omega_{\mathrm{am}} t)\sin(\omega_{\mathrm{c}} t)) \tag{2.16}$$

Where $\omega_{\mathrm{am}} = 2\pi f_{am}$ and $\omega_{\mathrm{c}} = 2\pi f_c$. The f_{am} is the amplitude modulation frequency and f_c is the ultrasonic carrier frequency (i.e., $f_c = 40\ kHz$).

Lamoré et al. (1986) measured and compared the tactile thresholds of non-modulated vibrations and AM vibrations, with modulation frequencies ranging from 10 Hz to 500 Hz. The carrier frequency used was 1 kHz. The target area was the fingertip, and the mechanical contactor had an area of 1.5 cm^2. The

study concluded that the thresholds for both types of stimuli exhibited a U-shaped behavior, with minimum values between $f_{am} = 100\ Hz$ to $300\ Hz$. Moreover, the thresholds for the AM stimulus were significantly lower than those for the non-modulated vibratory stimulus. Furthermore, the article pointed that the tactile perceptual thresholds were independent of the carrier frequency.

Tactile thresholds for AM stimuli generated through ultrasound were determined by (Dalecki et al., 1995). Measurements were taken from the finger for modulation frequencies (f_{am}) of 50 Hz, 100 Hz, 200 Hz, 500 Hz, and 1 kHz. The carrier ultrasonic frequency was 2.2 MHz. The results for the AM-thresholds show curve exhibiting an U-shaped profile, similar to that reported by Lamoré et al. (1986) and Verrillo (1963). This pattern suggests that the PC receptor system is responsible for the observed vibrotactile sensations. At 200 Hz the threshold reaches its minimum (0.4 mN) moreover, at 1 kHz the perceived tactile sensation was not vibratory but rather described as a “tap” or “push” (maybe resembling that of a pulse).

In the context of airborne ultrasonic haptics, the tactile thresholds for AM sensation have been primarily determined and documented in the works of Hasegawa and Shinoda (2018), Takahashi et al. (2018) and Takahashi et al. (2020). In all research studies, the carrier frequency was 40 kHz. In Hasegawa and Shinoda (2018) study, the main objective was to characterize the haptic system. To that end, among several experiments, the authors measured tactile thresholds for several f_{am} (i.e., 10 Hz, 20 Hz, 30 Hz, 50 Hz, 100 Hz, 200 Hz, 300 Hz, 500 Hz, and 1 kHz). The experimental setup, shown in Figure 2.11, consisted of four phased-array units.

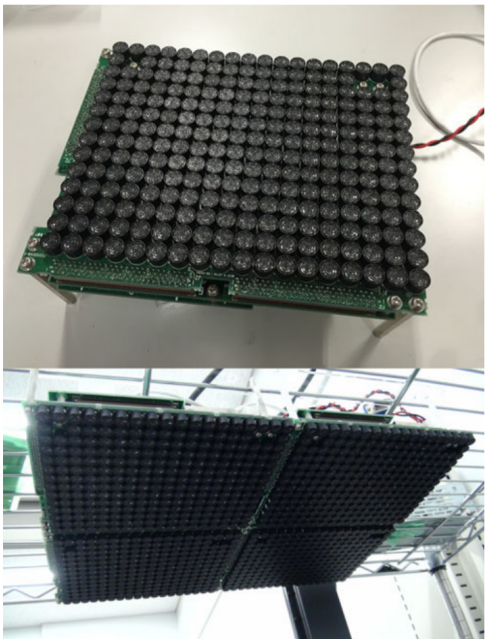

Figure 2.11: UMAH system used by Hasegawa & Shinoda (2018). (Top) The haptic array unit. (Bottom) The UMAH system, composed by four units.

The carrier frequency of the transducers is 40 kHz and each array consist of 249 elements, resulting in a total of 996 transducers for the entire system. The system generates a FP with 12 mm in diameter and at the maximum system power, the radiation force reaches approximately 20 mN (Hasegawa & Shinoda, 2018).

Tactile thresholds were measured using the method of limits (Dalecki et al., 1995; Hasegawa & Shinoda, 2018). The threshold's results obtained by (Hasegawa & Shinoda, 2018) show a similar curve as that reported in different studies (Dalecki et al., 1995; Lamoré et al., 1986) involving different stimulation methods (i.e., mechanical actuation (Lamoré et al., 1986) or underwater ultrasound (Dalecki et al., 1995)).

The minimum threshold occurred at $f_{am} = 200\ Hz$, with an estimated radiation force of approximately 0.4 mN. The researchers also commented that AM thresholds varied with other stimulus attributes, for example the modulation waveform's shape. For example, abrupt/sharp shapes were associated with lower thresholds when compared to their smoother, more sinusoidal counterparts. Finally, even at the system's maximum intensity, not all the participants were able to feel vibrations at the frequencies of 5 Hz or 1 kHz.

In the graph shown in Figure 2.12, the tactile detection thresholds for AM are represented. The thresholds were compiled from several works (Dalecki et al., 1995; Hasegawa & Shinoda, 2018; Takahashi et al., 2020; Takahashi et al., 2018). The modulation frequencies used in these studies ranged from 5 Hz to 1 kHz, although only Hasegawa and Shinoda, 2018 tested the full range. In the remaining works, only a subset of these frequencies were evaluated.

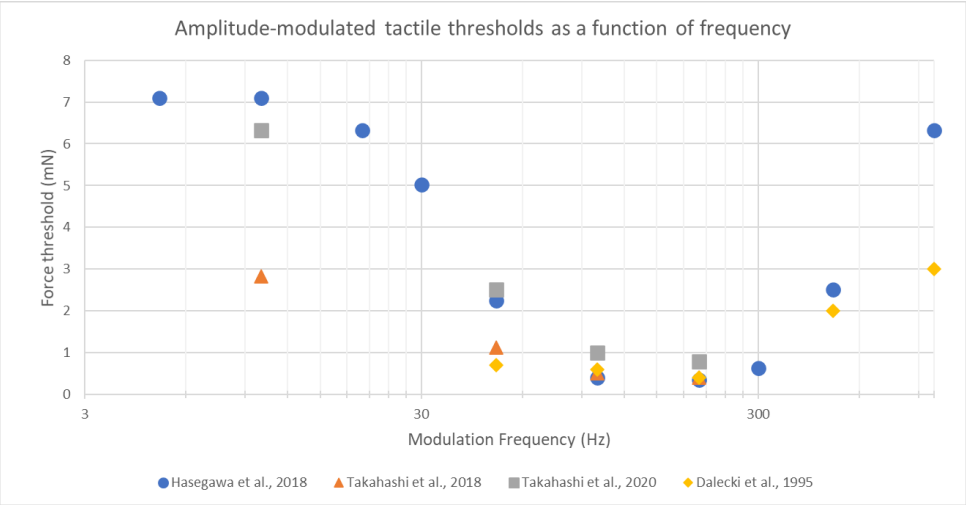

Figure 2.12: AM tactile thresholds as a function of modulation frequency. Data obtained from several research works on the field.

The studies by Hasegawa and Shinoda (2018), Takahashi et al. (2018) and Takahashi et al. (2020) used a stimuli (i.e., a 40 kHz generated FP) comparable to the stimuli of the present thesis. Nevertheless, Dalecki

et al. (1995) conducted experiments in underwater conditions, using high-intensity focused ultrasound with a carrier frequency of 2.2 MHz. Comparisons must therefore account for these experimental differences.

The horizontal axis of the graph represents the modulation frequency (Hz), and the vertical axis represents the radiation force (mN). The results from Hasegawa and Shinoda (2018) display an U-shaped profile. Tactile thresholds remain relatively constant up to approximately 30 Hz (around 7 mN). At about 50 Hz, the thresholds drop sharply, reaching a minimum at around 200 Hz (approximately 0.4 mN). Above 300 Hz, the sensitivity thresholds begin to increase again.

It is important to point-out that the most sensitive AM sensations (those at approximately $f_{am} = 200\ Hz$) have much lower thresholds than the tactile pulse stimuli described in the previous section (see Figure 2.9).

2.3.4 Spatial-Temporal Modulation

So far, two techniques capable of creating tactile sensation through ultrasound have been discussed. The ultrasonic pulsing creates a 'tap/click' sensation and the AM technique creates vibrotactile sensations.

There is also another modulation technique that creates sensations, the STM, which was discovered more recently than the others two techniques. It consists of varying the position of the FP along predetermined shapes (or patterns) while maintaining the FP's amplitude constant.

This modulation technique has gained attention due to the fact that it produce stronger sensations than the two previously discussed techniques. However, it is more complex in terms of its operation and underlying tactile mechanisms. Nonetheless, the STM has significant potential for improvement and further research, ultimately aiming at the creation of new and optimized sensations. The STM is described in detail in Chapter 3.

2.4 Conclusions

The chapter presented a mathematical and physical model for the creation of the FP (the basis for stimulation in UMAH). In addition, an expression for estimating the stimulus force was described, along with the technical challenges associated with reducing the size of the FP. The second part of the chapter addressed human touch perception. The main techniques for generating UMAH sensations were presented, namely ultrasonic pulsing and AM, along with a discussion of their tactile perceptual thresholds.

Spatio-Temporal Modulation

3.1 Introduction

In 2018, two independent groups (Frier et al., 2018; Takahashi et al., 2018) proposed a new modulation technique for haptic feedback. In this technique, the FP maintains constant amplitude (e.g., at the system's maximum power, $A(t) = 1$) while moving across the skin surface. The FP travels continuously along simple shapes (or patterns) such as lines, circles, or squares (Frier et al., 2022; Lim et al., 2025; Marti et al., 2022).

The modulation method under discussion is the core of this thesis and is known as spatial-temporal modulation (STM). In this modulation, the FP sweeps over a larger area of the skin (i.e., the spatial component), and its periodic motion produces 'continuous' deflections on the skin surface (i.e., the temporal component).

Takahashi et al. (2018) described a method in which the FP moves rapidly and repeatedly along short paths (up to a few centimeters in length). Using small lines (Takahashi et al., 2018) or circles (Takahashi et al., 2019) they were able to produce relatively intense vibrotactile sensations - this modulation technique was named Lateral Modulation (LM). In the same year, Frier et al. (2018) presented a technique based on a fast-moving FP traveling along large circular shape (around 20 cm in perimeter). They called this STM, which stimulates a wider region of the skin and according to the study, is felt strongly.

The main distinction between the methods of Takahashi et al. (2018) and Frier et al. (2018) lies in the size of the stimulus (or pattern). In the first case, the FP moves along short paths to create localized sensations, whereas in the second case the shapes are much larger, reaching several tens of centimeters in length. The LM and STM can therefore be described as two distinct modulation methods. However, both rely on a constant-amplitude, moving FP. Thus, these two (LM and STM) are forms of spatial-temporal modulations.

The STM has been the subject of considerable perceptual research (Ablart et al., 2019; Frier et al., 2018, 2019; Howard et al., 2019; Morisaki et al., 2022; Takahashi et al., 2020; Takahashi et al., 2018). Because they evoke stronger tactile sensations. As a result, the transducer array's total acoustic power (overall SPL) is better suited for mid-air haptic sensation when compared with other modulation techniques, such as ultrasonic pulsing or AM.

3.2 Technical operation of the modulation

The aim of this section is to explain the STM from a technical perspective. This technique includes several parameters that influence the sensation. Some of them are more explicit, while others are subtle and 'hidden' within the modulation technique. Nevertheless, all parameters are important for the resulting sensation.

For clarity and readability, Table 3.1 summarizes the STM parameters. These are described in detail throughout this section, however, the table is intended to serve as a reference during the discussion and to establish a consistent naming convention. Citations are provided for parameters defined in prior works. Additionally, parameters related to other modulation techniques, such as ultrasonic pulsing and AM, are also included in Table 3.1.

Table 3.1: Summary of modulation techniques and corresponding parameters.

Technique	Parameter	Description
Ultrasonic Pulsing	t_p	Pulse duration
AM	f_{am}	Amplitude modulation frequency
STM	d_{SP}	Distance between adjacent shape points (or positions) (Morisaki et al., 2022)
	f_{draw}	Drawing frequency of the shape pattern (Frier et al., 2018)
	l	Shape length
	N_{SP}	Number of points composing the shape
	SP	Shape Point (Frier et al., 2018)
	t_{SP}	Duration of each shape point
	T_{draw}	Drawing period of the shape
	UR	Update rate of the focal point (Frier et al., 2018)
	$\mathrm{UR}_{\mathrm{max}}$	Maximum update rate of the UMAH system
	v_{FP}	Focal point speed (Frier et al., 2018; Takahashi et al., 2020)
Other	d_{FP}	Diameter of the focal point

STM can be used to generate different shapes, such as lines and circles. Depending on how the shape is constructed, the stimulation rate along the path may vary (Frier et al., 2022; Takahashi et al., 2020). For example, when a circular pattern is generated using continuous motion of the FP, the stimulation rate remains constant along the entire path. However, if the circle is drawn using a back-and-forth motion of the FP. The stimulation rate at the center of the path becomes twice that at the endpoints.

In this section, the circular shape (drawn in a continuous fashion) is used during the explanation of the technical operation of the STM. Moreover, circular patterns are commonly used in studies of STM (Frier et al., 2018, 2019; Takahashi et al., 2020; Takahashi et al., 2019).

The position of the FP ($\vec{p}_{FP}(t)$) in a 2-D plane (at a certain height) is given by Equation 3.1 as described by Morisaki et al., 2022:

$$\vec{p}_{FP}(t) = \vec{c} + \vec{u}\, r \vec{f}(t) \quad \text{where} \quad \vec{p}_{FP}(t) \in \mathbb{R}^3 \tag{3.1}$$

Where $\vec{c}$ is the center of the pattern ($\vec{c} \in \mathbb{R}^3$). Note, explanation assumes a circular pattern with a fixed center. $\vec{u}$ is the direction of the FP movement ($\vec{u} \in \mathbb{R}^3$ and $\hat{u} = 1$). r is the radius of the circumference, and $\vec{f}(t)$ is the periodic function describing the circular shape. Figure 3.1 illustrates Equation 3.1 for the position of the FP in a circular pattern.

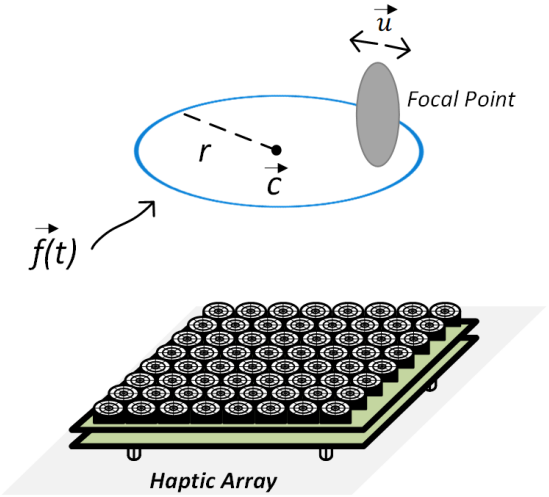

Figure 3.1: Variables representing a circular STM pattern.

The circular motion is represented by $\vec{f}(t)$ and is defined in Equation 3.2:

$$\vec{f}(t) = \begin{bmatrix} \cos(\omega_{draw} t) \\ \sin(\omega_{draw} t) \\ z_{FP} \end{bmatrix} \tag{3.2}$$

Where z_{FP} is the height of the pattern. ω_{draw} is the angular frequency ($\omega_{draw} = 2\pi f_{draw}$), where f_{draw} is the drawing frequency of the STM pattern (Frier et al., 2018). The duration that the FP requires to complete the pattern is given by f_{draw}^{-1} and this duration is known as the drawing period (T_{draw}).

The pattern length (l) corresponds to the shape's perimeter. The speed of the FP (v_{FP}) is calculated by the following equation Equation 3.3:

$$v_{FP} = l \cdot f_{draw} \tag{3.3}$$

The Figure 3.2 illustrates the parameters of the STM: i) the speed of the FP (v_{FP}), ii) the drawing period (T_{draw}), and iii) the pattern length (l).

The position of the FP along a pattern is updated at the position Update Rate (UR) (Frier et al., 2019). The temporal discretization of a drawing cycle can be represented by Equation 3.4 (Morisaki et al., 2022).

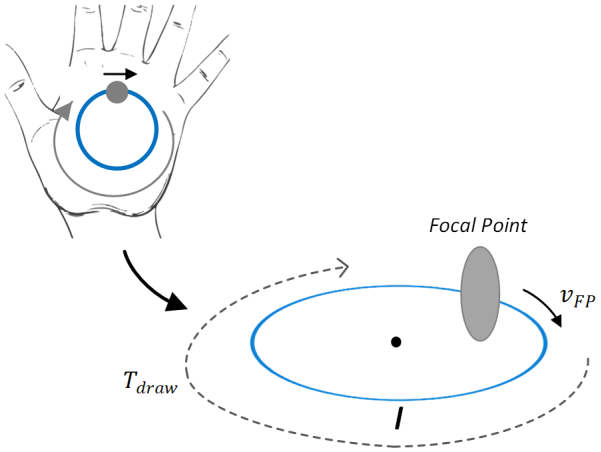

Figure 3.2: Spatial-temporal modulation main parameters.

$$t_i = \frac{i-1}{UR}, \quad \text{where } i \in [1, \ldots, N_{SP}] \tag{3.4}$$

Patterns or shapes are made of points that the FP travels in order to draw the shape. A position of the shape (e.g., the i-th position) is known as the Shape Position (SP). The total number of positions composing the shape N_{SP} is an important parameter for the STM (Frier et al., 2019; Morisaki et al., 2022). The Figure 3.3 depicts the discretization of a circular pattern into shape points.

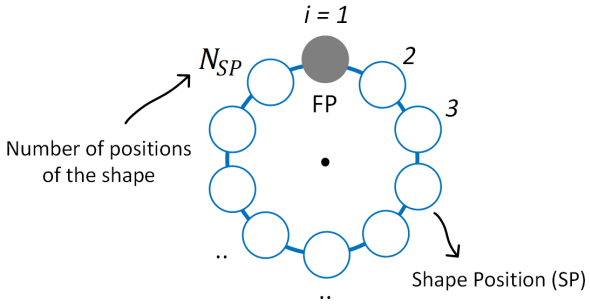

Figure 3.3: Shape discretization in positions (or shape points).

Consider that the positions of the shape are equidistant (Frier et al., 2019; Takahashi et al., 2020). The arc length between two SPs is known as the step-width (Morisaki et al., 2022), also referred to as d_{SP}. For the case of the circular pattern d_{SP} is given by Equation 3.5:

$$d_{SP} = r \cdot \theta \quad where\ \theta = \frac{2\pi}{N_{SP}} \tag{3.5}$$

Where r is the radious of the circle.

As can be seen, d_{SP} and the N_{SP} are directly related parameters. By increasing the amount of positions in a given shape, the positions become 'squeezed' and closer together. In same line of though, decreasing d_{SP} increases the spatial resolution of FP's movement.

The Maximum Update Rate (UR_{max}) is a parameter related with the UMAH system. It defines the maximum rate at which the FP's position can be updated. Often, to create the patterns, high update rates are required. Consider, for example, a pattern drawn at 80 Hz (f_{draw}) composed of 100 points (N_{SP}). Thus, the pattern requires a FP's position update rate given by $UR = f_{draw} \cdot N_{SP}$, which in this case is 8 kHz. Thus, f_{draw}, UR, and the N_{SP} are interrelated parameters. The UMAH's demonstrator UR_{max} must be high enough to enable the creation of patterns with the desired number of points (i.e., N_{SP}) drawn at the desired drawing frequency (i.e., f_{draw}) or FP's speed (v_{FP}). That is to say, $UR_{max} \geq UR$ (Frier et al., 2019).

While visiting the points of the shape, the FP remains on a SP for a short duration before jumping to the neighboring SP. As mentioned in Frier et al. (2018), this can be seen as a train of pulses, where each pulse has duration t_{SP} seconds.

The FP stays for t_{SP} seconds on a given shape position and re-visits the same location again after traveling all the SPs of the pattern, which takes T_{draw} seconds. The latter duration can also be obtained by the following Equation 3.6:

$$T_{draw} = N_{SP} \cdot t_{SP} \tag{3.6}$$

The traveling of the FP, seen as a train of pulses, is represented in Figure 3.4. In the upper part of the figure, the circular path is illustrated as a line segment. In the bottom part of the figure, the stimulation created by the FP (i.e., the pulses) are represented.

As detailed in Equation 3.5, the distance between adjoining pulses (d_{SP}) is shorter when the number of positions (i.e., the N_{SP}) is high. The opposite happens when the N_{SP} is low, in this case the SPs are further apart. Furthermore, for higher N_{SP} values, t_{SP} decreases due to the higher number of jumps the FP makes in a drawing cycle. Similarly, t_{SP} increases when the value of the N_{SP} is lower. Figure 3.5 illustrates the relationship between the N_{SP}, d_{SP}, and t_{SP} on a position of the pattern.

3.3 Research on mid-air haptic perception

The perception of STM has been mainly studied by two distinct groups: one from the University of Tokyo and another from Ultraleap company. This section is divided according to the type of stimuli investigated: short-path snesations (i.e., LM) were primarily studied by a group at the University of Tokyo. And sensation produced by larger patterns were mainly explored by Ultraleap. As mentioned at the beginning of this

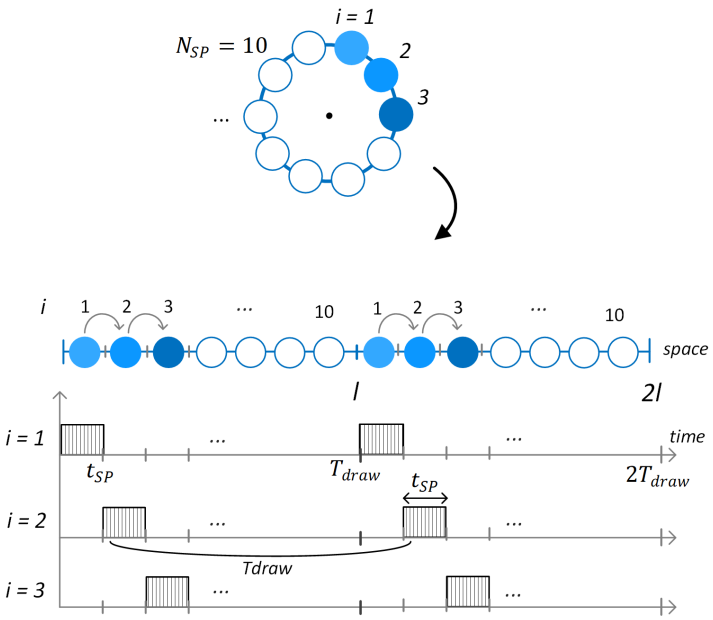

Figure 3.4: Circular pattern *seen* as a train of pulses.

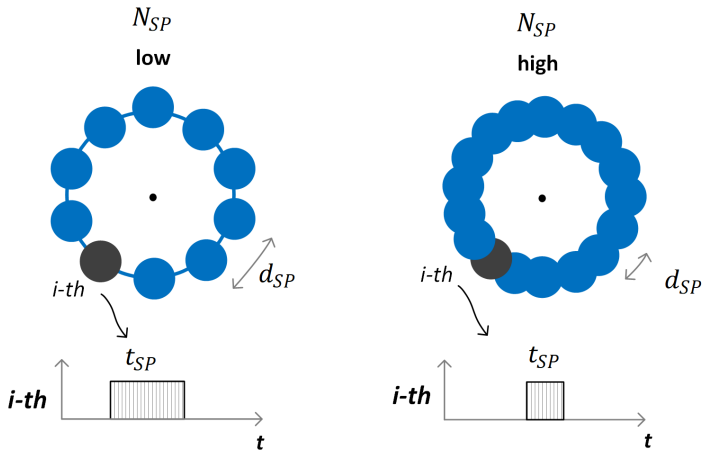

Figure 3.5: The relation between the N_{SP}, d_{SP} and t_{SP}.

chapter, both approaches fall under spatio-temporal modulation techniques. Nevertheless, the underlying perceptual mechanisms of both techniques differ. For an in-depth discussion of perception in the context of ultrasonic mid-air haptics, see Georgiou et al. (2022), Rakkolainen et al. (2019) and Rakkolainen et al. (2021).

3.3.1 Short path stimuli

The tactile detection thresholds for short spatio-temporal sensations (or LM) were measured in Takahashi et al. (2020) and Takahashi et al. (2018). The stimuli tested in these studies included short lines (Takahashi et al., 2018) and small circles (Takahashi et al., 2020). The size of the stimuli (l) varied from 6.3 mm to 4.4 cm (circular case). And the modulation frequencies (f_{draw}) that were tested varied from 10 Hz, 50 Hz,

100 Hz, and 200 Hz.

Note that, the stimuli used in the short path technique consist in the back and forth motion of the FP along the path or shape. The FP moves with a certain speed. Nonetheless, the perception of these types of sensations are normally specified in terms of f_{draw} rather than v_{FP}. Moreover, the l of the path was controlled trough the shape's amplitude parameter defined in Takahashi et al. (2020). This parameter which typically ranges from 1 mm to 7 mm defines, for the line segment, half of its length, and for the circular path, it radios.

These experiments were conducted using an ultrasonic phased array with nearly one thousand transducers operating at 40 kHz. The stimulated regions were the palm (i.e., glabrous skin) and the forearm (i.e., hairy skin). The FP diameter was about 10 mm.

It may seem contra-intuitive how moving an 1 cm FP over such short path may cause a sensation. Nevertheless, results for glabrous skin showed that increasing the stimulus size (l) and the modulation frequency f_{draw} led to lower tactile thresholds.

In Takahashi et al. (2020) a comparison between the tactile threshold of AM and these short path STM sensations was performed. The Figure 3.6 was adapted from the work of Takahashi et al. (2020). It shows the tactile thresholds for circular short path stimuli and AM, as a function of modulation frequency. Note, for the case of AM the modulation frequency is defined by f_{am} (see Section 2.3.3) and for the case of short spatio-temporal sensation, the modulation frequency is defined by f_{draw} (as explained in the previous section).

It can be seen from Takahashi et al. (2020) that a stimulus with 7 mm amplitude (i.e., 4.4 cm in length for the circular case) produces lower tactile thresholds than AM. For a 50 Hz stimulus a 20.2 dB reduction was observed. Conversely, when the stimulus amplitude is very small—such as the 1 mm case, tactile thresholds become comparable to those of AM. The graphic shows that the short path spatio-temporal sensations can create vibrotactile sensation with substantially lower tactile thresholds then AM.

The paths lengths (l) described so far are very short, in the order of the FP's diameter. The diameter depends on the phased array's aperture (see Equation 2.7) and in the context of Takahashi et al. (2020)'s work, the diameter is around 10 mm. The Figure 3.7 illustrates the FP moving in short paths, as the stimuli used by the University of Tokyo's research group.

The figure shows the movement performed by the FP in the linear and circular short paths. The image was drawn at scale, and as can be seen, the path's amplitude is in the same order as the FP's diameter.

As an example, for the case of the longer path (i.e., 7 mm amplitude) and considering the linear case, when the FP reaches one of the sides of the line, the line's centre becomes 'free' of the FP's direct

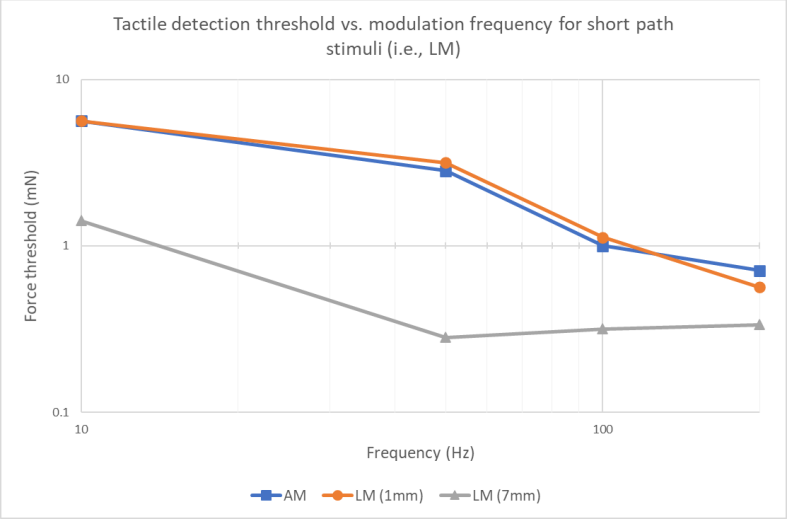

Figure 3.6: Short path stimuli (i.e., LM) sensitivity thresholds.

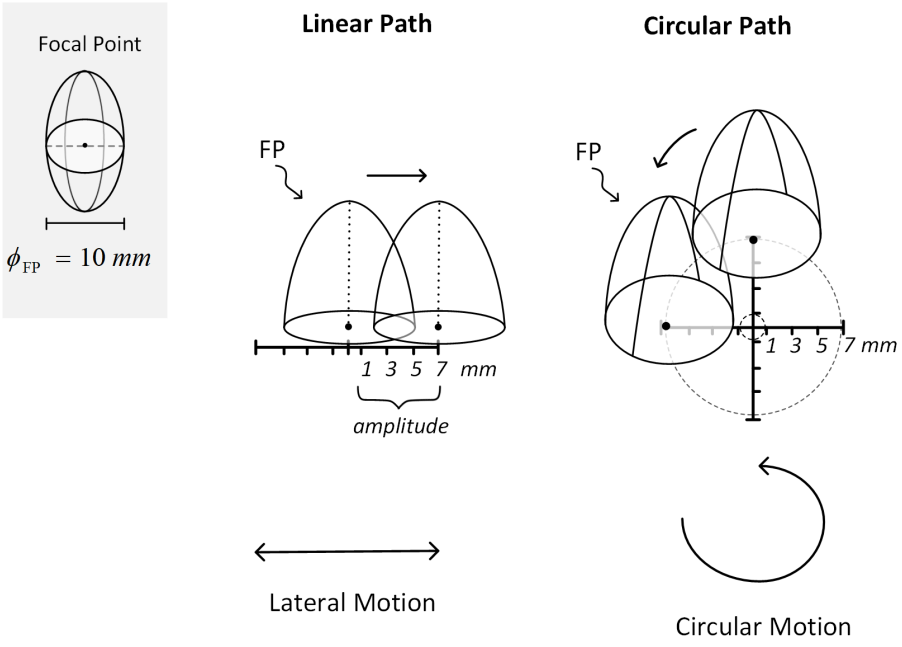

Figure 3.7: The FP's movement over short paths stimulus.

influence. By continuing the lateral motion, the FP reaches the centre again, and the skin in this region is stimulated once more. The Figure 3.8 (adapted from Takahashi et al., 2020) shows the stimulation signal in the center of the line path. As can be observed, the signal is sinusoidal, and resembles the envelope of an AM stimulus (see Section 2.3.3). Nonetheless, in the case of the spatio-temporal modulation the vibrotactile sensation occurs due to the back-and-forth motion of the FP and not through the modulation of the FP's amplitude (as in AM).

As already mentioned, for higher amplitude, the short path stimuli has substantially lower tactile detection thresholds than AM. The area covered by the FP is significantly larger in these stimuli than in the AM case,

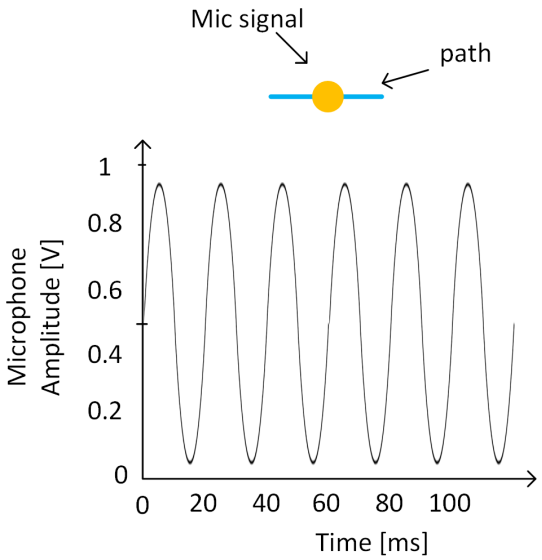

Figure 3.8: Stimulating signal of a 14 mm length line stimulus (signal measured in the center of the path).

even though the FP motion extends only a short distance from the path's centre. In fact, the motion length is in the order of the FP's diameter, which is close to the spatial resolution of touch (see Section 2.2.2.1). At higher f_{draw}, the rapid motion of the FP can elicit temporal summation in the stimulated region, further contributing to the intense vibrotactile character of the sensations.

In the research study by Morisaki et al. (2022), the effect of step-width (i.e., the d_{SP} parameter presented in Equation 3.5) on the perception of short path stimuli was investigated. The research study focused on modulation frequencies (f_{draw}) of 5 Hz, 10 Hz, and 15 Hz.

The goal was to examine the impact of d_{SP} on the quality of the resulting sensation. As base stimulus, a 6 mm line (i.e., 3 mm amplitude) was used. The haptic FP was produced using a wide-aperture ultrasonic phased array (57 cm $\times$ 30 cm) and the FP's diameter was about 10 mm. The maximum radiation force was 27 mN, and the FP was projected 26.5 cm above the array onto the palm.

The d_{SP} was varied from 0.2 mm to 3 mm. The authors found that when d_{SP} was smaller than 1 mm, the typical vibratory sensation associated with stimulus changed to a sensation of moving pressure, and this effect occurred regardless of f_{draw} used (i.e., 5 Hz, 10 Hz, 15 Hz). Thus, the study demonstrated that a non-vibratory pressure-like sensation can be achieved using short path spatio-temporal stimulus.

The stimuli used in Morisaki et al. (2022) had very low f_{draw} and the motion was confined to 6 mm linear paths. Given these characteristics, the stimulation signal at the center of the line is similar to that shown in Figure 3.8 (one that normally induces effective vibrotactile perception), though the signal's period is much longer due to the lower f_{draw} used.

The d_{SP} parameter controls the spacing between successive positions along the path's shape. The SA1 mechanoreceptors are linked to the spatial acuity of touch (see Section 2.2.1). These receptors respond weakly to static stimulation but are highly sensitive to motion across the skin. Therefore, when the motion resolution is high ($d_{SP} < 1$ mm), the FP's movement is perceived as smooth, likely activating these shallow mechanoreceptors. In contrast, when the motion resolution is low ($d_{SP} > 1$ mm), the line path becomes discretised. For example, with $d_{SP} = 3$ mm on a 6 mm path, the line shape is reduced to only two positions. The stimulation signal at each point becomes a *sinus-wave* signal at frequency f_{draw}, which leads to a pulsatile, vibratory sensation more readily detected by the deeper mechanoreceptors (e.g., the PC).

3.3.2 Bigger patterns

In the previous section, the perception of STM stimuli up to a few centimeters in length were discussed. Nevertheless, it remained unclear which parameters influenced the sensation of bigger patterns. A hypothesis was proposed by Frier et al., 2018 which drew an analogy with trains: when a train moves rapidly, specifically, when its velocity approaches the propagation speed of the surface waves it generates in the ground—the vibrations become significantly stronger. By analogy, if the moving FP (i.e., the train) travels along a path (i.e., the rails) at a speed close to that of the shear waves propagating through the skin (produced by the FP itself), the resulting sensation is stronger.

In a first experiment, the authors in Frier et al. (2018) characterized a skin-mimicking material in terms of the surface wave speed generated by an AM focus. An optical setup, consisting of a laser doppler vibrometer, a silicon slab (a skin-mimicking material), and a 256 ultrasonic transducer's phased array (16x16), operating at 40 kHz, was used to measure both the wavefront propagation speed and the induced surface displacement.

Because both human skin and the silicon slab are dispersive media, surface waves propagating through them exhibit frequency-dependent speeds, influenced by the AM's modulation frequency (i.e., f_{am}). In the experiment, the authors sought to determine the average surface wave velocity of the skin-mimicking material when excited by an AM FP. The results indicated an average surface wave speed of approximately 10 m/s Frier et al. (2018).

In a subsequent experiment, the displacement induced in the skin-mimicking material by STM patterns was analyzed. Circular patterns of three length sizes (l of 5 cm, 10 cm and 15 cm) were drawn at eight different FP's speeds (v_{FP}). The results showed that the induced displacement varied with the v_{FP}, and that the maximum displacement occurred at similar speeds for different pattern sizes—between 8 m/s and 10 m/s Frier et al. (2018). These findings supported the initial hypothesis that constructive interference occurs when the v_{FP} speed approaches the skin surface wave speed.

To examine how FP's speed affects perceived intensity of the pattern, a subjective experiment was conducted using a similar set of stimuli. A total of 39 circular patterns were tested on the palm, encompassing the same pattern sizes (i.e., 5 cm, 10 cm and 15 cm) and several v_{FP}s ranging from 2 m/s to 20 m/s. The results (shown in Figure 3.9) revealed a strong correlation between perceived intensity and v_{FP}. Patterns between 5 m/s and 8 m/s were perceived as stronger Frier et al. (2018). Moreover, the pattern size (l) also contributed to the perceived strength of the pattern.

The graphic of Figure 3.9 was adapted from the results of Frier et al. (2018) and shows the perceived intensity of circular patterns (i.e., 10 cm and 15 cm in length) with respect to the FP's speed. The data points are the speed values (retrieved from the author's work) and the curves represent spline interpolation for visual guidance (polynomial curve with 4-th order).

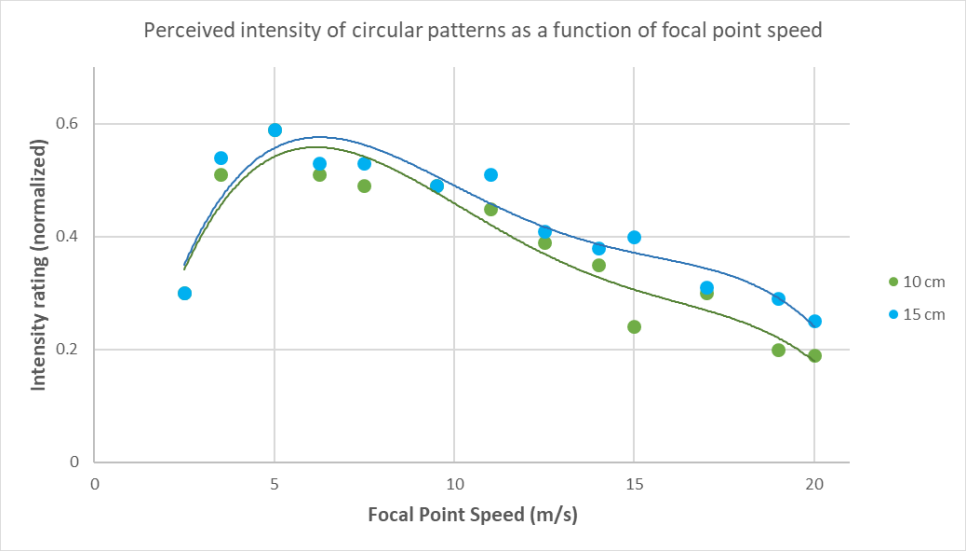

Figure 3.9: Perceived intensity of circular patterns (with 10 cm and 15 cm) as a function of FP's speed.

Relatively high FP's speeds (or drawing frequencies, f_{draw}) were used to build the sensations used to test the hypothesis of this study. The mid-air haptic perception generated under such speeds is a whole circumference (i.e., one can think of a cookie cutter pressed gently against the palm). The sensation was stronger for speeds between 5 m/s and 8 m/s, and at such fast speeds, spatio-temporal summation may occur (see Section 2.2.2.4), which may also contribute to the sensation. Consider an example from Figure 3.9, namely the 15 cm circumference drawn at a FP speed of 7.5 m/s. The drawing frequency (f_{draw}) of such stimulus is 50 Hz, and, respectively, the drawing period (T_{draw}) is 20 ms. Thus, the pattern is being repeatedly created at very short durations (in the vicinity of temporal resolution, see Section 2.2.2.2), and for that reason, temporal summation may occur. Moreover, the time gap between adjacent pulses (i.e., adjacent shape positions) is much smaller (exact duration given by $t_{sp} = T_{draw}/N_{SP}$. At these short delays between adjacent points, FP stimulations are felt simultaneously, invoking spatial summation.

The influence of the number of positions composing the shape (i.e., N_{SP}) on the perceived strength of the pattern was investigated by Frier et al. (2019). A circular pattern with 15 cm perimeter was created for several f_{draw}, namely 2 Hz, 5 Hz, 10 Hz, 20 Hz, 40 Hz, and 80 Hz. The N_{SP} changed from a few points to several hundreds, depending on f_{draw}. The haptic device was a common-size phased array composed of 256 transducers emitting at 40 kHz. The stimulation distance was 200 mm from the palm. The authors observed that the pattern N_{SP} affected the perceived strength of low-frequency patterns (those below 10 Hz). For higher frequencies, the pattern N_{SP} did not have any significant effect on perception.

In a second user study, researchers further examined the previous phenomenon for extended pattern sizes (i.e., 10 cm, 15 cm, and 20 cm). They calculated optimal pattern N_{SP} values for enhancing the sensation of the tested circumferences. For the 15 cm circumference, they estimated optimal values ranging from 15 points to 20 points, depending on the f_{draw}. Furthermore, they calculated that with 90 to 240 points (once again depending on thef_{draw}), the circumference would be rendered unnoticeable.

The perception of STM patterns was examined in the context of tactile experience by Ablart et al. (2019). The STM method was evaluated across five perceptual criteria: intensity, roughness, roundness, regularity, and valence. The system used to generate the patterns was an ultrasonic array equipped with a 16×16 transducers (40 kHz). The system operated at a 16 kHz update rate to provide high-resolution motion of the FP. Stimulation was delivered to the palm at a distance of 16 cm. The tested patterns consisted of circumferences of 5 cm, 10 cm, and 20 cm in length, drawn at frequencies ranging from 5 Hz to 100 Hz in 5 Hz increments (a total of twenty distinct f_{draw}).

The authors found that perceptual attributes such as intensity, roughness, roundness, and regularity varied systematically with the pattern's characteristics. The intensity results were consistent with results obtained by Frier et al. (2018), and are correlated with the FP's speed. Roundness depended strongly on pattern size: small patterns (e.g., the 5 cm circumference) had limited ability to convey shape compared with the larger 20 cm pattern. Roughness and regularity varied with drawing frequency. For instance, the 20 cm pattern was perceived as rough at f_{draw} of 25 Hz, whereas at 75 Hz it was perceived as smooth.

This study included a 5 cm circumference, as did Frier et al. (2018). In our view, perception of such short-path 'patterns' relates closely to the perception studies discussed in Section 3.3.1. The perceived intensity of localized stimuli seems to depend primarily on modulation frequency (f_{draw}) more than on v_{FP}. Moreover, results of roughness perception (Ablart et al., 2019) was less pronounced for the 5 cm pattern compared to the larger patterns, likely due to the more "vibrotactile-oriented" nature of such small trajectories.

The findings reported by Ablart et al. (2019) were later leveraged by Beattie et al. (2020). In their work, Beattie and colleagues developed an automated tool for generating ultrasonic mid-air sensations based on the estimated roughness of visual images. Depending on an image's rough-to-smooth rating, the tool

produced sensations with f_{draw} in the 25–75 Hz range, following the perceptual mapping reported by Ablart et al. (2019). Their study illustrates how perceptual knowledge of STM can be used to automate stimulus design in a multimodal (visuo-haptic) context.

3.4 Considerations about the modulation's sensations

This section was written based on our personal experience with the STM and considering the works discussed throughout this chapter. The spatio-temporal patterns or stimuli (now refered to as STM stimuli interchangeably) has a complex perceptual behavior. The speed of the FP is of major importance to the type of sensation produced.

3.4.1 Fast speed motion

When the FP moves rapidly, it generates a perception of simultaneity that enhances the sensation's intensity. For a *fast-moving* FP, consecutive and adjacent stimulation's inter durations (T_{draw} and t_{SP}, respectively) fall below or near the temporal resolution of touch. This underlies the simultaneity phenomenon mentioned in the previous section.

Under the temporal resolution, the sensation of short path STM stimuli is specified in terms of modulation frequency (f_{draw}), in a manner similar to AM (Takahashi et al., 2019). Conversely, for larger patterns, the sensation strength increases with FP speed (Frier et al., 2018). When focal speeds are high enough, tactile summation occurs (see Section 2.2.2.4) and the perceived intensity of the pattern is amplified.

3.4.2 Slow speed motion

When the motion of the FP is *slow* (which typically corresponds to low f_{draw}), the FP's movement becomes clearly detectable. In this situation, spatio-temporal simultaneity does not occur, and the sensation feeling depends on the haptic resolution of the pattern or stimulus.

Smaller stimuli

For small stimuli, when d_{SP} is *high*, the FP is felt as a moving pressure (Morisaki et al., 2022). Conversely, when d_{SP} is low, the stimulus acquires a vibratory character. Note, this should not be confused with vibrotactile sensations produced by AM.

Bigger patterns

Motion resolution influences the perception of larger patterns (Frier et al., 2019), too. In this case, resolution is defined by the N_{SP} parameter. Lower N_{SP} patterns are associated with stronger perception compared with higher resolutions. Furthermore, in the study presented in the Chapter 5, preliminary

evidence was provided that for slow-moving FP, resolution also affects the textural perception of the sensation. Depending on the number of positions in a shape, rough dynamic sensations (low N_{SP}) or smooth dynamic sensations (high N_{SP}) can be elicited.

3.4.3 Intermediary speed motion

So far, *slow* and *fast* FP speeds were considered. However, it has also been observed that intermediate speeds can evoke patterns with a rough texture. More specifically, texture perception varies with the speed of motion (v_{FP}) or modulation frequency (f_{draw}). Ablart et al. (2019) showed that roughness is perceived at 25 Hz ($\approx$ 5 m/s), whereas smoothness is perceived at 75 Hz ($\approx$ 12 m/s), the latter corresponding to a very fast motion.

3.4.4 Types of sensations

Relevant research works on the perception of STM were presented throughout the chapter. It is evident that STM can evoke various types of sensations, depending how the modulation parameters are tuned used. An investigation carried out in this thesis studied the sensation regimes produced by STM. Other research studies have also identified—or (at least mentioned) different sensations associated with the STM.

Vibrotactile

In section 3.3.1, the tactile detection thresholds for short path STM sensations were presented. The results presented there confirmed that at higher modulation frequencies ($f_{draw} = 100\ Hz\ to\ 200\ Hz$), thresholds were the lowest and the sensation had a vibrotactile quality. Nevertheless, for lower-frequency stimuli (such as 14 mm line at $f_{draw} = 10\ Hz$), some participants reported perceiving the physical movement of the FP (Takahashi et al., 2020).

Moving pressure

Another study by Morisaki et al., 2022 used similar stimuli (12 mm lines and f_{draw}, below 15 Hz) to test the impact of the d_{SP} on the quality of the sensation. They observed that when the d_{SP} was smaller than 1 mm, the vibratory sensation typically associated with short path STM stimuli changed to a sensation of moving pressure, regardless of frequency.

Considerations on bigger stimulus

In the same line of thought, for larger STM patterns, the N_{SP} (a parameter related to d_{SP}) was also found to affect STM produced sensation (Frier et al., 2019). The authors observed that the N_{SP} influenced the perceived intensity of patterns drawn at low frequencies (f_{draw} below 10 Hz). This finding—indicating that N_{SP} impacts sensations only at low frequencies—suggests the existence of distinct sensation regimes at low and high frequencies. The stimuli used by Frier et al. (2019) are comparable to those tested in our

perceptual study (discussed in the Chapter 5). The existence of different regimes at lower and higher FP speeds (directly related with f_{draw}) were verified.

The works of Ablart et al. (2019) and Beattie et al. (2020) similarly employed stimuli comparable to those used in Chapter 5. A 20 cm circumference drawn at f_{draw} of 25 Hz ($\approx$ 5 m/s) was perceived as a rough texture, whereas at 75 Hz ($\approx$ 12 m/s) it was perceived as smooth. Our findings align with these observations in that two distinct regimes under comparable speed conditions were specified. Our work differs from that of Ablart et al. (2019) and Beattie et al. (2020) in terms of pattern length (15 cm circumference was used in our work) and the interaction type: in our case, sensations were generated passively, while Ablart et al. (2019) relied on active exploration. Nonetheless, in our view, the two sensation regimes identified in our work (Mendes et al., 2024), corresponding to rough and smooth sensations, share the same underlying perceptual characteristics reported by Ablart et al. (2019).

Authors investigated optimal N_{SP} values for different circular patterns but did not found correlation with specific pattern properties (Frier et al., 2019). Based on our experience, better feeling is achieved when using the minimum N_{SP} necessary to cover the entire pattern—for instance, around 10 points for a 15 cm circle with a 15 mm FP's diameter, although this may depend on the exact size of the FP. However, excessively high N_{SP} values can cause the sensation to disappear. This may occur due to system limitations, such as an insufficient update rate (UR_{max}) preventing proper FP generation, or due to perceptual constraints related to critical pulse duration (see Section 2.3.2.2). In the latter case, since an STM pattern can be seen as a pulse-train, increasing N_{SP} reduces the duration of each pulse (or SP), potentially falling below the critical threshold required for tactile detection. In Chapter 6 these parameters are specified for a particular STM sensation, the dynamic haptic sensation.

3.5 Conclusions

In this chapter, the STM technique was explained. This haptic modulation strategy is fundamental to the work developed in this thesis. Two distinct groups from the University of Tokyo and Ultraleap company developed the STM for the case of short path stimuli and bigger patterns, respectively. In the beginning of the chapter, the operation of the STM was explained in a technical manner. Then, literature on the perception of the STM was reviewed. The explanation was divided in two sections, one considering the perception of short stimuli, and other for bigger patterns. In the last part of the chapter, the sensations produced by the STM were explained. This is a key aspect that motivated us to pursue the research developed in Chapter 5.

Ultrasonic Mid-Air Haptic Demonstrator

4.1 Introduction

The present chapter focus on the UMAH demonstrator developed by the ESRG team from University of Minho. This demonstrator was used extensively throughout the thesis and the development and construction of this system spanned several years. The purpose of this chapter is to document the effort carried out by the research and development team in which I took part.

This chapter begins with a description of the acoustic simulator. Then we detail the UMAH hardware, which is composed of three main components. The ultrasonic phased array, the system on module and the FPGA-based carrier board. The architecture of the embedded system implemented on the UMAH system-on-module is also presented in a dedicated section. By last, the chapter ends with results of the experimental measurements performed to the UMAH system.

4.2 Acoustic Field Simulator

An acoustic simulator was developed with the main purpose of visualizing the FP. The simulator generates acoustic field simulations that reliable estimate the field. The implementation of a simulator was one of the initial objectives of this thesis. For its implementation, the Python programming language was chosen, mainly for its simplicity and open-source nature.

Some of the physics fundamentals for the FP's generation were already explained in Chapter 2. In the present section, a new and improved explanation for the FP's creation is performed.

The acoustic model implemented was the small-source model. The model approximates the transducer as a point-source and it is explained in detail in the book Kinsler et al. (1999) and this model was chosen due to its simplicity. There are other more suitable models that simulate the FP more accurately, such as the piston model. Nevertheless, the small-source approximation (or monopole) was sufficient for visualization purposes and even provided quantitative satisfactory results. Note, the following explanation refers to the emitter, source and transducer interchangeably.

The pressure field calculation considers a harmonic solution of the wave equation. The pressure created by a pulsating sphere (p in [Pa]) of finite size (considering $ka < 1$) with homogeneous emission, at a point of space $\vec{r}$ (and assuming an unbaffled set) is given by Equation 4.1:

$$p(\vec{r}) = \rho_0 c U_0 \cos(\theta_a) \frac{a}{r} e^{-j(k(r-a)-\theta_a)}, \quad ka < 1, \quad r > a, \quad \theta_a = arccot(ka) \tag{4.1}$$

Where r is the distance in [m] from the emitter's center to the point $\vec{r}$. a is the ultrasonic transducer's radius (i.e., the Murata MA40S4S' radius), ρ_0 is the equilibrium medium density of air ($1.21\,\text{kg/m}^3$ at $23\,^\circ\text{C}$), and c is the speed of sound in air ($343\,\text{m/s}$ at $23\,^\circ\text{C}$), U_0 [m/s] is the amplitude of the radial velocity

of the emitter. This is a quantity related to the emission and can be calculated based on the transducer's datasheet, k is the angular wavenumber ($k = 2\pi/\lambda$). For the transducer used in the demonstrator, which emits at 40 kHz, λ (i.e., wavelength) is approximately 8.6 mm. $j^2 = -1$.

The Equation 4.1 is valid for distances greater than the radius of the source ($r > a$). When $r \leq a$ the equation is not valid because the pressure would increase drastically.

The complex specific acoustic impedance (z) is a physical quantity that appears in Equation 4.1 and that at the emitter's surface (i.e., $r = a$) is defined as:

$$z(a) = c\rho_0 \cos(\theta_a) e^{j\theta_a} \tag{4.2}$$

To obtain an approximation for the small-source model, the size of the emitter is shrunk (i.e., $ka \ll 1$). The emitter becomes a point source of spherical waves. By doing so, the term $\theta_a \longrightarrow \pi/2$ and the pressure created is mostly reactive. The $\cos(\theta_a)$ is approximated by ka, and the phase delay term $k(r-a)$ is no longer referenced to the emitter's radius. With these transformations, the Equation 4.1 simplifies to:

$$p(\vec{r}) = j\rho_0 c \frac{a}{r} U_0 ka\, e^{-jkr}, \quad ka \ll 1, \quad r > a \tag{4.3}$$

The small-size model allows the pressure calculation to become independent of the emitter's geometrical characteristics (e.g., size and shape). The expression can be defined in terms of the strength produced by the source (i.e., source strength Q) instead of how the source produces its strength. The Q produced by a spherical emitter is defined by: $Q = S_{\text{sphere}} U_0 = 4\pi a^2 U_0$. And it arises from the expression of the pressure, like is demonstrated in the next equality:

$$p(\vec{r}) = j\rho_0 c \frac{a}{r} U_0 ka\, e^{-jkr} \Leftrightarrow p(\vec{r}) = \frac{j}{2} \frac{\rho_0 c}{\lambda r} Q e^{-jkr} \tag{4.4}$$

This results means that the pressure calculation is agnostic to the geometrical aspects of the emitter. The Q for the Murata's ultrasonic transducer (the one present in the UMAH system) can be estimated and used directly on the above equation. To that end consider a circular-shaped diaphragm and Q is calculated as $Q = S_{\text{diaphragm}} U_0 = \pi a^2 U_0$.

By considering the amplitude term of the pressure and reordering its terms, an expression is obtained for the calculation of U_0:

$$U_0 = \frac{2|p(r)|r\lambda}{\rho_0 c S_{\text{diaphragm}}} \tag{4.5}$$

From the transducer's datasheet, the remaining parameters can be calculated, i.e., $S_{\text{diaphragm}}$, $|p(r)|$, and r. The a was defined as 4.5 mm, and the transducer creates 28.28 Pa (peak) at a distance of $r = 30$ cm.

So far, a mathematical expression based on the small source model has been developed to estimate the pressure created by the Murata's ultrasonic transducer. The developed expression was used for the calculation of the acoustic field produced by the UMAH system.

A cartesian coordinate system was adopted for describing the field space. The calculation of the distance r_i, from the i-th ultrasonic transducer (at position (x_i, y_i, z_i) where $i \in [1, N^2]$) to a point in space $\vec{r}$ (where $\vec{r} \in \mathbb{R}^3$) is given by:

$$r_i(\vec{r}) = \sqrt{(r_x - x_i)^2 + (r_y - y_i)^2 + (r_z - z_i)^2} \tag{4.6}$$

The transducer emission is not omnidirectional, as can be seen by the directivity graphic of Figure 2.2. It depends on the angle θ_i that is defined by the i-th transducer's normal ($\hat{n}$) to the observation point $\vec{r}$. Thus, the angle depend on the relative positions of the transducers ($\vec{r_i}$) to the point $\vec{r}$ (thus $\theta_i(\vec{r} - \vec{r_i})$). The directivity function of the Murata's transducer was approximated by a sinusoidal function, and the pressure attenuation due to directivity for the i-th transducer is set by $D(\theta_i(\vec{r} - \vec{r_i}))$.

Thus, the pressure generated by the i-th emitter at a point in space ($\vec{r}$) is given by:

$$p_i(\vec{r}) = \frac{1}{2r_i(\vec{r})} \frac{\rho_0 c}{\lambda} Q D(\theta_i(\vec{r} - \vec{r_i}) e^{-jkr_i(\vec{r})}, \quad r_i > a, \ i \in [1, N^2] \tag{4.7}$$

For the calculation of the pressure generated by the array at a point in space, the superposition of all individual pressures are considered as in Equation 4.8. And the magnitude of the pressure is calculated by (i.e., $|p(\vec{r})|$).

$$p(\vec{r}) = \sum_{i=1}^{N^2} p_i(\vec{r}) \tag{4.8}$$

For the calculation of the pressure field on a given plane, the above calculation is performed for all positions of the plane.

The amplitude (A) and phase (φ) of the transducer's are important parameters for controlling the creation of the FP. For correct calculation of the pressure, the expression 4.7 must account for that information. Consequently, the equation becomes:

$$p_i(\vec{r}) = \frac{A_i}{2r_i(\vec{r})} \frac{\rho_0 c}{\lambda} Q D(\theta_i(\vec{r} - \vec{r_i}) e^{-j(kr_i(\vec{r}) + \varphi_i)}, \quad r_i > a, \ i \in [1, N^2] \tag{4.9}$$

Where A_i is the pressure amplitude of the i-th transducer (and $A \in [0, 1]$) and φ_i is the phase of the i-th transducer (where $\varphi \in [-\pi, \pi]$ radians).

4.2.1 Results

The set of simulations presented in this section regards the acoustic field of the FP. The simulations presented here allow the estimation of the FP's diameter and the radiation force.

The simulations were carried out considering the following characteristics: the FP was created $20\,\text{cm}$ above the array's center and the focal intensity was set to 24% of the maximum power. This intensity value was chosen for comparative purposes, as will be discussed in Section 4.5.4.

The FP's acoustic field is shown in Figure 4.1. In the left image, a top view of the focus region (xy-plane) is represented, and on the right image, a lateral profile view of the focus (xz-plane) is shown (images not to the same scale).

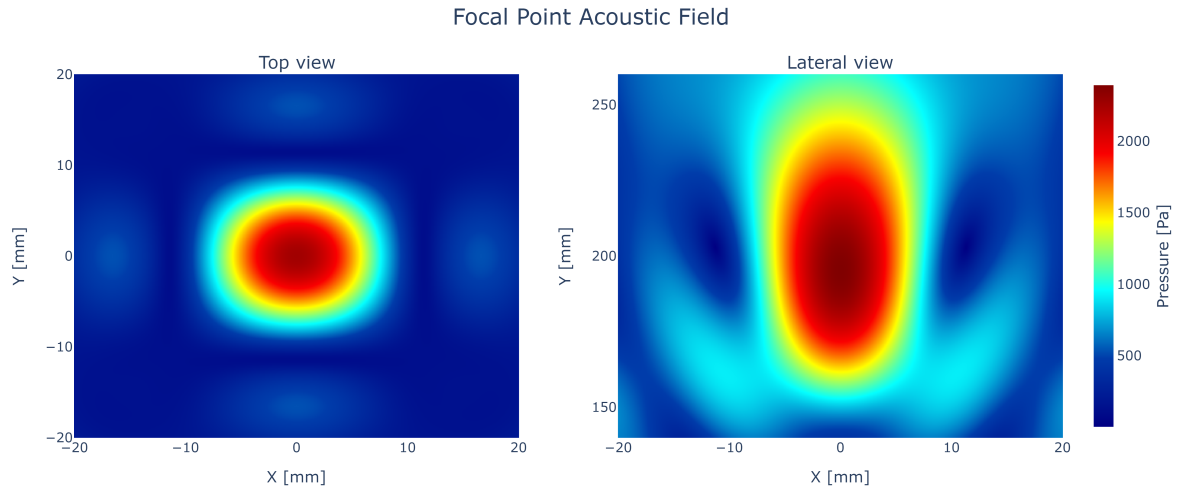

Figure 4.1: The FP field. (Left image) The FP's top view. (Right image) FP's side view.

As can be observed, the FP is a concentrated high-pressure zone which, in this case, is about $2250\,\text{Pa}$ (Peak) in the centermost part. As can be observed (left image), around the focus there are four less intense side lobes. Moreover, the FP has an elongated shape in its longitudinal dimension (right image), which matches its typical shape of an ellipsoid of revolution.

The focal diameter was measured in terms of Full-Width at Half-Maximum (FWHM). The focus' diameter, obtained from the top-view image, is $13.6\,\text{mm}$. The radiation force was calculated based on the circular area defined by the focus' diameter, and the calculated force was $3.23\,\text{mN}$.

The acoustic field produced by the phased array was simulated and the result is shown in Figure 4.2.

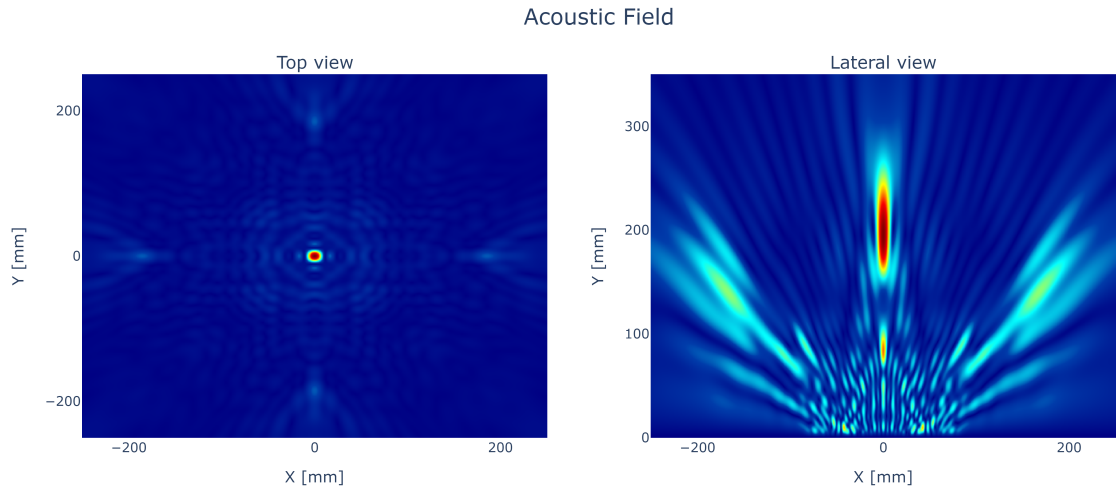

Figure 4.2: The UMAH system acoustic field. (Left image) Acoustic field's top view perspective. (Right image) field's side view.

A top view of the acoustic field is presented in the left image, and a lateral view of the field is shown in the image of the right. The pair of images provide visualization of the FP's relative dimensions (both images are around the same scale).

The top-view image shows the FP represented in the center, and it is possible to observe the grating lobes that are formed around a 20 cm distance from the FP. Grating lobes are fundamentally FP replicas, with lower energy, due to their distance from the phased array's center and the attenuation associated with the directivity of the transducers. The grating lobes occur due to the quadrangular geometry of the phased array. The image on the right is also illustrative of the appearance of the grating lobes. As can be observed, they appear below the FP's plane, more specifically around a 15 cm height.

The near-field's chaotic behavior is also observable in the right image of Figure 4.2 (bottom part of the field), which shows the interference pattern occurring at shorter distances from the phased array. In contrast, the far field occurs for larger distances (i.e., $r \gg \lambda$) and corresponds the region where the FP is created.

To complement the set of results presented so far, the images of Figure 4.2 were combined into a 3D isometric perspective. The Figure 4.3 and provides a better representation of the complete UMAH acoustic field.

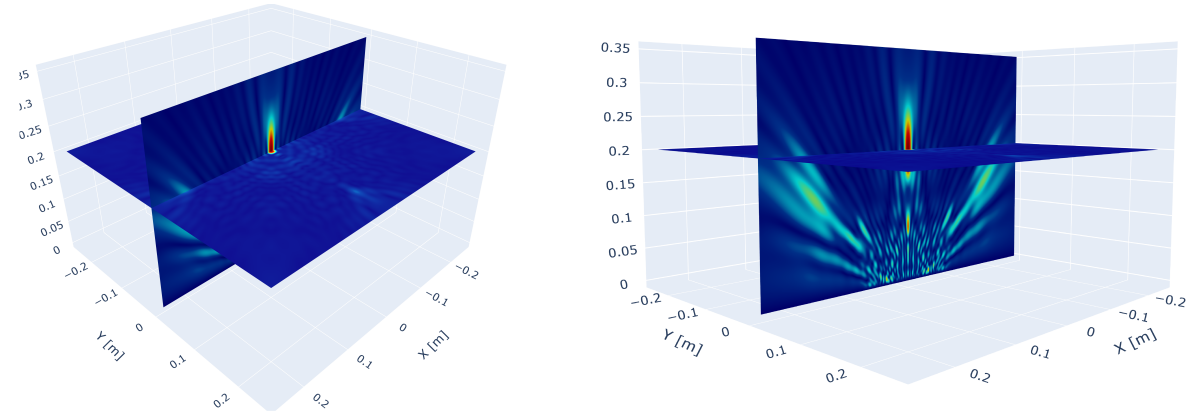

Figure 4.3: 3-D isometric perspective of the UMAH's generated acoustic field.

4.3 Ultrasonic Mid-Air Haptic prototype

The current section discusses the UMAH prototype which is composed of three main components: (i) the ultrasonic phased array, responsible for generating the acoustic field and, consequently, the haptic stimulus; (ii) a carrier platform, which groups all components together, namely the phased array and the System-on-Module (SoM), and also includes the board implementing support for several system features, such as debugging and external boot, etc; and (iii) the SoM, which was acquired commercially and contains the System-on-Chip (SoC) used to implement the system's software architecture.

4.3.1 Ultrasonic Phased Array

The phased array comprises the ultrasound transducers soldered onto a PCB. The array surface is composed of 248 ultrasound transducers (Murata MA40S4S) arranged in a quadrangular geometry. The total size of the phased array surface is approximately 17 cm × 17 cm. The total number of transducers is essentially limited by the number of available pins on FPGA's SoC, which are used to directly drive the transducers (the SoC is the core component of the SoM, and it will be discussed further in the section).

The signal exciting the transducers has a peak-to-peak amplitude of 20 V. As the signal generated by the FPGA has an amplitude of 1.8 V, amplification is required. The first step in this process is to level-shift the low-amplitude signal to 3.3 V, which is performed using voltage level-shifter transceivers (Texas Instruments, 2026). These signals are then amplified using a MOSFET driver (Microchip Technology, 2026) to reach 20 Vpp.

The signals generated by the FPGA are 40 kHz Pulse-Width Modulated (PWM) signals. After proper amplification, the PWM signal is used to excite the transducers. Since the transducers exhibit a very narrow frequency response around 40 kHz, they effectively act as a filter, attenuating the higher harmonics of the PWM signal and producing an almost pure 40 kHz sinusoidal acoustic wave.

In the Figure 4.4, the ultrasonic phased array is depicted. On the left side of the figure is the upper part of the phased array, and the right image depicts the bottom part of the PCB. There, it is possible to observe the connectors for mounting on the carrier board and also the 124 dual-MOSFETs used for amplifying the signal to 20 Vpp.

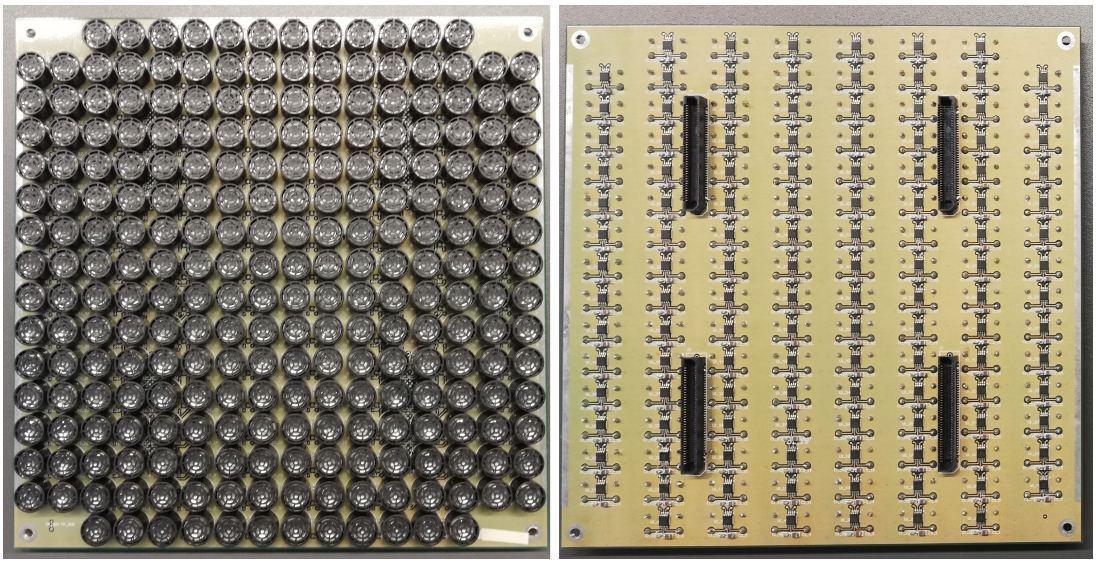

Figure 4.4: Ultrasonic phased array. (Left image) haptic array's top view. (Right image) haptic array's bottom view.

4.3.2 System on Module

The next component to be discussed is the SoM TE0745 (Trenz Electronic, 2026a) from Trenz Electronics. This module was selected to fulfill the project requirements, namely the need for a compact yet high-performance embedded system with a high number of available Input/Output (I/O) pins. The TE0745 SoM meets these requirements and is shown in Figure 4.5.

The Figure 4.5 was adapted from Trenz Electronic (2026b). The left image of the figure shows the top view of the module (where the SoC chip is in the middle). The right image of the figure shows the bottom view of the module, and it is possible to observe the high-density pin connectors of the module.

At its core, the module integrates a SoC, the AMD Zynq-7000. In general, the SoM provides all the necessary electrical infrastructure to ensure correct operation of the SoC. This support is implemented through a set of components mounted on the module's PCB, including oscillators and clock generators, a real-time clock, voltage level shifters, communication transceivers (e.g., USB 2.0 and Ethernet), volatile memory (1 GB of DDR3 SDRAM and QSPI Flash), as well as non-volatile firmware memory, among others.

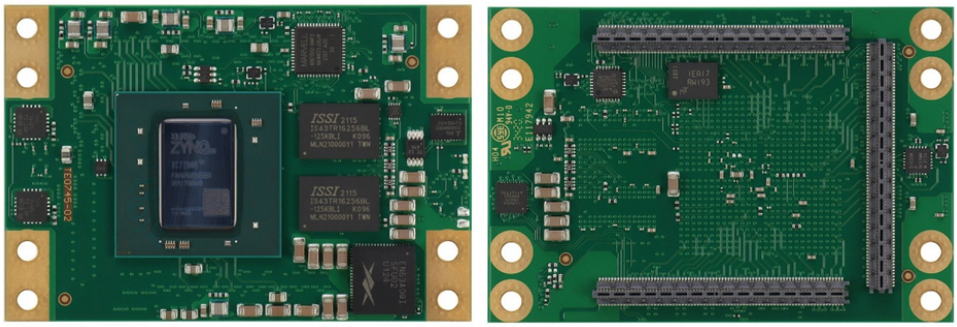

Figure 4.5: System on Module from Trenz electronics used in the UMAH demonstrator. (Left image) The SoM's the top part. (Right image) The SoM bottom part.

In addition, the SoM provides access to the processor's debug and trace infrastructure through the Joint Test Action Group (JTAG) interface and exposes 250 general-purpose I/O pins from the SoC's FPGA fabric.

To access the JTAG and Universal Asynchronous Receiver–Transmitter (UART) functionalities, Trenz Electronics provides a small auxiliary module, the TE0790 (Trenz Electronic, 2026c). This module is based on an Future Technology Devices International (FTDI) interface device, which converts USB into standard JTAG and UART signals. The module was connected to the carrier board described in next section.

As previously mentioned, the "brain" of the SoM is the Zynq-7000 device. It implements a hybrid embedded system architecture composed of a conventional microprocessor subsystem, referred to as the Processing System (Processing System (PS)), and an FPGA subsystem, referred to as the Programmable Logic (Programmable Logic (PL)). These two subsystems are interconnected through a set of high-performance data buses. This type of computational solution is highly versatile, as it combines the ease of software development typically associated with microprocessors with the ability to implement dedicated hardware accelerators using FPGA logic, all within a compact form factor and low-power device.

The PS is based on a general-purpose processor, namely a dual-core Advanced Risc Machine (ARM) Cortex-A9 running at up to 1 GHz. It includes a two-level cache hierarchy, an interrupt controller, UART peripherals, timers, and debug and trace infrastructure. Communication between the PS and the PL is achieved through 32-bit and 64-bit data buses implementing the Advanced eXtensible Interface (AXI) protocol. These buses allow the PS to access custom Intellectual Property (IP) cores instantiated in the PL, and several interrupt lines are also available for bidirectional signalling between the PS and the PL. The Zynq-7000 architecture is depicted in the block diagram of Figure 4.6 (the figure is original from AMD (2026).

The FPGA integrated within the SoC is the XC7Z045 device in the FBG676 package. This device belongs to the Kintex-7 FPGA family and provides one of the highest resource counts within this family. Due to its packaging characteristics, the FPGA exposes 250 general-purpose I/O pins, configurable for voltage

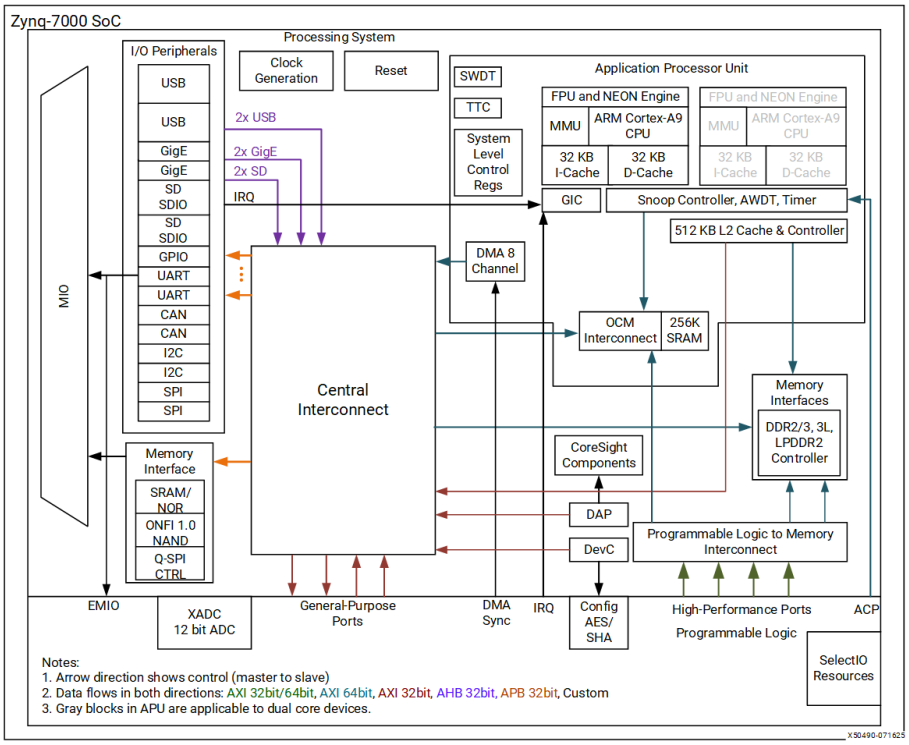

Figure 4.6: Zynq-7000 block diagram.

levels ranging from 1.2 V to 3.3 V. Not all the pins can be set to 3.3 V and for that reason the 1.8 V on all the FPGA's available I/Os was selected.

The SoC manufacturer provides several software tools for programming and debugging the Zynq-7000 device. In particular, the Vivado Design Suite enables the configuration and programming of both the PS and the PL. The tool includes several bare-metal C examples for programming the ARM processor. For FPGA development, a dedicated Integrated Development Environment (IDE) from Vivado supports hardware description languages such as Verilog, enabling the creation of custom hardware accelerators. In addition, the IDE provides a comprehensive IP core repository, allowing developers to easily instantiate, configure, and integrate pre-designed IP cores into their designs.

4.3.3 Carrier Board

The carrier board is the platform that mechanically and electrically connects the ultrasonic phased array to the SoM. The carrier board integrates all UMAH components into a more compact system. In addition, it provides the necessary interfaces and supporting circuitry required for programming, debugging, storage, communication, and reliable operation of the system. The carrier board is shown in Figure 4.7. The left image shows the bottom view of the carrier board. It is possible to observe the SoM already mounted in the center (it is covered by an aluminium heatsink). The right image shows the top part of the carrier, with its four connectors for mounting on the phased array PCB.

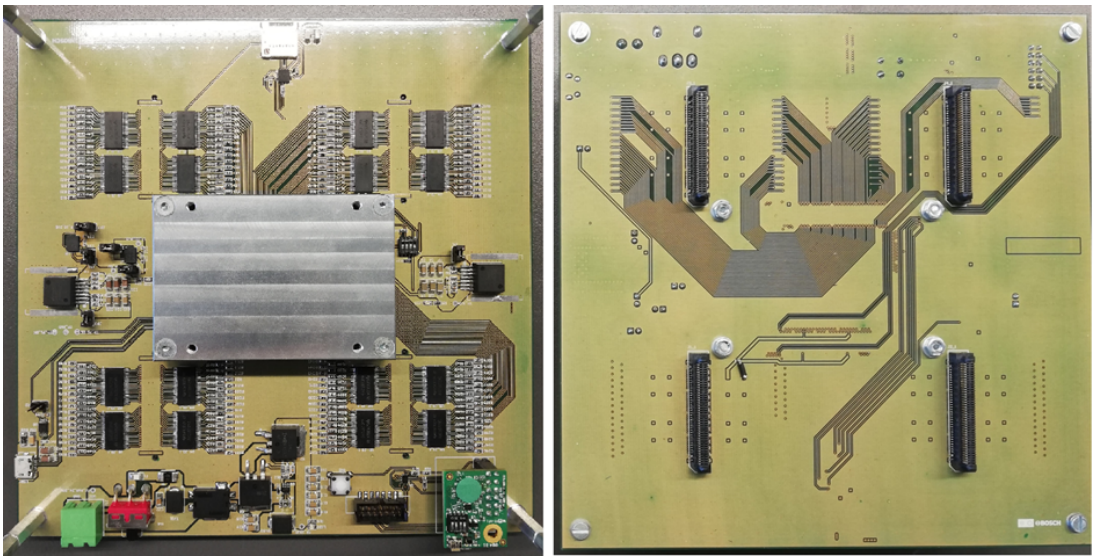

Figure 4.7: The carrier board developed for the UMAH system. (Left image) The carrier's bottom view. (Right image) The carrier's top part.

The connection to the phased array is achieved through four high-density board-to-board connectors (ERM8-040 from Samtec), each with 80 pins, of which 62 are dedicated to driving the ultrasound transducers. These connectors ensure mechanical stability and proper signal conditioning for the 248 transducer's drive signals (4 connectors × 62 signals per connector).

To interface the SoM, the bottom side of the carrier board hosts three Samtec SS5-80 female connectors each providing 160 pins that are used to interface the SoM with the carrier board.

The carrier board implements the electronic circuitry required for several key functionalities of the UMAH demonstrator and contributes significantly to the overall robustness of the system. For processor programming and debugging, the carrier provides support for JTAG through the TE0790 module, as described in previous section. The same module also provides UART serial communication.

The carrier board includes a microSD card connector that can be used as an external storage medium, commonly employed to boot or flash executable code to the processor. In addition, a micro-USB connector is available to support On-The-Go functionality, allowing the SoC to operate, for example, as a USB host device.

When operating at full power, the prototype exhibits a total power consumption of approximately 60 W. Furthermore, the carrier board incorporates several voltage level shifters and regulators to generate the internal supply rails (i.e., 5 V, 3.3 V, and 1.8 V), as well as multiple transceivers for interfacing with the ultrasound transducers, USB, and SD card. The fully mounted UMAH prototype is shown in Figure 4.8.

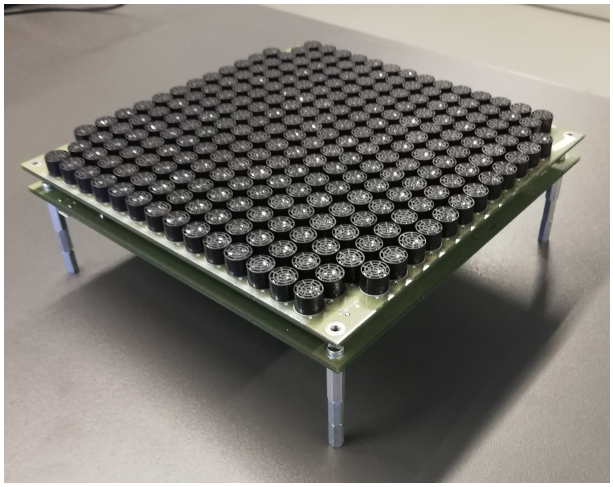

Figure 4.8: The full UMAH prototype developed by the ESRG team from University of Minho.

4.4 System's Architecture

This section concerns the implementation of the system architecture. The explanation is kept as simple as possible, while focusing on the main aspects related to stimulus generation. Despite the simplified approach presented here, the UMAH prototype was used in numerous demonstrations and supported several functionalities. For example, most interactive demos combined the UMAH with a gesture-tracking camera (Leap Motion) to enable more intuitive interaction. A photograph of one of these demonstrations is shown below.



Figure 4.9: Ultasonic Mid-Air Haptic setup used in a demonstration.

4.4.1 Overview

The system architecture was implemented on the Zynq-7000 SoC following a hybrid approach. Part of the implementation was carried out in the PS (i.e., CPU software), while another part was implemented in the PL (i.e., the FPGA).

The system architecture is illustrated in Figure 4.10. A stimulus can be programmed directly on the embedded system and the stimulus generation is performed in real time.

The phase calculations and the driving of the transducers in the phased array were offloaded to the FPGA. The creation of the stimulus, on the other hand, is performed by the CPU. A haptic sensation is created by the modulation of the FP's position (directly linked to the phase updates) and by the FP's amplitude (linked to the control of the transducer's duty cycle).

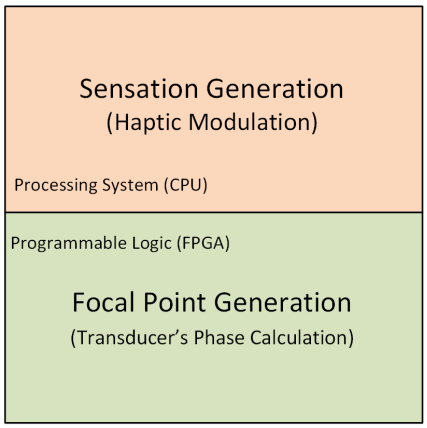

Figure 4.10: System architecture overview.

The phase calculations were offloaded to the FPGA in order to accelerate the phase calculation, mainly by exploiting the parallelism offered by FPGA technology. On the other hand, the haptic modulation is programmed in software (C code) on the embedded system's CPU. This approach provides flexibility and allowed to build haptic sensations that were used in demonstrators and perceptual tests.

In the Figure 4.11 the system architecture is further detailed. The figure provides a complete overview of the implementation of the system's architecture.

As can be observed, the user of the UMAH system interfaces via UART. Some of the parameters that the user can define are: (i) the FP position (FP_POS), (ii) the FP amplitude (FP_AMP), and (iii) the parameters for the creation of a STM stimulus.

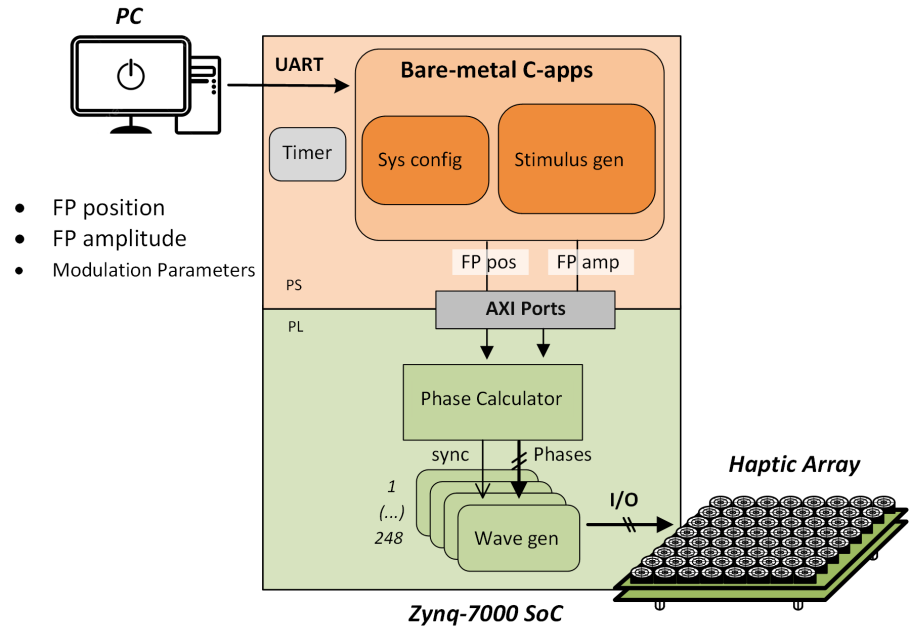

Figure 4.11: System architecture implementation.

On the PS side, there are essentially two main function routines. The SYS_CONFIG() configures the system to a known and safe operational state. For example, when the system is powered on, it sets the FP position to the center of the array and turns off the phased array ultrasonic emission as a safeguard. The second functionality (STIMULUS_GEN()) relates to the creation of STM haptic sensations, which will be briefly discussed in the next section.

As shown in the middle part of the figure, the parameters sent from the PS to the PL are FP_POS and FP_AMP. These parameters define the state of the FP.

4.4.2 Software – Processing System

The main goal was to generate STM haptic sensations that could be used for demonstrative and perceptual testing purposes.

The Vivado Design Suite provides built-in support for the development of bare-metal C-based applications. For this reason, and due to prior experience with this programming language,the software was coded in C-language.

As previously mentioned, and as shown in the upper part of Figure 4.11, the user can specify and create a STM stimulus, for example, a circular pattern. The routine responsible for generating the stimulus is STIMULUS_GEN().

The circular pattern is discussed as a demonstrative example. For its generation, the user defines the

circle's radius (r, see Equation 3.1), the drawing frequency (i.e., the rate that the pattern is draw, f_{draw}), and the number of points composing the pattern (N_{SP}). The set of parameters used, in other words, the r, f_{draw} and N_{SP} were explained in Section 3.2. Note that in the stimulus discussed here, the FP amplitude remains constant (i.e., there is no amplitude modulation). Nevertheless, the user can define the intensity (perceptual strength) of the pattern at any time through the FP_AMP parameter.

The first step in creating the stimulus is to calculate the positions of the shape points that compose the pattern. Since the spacing between the points is constant (or uniform), the positions were computed as explained in Section 3.2. The duration of each shape point is also constant and given by $\frac{T_{draw}}{N_{SP}}$. A CPU timer was configured to ensure this duration. In the interrupt service routine, the FP position was updated according to the positions of the shape. The updated position was then sent to the PL for the calculation of the new FP's phases.

4.4.2.1 Focal Point position

The FP position (FP_POS) parameter is specified in cartesian coordinates (i.e., $(x_{dst}, y_{dst}, z_{dst})$) in meters. Each coordinate ranges from 0 to 1 m. On the PS side, the FP_POS is converted to an 18-bit values before being sent to the PL. This numeric representation means, in practical terms, that the FP can be generated with a spatial precision higher than $10\,\mu m$.

Although the FP can theoretically be created within a volume of $1\,m^3$, the FP does not preserve the essential properties required for perceptual stimulation over such a large volume. This is mainly due to system performance limitations (e.g., available power and phased array size). In practice, the FP is typically generated within a volume of approximately $0.03\,m^3$ to $0.125\,m^3$, and always at a distance greater than $10\,cm$ above the phased array. This avoids unwanted effects associated with the acoustic near field. Regarding the FP amplitude (FP_AMP), it is specified by the user in the range from 0% to 100%. The PS software sends this value to the PL side to set the corresponding duty cycle.

4.4.3 Hardware – Programmable Logic

For the sake of simplicity in the explanation, some of the parameters were considered hardwired (i.e., constants) and therefore not accessible by the PS. These parameters are required for the calculation of the transducers' phases, namely the wavelength (λ) and the positions of the transducers on the PCB.

On the PL side, there are two main modules. The PHASE_CALC module (see Figure 4.11) is responsible for calculating the transducers' phases whenever an update of the FP's position is required. The WAVE_GEN module is responsible for generating the square signals that drive the ultrasonic transducers.

4.4.3.1 Phase Calculator Module

This module implements the mathematical operations required to calculate the transducers' phases. The equations implemented by the module are in Equation 4.10 and Equation 4.11.

$$\text{Distance}_n = \sqrt{(x_{FP} - x_{SRC_n})^2 + (y_{FP} - y_{SRC_n})^2 + (z_{FP} - z_{SRC_{(n}})^2} \tag{4.10}$$

$$\text{Phase}_n = 2\pi \left(\frac{\text{Distance}_n}{\lambda_{40\text{kHz}}} \right) \tag{4.11}$$

Where (x_{FP}, y_{FP}, z_{FP}) correspond to the FP's position, and $((x_{SRC_n}, y_{SRC_n}, z_{SRC_n}))$ correspond to the position of the *n*-th transducer (where $n \in [1, 248]$).

These operations are implemented using a pipeline architecture. This means that, for the calculation of the first phase, a few clock cycles are required. However, for the remaining 247 phases, each one is obtained in a consecutive clock cycle.

Figure 4.12 shows the pipeline implemented as part of the PHASE_CALC module. The mathematical sub-modules are shown in the figure. On the left side, the duration (in clock cycles) of each pipeline stage is indicated. The pipeline is composed of eight stages and the mathematical modules used were available in the Xilinx IP portfolio.

As can be observed, the module receives two inputs: the position of the transducer (SRC_n hardwired) and the position of the FP (FP_POS sent from the PS). Whenever a new FP destination arrives, the phase calculation begins. The input parameter (SRC_n), which represents the position of the transducers, starts being fed into the first pipeline stage.

The first operation performed is the subtraction, implemented by the module C_SUB_COORD (Xilinx, Inc., 2021a). Three instances of this module are used (one for each coordinate), allowing the subtraction to be performed in parallel. This stage requires 2 clock cycles.

The next operation is the squaring of the results from the previous stage. This is achieved using multiplier modules - MULT_GEN_COORD (Xilinx, Inc., 2015). Three modules are instantiated to perform the square operation in parallel. This stage requires 6 clock cycles.

The following stage computes the sum of the resulting squared values. Unlike the previous stages, the summation is performed in two steps (i.e., two pipeline stages). This is because each adder module - C_ADD_MOD_COORD (Xilinx, Inc., 2021a) has only two inputs, while the goal is to sum three-dimensional coordinates. First, the xx and yy coordinates are summed. Then, a second adder combines this intermediate result with the zz coordinate value to complete the addition. Each adder requires 4 clock cycles,

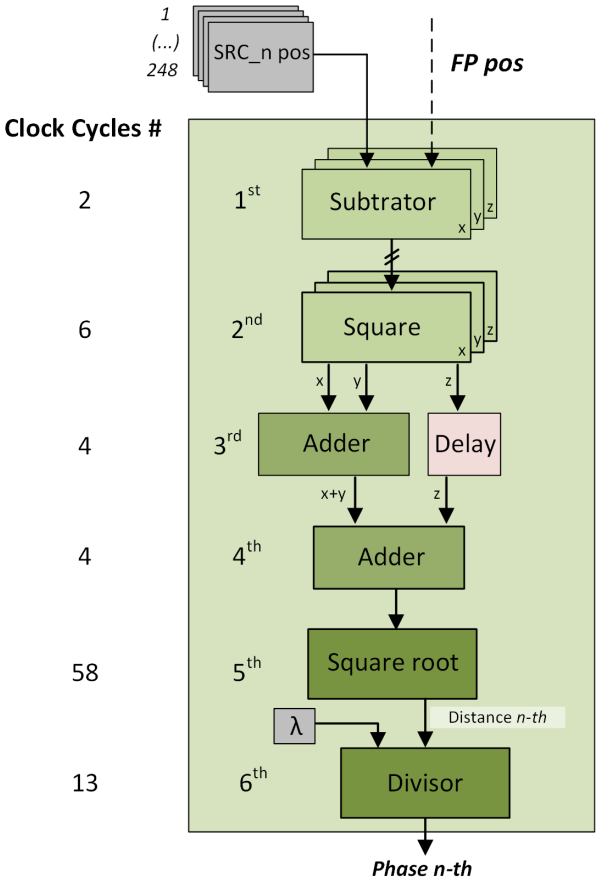

Figure 4.12: Phase calculation pipeline implemented on the Phase Calculator Module.

resulting in a total of 8 clock cycles for the full summation. To properly manage the data flow, a delay block was introduced, as represented in the third stage of Figure 4.12.

After the summation, the next stage performs the square root operation. The result corresponds to the distance between the n-th transducer and the FP's position. The square root is implemented using the CORDIC_SQUARE_ROOT (Xilinx, Inc., 2021b) module, which provides an AXI interface for configuration. This module requires 58 clock cycles.

The final stage implements the division operation - DIV_GEN_WAVE_LENGTH (Xilinx, Inc., 2021c). As shown in the figure, the phase calculation requires dividing the computed distance by the wavelength (λ). The division module is also an AXI-based IP-core. The divisor input is defined by the hardwired λ value, and the dividend corresponds to the distance obtained in the previous stage. This module requires 13 clock cycles to complete the operation.

The calculation of the first transducer phase requires 87 clock cycles (i.e., the total latency of the pipeline). To obtain the remaining 247 phases, an additional 247 clock cycles are required. Therefore, the complete calculation of all transducer phases (for the desired FP's position) requires a total of 334 clock cycles.

The typical FPGA clock frequency used in our system is 50 MHz, meaning that the complete set of phases are calculated in less than $10\,\mu s$.

In practice, however, the maximum phase update rate (UR_{max}, see Section 3.2) is not limited solely by the phase computation itself. Factors such as the communication between the PS and the PL (namely the transmission of the FP_POS parameter) or the calculation of the pattern's position, etc, impacts the UR_{max}. Measurements for the absolute maximum update rate of the UMAH system were not accomplish. However, the highest update rate used during pattern generation (e.g., as the one used in Chapter 5) was 4 kHz.

4.4.3.2 Wave generator

The WAVE_GEN module is responsible for generating the signal for driving the transducers. The module can be observed in the PL of Figure 4.11.

The signal is 40 kHz square wave, with controllable phase and duty cycle. A total of 248 WAVE_GEN modules were instantiated to drive all the transducers of the haptic array in parallel and synchronously.

As input parameters, the module receives the phase offset and the duty cycle values. There is also a synchronization flag (synq) used to synchronize the phase across all transducers.

An internal counter increments at every FPGA clock cycle. The increment step is calculated to produce a 40 kHz square wave. The duty cycle is controlled by a 32-bit register value, which is compared against the counter. The duty cycle value itself is defined by the PS.

The phase offset parameter is provided by the PHASE_CALC module. When the synchronization flag is asserted, the internal counter is loaded with the new phase value and starts counting from that value.

The synchronization flag is asserted simultaneously for all WAVE_GEN modules to ensure that the driving signals are generated in a fully synchronous manner.

4.5 Experimental Measurements

The present section focuses on the characterization of the FP. To this end, several measurements were performed, including acoustic field scanning and force estimation using a precision scale.

4.5.1 Measurement Equipment

A microphone set (composed of the microphone cartridge and preamplifier) was used for the acoustic field measurements. The microphone used was the GRAS 46BE. This is a free-field type of microphone,

meaning that it was optimized for acoustic measurements directly pointed at the source of sound (in our case, the FP) and for the microphone's body to not interfere with the measurement. The microphone set is shown in Figure 4.13 (adapted from GRAS, 2026).



Figure 4.13: GRAS 46BE free-field microphone set.

The GRAS 46BE has a very small diaphragm (6.35 mm in diameter) and it senses a broad range of sound frequencies (4 Hz to 80 kHz). The dynamic range of the microphone is also large (35 dB to 160 dB SPL re 20 μPa). Nevertheless, the microphone's dynamic range upper limit is not enough for measuring the FP the system's full intensity. The microphone's sensitivity is 3.6 mV/Pa, and the equipment was calibrated at the time of measurement.

The microphone was optimized to work without the protection grid of the diaphragm for frequencies above 20 kHz (GRAS, 2026). Thus, all the measurements were performed without the protection grid, since the frequency of interest was 40 kHz.

The GRAS 46BE was powered by a power module from the same manufacturer—the GRAS 12AK. Besides powering the microphone set, this module allows other functionalities such as analog filtering and gain.

For the acoustic field measurements, a positioning system to precisely control the location of the microphone in space was used. To that effect, the microphone's position was controlled via a staging system with two degrees of freedom. The stages that make up the positioning system are the LTS300 from Thorlabs. They are 30 cm in length, possess a spatial precision greater than 1 mm, and are fully controllable via software. The LTS300 stage is depicted in Figure 4.14 (Adapted from Thorlabs, 2026).

The conversion of the analog acoustic signal to digital was carried out by an Analog-to-Digital Converter (ADC) from National Instruments (NI USB 6356). The ADC allows a sampling rate of up to 1.25 MHz (single channel), which is more than enough for the measurements. A sampling rate configuration of 500 kHz was used, which corresponds to ten times of the sampled signal's frequency.



Figure 4.14: One axis-stage used for the positioning system.

For the radiation force measurements, a precision scale (or balance) was used. The scale was the Denver SI2002, which has a maximum capacity of 2 kg and a reading resolution of 0.01 g (approximately 0.1 mN). This is a digital device that has a serial port interface. This is an important characteristic because it enables readings to be done automatically via software and without interferences (such as small vibrations or touches). The Denver SI2002 scale is depicted in Figure 4.15 (adapted from Denver Instrument (n.d.)).



Figure 4.15: The Denver SI2002 scale used for measuring the FP's radiation force.

All the equipment used in the different test scenarios were always controlled using Matlab. Several scripts were developed to automate the acoustic-field measurements.

4.5.2 Acoustic Field Scanning

In this section, the field measurements made to the FP's acoustic field are presented, as well as some comments on the field produced by the demonstrator. From the FP's results in particular, it was possible

to calculate its diameter and its force, two important features of the stimulus.

For the acoustic field scanning, the ultrasonic mid-air system was fixed on an optical table, in order for it to be static throughout the measurement. The goal of the experiment was to measure the FP's acoustic field. The staging system was used with the microphone attached to it. This ensured the precise positioning of the microphone relative to the xy-plane (in this case situated at a 20 cm distance above the array). Figure 4.16 shows the setup used for the acoustic scanning of the FP.

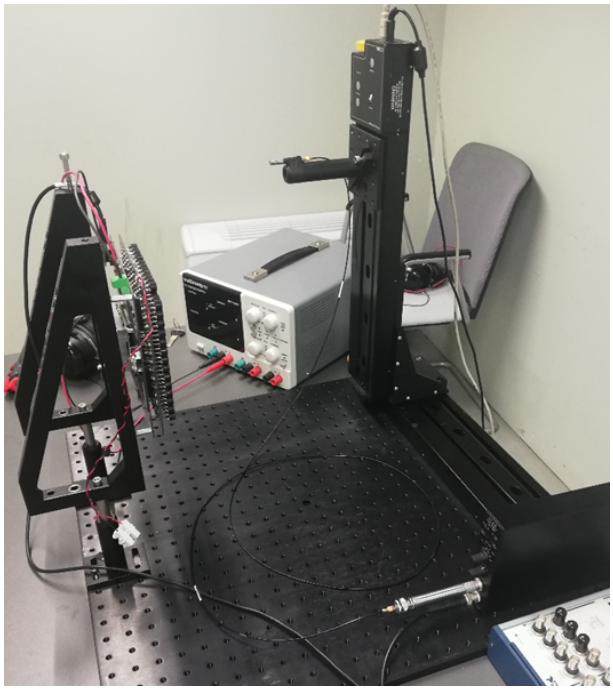

Figure 4.16: Experiment setup used for the acoustic field scanning of the FP.

The microphone was connected to and powered by the power module, and the acoustic signal was acquired by the ADC. A Matlab script controlled all the setup devices in the experiment. The acoustic signal was digitally filtered in Matlab. A $1/3$-octave band filter provided by the software was used and configured with a central frequency of 40 kHz and an order of 8. The goal of this filtering was to obtain a cleaner 40 kHz signal by eliminating noise artifacts, such as harmonics and unwanted noise.

The acoustic field scanning was done in the following manner. The FP was created at a 20 cm distance (center of the array) and at 24% intensity. This ensured that the generated pressures did not exceed the maximum dynamic range of the microphone (i.e., 160 dB SPL re 20 μPa). The measured plane's size was 40 mm $\times$ 40 mm, centered relative to the focus. The stages' step were configured to 0.5 mm, and in total 3200 spatial samples (2 samples p/mm $\times$ 40 mm $\times$ 40 mm) were made. For each spatial sample, the acoustic signal was acquired for 1 s (the sampling rate of the ADC was set to 500 kHz). The acoustic field measurement was performed in the ESRG laboratory in a controlled environment (humidity and temperature) and took around 60 minutes.

The result of the FP's field is shown in Figure 4.17. The FP is characterized by a high-pressure circular shape, surrounded by four less intense side lobes. The maximum pressure value (measured at the center of the focus region) was around 2126 Pa (peak). In terms of Root Mean Square (RMS) intensity level, this corresponds to 157.8 dB SPL (re $20\,\mu$Pa), which is at the limit of the maximum dynamic range of the microphone.

In the Figure 4.17, it is also possible to observe a dashed line that represents the FP's diameter defined by the FWHM. The diameter of the FP defined in these terms is around 15 mm. Moreover, the radiation force was measured considering the defined circular region. The obtained radiation force for the focus was 3.54 mN.

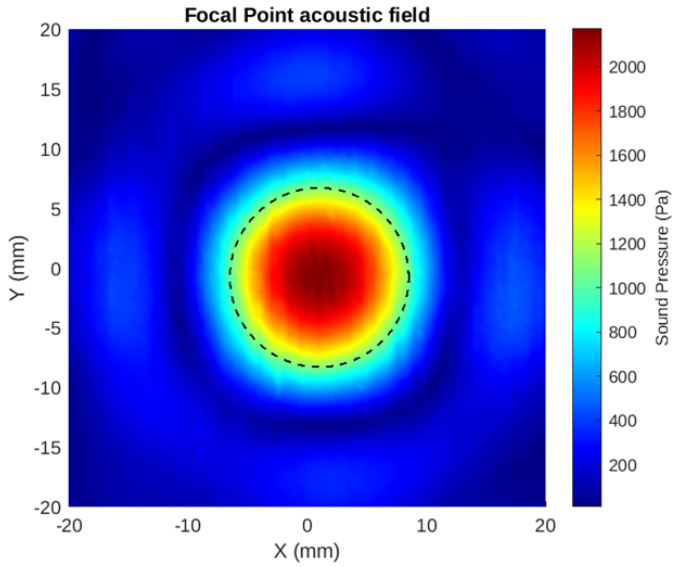

Figure 4.17: The FP's acoustic field. The dashed line represents the FP's diameter defined by the FWHM.

The acoustic field produced by the phased array was also scanned. This type of measurement is difficult to perform due to the large scanning area, which complicates the relative positioning of the entire system. Together with a colleague from the ESRG team, the UMAH's acoustic field was measured.

The measurement setup is similar to the one previously described. The FP was created 15 cm above the transducer array, and the scanning plane covered an area of 30 cm $\times$ 30 cm. The scanning step was 0.5 cm, resulting in a total of 1800 measurement points (2 samples per cm $\times$ 30 cm $\times$ 30 cm). Moreover, the FP was created at 6% maximum intensity. The resulting acoustic field is shown in Figure 4.18, adapted from Camelo (2020).

There are two different field perspectives in the Figure 4.18. The top-view or xy-plane (left image) and the lateral-view or xz-plane (right image). In the left image, it is possible to observe the FP situated roughly

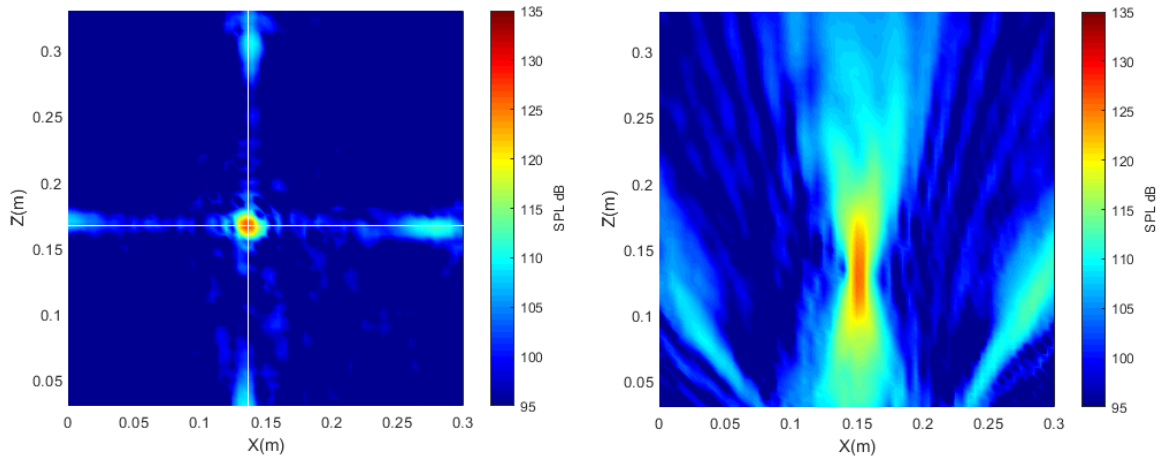

Figure 4.18: The UMAH's acoustic field. (Left image) Acoustic field top view. (Right image) field's side view.

in the center, and the four grating lobes located at the edges. The grating lobes are approximately 13 cm distance from the FP.

The right image of Figure 4.18 shows the FP. There is a disparity between the two grating lobes. This is due to the mismatch in the orientation of the measuring plane. This problem was due to the fact that the testing bed was not fixed to the haptic system (as happened in the test for the FP's field), which difficulted the positioning of the measurement system relative to the plane. This problem is better illustrated by the white lines present in the figure on the left.

4.5.3 Focal Point force measurement

To measure the radiation force created by the FP, a new measurement setup using the microscale was design. This specific test was conducted due to the fact that the microphone was not able to measure the FP at its maximum intensity. In this sense, a weighting setup was created for measuring the FP's radiation force with the help of the precision scale. This type of equipment is capable of measuring minute force variations (0.1 mN) created by the FP.

The setup used for the measurement is shown in Figure 4.19. As can be seen, a wooden structure was built to support the ultrasonic haptic system upside down. The wooden structure was dimensioned so that system faced the measuring target at a around 20 cm distance. The scale was positioned at the bottom of the setup, and it was 'covered' by a surface (in the middle) that acted as a barrier to the acoustic field produced by the ultrasonic haptic system. The FP was sensed, however, by the plastic target in direct contact with the scale's plate.

Resting in the middle support is an acoustic foam, physically separated (air gap) from the scale's plate,

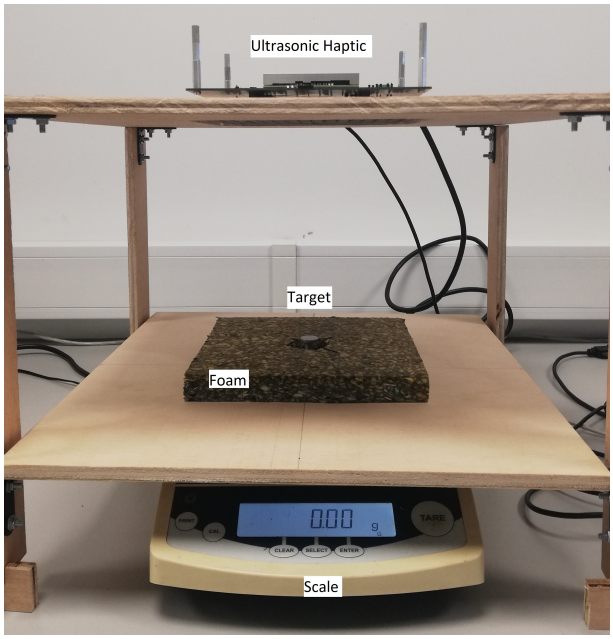

Figure 4.19: Weighting setup used for sensing the FP radiation force.

that absorbed the unwanted acoustic field. A small circular plastic target (total reflector, $\alpha = 2$) with 15 mm in diameter was inserted in the middle of the acoustic absorbent. It was in direct contact with the scale's plate.

The FP was created directly on the target. For the radiation force measurement, the intensity of the FP was varied from 0% to 100% in 2 pp steps. For each intensity, five weight measurements were realized, and the radiation force was calculated as the average of those measurements. Moreover, the weight reading was done 5 s after the creation of the FP on the target. This ensured the stability of the readings and was done for all weight measurements. In total, 250 measurements were performed (5 readings $\times$ 50 intensities). The experiment took about 25 min and it was performed in a controlled environment within the Pólo de Inovação em Engenharia de Polímeros (PIEP) facilities.

The results are shown in Figure 4.20. The horizontal axis corresponds to the FP's intensity (varying from 0% to 100%), and the vertical axis displays the respective radiation force (mN). It can be observed that for intensities under 8%, the scale did not detect any force. For intensity levels above 8%, and up to 50%, the force displays a constant increasing linear behaviour. Between 50% and the maximum intensity, the force shows a non-linear evolution, reaching a plateau at around the 80% level. The maximum radiation force created by the FP was 7.8 mN at around 20 cm.

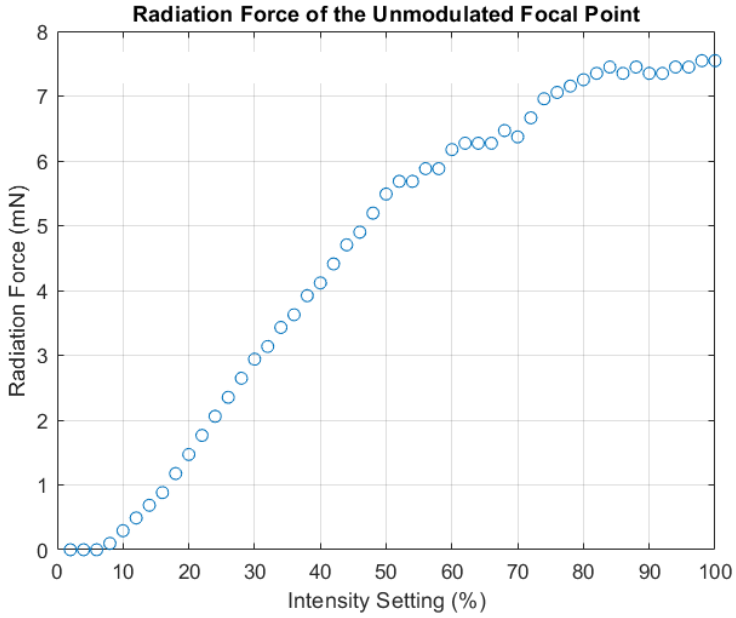

Figure 4.20: Radiation force results of the FP.

4.5.4 Experimental versus Simulated results

In Section 4.2.1, the simulator was used to obtain some preliminary results of the FP's field. Those results are compared with the FP measurements obtained using the two measurement setups.

The comparison was made to support the implementation of the simulator, nonetheless, the purpose of the simulator wan mainly for visualization of theFP and not to provide a rigorous quantitative analysis. Table 4.1 summarizes the results for the FP's pressure, diameter and force.

Table 4.1: Comparison between simulation, microphone measurement and scale measurement results.

Quantity	Simulation	Microphone Measurement	Scale Measurement	Sim÷Mic [%]
Sound Pressure Peak [Pa]	2250	2126	–	5.8
FP's diameter (FWHM) [mm]	13.6	15	–	-9.3
Radiation Force [mN]	3.23	3.54	2.1	–

In terms of sound pressure, there is a small difference, with the simulated value being approximately 5.8% higher than the one measured through the microphone. Regarding the FP diameter, the value obtained in simulation is approximately 9.3% lower than the microphone measurement. Several factors may explain this discrepancy. One possible factor is related with inaccuracies in the soldering positioning of the transducers on the PCB, which can introduce imprecisions that affect the focusing of the FP. Another reason that affected the focusing is related to the accuracy of the phase computations, which are typically

higher in computational simulations. Additionally, some of the transducers may be not be performing well due to prolonged use and that also negatively impact the focusing.

Lastly, with respect to the radiation force measurement, the simulated value is approximately 8.8% lower than the value obtained from microphone's measurements. An explanation for this difference is related to the FP's area used in the force calculation. For the simulation case the diameter considered was 13.6 mm and for the microphone case the diameter was 15 mm. The latter was specified in terms of FWHM, a common way to specify the FP's spot (Cataldo et al., 2023; Frier et al., 2022). As can be observed through the Table 4.1 in the simulation case, the FP's FWHM is about 9.3% smaller.

There is a considerable discrepancy between the radiation force obtained from the microphone measurements and that measured using the precision scale. For the same FP intensity, the force measured with the scale was 2.1 mN, which is approximately 41% lower than the value obtained from the microphone's measurement. This discrepancy may be related to difficulties associated with the scale's measurement setup, namely the accurate positioning of the FP on the plastic target. Moreover it is important to refer that the access to the precision scale was limited and only accessible through the cooperation with PIEP.

4.6 Conclusions

The objective of this chapter was to explain and document the UMAH demonstrator developed by the ESRG team. The team is multidisciplinary and was responsible for the various subcomponents of the project, namely simulation, implementation of the system architecture on the embedded platform, construction of the UMAH demonstrator itself, as well as the measurement and acoustic characterization of the system.

The demonstrator described in this chapter was extensively used in public demonstrations and was also employed in the experiments presented in Chapter 5. Therefore, the UMAH demonstrator constitutes a fundamental component of the research carried out in this thesis.

Specification of Spatio-temporal's Haptic Sensations

5.1 Introduction

The STM is a complex modulation technique. As demonstrated in the end of the previous chapter, it can evoke different haptic sensations depending on how its parameters are tuned. Several works have investigated the perception of STM, but most treated the technique as a unified whole, without distinguishing between its multiple possible sensations. However, it is important to recognize that different sensations originate from distinct physiological mechanisms. Therefore, perceptual research on STM should be conducted with these principles in mind.

Investigating the haptic sensations of the STM provides deeper insight into the perception of this intricate modulation technique. Such knowledge can contribute to the development of improved sensations, ultimately leading to more optimized haptic perception (Georgiou et al., 2022). The present chapter discusses the specification of the haptic sensations produced by STM. The chapter is based on a scientific article published in the context of this thesis (Mendes et al., 2024).

Larger circular patterns (roughly palm size), similar to those used by Frier et al. (2018, 2019) and Ablart et al., 2019, were used in this research study. As explained in the previous chapter, when the FP moves fast, the resulting haptic sensation feels as a 'uniform' pattern (Hajas et al., 2020). By varying the FP's speed, distinct sensations can be produced. To better illustrate the perception involved, consider the following analogy: imagine a ball attached to the tip of a helicopter blade. When the helicopter begins to take off, the propeller initially moves slowly, and the ball's motion can be followed visually. As the rotation speed increases, the blade moves too fast for the eye to track the ball's motion, and instead the entire circular area swept by the ball is perceived. According to user studies carried out in this chapter, when the FP moves slowly its motion can be directly felt, whereas at higher FP's speeds the haptic sensation corresponds to the overall shape or pattern.

The remainder of this chapter extends the work of the article above mentioned (Mendes et al., 2024). The in-house developed UMAH demonstrator (discussed in Chapter 4) was used to generate the haptic sensations and to vary the parameters that influence the haptic perception—namely, the focal-point speed (v_{FP}) (Frier et al., 2018; Takahashi et al., 2020) and the number of point composing the pattern (N_{SP}) (Frier et al., 2019; Morisaki et al., 2022). For more details about the STM's parameters, refer to Table 3.1.

In the first user study, a specification for the haptic sensations elicited by STM was proposed and three distinct sensation regimes were specified. Sensation regimes, in the context of our research study (Mendes et al., 2024), refer to the configuration range of the haptic stimulus parameters that correspond to a haptic sensation of a given *quality*. For example, in the context of this research study, three sensation regimes were specified, Dynamic, Vibratory and Uniform. Furthermore, in a second user study, a preliminary validation of the specification was performed. Sensation identification experiment was realized and the specified haptic sensations were effectively recognized. Furthermore, the haptic sensations were

combined into a stimulus and for some particular combinations participants were able to identify the constituents haptic sensations.

5.2 User study 1 – Sensation's specification

The FP's speed v_{FP} and the number of points composing the pattern (N_{SP}) influence the sensations produced by an STM pattern. In the following user study, the sensations elicited by an STM circumference were specified, by varying the v_{FP} and the N_{SP}.

5.2.1 Methodology

The characterization the STM sensations was performed in a first place. Based on our experience with the modulation, the haptic sensations involved were described. When the v_{FP} is low, the dynamics of the FP's motion can be sensed. In contrast, according to research studies, at higher v_{FP} the pattern is perceived as having a static shape (Frier et al., 2018; Hajas et al., 2020). However, the mid-air haptic perception is not entirely static but rather a uniform, high-frequency vibration distributed along the pattern. Additionally, according to our user-studies, a third type of haptic sensation emerges when the v_{FP} lies between the dynamic and uniform conditions. In this case, a low-frequency vibratory sensation occurs simultaneously at some positions (or shape points, SP) of the pattern.

A summary of the individual sensations generated by the STM pattern is presented in Table 5.1. The names assigned to each mid-air haptic sensation are merely suggestive and, for simplicity, are represented by different letters. A visual representation of the sensations is shown in Figure 5.1.

Table 5.1: Description of the haptic sensations produced by STM.

Identifier	Suggestion	Description
D	Dynamic	Slow moving FP along the pattern (travelling direction is perceivable).
V	Vibratory	Localized or uneven low-frequency vibrations at some SP locations.
U	Uniform	Uniform high-frequency vibration felt at the whole pattern.

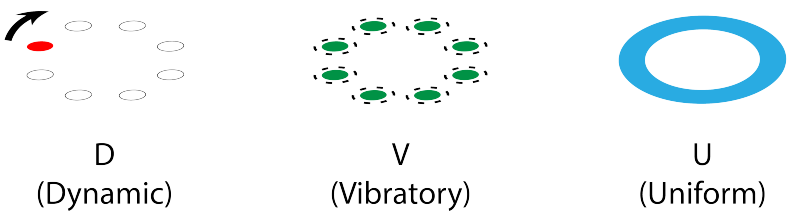

Figure 5.1: Illustration of the STM's sensations generated by the circular pattern.

The specification of the sensations was carried out as follows. Each of the haptic sensations under study—Dynamic (D), Vibratory (V), and Uniform (U)—is associated with a specific range of FP speeds. Furthermore, there are speed intervals where transitions between sensations occur. In these regions, the perception is ambiguous. The regions are called boundary regions and the two boundary regions are: Dynamic–Vibratory (D–V) and Vibratory–Uniform (V–U).

To specify the three haptic sensations, the limits of their corresponding boundary regions were determined. An overview (only illustrative) of this specification procedure is illustrated in Figure 5.2.

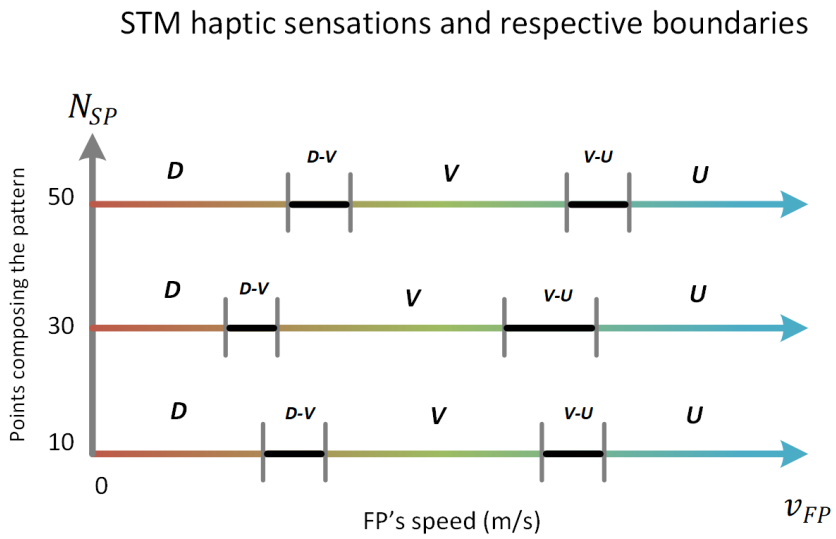

Figure 5.2: Overview of the specification of the haptic sensations (merely illustrative).

The haptics sensations of a circular pattern with a length (l) of 157 mm (i.e., 25 mm radius), displayed 200 mm above the transducer array ($\vec{c}$ = (85, 85, 200) mm), were specified. Boundary sensations were evaluated for N_{SP} values of 10, 30, and 50 points.

Since pattern size (157 mm) is significantly larger than the FP's diameter (around 15 mm) the SP's will not overlap for the pattern composed of 10 shape points. Nonetheless, the SPs will overlap for the other two N_{SP} configurations (i.e., 30 and 50 points).

The experimental method for specification of the STM haptic sensations was also described in a preliminary assessment by Mendes et al. (2022). The article, conducted as part of this thesis, was our initial effort to study STM haptic sensations. Compared to that work, the present user study (Mendes et al., 2024) provides a detailed experimental procedure and increased the number of participants from 13 to 18.

Before the boundary specification test, participants were introduced to the STM haptic sensations. These were verbally explained (as in Table 5.1), visually illustrated (as in Figure 5.1), and then experienced by touch (through the UMAH's haptic device). This recognition phase aimed to familiarize the participants

with the sensations since they would be experiencing sensations with ambiguous character during the main specification test.

Participants were subsequently informed that they would evaluate pairs of sensations during the boundary specification tests. Each boundary was tested independently, and participants experienced the sensations spanning that boundary. The speed ranges (v_{FP}) defining the boundaries (D–V and V–U) and subjectively evaluated by participants were as follows:

- D–V boundary: minimum speed (v_{FPmin}) of 0.314 m/s, and maximum speed (v_{FPmax}) of ∼2 m/s;
- V–U boundary: v_{FPmin} of about 3.5 m/s, and v_{FPmax} of about 9 m/s;

These speed ranges were chosen such that the haptic sensations at the delimiting speeds were perceptually clear and unequivocally distinct.

During the specification test, the boundary speed thresholds were obtained using the method of constant stimuli (Dalecki et al., 1995; Mendes et al., 2022). Each boundary speed range was discretized into six equally spaced values, which participants evaluated in terms of perceived sensation. Only unequivocal responses were allowed (e.g., for the D-V boundary, only "D" or "V" were accepted answers). The FP's speed threshold was chosen as the value with 50 % answers ratio. That corresponded to the sensation most difficult to judge by the participant. If no FP' speed value yielded exactly 50 % responses, the average of the two closest response rates was used.

Each FP speed was tested ten times in a pseudo-random order. Participants completed a total of 360 subjective evaluations (2 boundaries × 3 N_{SP} × 6 v_{FP} × 10 repetitions). Participants were comfortable with the palm of their right hand opened and still on top of a frame. Headphones playing pink noise and protective earbuds were used to eliminate auditory cues (as demonstrated in Figure 5.3). A user interface was developed for the data acquisition. When participants were sure about the sensation's feeling, they signaled it and the answer was recorded using a specifically developed user interface.

Participants were aged between 21 to 41 years old, all healthy, and provided written informed consent before the study. All procedures adhered to the Declaration of Helsinki (2008) and were approved by the Ethical Committee of the University of Minho (CEICVS 075/2021) .

5.2.2 Results

This section discusses the results obtained for the D-V and V-U boundaries. As already mentioned in the beginning of the chapter, eighteen participants were involved in the specification trials.



Figure 5.3: Participant during the specification trials.

Figure 5.4 intends to illustrate how the speed thresholds for a particular boundary region were processed for a participant. The exemplificative graphic shows the results obtained for a participant for the D-V boundary region for a pattern composed of 30 points.

The x-axis represents the FP's speed (v_{FP}), while the y-axis corresponds to the response rate. In this case, the response rate corresponds to the rate of Vibratory answers (the rate of Dynamic answers corresponding to the inverse of this 'curve').

As can be seen, in this case there is no exact speed answer corresponding to a 50 % response rate. Therefore, the speed threshold for this particular boundary is calculated as the average of the two nearest response values to 50 % (i.e., 1.00 m/s and 1.35 m/s).

Similar procedure was performed for all tested boundaries, and after calculating all boundaries' speed thresholds, the STM haptic sensation boundaries regions were specified.

5.2.2.1 Dynamic-Vibratory Boundary

The FP's speed thresholds obtained for the D–V boundary region are shown in Figure 5.5. Results are organized by N_{SP} using notched boxplots. The v_{FP} is represented on the y-axis, while N_{SP} is shown on the x-axis. The line inside each box represents the median value ($\tilde{x}$), the cross indicates the mean value ($\bar{x}$), and the notches correspond to the two inverted triangles.

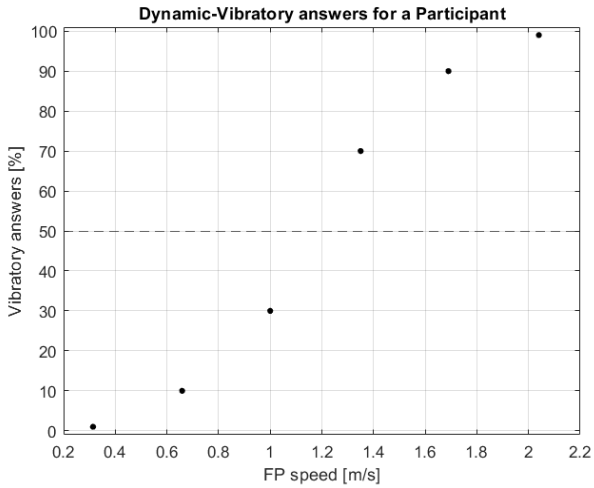

Figure 5.4: Psychometric curve obtained for a participant during the D-V boundary region for a 30 points pattern.

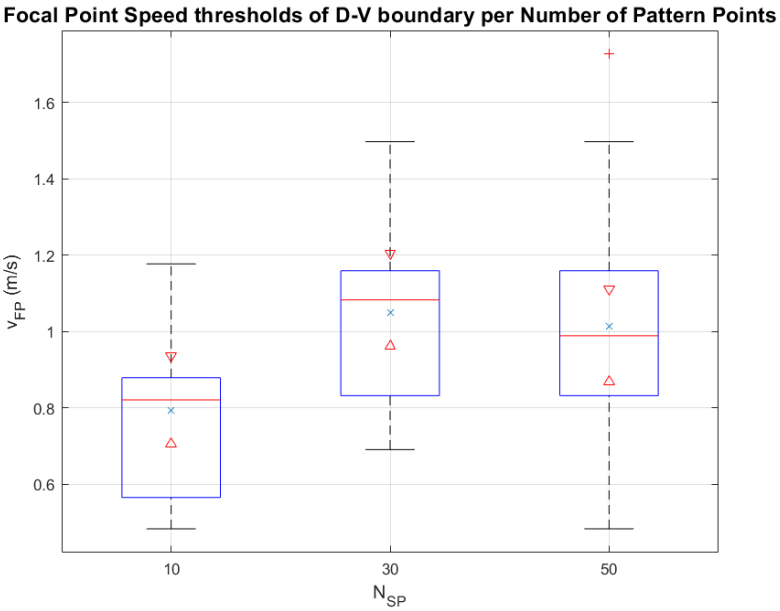

Figure 5.5: D-V boundary FP speed thresholds per number of pattern points N_{SP}.

A Shapiro–Wilk normality test was performed on the results. A low p-value ($p < 0.05$) indicates rejection of the null hypothesis, suggesting that the data are not normally distributed. The tests show that the data is normally distributed, with p-values of 0.07, 0.51, and 0.25 for 10, 30, and 50 points, respectively. A summary of the Shapiro–Wilk normality results can be found in Table 5.2.

The Table 5.3 shows the results of Figure 5.5, relative to the D–V boundary. The $\bar{x}$ values of the boxplots with 30 and 50 points are similar (1.05 m/s and 1.0 m/s, respectively). The $\bar{x}$ value increased by approximately 30% from the 10-point boxplot to the 30 or 50-point boxplots (e.g., from 0.8 m/s to 1.05 m/s).

Table 5.2: Results of the Shapiro–Wilk normality test for different N_{SP} values (n=18).

N_{SP}	*10*	*30*	*50*
h_{null}	Rejected		
p-value	0.07	0.51	0.25

The $\tilde{x}$ shows similar behaviour, too. The measures related to the dispersion of the data, in particular the Inter Quartile Range (IQR), show little variability. An exception was the 30% increase of the σ from the 30-point to the 50-point boxplots. On average, the σ was 0.26 m/s.

Table 5.3: Results of the D–V boundary region.

	N_{SP}		
	10	*30*	*50*
$\overline{x}$	0.8 m/s	1.05 m/s	1.0 m/s
σ	0.23 m/s	0.23 m/s	0.31 m/s
$\tilde{x}$	0.82 m/s	1.08 m/s	1.0 m/s
IQR	0.31 m/s	0.33 m/s	0.33 m/s
Q1	0.57 m/s	0.83 m/s	0.83 m/s
Q3	0.88 m/s	1.16 m/s	1.16 m/s
Min	0.48 m/s	0.7 m/s	0.48 m/s
Max	1.18 m/s	1.5 m/s	1.72 m/s

The boxplot data suggest differences in the median speed thresholds. A matched-sample t-test for all N_{SP} combinations was performed, with the null hypothesis that there is no difference in the median speed thresholds (significance level $p < 0.05$). The results of the matched-sample t-test are shown in Table 5.4.

Significant differences were found between the 10-point and 30-point boxplots ($p = 0.001$), and between the 10-point and 50-point boxplots ($p = 0.031$). These results indicate that the speed thresholds increase as N_{SP} increases, particularly from 10 to 30 points and from 10 to 50 points.

Table 5.4: Results of the matched-sample t-test for different N_{SP} combinations.

	N_{SP} *Comparison*		
	10 → 30	*10 → 50*	*30 → 50*
h_{null}	Rejected		Not Rejected
p-value	0.001	0.031	0.606

5.2.2.2 Vibratory-Uniform Boundary

The speed thresholds obtained for the V–U boundary region are shown in Figure 5.6. The Shapiro–Wilk test was performed on the obtained results, which indicated that the data were normally distributed. The p-values were 0.42, 0.89, and 0.12 for 10, 30, and 50 points, respectively. These are summarized in Table 5.5.

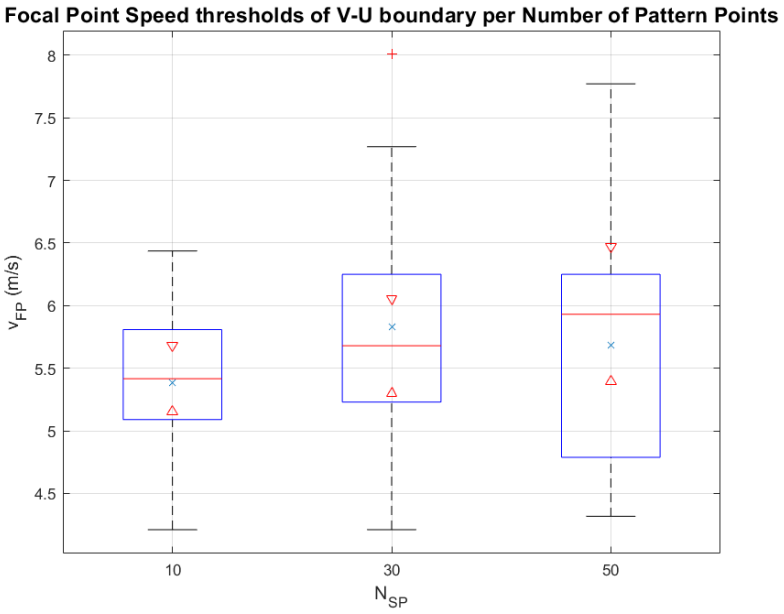

Figure 5.6: V-U boundary FP speed thresholds per number of pattern points N_{SP}.

Table 5.5: Results of the Shapiro–Wilk normality test for different N_{SP} values (n = 18).

N_{SP}	*10*	*30*	*50*
h_{null}	Rejected		
p-value	0.42	0.89	0.12

The Table 5.6 summarizes the results shown in Figure 5.6. The mean ($\bar{x}$) and median ($\tilde{x}$) values do not vary substantially with N_{SP} (compared to the D–V boundary) and are approximately constant, averaging around 5.6 m/s. In terms of dispersion, both metrics increase with N_{SP}. The standard deviation (σ) rises by 43% from the 10-point to the 30-point boxplot (0.7 m/s to 1.0 m/s) and by 10% from the 30-point to the 50-point boxplot (1.0 m/s to 1.1 m/s). The IQR shows a similar trend, except for a 30% increase from the 30-point to the 50-point boxplot (1.1 m/s to 1.45 m/s). These results suggest that the dispersion of the speed thresholds increases as N_{SP} increases.

Table 5.6: Results of the V–U boundary region.

	N_{SP}		
	10	*30*	*50*
$\bar{x}$	5.4 m/s	5.8 m/s	5.6 m/s
σ	0.7 m/s	1.0 m/s	1.1 m/s
$\tilde{x}$	5.4 m/s	5.7 m/s	6.0 m/s
IQR	0.7 m/s	1.1 m/s	1.45 m/s
Q1	5.1 m/s	5.2 m/s	4.8 m/s
Q3	5.8 m/s	6.3 m/s	6.25 m/s
Min	4.2 m/s	4.2 m/s	4.3 m/s
Max	6.4 m/s	8.0 m/s	7.7 m/s

5.2.3 Specification of the Boundaries

A boundary region is defined by its *most* ambiguous speed and upper and lower limits. The ambiguity speed corresponds to an FP's speed at which the associated haptic sensations is not clearly identifiable by the user. The boundary limits, in turn, define a speed range where the haptic sensation is less vague to the user. Outside this range, the sensation is expected to be clear to the perception. An illustration of the stated idea for the specification of the STM sensation's boundary regions is shown in Figure 5.7.

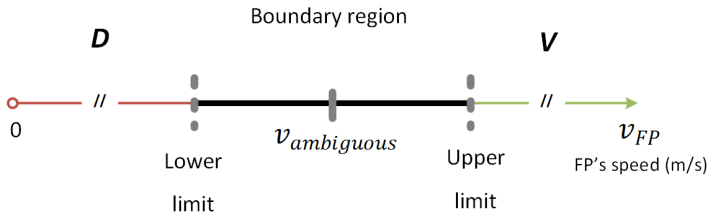

Figure 5.7: Example of a boundary region specification (in this case D-V).

The expected value of the speed thresholds ($\bar{x}$) was used to specify the boundaries ambiguity speeds. The median ($\tilde{x}$) showed similar values to the mean, supporting its use as the boundary ambiguity speed. Note that for the D–V boundary, the median speed thresholds increased with N_{SP} (see Table 5.4). The ambiguity speeds for the boundary were 0.8 m/s, 1.05 m/s, and 1.0 m/s for each N_{SP} value. For the V–U boundary, the speed thresholds remained nearly constant with increasing N_{SP}. By averaging them an ambiguity speed of 5.6 m/s, was obtained.

The standard deviation (σ) was used to define the boundary range. The IQR generally yielded similar results to σ, supporting its use as a measure of the boundary range. For the D–V boundary, the σ values were not significantly affected by N_{SP}. Therefore, the σ values across all boxplots were averaged, resulting in a boundary range of 0.26 m/s. In the case of the V–U boundary, σ increased with N_{SP}, so the range

was specified using the σ value of each individual boxplot (i.e., 0.7 m/s, 1.0 m/s, and 1.1 m/s). The final boundary specifications are provided in Table 5.7.

Table 5.7: Boundary regions specification: D–V and V–U.

	D–V boundary			*V–U boundary*		
N_{SP}	*10*	*30*	*50*	*10*	*30*	*50*
Ambiguity speed	0.8 m/s	1.05 m/s	1.0 m/s		5.6 m/s	
Lower limit	0.54 m/s	0.79 m/s	0.74 m/s	4.9 m/s	4.6 m/s	4.5 m/s
Upper limit	1.06 m/s	1.31 m/s	1.26 m/s	6.3 m/s	6.6 m/s	6.7 m/s

The specifications for the mid-air haptic sensations were obtained based on the findings presented in Table 5.7 and further detailed in Figure 5.8. The figure illustrates the haptic sensations along with their corresponding boundaries. Dashed lines denote the lower and upper limits (leftmost and rightmost, respectively), while the solid line represents the boundary's ambiguity speed. The horizontal axis represents the FP's speed on a logarithmic scale, and the vertical axis represents N_{SP}. The minimum speed was set to 0.1 m/s, and the maximum speed was set to 20 m/s. These speeds are merely illustrative.

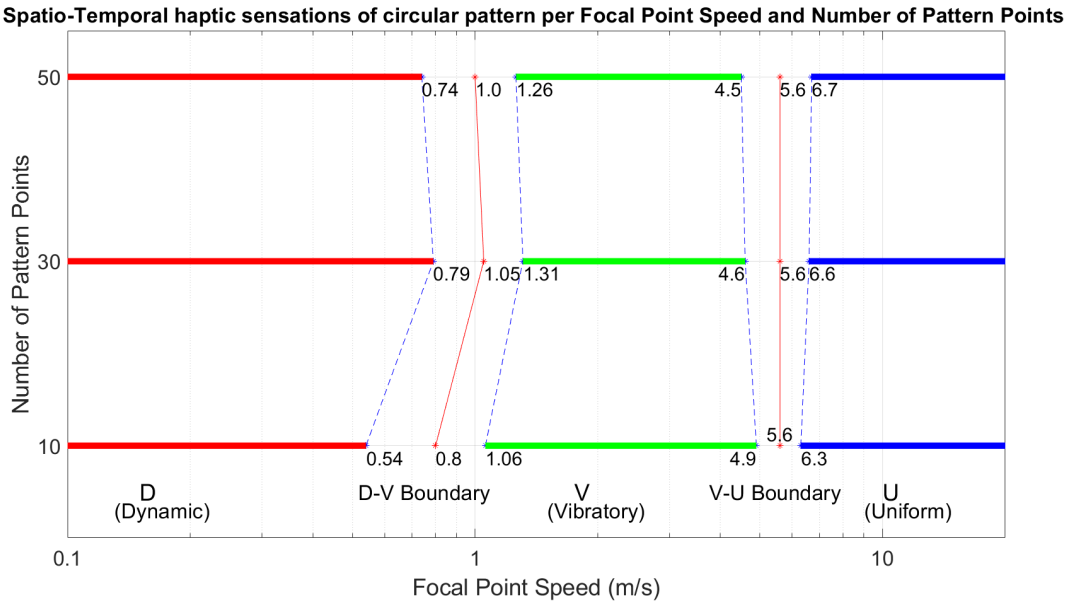

Figure 5.8: Specification of the STM's sensations and boundaries.

5.3 User study 2 - Preliminary Validation of the Sensations

The present user-study aims to provide a preliminary validation of the specification of the previous section. The validation was based on the identification of the haptic sensations. Additionally, pairs of sensations

were combined into a unique stimulus (i.e., combined sensations) to study if its constituents could be selectively identifiable.

5.3.1 Combined Mid-Air Haptic Sensation

A combined mid-air haptic sensation was developed to expose participants to pairs of simultaneous STM sensations. The combined sensation is a stimulus composed by two distinct STM haptic sensations. Such a stimulus was achieved by spatially multiplexing the UMAH transducer array in half to create two independent, overlaid patterns with the same size and position. The FP's speed and number of points of the pattern were independently controlled for each pattern, meaning that each haptic sensation (composing the combined sensation) can be independently controlled.

The spatial multiplexing approach has a few shortcomings. Two of these include: i) a reduction in the contribution of the haptic array's acoustic power for each haptic sensation, meaning that each individual haptic sensation becomes weaker; and ii) there is acoustic interference between the fields of both halves of the array. A combined sensation is the sum of two haptic sensations and, therefore, constructive interference should occur. For constructive interference to occur, the phases of each stimulus's FP must be synchronized. This requirement was achieved by using one of the FP's phases as a reference.

In the remainder of this section, the combined sensation is reviewed in detail. Combined stimuli were analysed with the acoustic setup presented in Section 4.5.1. For the sake of simplicity, the explanation focuses on discussing only one combined sensation — the Dynamic and the Uniform combination (D+U), which is representative of the overall findings.

The acquisition rate of the ADC was set to 500 kHz. The position of the microphone was accurately controlled by the staging system discussed in Section 4.5.1. The microphone height was the same as the stimulus — $200\ \mathrm{mm}$.

For the spatial scanning of the acoustic field, the staging system was configured with resolution step of $2.5\ \mathrm{mm}$ and for each position the microphone signal was recorded for $3\ \mathrm{s}$. The scanning an area encompassed the whole pattern (i.e., $80\ \mathrm{mm} \times 80\ \mathrm{mm}$), thus, given the spatial step given above, 1024 measurements were needed to scan the whole field (i.e., 32 measurements per row and column). The total field scanning took approximately 1 h ($32 \times 32 \times 3\ s$). Lastly, for the temporal measurements, the microphone's signal was acquired from a SP.

Next, the first two results corresponding to *single* STM haptic sensation will be presented. Namely,the Dynamic sensation (Figure 5.9) and the Uniform (Figure 5.10). Then, the result of the combined sensation, Dynamic+Uniform is presented in Figure 5.11.

Figure 5.9 shows the measurements of a Dynamic (D) sensation. The v_{FP} was $0.16\ \mathrm{m/s}$ (i.e., $f_{\text{draw}} =$

1 Hz) and patterns were created with 10 SPs (upper part of the figure) and 50 SPs (bottom part of the figure). The pattern length was the same for all measurements (l of 157 mm), the same size used in the previous user-study.

For the pattern composed of 10 points, the stimulation signal is shown in Figure 5.9 (a), and the drawing period (T_{draw}) corresponds to 1 s. Figure 5.9 (b) displays the SP's signal (which is a pulse stimulation) in greater detail. The SP pulse has an ON/OFF shape, with a duration of 100 ms. The SP duration (or t_{SP}) is consistent with the value of the N_{SP}, as estimated by Equation 3.6. Figure 5.9 (c) depicts the stimulus's acoustic field. One can observe the ten SP constituting the pattern. Circular dashed lines were added around the SP (consistent with the FP's diameter, 15 mm) to highlight that the SP are on the limit of overlapping each other.

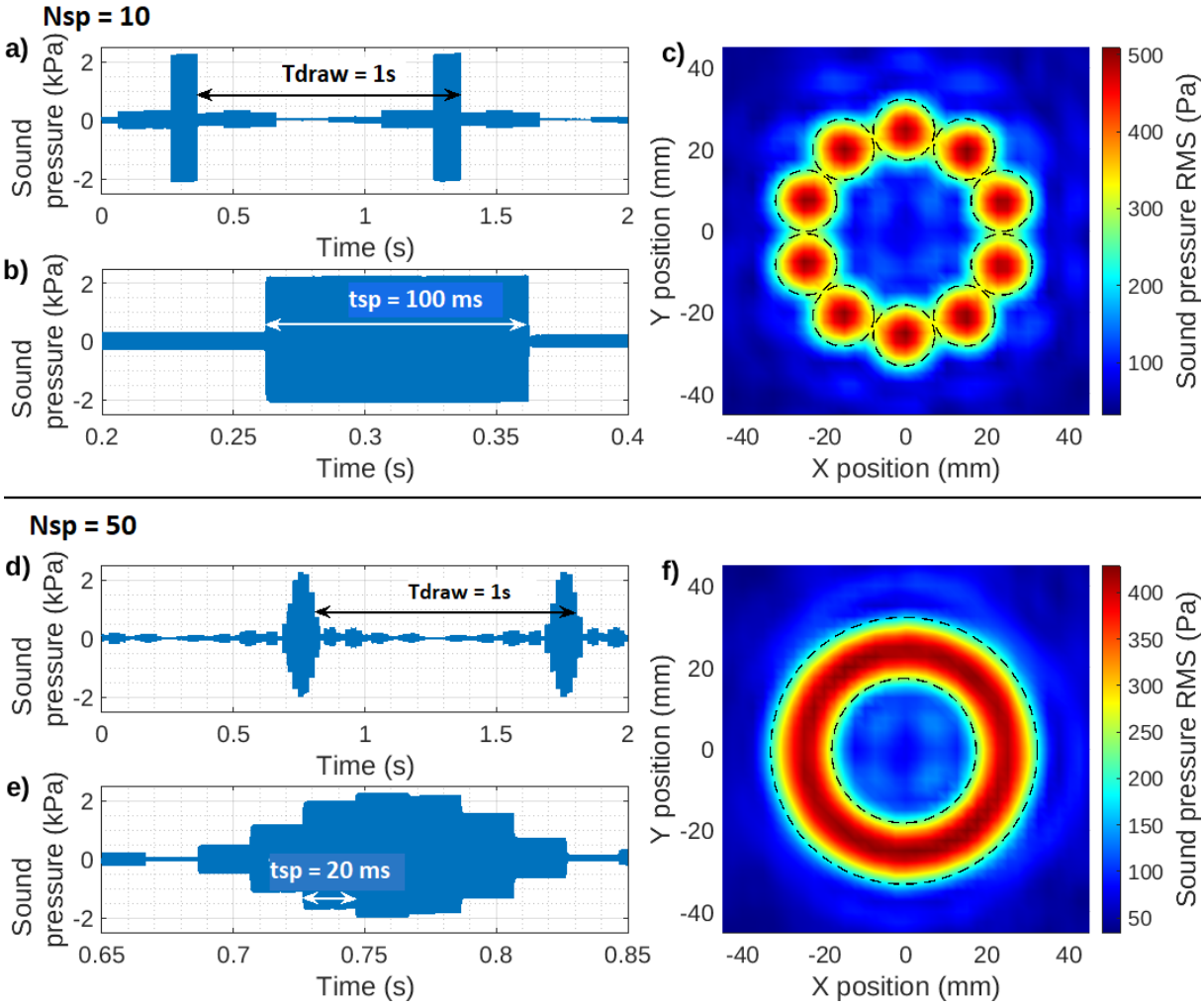

Figure 5.9: Results of the Dynamic sensation (v_{SP} of 0.16 m/s or T_{draw} of 1 Hz) for 10 and 50 N_{SP}. (a) and (d) Temporal signals acquired at a SP; (b) and (e) *zoom* of the temporal signal for pulse observation; and (c) and (f) the acoustic field of the stimulus.

Still in the Figure 5.9, the measurements for the 50-SP configuration are shown. Figure 5.9 (d) shows

that the temporal characteristics remain identical to the previous case (i.e., $T_{\text{draw}} = 1$ s). Figure 5.9 (e) demonstrates the influence of the higher N_{SP} on the SP pulse shape, with a stair-step shape visible due to the FP completing the trajectory with more jumps over shorter distances (see the explanation of Figure 3.5). Figure 5.9 (f) shows the acoustic field of the pattern with dashed lines delimiting it (using the FP's transversal distance as reference). In this case, the pattern appears "continuous" due to the higher number of shape points.

Figure 5.10 shows measurements of the Uniform haptic sensation (U) with an v_{FP} of 7.85 m/s (i.e., $f_{\text{draw}} = 50$ Hz). Measurements were performed for patterns with 10 SPs (top of the figure) and 50 SPs (bottom of the figure).

Considering the 10-point case, Figure 5.10 (a) shows a periodicity (T_{draw}) of the stimulating signal of 20 ms ($T_{\text{draw}} = f_{\text{draw}}^{-1}$). *Zooming* in on the temporal (stimulating) signal, Figure 5.10 (b) shows a pulse (ON/OFF shape) with a duration of 2 ms (t_{SP}, as predicted by Equation 3.6). Figure 5.10 (c) shows the stimulus's acoustic field, and one can observe the ten points constituting the pattern.

The bottom part of Figure 5.10 (d) focuses on the Uniform haptic sensation for the 50-point configuration. Figure 5.10(d) shows that the stimulating signal has the same periodicity as the 10-point case (i.e., $T_{\text{draw}} = 20$ ms). Figure 5.10 (e) demonstrates a stair-shaped signal composed of short pulses with a duration of 0.4 ms (t_{SP}, consistent with Equation 3.6). The acoustic field of Figure 5.10 (f) shows a line-shaped pattern due to the increased number of shape points, as expected.

Next, a combined sensation was measured, corresponding to the combination of a Dynamic sensation (with N_{SP} of 10 points) and a Uniform sensation (with N_{SP} of 50 points). As explained in the beginning of the section, the transducer phased array was spatially multiplexed to create the combined sensation. The haptic array surface was multiplexed in two halves, with each half responsible for the generation of a particular haptic sensation. The results are shown in Figure 5.11.

In Figure 5.11 (a), it is possible to observe the low-frequency signal of the Dynamic sensation (i.e., f_{draw} of 1 Hz) and the high-frequency signal of the Uniform sensation (i.e., $f_{draw} = 50$ Hz). The stimulating signals of the Dynamic and Uniform sensation are better represented in Figure 5.11 (b). As can be seen, they correspond to the pulses shown in Figure 5.9 (b) and Figure 5.10 (e), respectively. When the pulses of both stimuli occur at the same position and at the same time instant, they constructively interfere (see Figure 5.11 (a) at around 300 ms). As mentioned at the beginning of this section, the FP's phases were synchronized for this purpose.

The acoustic field of the combined stimulus is shown in Figure 5.11(c). Both constituent stimuli are present in the field. The Dynamic sensation corresponds to the pattern composed of ten points, while the Uniform sensation is represented by the line-shaped pattern (N_{SP} of 50 points). Still in Figure 5.11 (c),

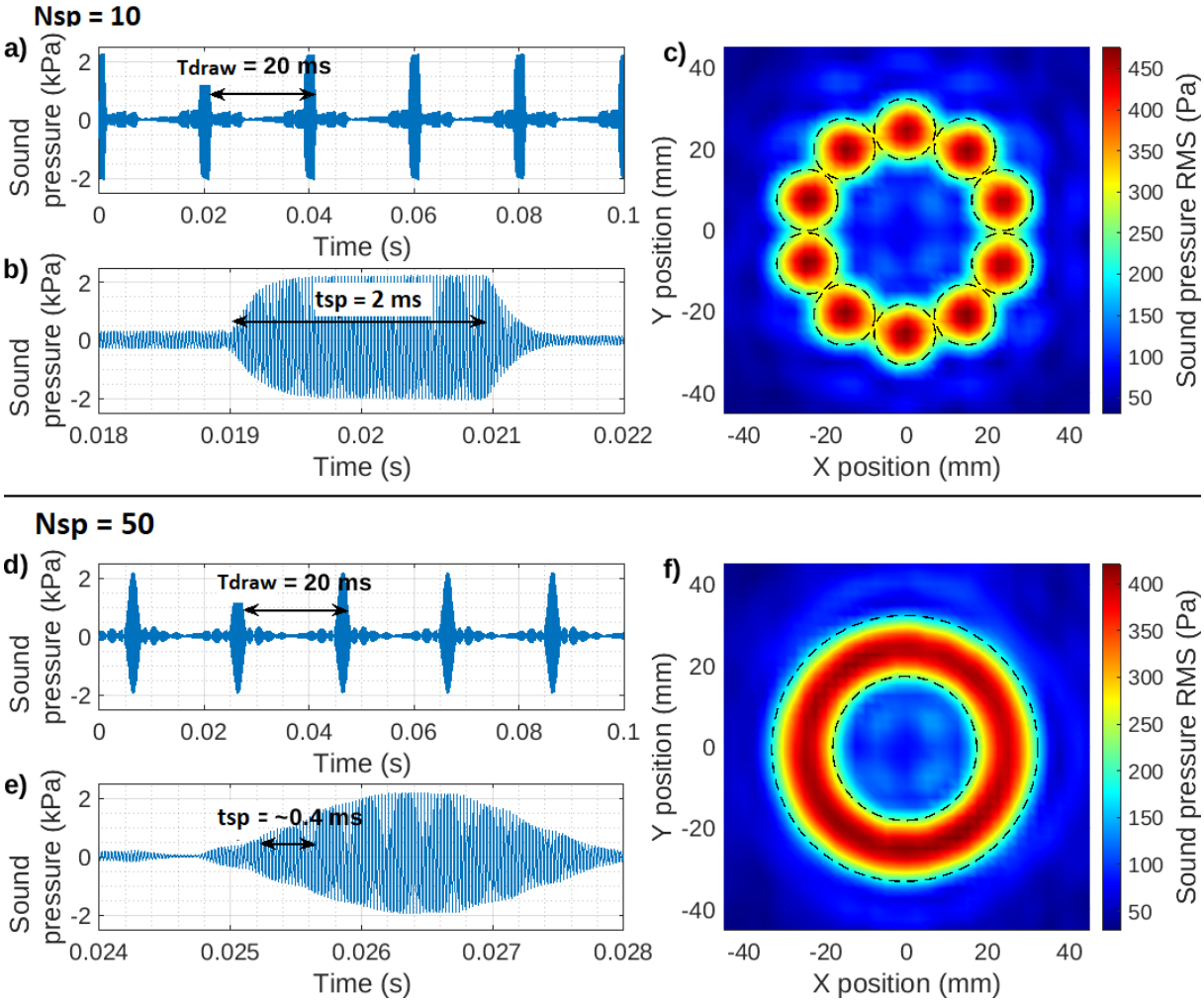

Figure 5.10: Results of the Uniform sensation (v_{SP} of 7.85 m/s or T_{draw} of 50 Hz) for 10 and 50 N_{SP}. (a) and (d) Temporal signals acquired at a SP; (b) and (e) *zoom* of the temporal signal for pulse observation; and (c) and (f) the acoustic field of the stimulus.

the occurrence of constructive interference between both sensations is observable through the sum of the acoustic pressures at the positions of the Dynamic shape points.

5.3.2 Experiment Overview and Methodology

An experiment was designed with the goal of evaluating whether mid-air haptic STM sensations evoke distinctive perception. The haptic sensations (specified in Figure 5.8) were used to create the combined sensations. In this study three distinct combined sensations were created:

1. Dynamic + Uniform (D+U);
2. Dynamic + Vibratory (D+V);
3. Vibratory + Uniform (V+U);

The Figure 5.12 illustrates the creation of the combined sensations used in the experiment.

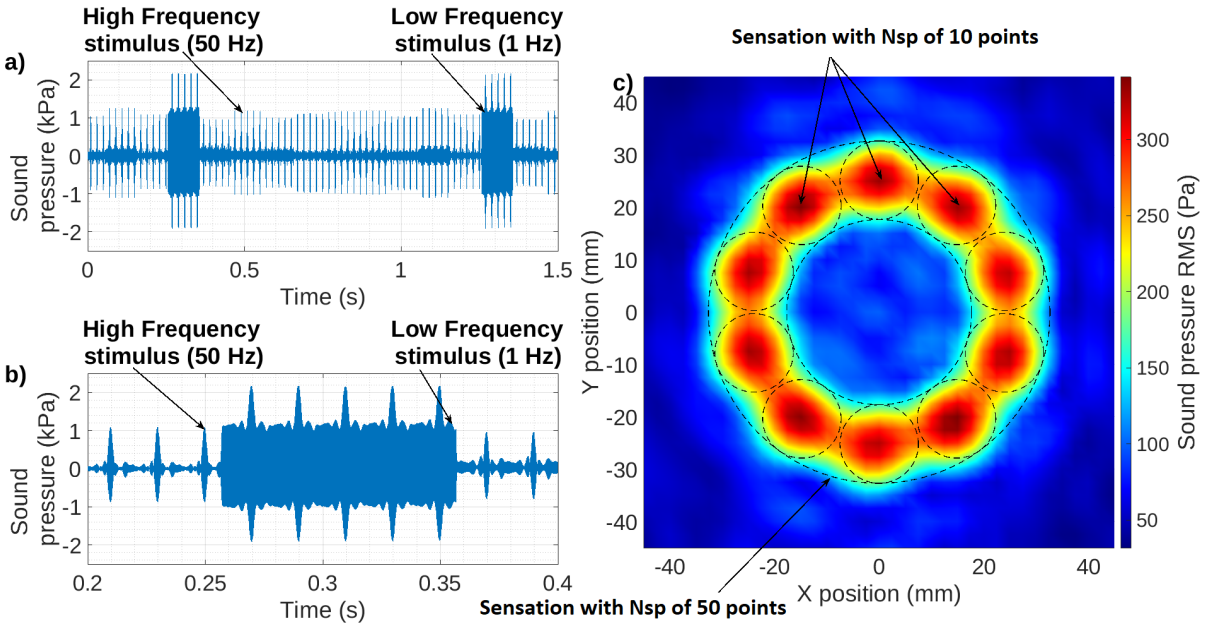

Figure 5.11: Results of the combined Dynamic sensation (10 points) and the Uniform sensation (50 points). (a) Temporal signal acquired at a shape point's position; (b) *zoom* of the temporal signal for pulse observation; and (c) stimulus's acoustic field.

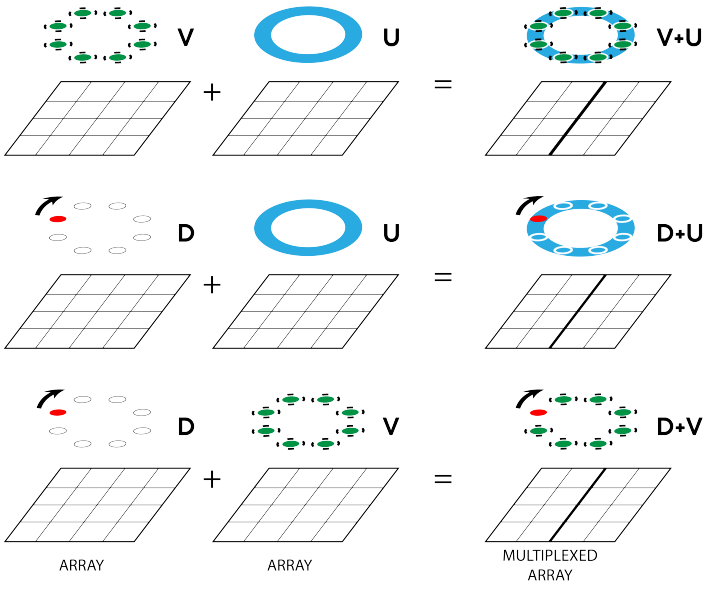

Figure 5.12: Creation of a combined sensation.

As can be observed through the Figure 5.12, each sensation was graphically illustrated and were given distinct colors. Moreover, when representing a combined sensations (which can be found on the rightmost part of the figure), it essentially correspond to the overlap of the two constituent sensations. The Dynamic sensation is represented by a moving FP. The Vibratory sensation, is illustrated as multiple vibrations

occurring along the circular shape. And the Uniform sensation is represented as a complete circular trace. These illustrations are in accordance with the descriptions of the STM haptic sensations, which can be found in Table 5.1.

In the experiment, the identification of individual sensations alone and their presence in the combined sensation were evaluated. Twelve STM sensations were used as the baseline, these can be found in Table 5.8.

Table 5.8: STM sensations used in the experiment.

	D1		*D2*		*V1*		*V2*		*U1*		*U2*	
Speed (m/s)	0.16	0.16	0.21	0.21	2.51	2.51	3.14	3.14	7.85	7.85	12.6	12.6
N_{SP}	10	50	10	50	10	50	10	50	10	50	10	50

For each type of sensation (e.g., D, V and U), two FP speeds were defined. The different sensation speeds were identified by the prefix 1 or 2 (e.g., D1 and D2, etc). Moreover, for each sensation v_{FP}, two N_{SP} were chosen. A combined stimulus is a composition of two haptic sensations. As such, in this experiment, a combined stimulus can have four possible v_{FP} configurations. For example, the D+U combination has the following variants: D1+U1, D1+U2, D2+U1, and D2+U2. Moreover, each variant has four possible N_{SP} configurations (e.g., $D1_{10}$+$U1_{10}$, $D1_{10}$+$U1_{50}$, $D1_{50}$+$U1_{10}$, and $D1_{50}$+$U1_{50}$).

The type of sensation (e.g., D, V and U) plus its speed prefix (i.e., 1 or 2) followed by a subscript defining the N_{SP} configuration (e.g., $D1_{10}$) was the nomenclature adopted for representing each haptic sensation used in the experiment. Table 5.9 shows all the combined sensations used in the experiment.

Prior to the selective identification test, participants experienced the STM haptic sensations to become confident with their perception. Once that happened, a short pre-test was conducted to introduce them to the combined sensations. In line with user-study 1 (presented in Section 5.2), sensations were produced at maximum system power. As previously noted, the constituents sensations of a combined sensation felt weaker compared to the individual sensations presented alone (in a combined sensation, the system output is equally divided for each of the haptic sensations). It is important to point out that this limitation does not conflict with our main goal, which is to explore the selective identification of specific haptic sensations. Therefore, when comparing results from various sensation types (individual and combined), consider potential pressure differences. The setup and the interaction with the participant were identical to the user-study 1. Similarly, the pattern length was the same ($l = 157mm$). A total of ten participants (24 to 29 years of age) did the experiment. All procedures agreed with the ethical requirements.

Table 5.9: Combined STM sensations used in the experiment.

D+V		D+U		V+U	
D1+V1	$D1_{10} + V1_{10}$	*D1+U1*	$D1_{10} + U1_{10}$	*V1+U1*	$V1_{10} + U1_{10}$
	$D1_{10} + V1_{50}$		$D1_{10} + U1_{50}$		$V1_{10} + U1_{50}$
	$D1_{50} + V1_{10}$		$D1_{50} + U1_{10}$		$V1_{50} + U1_{10}$
	$D1_{50} + V1_{50}$		$D1_{50} + U1_{50}$		$V1_{50} + U1_{50}$
D1+V2	$D1_{10} + V2_{10}$	*D1+U2*	$D1_{10} + U2_{10}$	*V1+U2*	$V1_{10} + U2_{10}$
	$D1_{10} + V2_{50}$		$D1_{10} + U2_{50}$		$V1_{10} + U2_{50}$
	$D1_{50} + V2_{10}$		$D1_{50} + U2_{10}$		$V1_{50} + U2_{10}$
	$D1_{50} + V2_{50}$		$D1_{50} + U2_{50}$		$V1_{50} + U2_{50}$
D2+V1	$D2_{10} + V1_{10}$	*D2+U1*	$D2_{10} + U1_{10}$	*V2+U1*	$V2_{10} + U1_{10}$
	$D2_{10} + V1_{50}$		$D2_{10} + U1_{50}$		$V2_{10} + U1_{50}$
	$D2_{50} + V1_{10}$		$D2_{50} + U1_{10}$		$V2_{50} + U1_{10}$
	$D2_{50} + V1_{50}$		$D2_{50} + U1_{50}$		$V2_{50} + U1_{50}$
D2+V2	$D2_{10} + V2_{10}$	*D2+U2*	$D2_{10} + U2_{10}$	*V2+U2*	$V2_{10} + U2_{10}$
	$D2_{10} + V2_{50}$		$D2_{10} + U2_{50}$		$V2_{10} + U2_{50}$
	$D2_{50} + V2_{10}$		$D2_{50} + U2_{10}$		$V2_{50} + U2_{10}$
	$D2_{50} + V2_{50}$		$D2_{50} + U2_{50}$		$V2_{50} + U2_{50}$

5.3.3 Results

Each participant evaluated 48 combined sensations and 24 individual sensations (see Table 5.8 and Table 5.9). The latter was tested twice to balance the number of trials between individual and combined sensations. A total of 720 stimuli were evaluated, of which 480 were combined sensations (10 participants x 48 combined sensations) and 240 were single sensations (10 participants x 24 individual sensations).

The tables presented in this section show sensation confusion matrices, where the rows represent the displayed sensation and the columns represent the answers' rate (in percentage). Note that the columns are divided into single sensations (D, V and U) and combined sensations (D+U, D+V, V+U).

Table 5.10 shows the results for single sensations with the N_{SP} as the independent variable. The FP's speed in Table 5.10 was averaged, for example, for the case of a Dynamic sensation of 10 points (D_{10}), the results of the two tested speeds (i.e., D1 and D2, see Table 5.8) were averaged.

Results show that the N_{SP} parameter does not have significant influence on the discrimination of the sensations. Percentage rates are very similar between different N_{SP}, with the exception of the Uniform sensation (i.e., U_{10} and U_{50}).

Single sensations were organized by FP's speed in Table 5.11. The results were average in terms of N_{SP}. For example, for the case of a Dynamic sensation draw at D1 speed, results of the two tested N_{SP} (i.e., $D1_{10}$ and $D1_{50}$) were averaged, see Table 5.8. Under these terms, success rates for the Dynamic sensations (D_1 and D_2) were, on average, 91.7%. The sensations V_1 and V_2 have a correct identification

Table 5.10: Sensation identification rates per N_{SP} (confusion matrix).

Sensation / % Rate	***D***	***V***	***U***	***D+U***	***D+V***	***V+U***	***TOTAL***
$\boldsymbol{D}_{10}$	95.0%	0.0%	0.0%	0.0%	5.0%	0.0%	100.0%
$\boldsymbol{D}_{50}$	87.5%	0.0%	2.5%	7.5%	2.5%	0.0%	100.0%
$\boldsymbol{V}_{10}$	0.0%	70.0%	0.0%	0.0%	0.0%	30.0%	100.0%
$\boldsymbol{V}_{50}$	0.0%	70.0%	0.0%	0.0%	0.0%	30.0%	100.0%
$\boldsymbol{U}_{10}$	0.0%	10.0%	90.0%	0.0%	0.0%	0.0%	100.0%
$\boldsymbol{U}_{50}$	0.0%	10.0%	75.0%	0.0%	0.0%	15.0%	100.0%

rate of 65% and 75%, respectively. They were mistaken for the $V+U$ sensation, 35% for V_1 and 25% for V_2. The Uniform sensations (U_1 and U_2) have been successfully identified with 87.5% and 77.5%, respectively. They were confused with the Vibratory sensation (7.5% and 10% for U_1 and U_2, respectively), and U_2 was confused with the $V + U$ combined sensation by 12.5%.

Table 5.11: Sensation identification rates per v_{FP} (confusion matrix).

Sensation / % Rate	***D***	***V***	***U***	***D+U***	***D+V***	***V+U***	***TOTAL***
D1	90.0%	0.0%	2.0%	4.0%	4.0%	0.0%	100.0%
D2	93.3%	0.0%	0.0%	3.3%	3.3%	0.0%	100.0%
V1	0.0%	65.0%	0.0%	0.0%	0.0%	35.0%	100.0%
V2	0.0%	75.0%	0.0%	0.0%	0.0%	25.0%	100.0%
U1	0.0%	7.5%	87.5%	2.5%	0.0%	2.5%	100.0%
U2	0.0%	10.0%	77.5%	0.0%	0.0%	12.5%	100.0%

The combined sensations' results are presented in Table 5.12. The obtained results are more dispersed than the single sensations (of Table 5.11). From Table 5.12, it is possible to see that, in general, each combination's results yielded similar profiles independent of the speed configurations.

The identification rates of Table 5.12 were averaged because of the reasons stated before and the average results are displayed in Table 5.13. The $V + U$ combination was identified correctly in 40% of the trials. Moreover, in approximately 30% of the trials, it was misidentified as the Vibratory and Uniform sensations (that are its constituents). As for the $D+V$ sensation, success rates were also 40%. The combination was confused with other combinations (i.e., 18% with $D + U$ and 13% with $V + U$, respectively). Additionally, in 20.6% of the cases, this combination was perceived as Vibratory. At last, the $D + U$ combination was correctly identified in 74.4% of the trials and in 16.9% it was confused with Dynamic sensation.

Table 5.12: Confusion matrix for the combined sensations (FP's speed).

Sensation / % Rate	***D***	***V***	***U***	***D+U***	***D+V***	***V+U***	***TOTAL***
				D+U			
D1+U1	20.0%	0.0%	0.0%	80.0%	0.0%	0.0%	100.0%
D1+U2	17.5%	0.0%	0.0%	67.5%	12.5%	2.5%	100.0%
D2+U1	22.5%	0.0%	0.0%	77.5%	0.0%	0.0%	100.0%
D2+U2	7.5%	0.0%	10.0%	72.5%	7.5%	2.5%	100.0%
				D+V			
D1+V1	7.5%	17.5%	2.5%	10.0%	52.5%	10.0%	100.0%
D1+V2	10.0%	17.5%	2.5%	17.5%	40.0%	12.5%	100.0%
D2+V1	5.0%	25.0%	0.0%	22.5%	32.5%	15.0%	100.0%
D2+V2	5.0%	22.5%	0.0%	22.5%	35.0%	15.0%	100.0%
				V+U			
V1+U1	0.0%	25.0%	22.5%	0.0%	0.0%	52.5%	100.0%
V1+U2	0.0%	40.0%	25.0%	0.0%	0.0%	35.0%	100.0%
V2+U1	0.0%	20.0%	47.5%	2.5%	0.0%	30.0%	100.0%
V2+U2	0.0%	40.0%	17.5%	0.0%	0.0%	42.5%	100.0%

Table 5.13: Sensation confusion matrix for the combined sensations (averaged per FP's speed).

Sensation / % Rate	***D***	***V***	***U***	***D+U***	***D+V***	***V+U***	***TOTAL***
D+U	16.9%	0.0%	2.5%	74.4%	5.0%	1.3%	100.0%
D+V	6.9%	20.6%	1.3%	18.1%	40.0%	13.1%	100.0%
V+U	0.0%	31.3%	28.1%	0.6%	0.0%	40.0%	100.0%

5.4 Discussion

The first part of this section discusses the results of the two user studies presented in this chapter. Moreover, in the end of the section, the perceptual aspects that in our opinion are relevant to the discussion are addressed.

5.4.1 Results of the User Studies

The results of the Dynamic-Vibratory boundary (presented in Section 5.2.2.1) show that the median speed thresholds increase with the increase in N_{SP}. The increase was approximately 30% when the N_{SP} increased from 10 points to 30 or 50 points.

The Dynamic sensation is defined by the lower limit of the Dynamic-Vibratory boundary (see the final specification in Figure 5.8). And, the N_{SP} influences the ability to perceive the FP's motion at high dynamic FP's speeds. For a N_{SP} of 10 points, the v_{FP} is 0.54 m/s, and for 30 or 50 points, the v_{FP} are 0.79 m/s and 0.74 m/s, respectively. This is an interesting phenomenon, suggesting that the ability to

discriminate motion is somehow influenced by the spatial resolution of the motion itself.

The Vibratory-Uniform boundary expands with the increase in N_{SP} (see Figure 5.8). The σ increases by over 50% when the N_{SP} changes from 10 to 50 points (i.e., from 0.7 m/s to 1.1 m/s, respectively). Participants noted that distinguishing between the Vibratory and Uniform sensations was sometimes challenging. The Vibratory sensation is characterized by a low-frequency vibration that is uneven (along the SPs of the pattern), while the Uniform sensation also involves vibration but with higher frequencies throughout the entire pattern (see Table 5.1 for a complete description of the haptic sensations' perception). The presence of a vibration component in both haptic sensations may have complicated the evaluation process.

In the identification study (of Section 5.3), the results showed identification rates of 92% for the Dynamic sensation, 82.5% for the Uniform sensation, and 70% for the Vibratory sensation. These high identification rates for single sensations support the hypothesis that the STM creates perceptually distinct mid-air haptic sensations. Furthermore, the results did not vary based on speed variants (i.e., different v_{FP} within the same sensation) or N_{SP}.

Combined sensations were developed to create sensations that joined different types of perceptions. To provide evidence of their creation, a specific type of combined stimuli was measured, namely the Dynamic+Uniform combination and demonstrated that the stimuli exhibited constructive interference (refer to Figure 5.11). The results for the combined sensations were averaged and presented in Table 5.13, with the Dynamic+Uniform combination achieving the highest identification rate - 74.4%.

This finding suggests that selective identification of the sensations was successfully achieved. Moreover, the Dynamic and Uniform sensations had the highest rates among the single sensations. These two haptic sensations may involve distinct perceptual mechanisms. Furthermore, the results indicate that combinations involving the Vibratory sensation had the lowest identification rates - 40% for the Dynamic+Vibratory and Vibratory+Uniform combinations (see Table 5.13). The Vibratory sensation is a transition between the Dynamic and Uniform haptic sensations. These results suggest that when the Vibratory sensation is present in a combination, it is more difficult for the participant to correctly identify the specific sensation.

One factor that likely affected the identification rates for the combined sensation was the decrease in sensation strength due to spatial multiplexing of the array.

5.4.2 Psychophysical Explanation of the haptic sensations

In the Dynamic sensation, the N_{SP} not only influences the perception of motion but also the feeling of the sensation. At lower N_{SP} (e.g., 10 points), the FP's movement is felt with sharp, perceptible pulse transitions. On the other hand, at higher N_{SP} (e.g., 30 or 50 points), the motion is felt smoothly without noticeable pulse transitions.

Previous studies (Frier et al., 2019; Morisaki et al., 2022) have shown that the N_{SP} affects the perception of low-speed stimuli, and the SA1 mechanoreceptive system is associated with the perception of these stimuli. With a lower N_{SP}, the pulse duration (t_{SP}) increases, resulting in noticeable skin deflection and pulse transitions (Frier et al., 2019; Gavrilov, 2014). As the N_{SP} increases, the FP executes shorter and more frequent jumps, creating a perception of continuous movement. Although the stimuli tested in (Morisaki et al., 2022) were much smaller than those in this study (see Section 3.3.1 for detailed explanation), the Dynamic sensation at higher N_{SP} (i.e., 30 or 50 points) also resembled a moving pressure.

The Vibratory sensation is characterized by localized low-frequency vibrations occurring at specific SPs on the circular pattern. This sensation appears to be influenced by the drawing frequency (f_{draw} parameter). For the pattern length used in the studies (157 mm), the f_{draw} values ranged between 8 Hz and 30 Hz (on average). The Vibratory sensation is a transition between the Dynamic and Uniform sensations, and its perception may be related to the temporal resolution of touch (more specifically, the temporal order judgement discussed in Section 2.2.2.2). The FP movement is too fast to be individually perceptible (as in the Dynamic sensation), and it is also too slow to create the tactile illusion of simultaneous perception of the entire pattern (as in the Uniform sensation). For instance, in the case of 10 points, the time between adjacent pulses is less than 15 ms (near the judgment threshold, see Section 2.2.2.2) but greater than 3 ms (above the temporal resolution threshold).

The Uniform sensation is perceived as a uniform high-frequency vibration. The movement of the FP is very fast, and a tactile illusion of simultaneity seems to occur in time and space. Based on our results, the N_{SP} parameter influenced the perception of this sensation. However, a better understanding of this phenomenon is required because the similarities of the feelings of the Vibratory and Uniform sensations may have influenced the results. Previous studies have shown that high-speed patterns are strongly felt within the speed range of 5 m/s to 8 m/s (Frier et al., 2019), and our results specify the Uniform sensation for speeds greater than 6.5 m/s (on average), for a 157 mm circular pattern. The RA mechanoreceptive system is associated with the perception of high-speed spatio-temporal stimuli (Takahashi et al., 2020). In our study, the feeling of the Uniform sensation is specified for drawing frequencies (f_{draw}) above 40 Hz. These results are consistent with the RA's response, as it is known to be more sensitive to frequencies around 40 Hz to 60 Hz (see Section 2.2.1).

5.5 Conclusions

The haptic sensations produced by an STM pattern (with palm size) were specified by the v_{FP} and N_{SP}. They are the Dynamic, Vibratory, and Uniform sensations. The Dynamic is a slow-moving FP whose direction of movement is perceived. It occurs for speeds up to 0.54 m/s, 0.79 m/s, and 0.74 m/s, for 10, 30, and 50 points, respectively. The Vibratory sensation feels like low-frequency vibrations on localized positions of the pattern. Its associated speeds are 1.06 m/s to 4.9 m/s, 1.31 m/s to 4.6 m/s,

and 1.26 m/s to 4.5 m/s, for 10, 30, and 50 points, respectively. At last, the Uniform sensation feels like high-frequency vibration along the whole pattern. It is created for speeds above 6.3 m/s, 6.6 m/s, and 6.7 m/s, depending on the N_{SP} configuration. Refer to Figure 5.8 for a visual representation of the haptic sensation's specification.

In the second user study, a sensation identification experiment was performed. The identification rates for the single sensations were high and supported the specification of the first user study. On average, they were 92.5% for the Dynamic sensation, 82.5% for the Uniform sensation, and 70% for the Vibratory sensation. Combined stimuli were created and evaluated in the same study. The constituents of the Dynamic + Uniform combination were selectively identified in 74.4% of the trials, suggesting that they may involve their own psychophysical processes.

5.6 Next Steps

The creation of STM haptic sensations is not a trivial task. It requires an experienced designer (or haptic researcher) to create such stimuli. As demonstrated throughout this thesis, STM sensations depend on the careful manipulation of several parameters (these can be found in Table 3.1). The complexity of the STM modulation limits its adoption and by consequence the UMAH technology.

To create STM sensations with less effort, stimulus generation tools are required to abstract the user of the tool from the technical complexities of the STM. Moreover, such tools can aid in the development of novel and optimize haptic sensations.

The next chapters, namely Chapter 6, 7 and 8 regard the implementation and validation of an in-development haptic sensation generator tool, based on the STM. The following chapters represent our effort developing a sensation generator tool to aid in the development of haptic sensations.

Dynamic Haptic Sensations

6.1 Context

The aim of this chapter is to perform a detailed analysis of the dynamic haptic sensation specified in the previous chapter. A deeper understanding of this haptic sensation enables a more accurate identification of the parameters that influence its perception. Such analysis contributes to a better understanding of the haptic sensation and can be used to guide its generation.

In this chapter, only the dynamic sensation is analyzed. This type of haptic sensation can give rise to different sensations, making it a particularly relevant case study.

Qualitative (or subjective) tests involving participants were not conducted for the sensations discussed in this chapter due to time constraints. Therefore, this chapter should be regarded as a theoretical foundation for future work. Nevertheless, the work presented here resulted in a comprehensive specification of the dynamic haptic sensation, which is incorporated into the stimulus generation module described in the following chapter.

The first part of this chapter focuses on justifying the maximum speed of the FP (v_{max}) and maximum number of points (N_{max}) that can be used in the dynamic sensation. Further in the chapter, the four sensations that can be created in the dynamic regime are discussed. These depend on specific parameters of the STM. In the end of the chapter, some suggestions for optimizing dynamic sensations are discussed.

To support the explanation throughout the chapter, the following equations related to STM (already presented in Section 3.2) associated with STM are provided:

$$\text{Drawing Period (from Equation 3.3):} \quad v_{FP} = \frac{l}{T_{draw}} \Leftrightarrow T_{draw} = \frac{l}{v_{FP}} \tag{6.1}$$

$$\text{Distance b/w shape points (from Equation 3.5):} \quad d_{SP} = r \cdot \frac{2\pi}{N_{SP}} \Leftrightarrow d_{SP} = \frac{l}{N_{SP}} \tag{6.2}$$

$$\text{Duration of a shape point (from Equation 3.6):} \quad T_{draw} = N_{SP} \cdot t_{SP} \Leftrightarrow t_{SP} = \frac{T_{draw}}{N_{SP}} \tag{6.3}$$

The v_{max} and the N_{max} are important parameters for the perception of the dynamic haptic sensation and they will be discussed in the next sections.

6.2 Maximum focal point's speed

The dynamic sensation is characterized by the perception of the FP's motion. Given the characteristics of the sensation, as the FP's moves throughout the shape, the order of SP's occurrence must be perceived.

The v_{max} for the dynamic sensation was experimentally obtained in the Chapter 5. In the present section, v_{max} was estimated based on theoretical arguments related to tactile perception.

As introduced in Section 2.2.2.2, the temporal order judgment threshold (TOJ) is the minimum time required for discerning the order of occurrence of consecutive stimulations. As discussed in the same section, the TOJ threshold (t_{TOJ}) is approximately 20 ms.

The duration of consecutive stimulations is typically defined by the Stimulus Onset Asynchrony (SOA) parameter. t_{SOA} defines the time between the beginning of a stimulation event and the start of the next one. In the context of STM patterns, t_{SOA} is equal to the SP duration (t_{SP}).

The Figure 6.1 illustrates the stimulation caused by a moving FP. When it enters a SP, a stimulation occurs and the stimulation ends when the FP jumps to the next SP. The transition between SPs (leaving the old position and entering the new one) occurs very fast (instantaneously to the tactile sense).

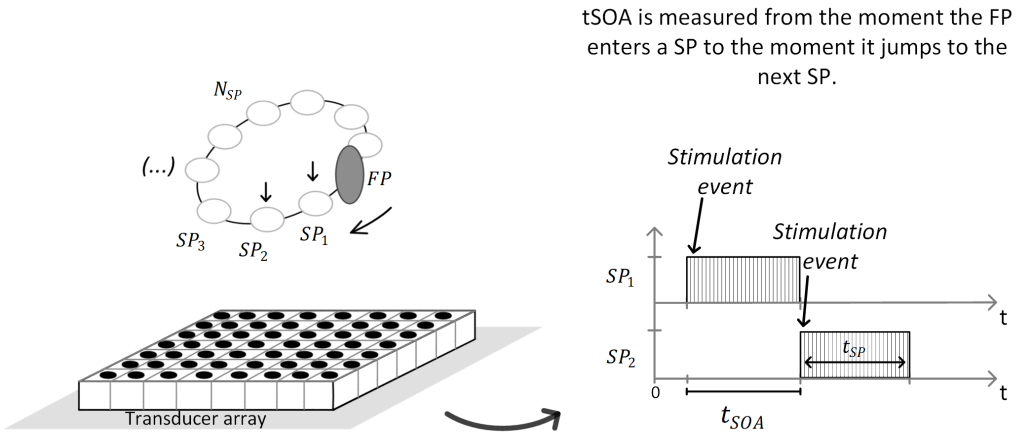

Figure 6.1: Stimulus Onset Asynchrony in the context of the dynamic haptic sensation.

It is reasonable to assume that, for the motion of the FP to be perceived (like happens in the dynamic sensation), the order of occurrence of the SPs must be perceived. In other words, t_{SOA} should be greater than t_{TOJ}. Conversely, if t_{SOA} is less than t_{TOJ}, then the perception of motion is likely to be unperceivable, as SPs will be perceived simultaneously. Figure 6.2 illustrates the mentioned phenomenon.

Due to the way the STM pattern is created, as the number of SPs increases, the distance between them (d_{SP}) decreases (they become closer). Accordingly, the duration of each SP (t_{SP}, which is equal to t_{SOA}) also decreases. As was mentioned, there is a direct relationship between d_{SP} and t_{SP} (see Section 3.2).

Consider Equation 6.2 and Equation 6.3. By matching both equations through N_{SP}, the speed of the FP (v_{FP}) is obtained:

$$\frac{l}{d_{SP}} = \frac{T_{draw}}{t_{SP}} \Leftrightarrow \frac{d_{SP}}{t_{SP}} = \frac{l}{T_{draw}} \Leftrightarrow v_{FP} = \frac{d_{SP}}{t_{SP}} \tag{6.4}$$

As can be concluded, v_{FP} is given by the ratio of d_{SP} to t_{SP}.

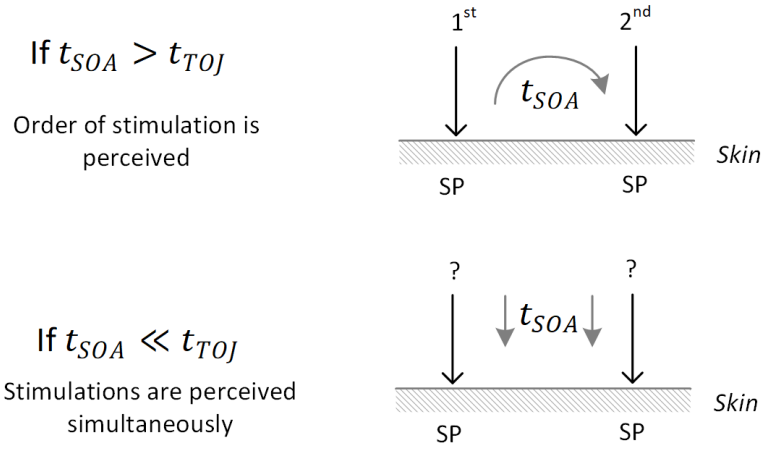

Figure 6.2: Temporal requirement for movement perception of the FP.

To estimate the theoretical v_{max}, the t_{TOJ} was considered as the minimum duration of a SP (i.e., $t_{SPmin} = t_{TOJ}$). By ensuring this, the perception of the SP's order is likely to be preserved. Regarding the distance between stimulations or shape points (d_{SP}), the FP's diameter (i.e., d_{FP}) was considered. By doing that, the adjacent FP stimulations happen closer together but not overlapping each other. With these considerations, an expression for the theoretical v_{max} is obtained.

$$v_{max} = \frac{d_{FP}}{t_{TOJ}} \tag{6.5}$$

By considering a d_{FP} measured in Section 4.5 of 15 mm and a t_{TOJ} of around 20 ms, a v_{max} of about 0.75 m/s is obtained.

Note, the v_{max} highly depends on the t_{TOJ}, which in turn is highly difficult to estimate precisely. Thus, more precise estimations of t_{TOJ} will likely to improve the v_{max} for the dynamic sensation.

6.3 Maximum number of shape points

The next parameter to be discussed is the maximum number of SPs (N_{max}) composing a pattern that can be achieved while preserving a dynamic haptic sensation. The analysis is primarily theoretical; however, deriving insights for estimating N_{max} is important, as rendering a pattern with too many SPs may cause the sensation to become unnoticeable.

The goal is to render a pattern with a maximum number of points without compromising its perception. The STM can be interpreted as a train of pulses and, as defined in Section 2.3.2.2, the perception of each pulse depends on its critical duration ($t_{critical}$). For pulse durations shorter than $t_{critical}$, the pulse becomes difficult to perceive. Therefore, $t_{critical}$ is considered for estimating N_{max}, specifically to define the minimum SP duration (t_{SPmin}) required to preserve pattern perception.

Consider Equation 6.4 and set $t_{SP} = t_{critical}$. The corresponding distance between SPs (d_{SP}) is thus given by:

$$d_{SP} = v_{FP}\, t_{critical} \tag{6.6}$$

Using Equation 6.2 and substituting d_{SP} with the result from Equation 6.6, the expression for N_{max} is obtained:

$$N_{max} = \frac{l}{v_{FP}\, t_{critical}}. \tag{6.7}$$

As can be observed, the maximum number of SPs that ensures perception depends on the pattern length (l) and the critical duration for pulse ($t_{critical}$). The relationship of Equation 6.7 also indicates that higher FP speeds result in lower values of N_{max}, in order to maintain the minimum pulse duration required for perceptual detection.

6.4 Rough and smooth pressure sensations

As identified in the research study presented in Chapter 5, the perception of the dynamic sensation varies with the N_{SP}. As discussed in Section 3.2, d_{SP} and N_{SP} are directly related quantities. When d_{SP} is approximately equal to 15 mm (i.e., N_{SP} of 10 points) the perception is rough (i.e., the FP movement is perceived as discrete). In contrast, for smaller values of d_{SP}, the FP movement is perceived as continuous or smooth.

The precise specification of the d_{SP} at which this perceptual transition occurs is not the goal of this section. Nevertheless, a perceptual factor that may be related to this transition is the 2PDT. This factor was introduced in Section 2.2.2.1 and is approximately 8 mm for the palm.

In dynamic haptic sensations, the perceived motion of the FP varies between discrete, consecutive jumps (rough perception) and continuous movement resulting from closely spaced shape points (smooth perception). In our view, the 2PDT may help explain this perceptual transition.

Consider the circular pattern used in the research study of Chapter 5, with a length $l = 157$ mm, discretized into 10, 30, or 50 SPs. When the sensation is rough, adjacent SPs appear to be spaced at distances greater than the 2PDT. For example, when the trajectory consists of 10 points (associated with rough perception), d_{SP} is approximately 15 mm, meaning that $d_{SP} > 2PDT$ (in fact, for this case, d_{SP} is around the diameter of the FP, d_{FP}). In contrast, for trajectories with 30 or 50 points, d_{SP} is smaller than the 2PDT ($d_{SP} < 2PDT$), and the perception of discrete points diminishes, giving rise to a continuous and smooth motion (like a moving pressure (Morisaki et al., 2022)).

Figure 6.3 illustrates this perceptual phenomenon. The pair of images at the top shows a case where $d_{SP} > 2PDT$, meaning clearly separated SPs and resulting in a rough dynamic sensation. In contrast, the images at the bottom show closely spaced SPs, where overlap occurs, producing a continuous perceptual effect.

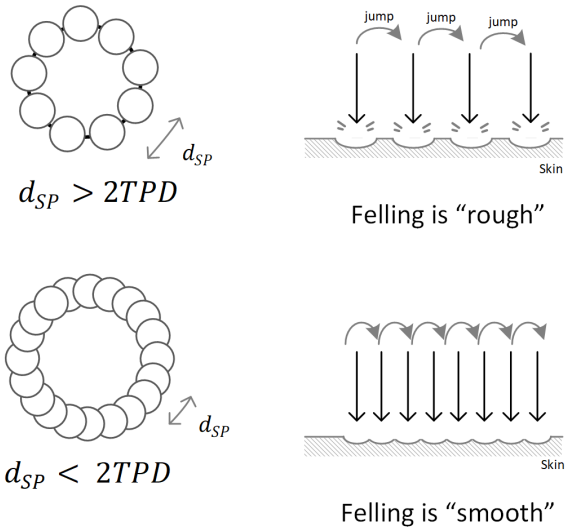

Figure 6.3: Dynamic rough and smooth perception and its association with 2PDT thresholds.

6.5 Pressure and vibrotactile dynamic sensations

The next parameter to be discussed is the amplitude modulation frequency (f_{am}). As in AM (discussed in Section 2.3.3), the parameter f_{am} refers to the frequency at which the FP's amplitude is modulated.

In the context of STM, the parameter f_{am} is typically not considered, since the FP is typically maintained at a constant amplitude (i.e., $A(t) = 1$). However, in the context of dynamic haptic sensations, it is reasonable to modulate the FP's amplitude, as in AM, in order to alter the type of haptic dynamic sensation.

Two distinct dynamic sensations can be produced. The first corresponds to the unmodulated case, which reflects the traditional STM scenario, where the FP amplitude remains constant ($A(t) = 1$, or equivalently $f_{am} = 0$ Hz). From a perceptual standpoint, this sensation is typically described as a “moving pressure” (Hajas et al., 2020; Morisaki et al., 2022) and corresponds to a dynamic pressure sensation.

In the second case, f_{am} is set to match the sensitivity range of the skin's vibrotactile receptors—namely, 150–250 Hz for PC and 40–50 Hz for RA1. When the FP's amplitude is modulated at these frequencies, the dynamic pressure sensation acquires a vibrotactile character and can be described as a dynamic vibrotactile sensation. Figure 6.4 illustrates the two dynamic sensations described above.

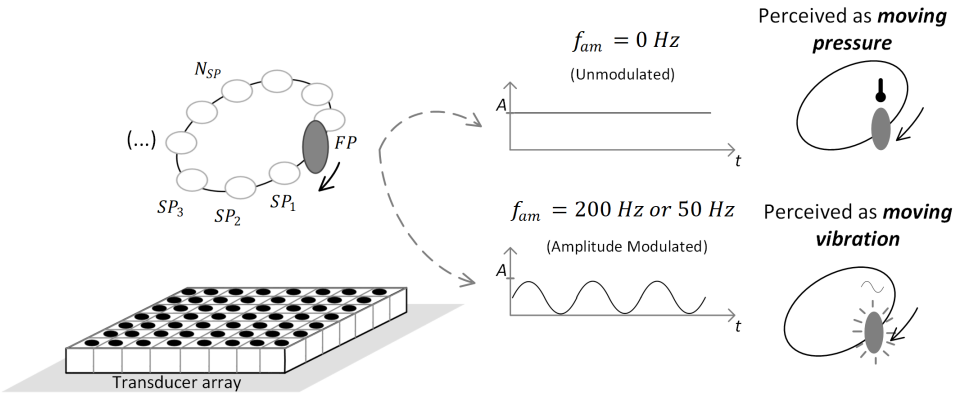

Figure 6.4: Types of dynamic sensations - moving pressure (top) and moving vibration (bottom).

The two haptic dynamic sensation types described so far are fundamentally different at the physiological level. Therefore, it is important to highlight the following point: the sensations referred to as moving pressure and moving vibration are most likely governed by distinct perceptual mechanisms. The specifications developed in the first two sections of this chapter (i.e., those related to v_{max} and N_{max}) are only valid for pressure-based dynamic sensations.

6.6 Overview of the dynamic sensation's specification

The focus of this section is to provide a visual representation of the haptic dynamic sensations defined in this chapter. Figure 6.5 consists of two subfigures (a) and (b), and the analysis begins with Figure 6.5 (a).

In Figure 6.5 (a), two axes are shown: the x-axis represents the length of the pattern (l), and the y-axis represents the speed of the FP (v_{FP}).

The dynamic sensation is defined within the following boundary limits. If l is too short (i.e., $l < l_{min}$), the circular pattern may be perceived as a single FP, and no motion is detected. Conversely, if l is too long (i.e., $l > l_{max}$), the trajectory may not fit within the interaction area (e.g., the palm), making it unuseful.

Regarding the y-axis, which represents v_{FP}, if the speed is too low (i.e., $v_{FP} < v_{min}$), the resulting sensation may not be perceptually meaningful, as no motion is perceived. On the other hand, if v_{FP} is too high (i.e., $v_{FP} > v_{max}$, as specified in Section 6.2), the dynamic sensation transitions into a vibratory sensation, as discussed in Chapter 5.

Within the valid parameter ranges—$l \in [l_{min}, l_{max}]$ and $v_{FP} \in [v_{min}, v_{max}]$—the haptic dynamic sensation is expected to occur.

Proceeding with the analysis of the figure, the focus is now on Figure 6.5 (b). Assuming that the dynamic haptic sensation occurs, it can manifest as four distinct types of sensations. Two axes define these types:

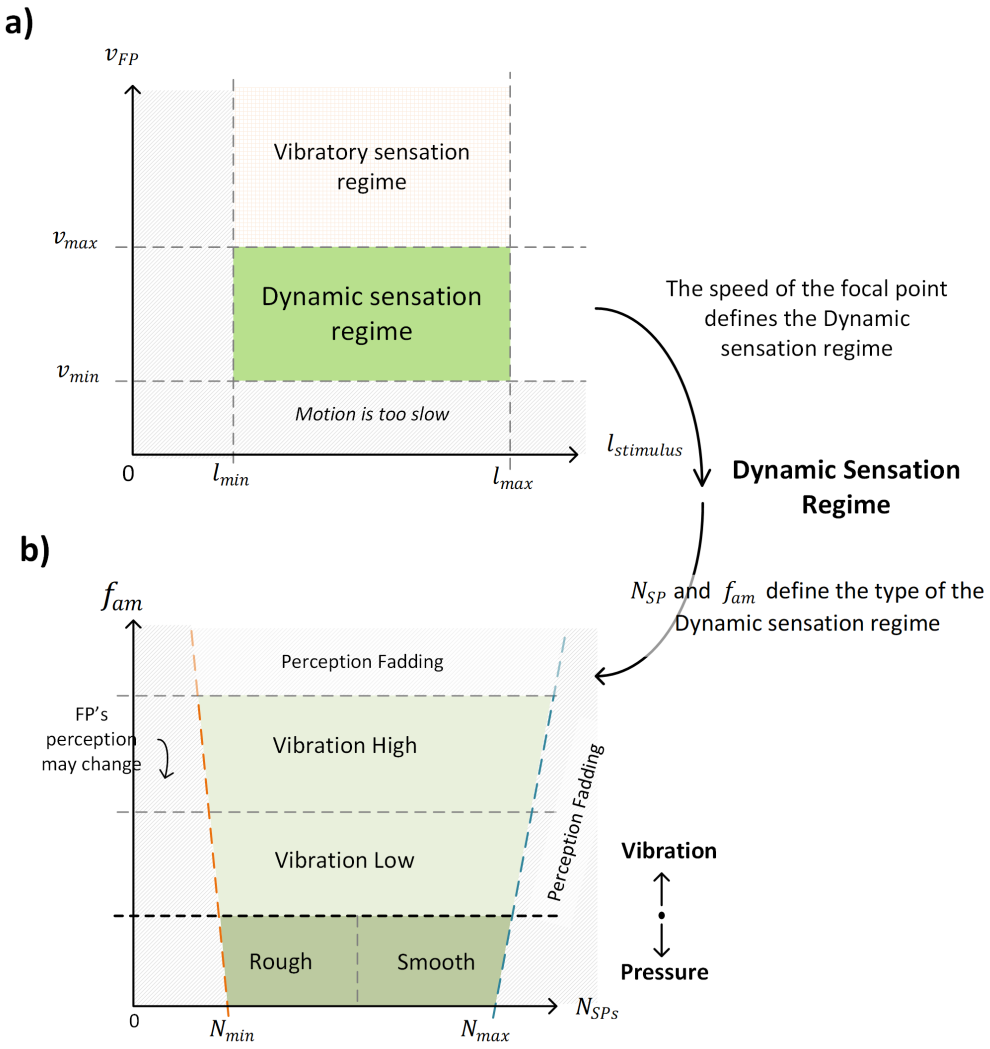

Figure 6.5: The types of haptic dynamic sensation regimes. (Top) Parameter defining the dynamic sensation regime. (Bottom) Parameters defining the type of the dynamic sensation.

the x-axis represents the number of points composing the pattern (N_{SP}), while the y-axis represents the amplitude modulation frequency (f_{am}).

N_{min} denotes the minimum number of SPs that a pattern can have. Based on our experience, N_{min} is typically defined as the minimum number of points required to faithfully represent the shape of the pattern. Its estimation considers the size of the FP (i.e., its diameter, d_{FP}), as follows: $N_{min} \approx l \div d_{FP}$.

When f_{am} is very low (i.e., close or equal to 0 Hz), the resulting sensation is of the pressure type. The SA1 mechanoreceptive system may be predominantly activated in this case. In this scenario, varying N_{SP} leads to two subtypes of sensations:

- A rough sensation, which occurs when N_{SP} is low and is associated with $d_{SP} >\sim 2PDT$;

- A smooth sensation, which occurs when N_{SP} is high and is associated with $d_{SP} <\sim 2PDT$.

As f_{am} increases, the dynamic haptic sensation transitions from pressure to vibrotactile. In this regime, two types of vibrotactile feeling may occur depending on the value of f_{am}:

- High-frequency vibration (f_{am} in the range of 150–250 Hz), where PC mechanoreceptors are predominantly stimulated, and the FP's motion feeling is vibrotactile.
- Low-frequency vibration (f_{am} in the range of 40–50 Hz), where SA1 mechanoreceptors are primarily activated, and the FP's motion feeling may resemble fluter (i.e., light) like vibrations.
- For higher modulation frequencies, the sensation may become imperceptible.

An important observation is that, since pressure and vibrotactile dynamic sensations are likely associated with different mechanoreceptive systems, the perceived size of the FP may vary (as spatial resolution depends on the type of mechanoreceptive system (Cataldo et al., 2023)). Consequently, the minimum number of SPs of the shape (N_{min}) may depend on the type of dynamic sensation. This is represented by the dashed line on the left side of Figure 6.5(b). Similarly, the dashed line on the right represents the corresponding concept for N_{max}.

6.7 Possibilities of optimization for dynamic haptic sensations

The present section aims to provide two possibilities for the creation of optimized haptic dynamic sensations. An optimized haptic sensation is a stimulus that requires less acoustic energy to evoke a percept similar to that of the original stimulus on which it is based. The optimization strategies presented in this section are conceptual and were not subjectively validated. Nevertheless, they represent approaches for improving the efficiency of dynamic haptic sensation.

The two proposed strategies are applicable to dynamic pressure sensations. In such sensations, the duration of each SP (i.e., t_{SP}) typically spans a few tens of milliseconds. These pulse (or shape points) characteristics are essential for implementing the strategies described below.

6.7.1 Optimization Strategy 1

The first optimization strategy for the dynamic sensation is based on a pulse modulation approach described in Gavrilov et al. (1977) (see Section 2.3.2).

The authors report that a long 400 ms pulse is perceptually similar to two shorter pulses (approximately 10–20 ms) separated by a *long* OFF interval (approximately 360–380 ms). For a clearer visualization of these stimuli, refer to Figure 6.6.

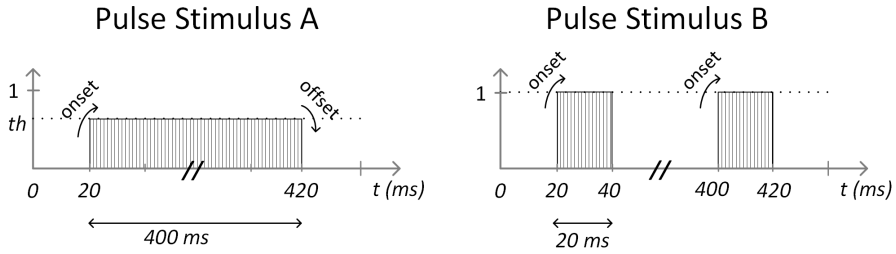

Figure 6.6: Perceptually similar pulses. The pulse stimuli A and B evoke similar sensations.

Figure 6.6 shows two pulse stimuli (A and B). Stimulus A corresponds to a single 400 ms pulse created at threshold intensity (Gavrilov et al., 1977; Gavrilov, 2014), while stimulus B consists of two shorter pulses (in this case, 20 ms) separated by a 360 ms interval.

According to Gavrilov et al. (1977), both stimuli evoke similar perceptual responses. Sensitivity to long pulses (as in A) primarily occurs at the onset and offset of the pulse (i.e., its beginning and end). In contrast, for shorter pulses, the sensation is elicited at each individual pulse onset (as shown in B). Theoretically, the two short pulses in B replicate the sensation of the longer pulse in A.

This perceptual mechanism can be exploited in the context of the pressure-based dynamic sensation. To illustrate this, consider a circular pattern with $l = 157$ mm, composed of 10 SPs and a drawing period (T_{draw}) of 1 s. Thus, each SP has 100 ms duration. Figure 6.7 illustrates the temporal stimulation signal corresponding to the dynamic pressure sensation for this pattern.

Figure 6.7 (a) shows the signal associated with a single SP, which consists of a 100 ms pulse. Figure 6.7 (b) shows this pulse replicated across all SPs of the pattern. Note that the signals are time-shifted to account for the temporal instants at which each SP occurs in the pattern.

Next, the dynamic sensation signal shown in Figure 6.7 is modulated to obtain a perceptually similar stimulation, as described by Gavrilov et al. (1977). The resulting signal is shown in Figure 6.8.

Figure 6.8 (a) shows the signal associated with a single SP. As can be observed, the signal consists of two shorter pulses, each with a duration of $t_p = 20$ ms. Figure 6.8 (b) shows this pulse signal replicated across all SPs of the pattern.

The duration of the short pulses is controlled by the parameter t_p, as defined in Equation 6.8.

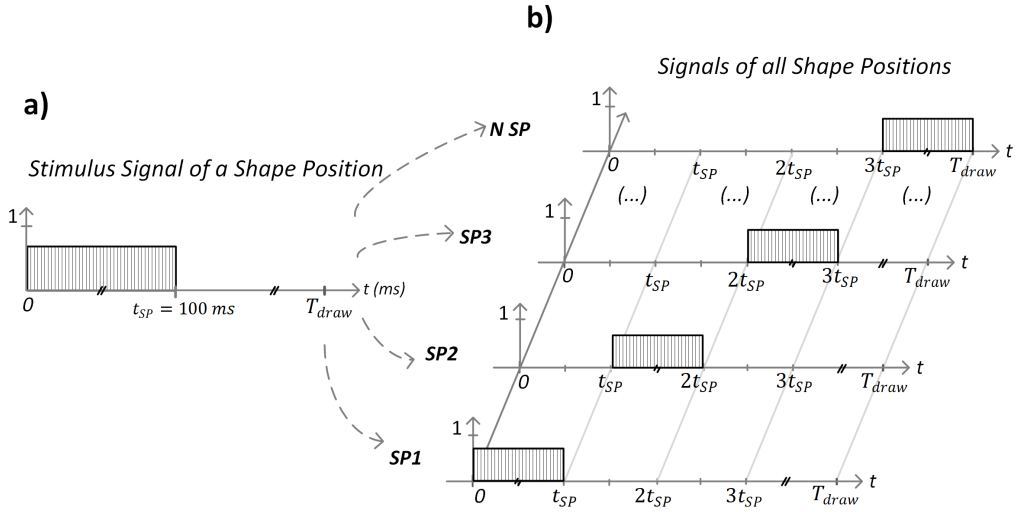

Figure 6.7: Shape point's signal for a dynamic pressure sensation. (a) Pulse signal of a single SP and (b) signals of *all* SPs of the pattern.

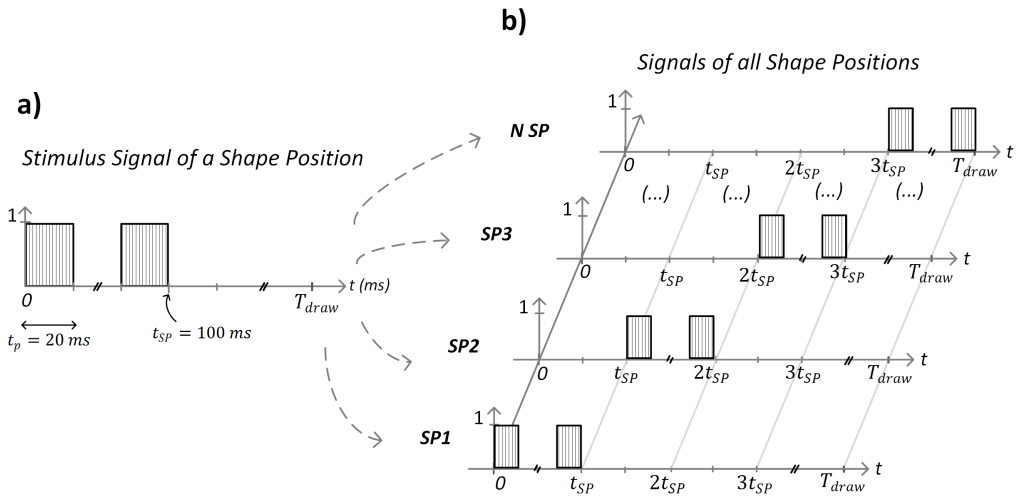

Figure 6.8: Shape point's signal of optimized dynamic pressure sensation. (a) Pulse signal of a single SP and (b) signals of *all* SPs of the pattern.

$$f(t) = \begin{cases} 1, & 0 \leq t < t_p \ \wedge \ t_{SP} - t_p \leq t < t_{SP} \\ 0, & \text{otherwise} \end{cases} \tag{6.8}$$

Care must be taken when specifying the value of t_p. The minimum value should be defined according to the considerations about critical pulse duration outlined in Section 2.3.2.2. Regarding the maximum value, if t_p is too large (e.g., $t_p > 20$ ms), the pulse may no longer be perceived as a single stimulation but rather as two distinct events (corresponding to the onset and offset of the each pulse). This effect alters the perception of the intended original sensation.

6.7.2 Optimization Strategy 2

The second proposed strategy, similarly to the first, aims to exploit a characteristic of touch perception in order to create an optimized dynamic sensation.

Consider Figure 6.9, which shows the SP's signal (a pulse) being modulated, more specifically the duration of the pulse within the SP is varied.

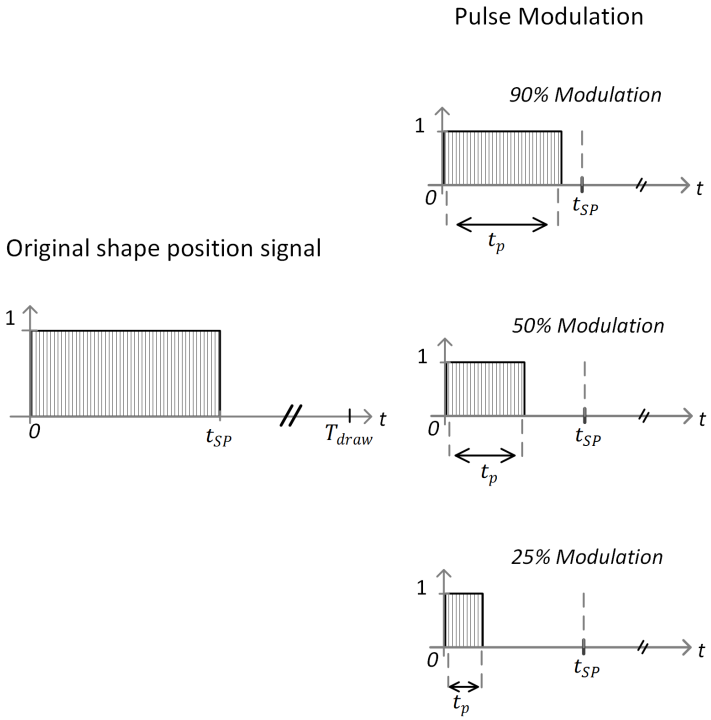

Figure 6.9: Modulation of the pulse signal of the SP.

The analytical description of this *pulse modulation* technique is given by Equation 6.9.

$$f(t) = \begin{cases} 1, & 0 < t \leq t_p \\ 0, & t_p < t \leq t_{SP} \end{cases} \tag{6.9}$$

It is intuitive to assume that shortening the pulse duration will reduce the strength of the haptic sensation. However, consider the following scenario involving a circular pattern ($l = 157$ mm) drawn with a period (T_{draw}) of 1 s. The duration of each SP (i.e., t_{SP}) is 100 ms. Two variants of this pattern are defined:

1. Pattern A is composed of 10 SPs, and each SP is pulse-modulated by 50%. Thus, the active pulse duration (t_p) is 50 ms.

2. Pattern B is composed of 20 SPs and is not pulse-modulated. Therefore, each SP duration (t_{SP}) is also 50 ms.

The Figure 6.10 shows the SP's signals corresponding to pattern variants A and B.

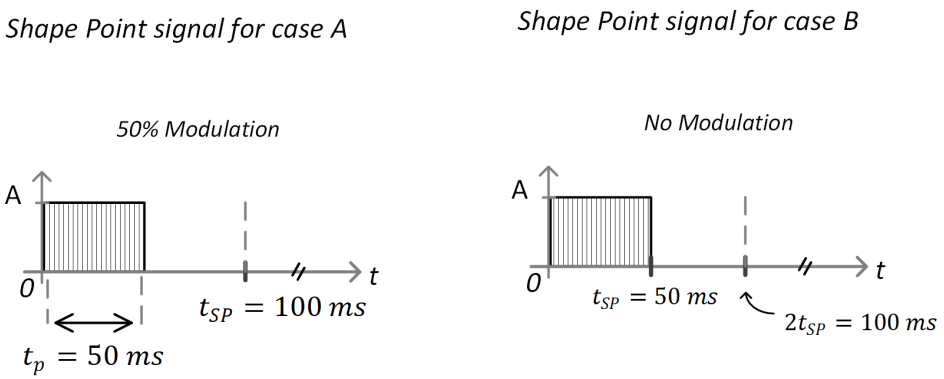

Figure 6.10: SP's signals considered in the perceptual analysis. SP's signal for pattern A is 50% pulse-modulated. SP's signal for pattern B is not pulse-modulated but has half the SP duration of A.

Now discussion will be on the perception of these two stimulation cases for the context of the haptic pressure based, dynamic sensations.

For the case of pattern A, the signal is pulse-modulated at 50%. Consider Figure 6.11. As can be observed, two stimulation events occur per SP: one at $t = 0$ s (when the FP enters the SP) and another at $t = 50$ ms (i.e., t_p, when the FP is turned off). The FP remains inactive until $t = 100$ ms (i.e., t_{SP}), when it jumps to the next SP. This stimulation cycle repeats for all SPs of the pattern.

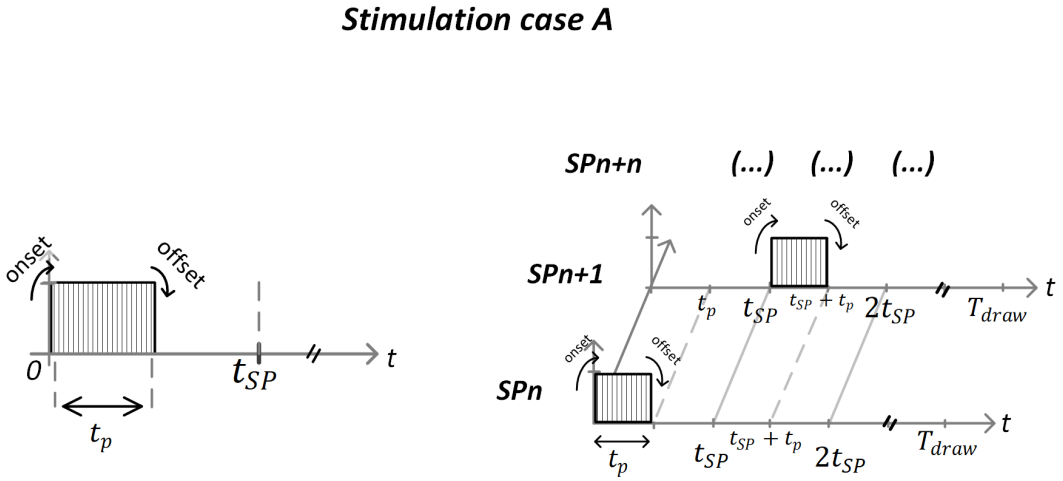

Figure 6.11: Perceptual analysis of stimulus A in the context of the dynamic sensation.

Pattern B, in contrast, is composed of twice the number of N_{SP}s of pattern A. The tactile events occur when the FP enters each SP (i.e., at $t = 0, t_{SP}, 2t_{SP}, \ldots, N_{SP}$). Note that transitions between SPs are *instantaneous* from a tactile perspective. The SP's signal B in the context of the dynamic sensation is illustrated in Figure 6.12.

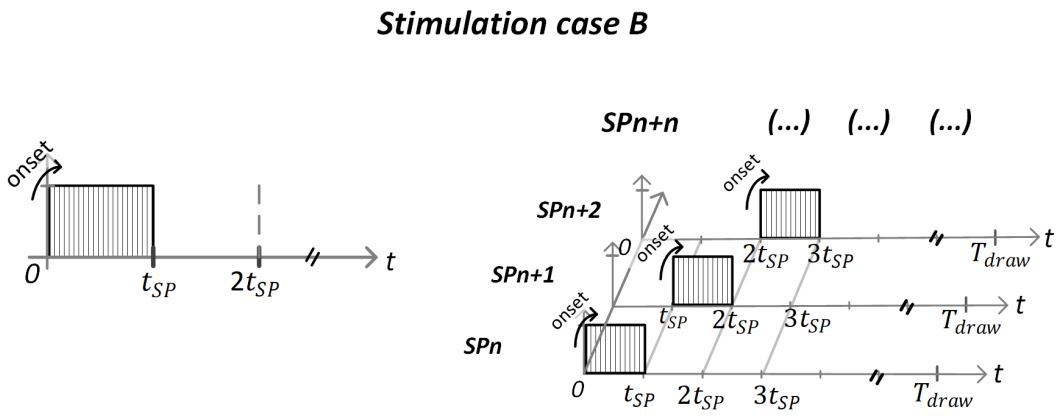

Figure 6.12: Perceptual analysis of stimulus B in the context of the dynamic sensation.

Although it may not be immediately apparent, perceptual cases A and B evoke may similar sensation. To better understand this, consider Figure 6.13, which compares the temporal behavior of both sensations over one drawing period (T_{draw}).

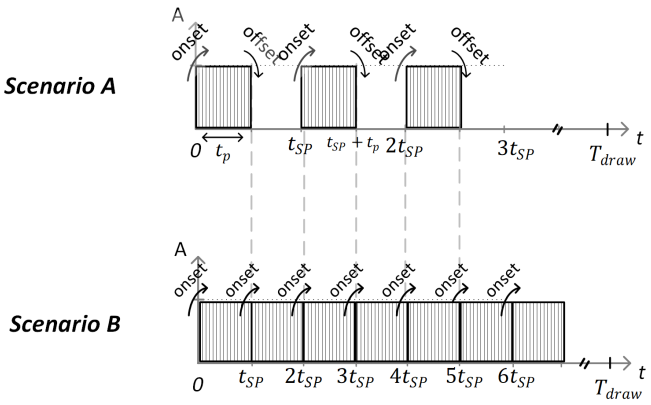

Figure 6.13: Comparison of the sensations for the case A and case B.

For the case of pattern B, the FP is continuously active, with tactile events occurring at regular intervals, as shown in the bottom of Figure 6.13. In contrast, the case A includes inactive periods of stimulation. However, due to the alignment of tactile events in both stimuli, the perceived sensations maybe similar. Importantly, the case A achieves this perceptual equivalence while requiring 50% less energy.

It is important to note, however, that the spatial spacing between SPs differs in both cases. In pattern B, the SPs are spaced at half the distance compared to pattern A (i.e., $d_{SP_B} = d_{SP_A} \div 2$).

6.8 Conclusions

This chapter addresses the specification of the haptic dynamic sensation. Although this sensation was previously introduced in Chapter 5, the specification presented here is tailored to its specific characteristics. Among other parameters, the maximum focal point velocity and the maximum number of positions for a pattern with dynamic properties are defined. Additional factors influencing the characteristics of the dynamic sensation are also analyzed, leading to the identification of four distinct types of sensations. These sensations are summarized in Section 6.7 and can be categorized into two main types: pressure-based dynamic sensation and vibrotactile dynamic sensation. Optimization strategies for the dynamic pressure sensations are presented in the end of the chapter, representing potential approaches for generating optimized haptic sensations.

The specification developed in this chapter for the haptic dynamic sensation was implemented in Matlab and is a core component of the haptic sensation generator tool. The specification acts as an abstraction layer for the tool user, abstracting the parameterization of the haptic stimulus corresponding to the desired haptic dynamic sensation.

Haptic Stimulus Generation Module

7.1 Context

The present chapter focuses on haptic stimuli generator module based on the STM. This module requires the STM parameters of the haptic stimuli and produces the signals to drive the UMAH system. The haptic stimuli generator module was implemented in Matlab.

This component is particularly relevant because it automates the generation of STM haptic sensations discussed in Chapter 5 and Chapter 6. By enabling users with different levels of expertise to easily create STM haptic sensations—whether for perceptual studies or experimental purposes—this component lowers the barrier for UX designers.

The chapter is organized as follows. A brief state-of-the-art review of stimulus generators is first presented. Then, in the next section—which can be considered the core of the chapter—the implemented algorithm for the stimulus generator is described. The algorithm is initially introduced at a high level and subsequently analyzed in detail. The technical challenges encountered during implementation are discussed in a following section. Additional sections are dedicated to the creation of combined haptic stimuli (i.e., involving more than one FP) and to the phase discontinuity problem.

7.1.1 Tool Overview

The haptic stimuli generator module discussed in this chapter is part of the haptic sensation tool currently being developed. Another component of the tool is the sensation abstraction layer discussed in the previous chapter. Moreover, the acoustic simulator (results shown in Chapter 8) allow the visualization of the haptic sensations generated by the tool, and thus to validate the signals produced by the haptic stimuli generator module.

As mentioned, the haptic sensation tool is currently being developed. The three main components are already finished, the sensation abstraction layer (discussed in Chapter 6), the haptic stimuli generator module (the topic of the current chapter), and acoustic simulator presented in Section 4.2. The simulator was integrated into the tool, and provided the simulation results discussed in Chapter 8.

7.2 State-of-the-art

In the context of UMAH, three main tools for haptic stimulus design are currently available. Among their various components, these tools implement algorithms for generating the stimulus signals that drive the haptic device and produce the intended haptic stimuli. The Sensation Designer (Ultraleap, 2026) is a proprietary tool developed by Ultraleap and is accessible only with the purchase of their ultrasonic haptic systems. The Feellustrator design tool (Seifi et al., 2023) is also closed-source but freely available and can be considered a semi-professional stimuli design tool. It was developed based on requirements

established by experienced mid-air haptic designers and is therefore intuitive, feature-rich, and suitable for a wide range of applications and UX levels. Lastly, the Dolphin stimulus design framework (Mulot et al., 2021) is an open-source tool specifically developed for psychophysical experiments.

In general, these tools share several common components or modules, including: i) a stimulus generator component (such as the one discussed in this chapter); ii) a field simulator used for visualization and debugging of the generated haptic stimulus; iii) a communication component responsible for interfacing with the ultrasonic haptic system (which physically produces the stimuli); iv) additional functionalities such as sensation libraries, stimulus import/export features, and integration with third-party tools; and v) a graphical user interface that integrates all components. These tools are typically designed to be intuitive and easy to use, while still offering advanced configuration options for haptic stimulus design.

The central component in this discussion is the haptic stimulus generator module. It is responsible for configuring the spatial aspects of the stimulus, such as the shape of the pattern and the distribution of shape points. Additionally, it defines the temporal aspects of the stimulus, including the FP's amplitude (f_{am}), the duration of the SPs (t_{SP}), and the overall drawing period (T_{draw}). Ultimately, the module generates the signals corresponding to the configured STM haptic stimulus.

Both the Sensation Designer and Feellustrator are closed-source tools. Nevertheless, Feellustrator employs a canvas-based interface for defining the spatial pattern, allowing users to freely position SPs. A separate interface is used to define the temporal behavior of the stimulus, including SP durations and the FP's amplitude, which can be controlled with high precision. However, implementation details regarding how the stimulus signals are generated are not publicly available.

In contrast, the Dolphin framework is open source and provides insight into how stimulus signals are generated. In this framework, a haptic stimulus is described by two main aspects. The first is the spatial component, which defines the pattern geometry and its position in space. The second is the spatial strategy, which governs both spatial sampling (i.e., how SPs are distributed along the pattern) and temporal evolution (i.e., the order and duration of SPs) (Mulot et al., 2021). The temporal evolution also includes the variation of the FP's amplitude over time. More specifically, the authors define the sampling order as a finite sequence and assign a dwell time to each SP. By combining this information with an amplitude overlay and the spatial position of each SP, the system determines the signal configuration—both amplitude and phase—at each time step. Three sampling strategies are implemented: one follows a traditional STM approach with evenly distributed SPs and fixed step size (d_{SP}), while two additional strategies provide explicit control over sampling order and SP duration.

The fundamental distinction of the haptic tool developed in this work lies in its focus on generating STM haptic sensations rather than arbitrary stimuli. Sensations evoke specific perceptual responses, whereas arbitrary stimuli may not. This distinction motivates, for example, the inclusion of features such as support

for combined sensations, which are not commonly found in existing tools. Furthermore, the sensation abstraction layer developed in Chapter 6 can be used as an intermediate layer for generating meaningful haptic sensations.

Additionally, the proposed generator includes a method for smoothing phase transitions between transducers, thereby reducing noise caused by abrupt phase changes—a common issue in UMAH systems. Finally, the haptic stimulus generator module, as well as the overall tool, is fully described in this PhD thesis and will be made available online as open-source software.

7.3 Algorithm

The present section discusses the algorithm implementing the stimulus generation module responsible for generating the STM signals. Throughout the chapter, the terms stimuli and patterns are used interchangeably.

7.3.1 Spatiotemporal signal's components

A circular pattern is depicted in Figure 7.1 (top of the figure) and consists of a constant-amplitude FP traveling along the SPs of the shape. The spatial component of the haptic pattern corresponds to the positions traveled by the FP (i.e., the SPs). These define the shape of the pattern and other spatial characteristics. Moreover, the temporal component is defined by the amplitude of the FP over time. In this case, the FP's amplitude is constant; however, as mentioned in Chapter 6, it can be temporally modulated to create diversified haptic sensations.

The haptic pattern is created by the ultrasonic haptic phased array, which is driven by properly calculated signals, as illustrated at the bottom of Figure 7.1. The position of the FP is controlled by the phases of the ultrasonic transducers (as explained in Section 2.1), while the FP's amplitude is directly related to the amplitude of the emitting transducers.

The STM signal is the combination of two independent components: the spatial component, which defines the phases of the ultrasonic transducers (φ_{ab}), and the temporal component, which defines the amplitude of the emitting transducers ($A_{ab}(t)$). The variables a and b represent the row and column of the transducer in the haptic array and range from 1 to N_{source} (i.e., the number of transducers per row or column in the array).

For a better understanding of the spatial and temporal components of the STM signal, consider the case of a single SP, as shown in Figure 7.2.

The SP's signal (u_n) is composed of a temporal component ($A_n(t)$) and a spatial component ($\varphi_{n,ab}$). The

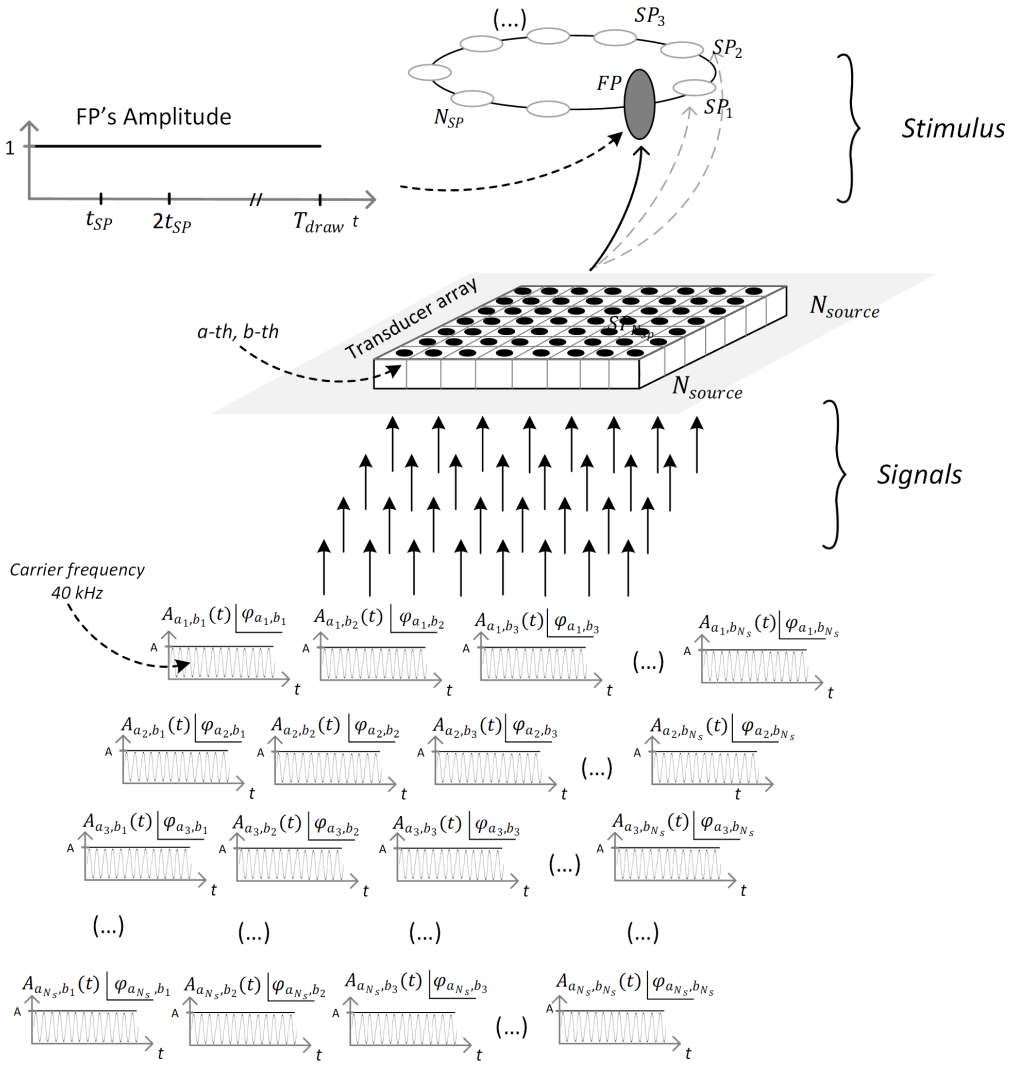

Figure 7.1: Spatiotemporal haptic stimulus and the signals involved in its creation.

spatial part represents the SP's location and is defined by the individual phases of the transducers (a, b), more precisely $\varphi_{n,ab}$. The variable n represents the SP index and varies from 1 to N_{SP} (i.e., the total number of SPs in the pattern).

The temporal signal specifies the amplitude behavior for that SP and is represented by $A_n(t)$. In the pattern under analysis, the FP's amplitude is constant throughout its duration; thus, for a single SP, $A_n(t)$ can be interpreted as a pulse with duration t_{SP}.

Let us now further analyze the STM signal over the full pattern duration. To that end, consider Figure 7.3, which illustrates the motion of the FP across time and space.

The temporal and spatial components are represented along distinct axes, resulting in the helix-shaped representation in Figure 7.3. The temporal axis is vertical, showing that the FP visits a new SP every t_{SP} seconds and completes the pattern in T_{draw} seconds. The spatial dimension is represented in the x–y

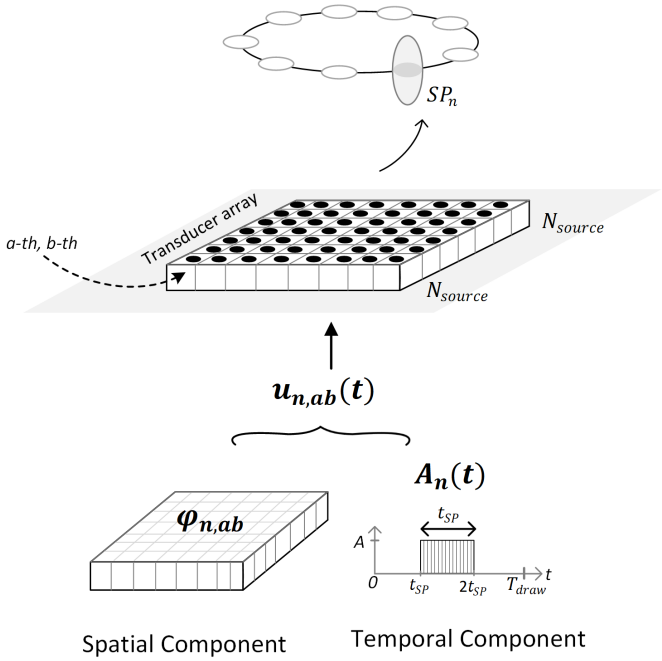

Figure 7.2: The spatial and temporal components of the SP's signal.

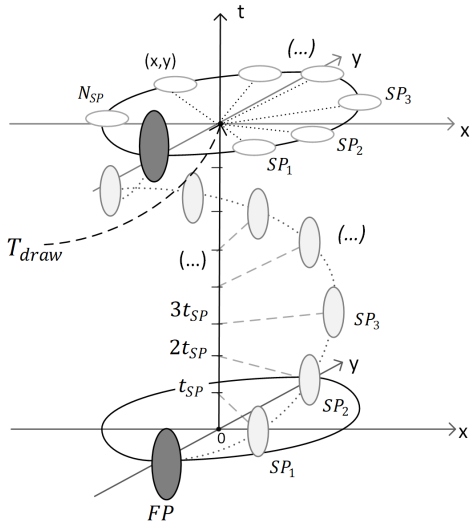

Figure 7.3: Discretization of the haptic pattern in time and space dimensions.

plane, where each SP is defined by an (x, y) position.

As previously explained, each SP signal consists of spatial and temporal components that can be handled independently. For the complete pattern, these components are generated individually for all SPs.

Figure 7.4 shows the spatial signal for the complete pattern. The lower part of the figure illustrates all phase configurations required to generate all the SPs of the pattern. For instance, $\varphi_{1,ab}$ corresponds to the first SP, $\varphi_{2,ab}$ to the second, and so on.

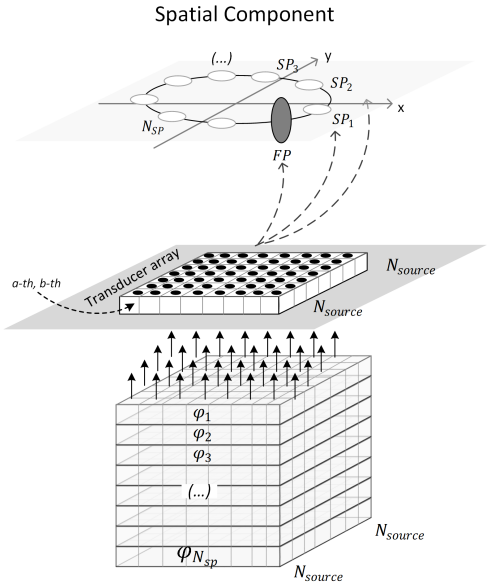

Figure 7.4: Illustration of the spatial signals for the SPs of the pattern.

The temporal component of the pattern is illustrated in Figure 7.5. It defines the amplitude behavior of the FP over the entire pattern duration. In this case, the amplitude is constant, and therefore all SP signals are identical.

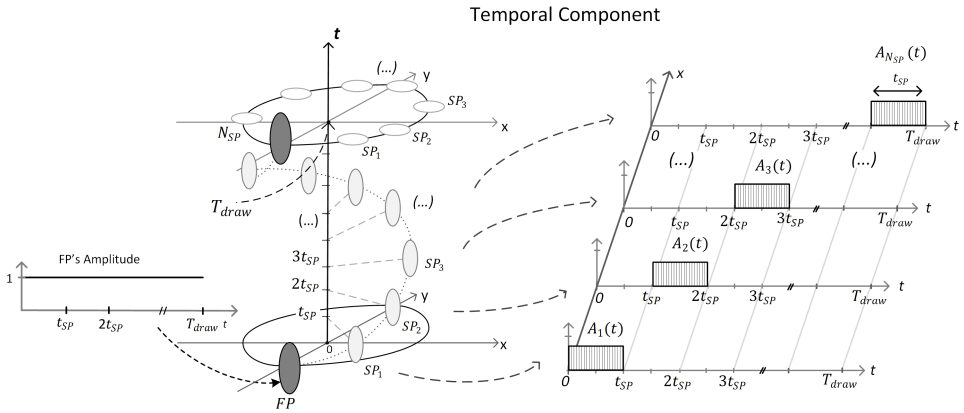

Figure 7.5: Illustration of the temporal signals for the SPs of the pattern.

The SP signals are shown in more detail on the rightmost side of Figure 7.5. For simplicity, the spatial dimension is represented along a single axis. Each signal corresponds to a pulse of duration t_{SP}, and the pulses are time-shifted according to their occurrence in the pattern.

To construct the complete STM signal, the spatial and temporal components of each SP are combined through complex multiplication, as shown in Figure 7.6. The amplitude of the exponential corresponds to the temporal component, while the phase encodes the spatial information. This results in signals such as $u_1(t)$ and $u_2(t)$ for each SP.

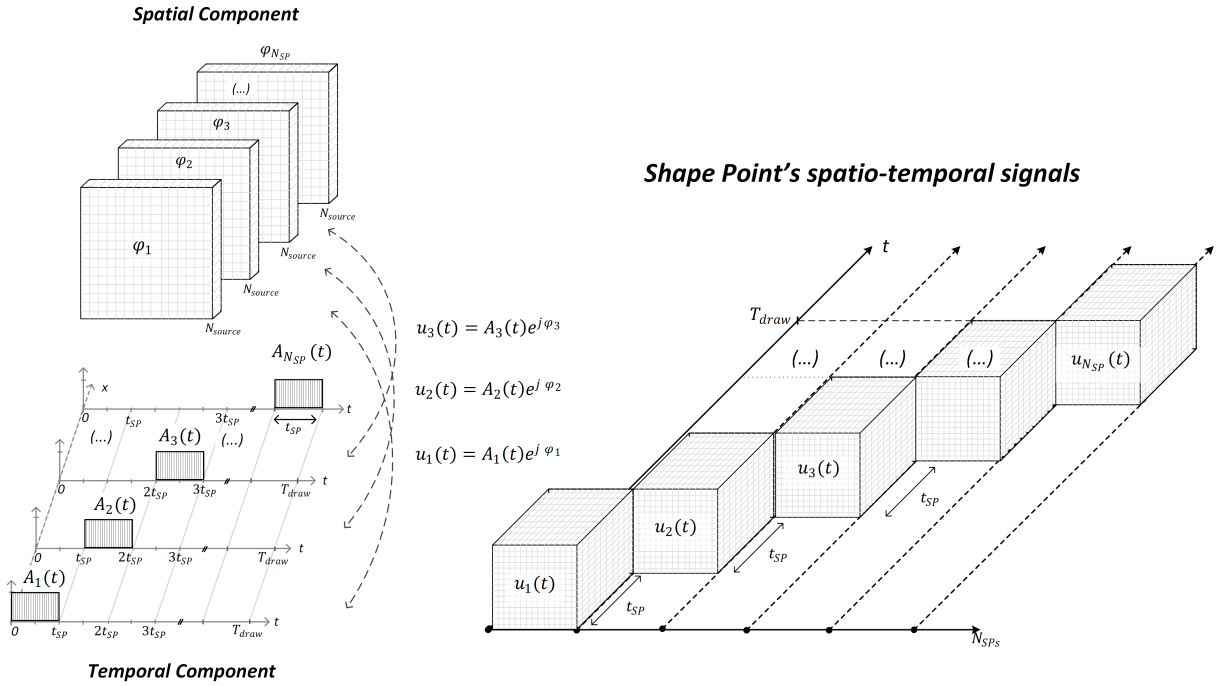

Figure 7.6: Creation of the SPs' signals.

Figure 7.7 shows the final STM signal. The temporal components are properly time-shifted over the full pattern's duration (T_{draw}), ensuring no overlap between SP signals. The final signal $u(t)$ is obtained by summing all individual signals ($u_1, u_2, \ldots$), fully encoding the spatiotemporal behavior of the haptic pattern.

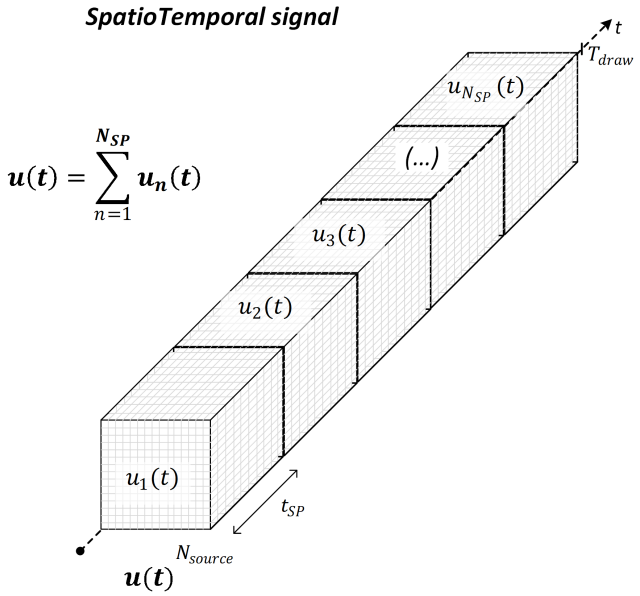

Figure 7.7: Illustration of the haptic pattern spatiotemporal signal, as a summation of the composing SPs' signals.

7.3.2 Analytical description

An overview of the algorithm has been explained and graphically illustrated so far. The remainder of this section focuses on describing mathematically the STM haptic signal. The signal of the n-th SP is represented by the following expression:

$$u_{n,ab}(t) = A_n(t)\, e^{j\left(\omega_c t + \varphi_{n,ab}\right)}, \tag{7.1}$$

$$t \in [nt_{SP}, (n+1)t_{SP}[,\ n \in [1, N_{SP}],\ a, b \in [1, N_{source}]$$

The n is the SP number and $n \in [1, N_{SP}]$, where N_{SP} is the number of SPs composing the pattern (as defined in Table 3.1). $A_n(t)$ is the amplitude (temporal signal) of the n-th SP. Since the signal is defined at the SP level, its duration is t_{SP} seconds and is defined over $t \in [nt_{SP}, (n+1)t_{SP}[$.

The spatial component of the n-th SP is $\varphi_{n,ab}$, corresponding to the phases required for its creation in space. The variables a and b represent the row and column indices of the ultrasonic transducer in the haptic array and vary from 1 to N_{source}. Here, N_{source} is the number of transducers per row (or column) of the square array. The imaginary unit satisfies $j^2 = -1$, and ω_c is the angular frequency ($\omega_c = 2\pi f_c$), where f_c is the carrier frequency (e.g., 40 kHz).

The term ω_c is associated with the carrier frequency of the ultrasonic transducers. In the current implementation, this frequency is not generated by the generator module, as it is handled by the internal hardware of the UMAH system. Therefore, the ω_c term can be omitted, and the expression simplifies to:

$$u_{n,ab}(t) = A_n(t)\, e^{j\varphi_{n,ab}}, \tag{7.2}$$

$$t \in [nt_{SP}, (n+1)t_{SP}[,\ n \in [1, N_{SP}],\ a, b \in [1, N_{source}]$$

The complete STM signal of the pattern corresponds to the sum of all time-shifted SP signals. Thus, the complete STM signal $u_{a,b}(t)$ is given by:

$$u_{a,b}(t) = \sum_{n=1}^{N_{SP}} u_n(t - (n-1)t_{SP}) = \sum_{n=1}^{N_{SP}} A_n(t - (n-1)t_{SP})\, e^{j\varphi_{n,ab}}, \tag{7.3}$$

$$t \in [0, T_{draw}],\ n \in [1, N_{SP}],\ a, b \in [1, N_{source}]$$

Since $u_{a,b}(t)$ represents the complete haptic spatio-temporal stimulus, it is defined over the entire duration $t \in [0, T_{draw}]$. The temporal components are time-shifted to avoid overlap, ensuring that the information from each SP is preserved.

7.3.3 Temporal component

In the beginning of the chapter, the general approach for generating STM haptic signals was introduced. This section focuses on the implementation of the temporal component. For clarity, only haptic dynamic sensations are considered (see Chapter 6), although the method here described can be generalized for all haptic spatiotemporal stimuli.

So far, constant amplitude stimuli ($A(t) = 1$) have been considered. However, the temporal signal can be modulated. Two practical cases are considered: dynamic pressure (constant amplitude) and vibrotactile (sinusoidal amplitude modulation), as discussed in Section 6.5.

The first step is the generation of a temporal reference signal, which defines the stimulation behavior over the entire duration. Figure 7.8 shows examples for both cases.

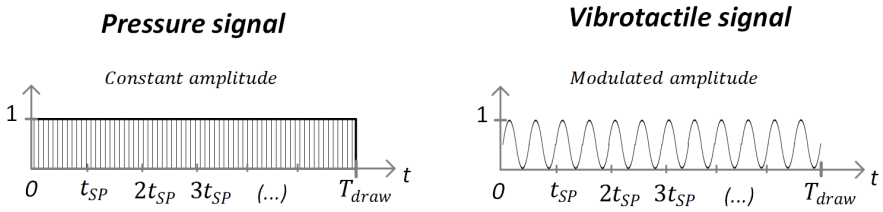

Figure 7.8: Amplitude modulation scenarios considered for the temporal reference signal.

The reference signal is used to generate the SP's temporal signals. A window signal $w(t)$ is defined as a pulse of duration t_{SP}, centered at $t = 0$, as shown in Figure 7.9.

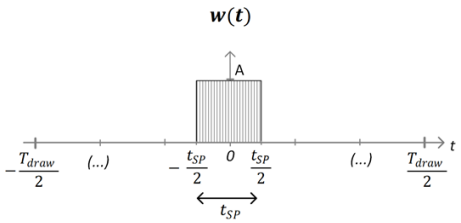

Figure 7.9: Window signal used in the generation of the SP's temporal signals.

The window slides over the reference signal to *extract* each SP's temporal information, as illustrated in Figure 7.10.

The window signal is generated by convolving $w(t)$ with time-shifted impulses corresponding to the SP occurrence instants in the pattern, as shown in Figure 7.11.

The convolution of $w(t)$ with $\delta(t - t_0)$ produces a shifted window $w(t - t_0)$. This basic convolution operation is illustrated in Figure 7.12.

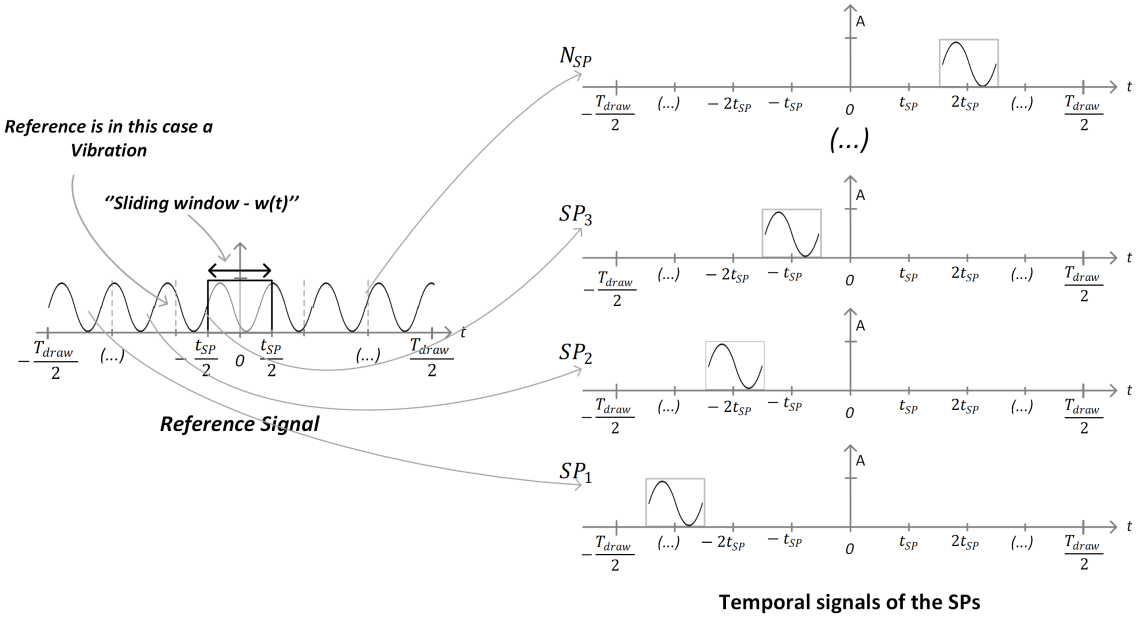

Figure 7.10: Sliding window approach for generating SP's temporal signals.

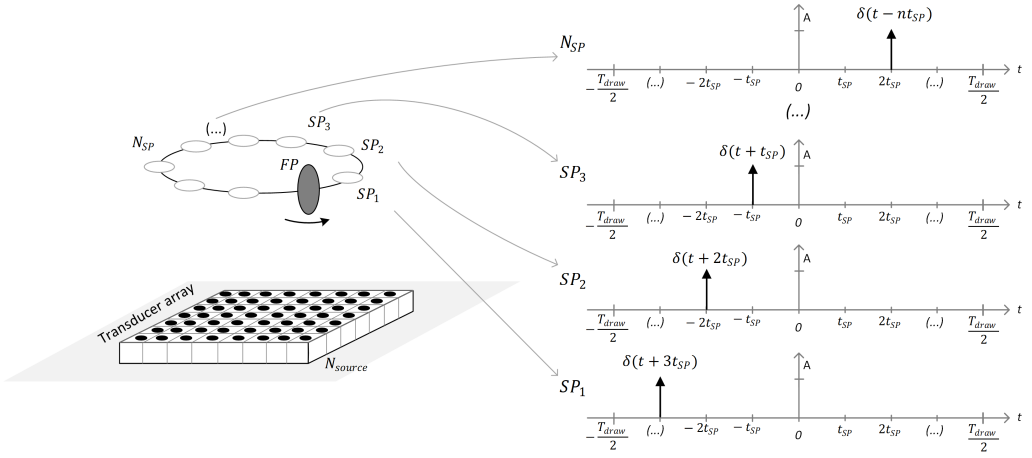

Figure 7.11: Occurrence time instants of the SPs of the patterns, encoded by shifted impulses.

Repeating this process yields a set of shifted windows aligned with the occurence instants of each SPs of the pattern, as shown in Figure 7.13.

Multiplying these shifted windows by the reference signal yields the temporal signals for all SPs of the pattern, as shown in Figure 7.14.

7.3.4 Spatial component

The spatial component consists of the haptic arrays' phase distributions that define the SP's positions of the pattern.

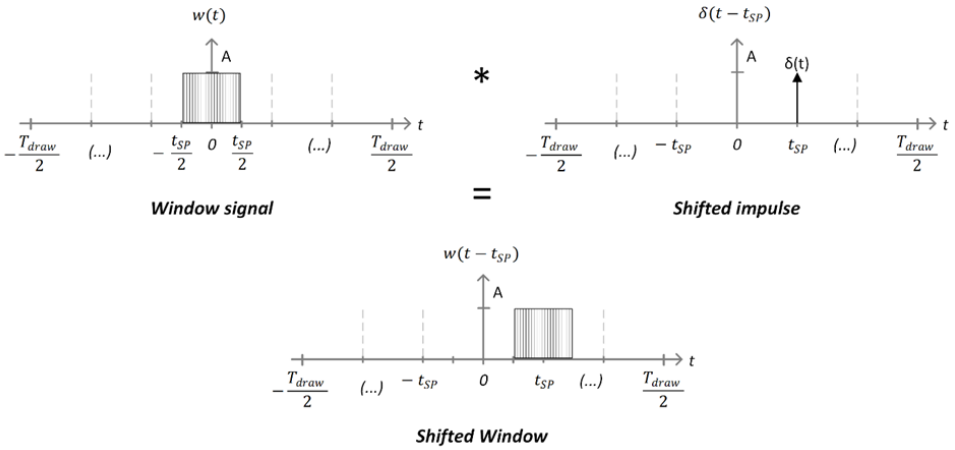

Figure 7.12: Shifted window obtained through convolution.

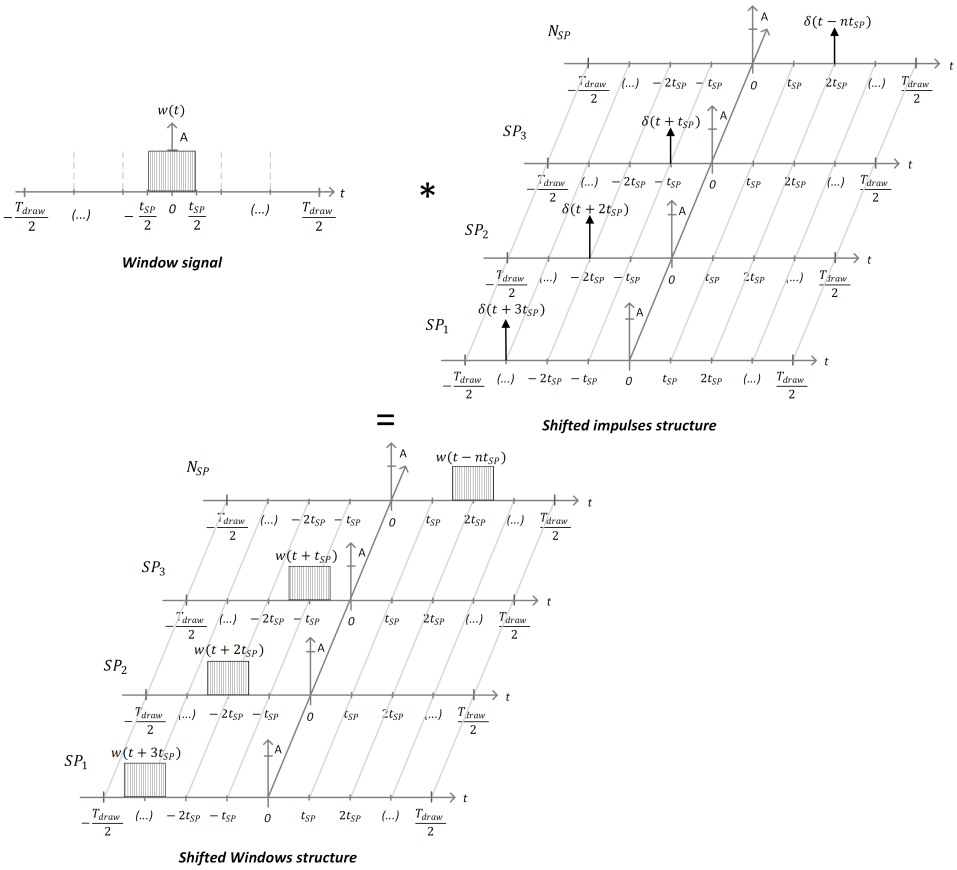

Figure 7.13: Time-shifted windows associated with the temporal occurrence of the SPs of the pattern.

A spatial reference signal $\varphi_{ref,ab}$ defines a reference FP, as shown in Figure 7.15. This serves as a basis for generating all other SPs of the haptic pattern.

Spatial convolution is used to generate shifted versions of the reference FP, corresponding to the different SP positions of the haptic pattern, as shown in Figure 7.16.

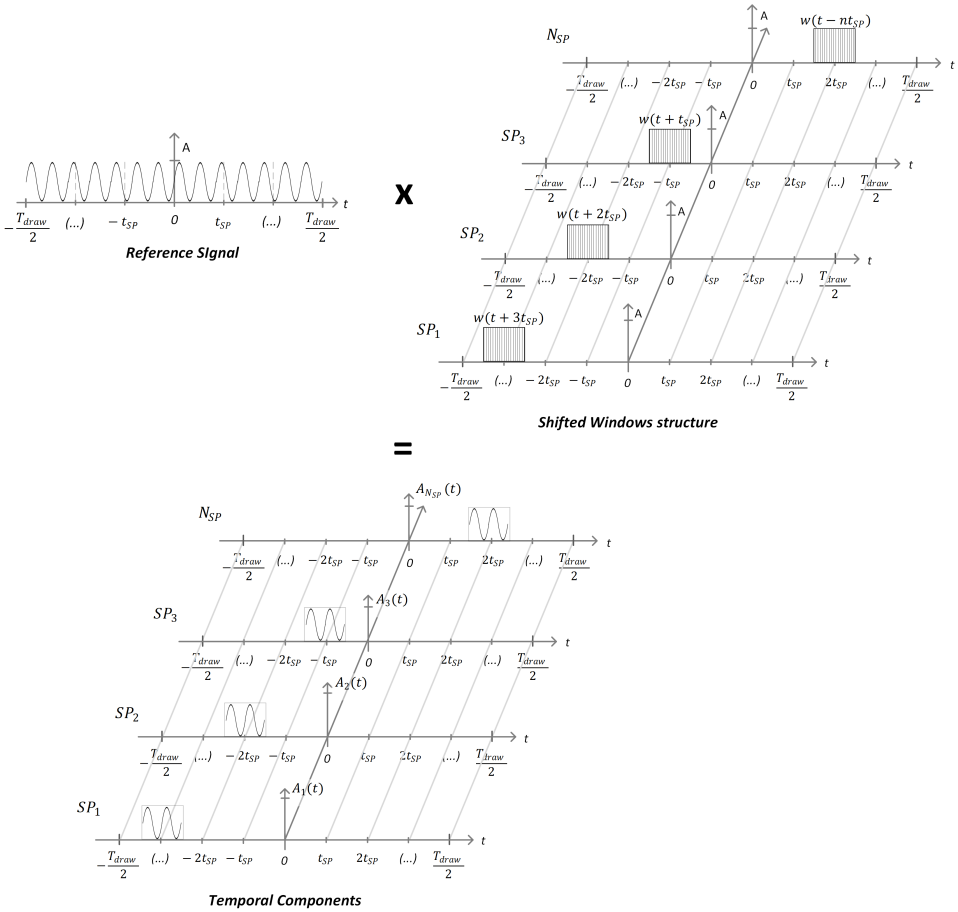

Figure 7.14: SP's temporal signals of the pattern obtained from windowing approach.

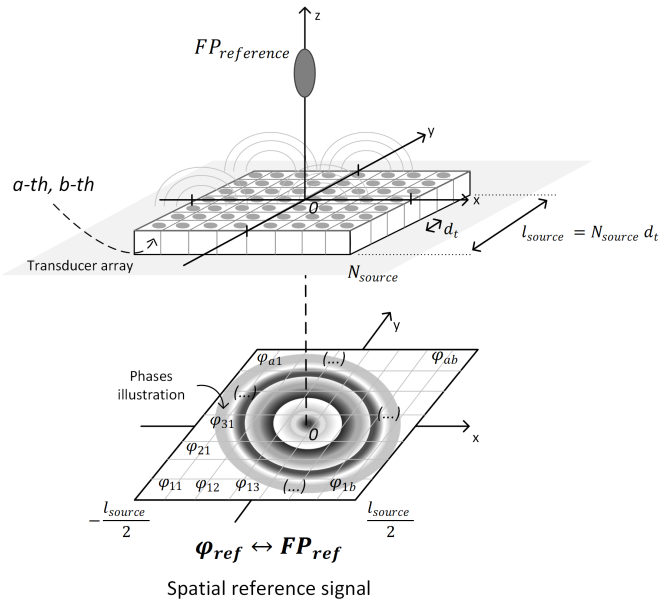

Figure 7.15: Spatial reference signal and corresponding FP generation.

The positions of all SPs of the pattern are encoded using spatially shifted impulses, as illustrated in

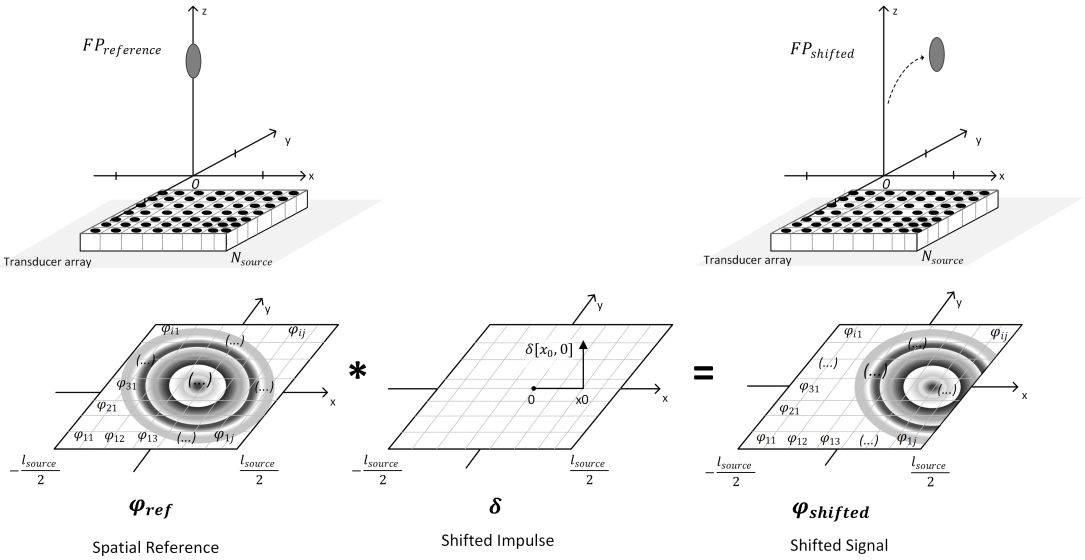

Figure 7.16: Spatial convolution for generating SP's phases.

Figure 7.17.

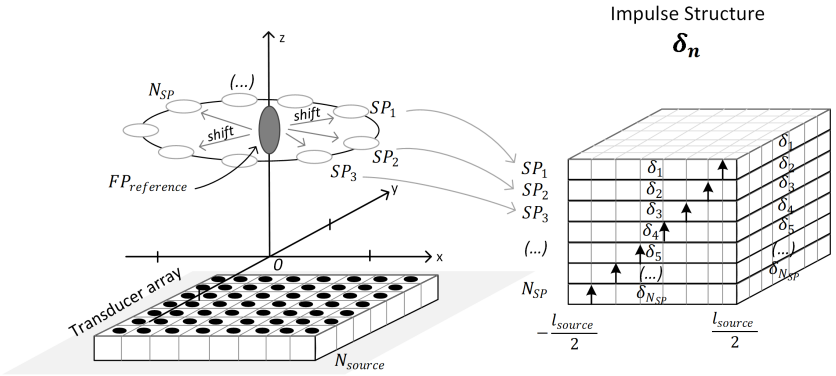

Figure 7.17: SP positions of the pattern represented as spatial shifted impulses.

Convolution of these impulses with the spatial reference signal (i.e., the FP's reference) yields the phase distributions for each SP of the pattern. The resulting structure represents the spatial component of the spatio-temporal stimulus, as shown in Figure 7.18.

7.4 Technical challenges

The approach for generating the haptic stimulus spatial component faced difficulties in its implementation. These will be the focus of this section and the first difficulty is related to the resolution of the FP's movement.

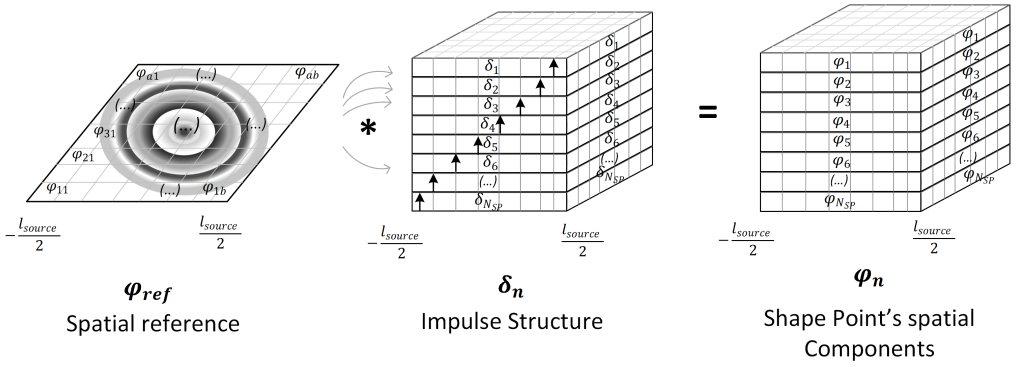

Figure 7.18: Spatial component obtained via convolution.

7.4.1 Resolution of the Focal Point's movement

The spatial shifting method (described in the previous section) involves the convolution of the reference signal (i.e., FP's reference) with a spatially shifted impulse signal. The resolution of the FP's movement is directly related to the spatial resolution of those signals (i.e., the spatial discretization step of the convolved signals). The reference signal represents the set of phases of the ultrasonic transducers in the haptic array, responsible for creating a reference FP. For the UMAH system developed (see Chapter 4), the haptic array consists of 16×16 transducers with an inter-element spacing (d_t) of approximately 1 cm. This spacing determines the spatial resolution of the FP's movement.

The motion resolution of a STM haptic pattern is directly related to the number of SPs composing the pattern (N_{SP}). Specifically, the resolution is given by Equation 3.5 and, in many cases, exceeds 1 cm. To overcome this limitation, the spatial discretization resolution of the signals used in the convolution must be increased.

Consider, therefore, a new reference signal with higher spatial resolution (i.e., inter-element spacing $d_t <$ 1 cm). This signal is referred to as the virtual reference signal. It was generated with a spatial step of 1 mm, allowing the FP movement to achieve a spatial resolution of 1 mm, which is sufficient for most practical cases.

Figure 7.19 illustrates this concept. A spatial reference signal ($\varphi_{ref-real}$) with the resolution of the real system ($d_t \sim 1$ cm) is insufficient to produce high-acuity haptic pattern. To address this, a virtual reference signal ($\varphi_{ref-virtual}$) is used to assist in generating the pattern's spatial component, enabling pattern creation with up to 1 mm spatial resolution (i.e., d_{SP} of 1 mm).

Note that the virtual array has a higher number of 'virtual' transducers (defined by $N_{virtual}$). Although only the reference signal was discussed, the same procedure must also be applied to the other convolved signal (i.e., shifted impulse).

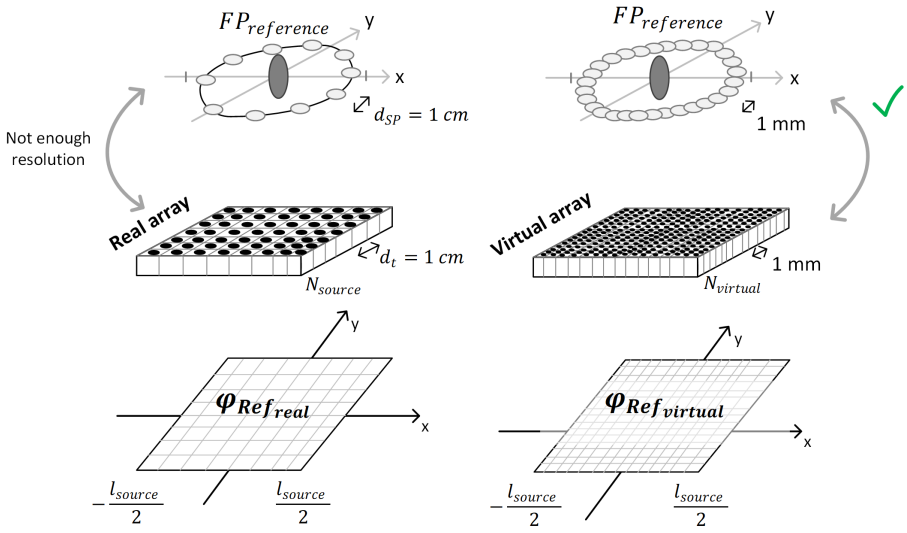

Figure 7.19: Representation of the 'real' and 'virtual' reference signals.

7.4.2 Convolution computational shortcoming

Another difficulty arises in the implementation of the spatial component. As previously discussed, convolution with a shifted impulse produces a shifted version of the original signal. However, when implemented computationally, the resulting signal may contain null regions, as illustrated in Figure 7.20. In practice, this means that some transducers would be assigned null phases, preventing effective FP generation.

The signals involved in the convolution have the same size, defined by l_{source} (related to the number of transducers N_{source}). When convolving the reference phase signal with an impulse shifted by x_0, the resulting signal contains a null region.

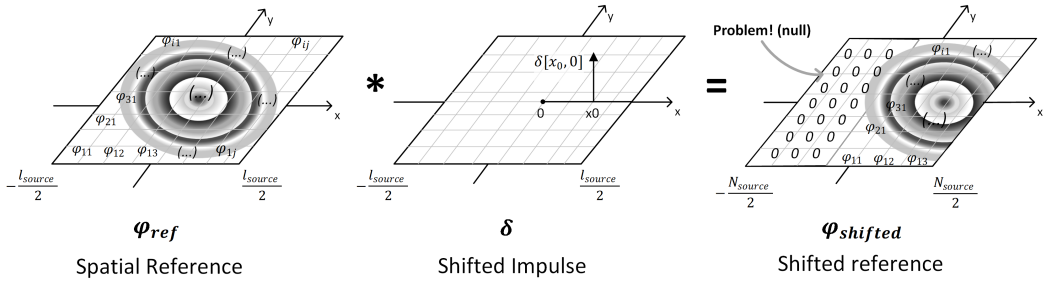

Figure 7.20: Illustration of the computational convolution shortcoming.

To mitigate this issue, the signal size is increased from l_{source} to $l_{virtual}$. The virtual signal must be sufficiently large to ensure correct generation of the SP phases. Figure 7.21 illustrates this approach.

By increasing the signal's size to $l_{virtual}$, the null-region issue is resolved. The resulting shifted signal $\varphi_{shifted}(x, y)$ now contains valid phase information within the region of interest (l_{source}).

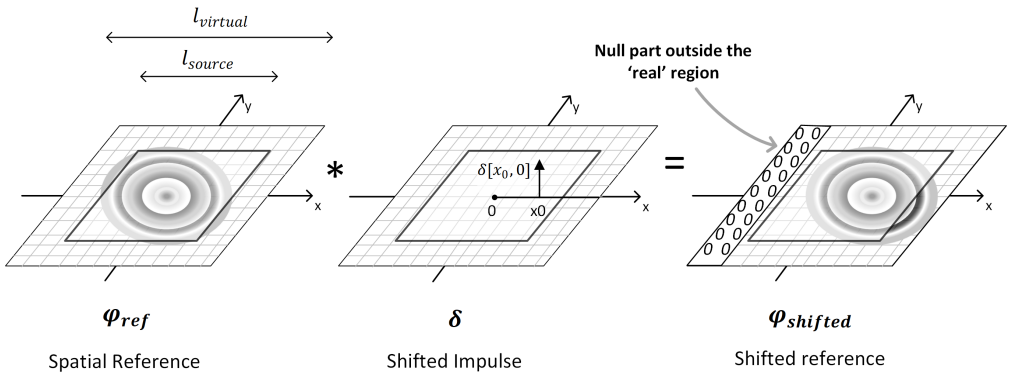

Figure 7.21: Convolution limitation overcoming by increasing signal dimensions.

The shifted signal obtained from convolution has resolution $N_{virtual}$ and size $l_{virtual}$, and thus cannot directly drive the ultrasonic transducer's haptic array (which has only 16×16 transducers). Therefore, the relevant phase values must be extracted from the virtual signal by mapping them to the positions of the real transducers.

This matching process is performed for all SP's spatial signals. The resulting signals are free from both the spatial resolution limitation and the convolution artifact discussed previously.

In summary, two main challenges were addressed in the implementation of the spatial component: the limited spatial resolution of FP's movement and the computational limitation of convolution with shifted impulses. Both issues were resolved through the use of virtual representations with higher spatial resolution and larger spatial extent.

7.5 Combined haptic patterns

So far, the algorithm discussed during this chapter has only considered the generation of a single FP. However, as shown in the research study of Chapter 5, a haptic pattern can be composed of more than one haptic sensation. In this section, the generation algorithm for creating haptic patterns with several FPs combined is explained.

The UMAH system is linear, meaning that the response to the sum of multiple inputs is equal to the sum of the responses produced by each input individually. As can be observed through Figure 7.22, input 1 generates the acoustic field for FP 1, and input 2 creates the acoustic field for FP 2. By summing both fields, the resulting field contains both FPs combined.

Figure 7.23 presents the summation of two spatio-temporal signals from a more technical perspective. Two distinct sensations are considered: (1) a dynamic pressure sensation (left) and (2) a dynamic vibration sensation (right). The corresponding STM signals are shown beneath each haptic array. By summing the

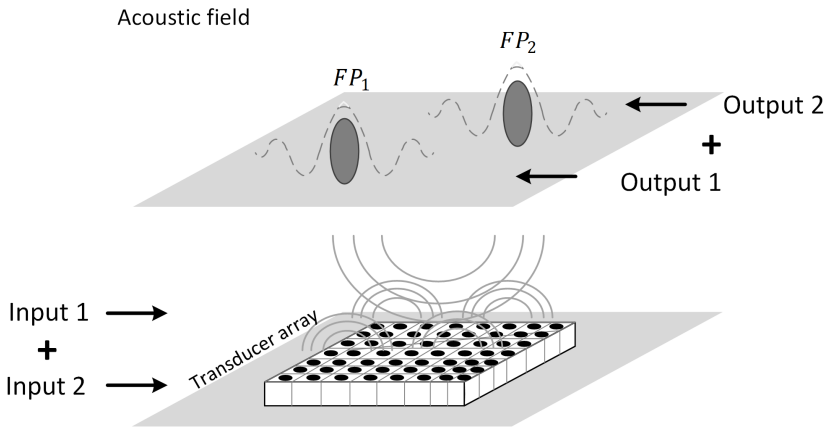

Figure 7.22: Creation of multiple FPs by means of the linearity property of the UMAH system.

STM signals (u_1 and u_2, sample-wise), a new haptic stimulus ($u_{combined}$) containing both sensations is obtained.

As explained at the end of Section 7.3.1, each time sample of the STM signal corresponds to a matrix of complex phasors. Therefore, the sample-wise complex summation is performed, resulting in a signal representing the combined pattern.

Multiple haptic sensations can be combined in this manner. However, UX designers must consider the UMAH system's acoustic power limitations. The available energy is distributed among all FPs of the combined pattern. Thus, increasing the number of FPs may reduce the perceptibility of each sensation.

7.6 Approach to suppressing noise due to phase discontinuity

UMAH systems produce an unwanted 'crackle' sound associated with the ultrasonic carrier emission (i.e., 40 kHz), particularly when phase discontinuities occur (Hoshi, 2016; Hoshi et al., 2010).

Phase discontinuity occurs, for example, when the FP jumps from one SP to another. At that instant, the phases of the ultrasonic transducers change abruptly, generating a 'click' sound effect. Since the haptic array is composed of hundreds of transducers, the sound effect is amplified. Moreover, at high FP's speeds (i.e., frequent phase changes), the resulting 'crackling' noise becomes very loud.

Figure 7.24 illustrates this phenomenon. The ultrasonic carrier wave is shown, and at instant t_{SP}, an abrupt phase change occurs due to the FP transitioning to the next SP. This abrupt change produces the audible 'click' sound.

This issue can be mitigated by smoothing the phase transitions (Hoshi, 2016). The algorithm proposed in this chapter enables gradual phase variation between consecutive SPs.

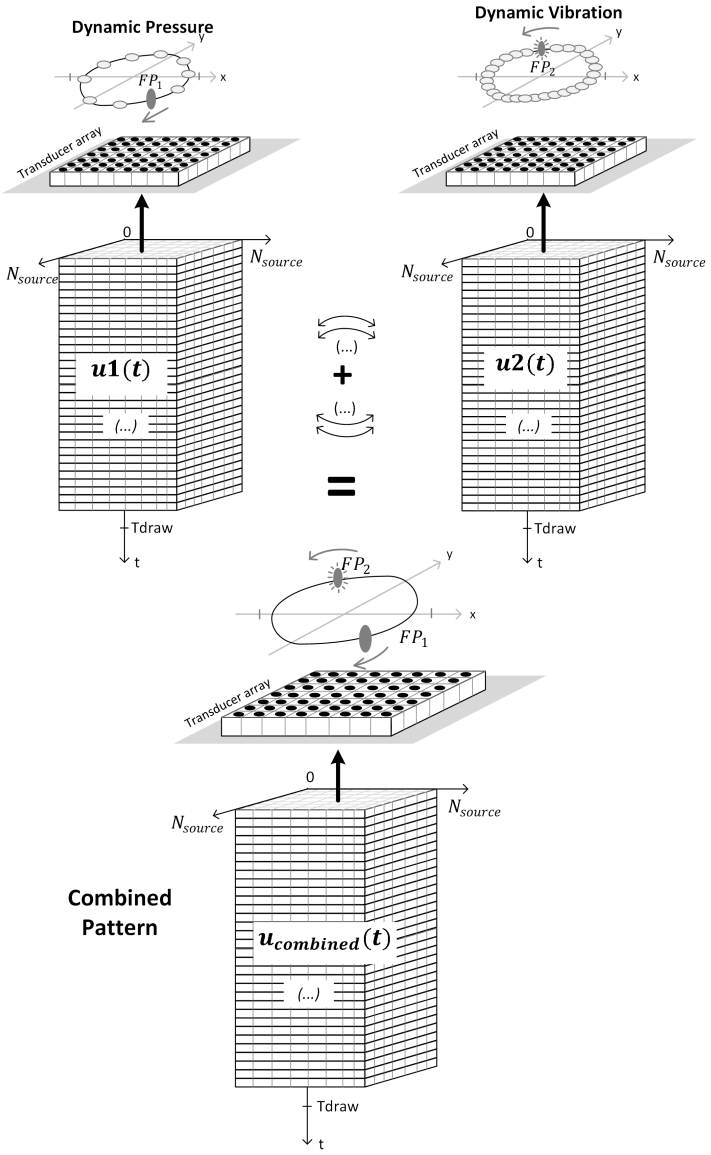

Figure 7.23: Generation of a combined sensation's spatiotemporal signal obtained by adding individual dynamic sensation spatio-temporal signals.

Figure 7.25 shows the STM signal for a single transducer in complex form. The amplitude is represented over time, while the phase is represented in the complex plane. The signal transitions abruptly from v_1 to v_2, corresponding to a phase change from φ_1 to φ_2, which produces a noise.

To address this, a modified window function is introduced to smooth the transition between phases. This function is shown in Figure 7.26.

The waveform resembles a charging/discharging capacitor, with rise and fall rates controlled by parameter τ. Its analytical form is given by:

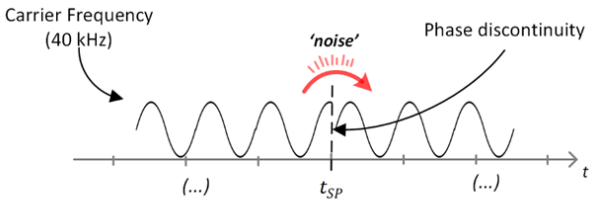

Figure 7.24: Phase discontinuity problem in ultrasonic mid-air systems.

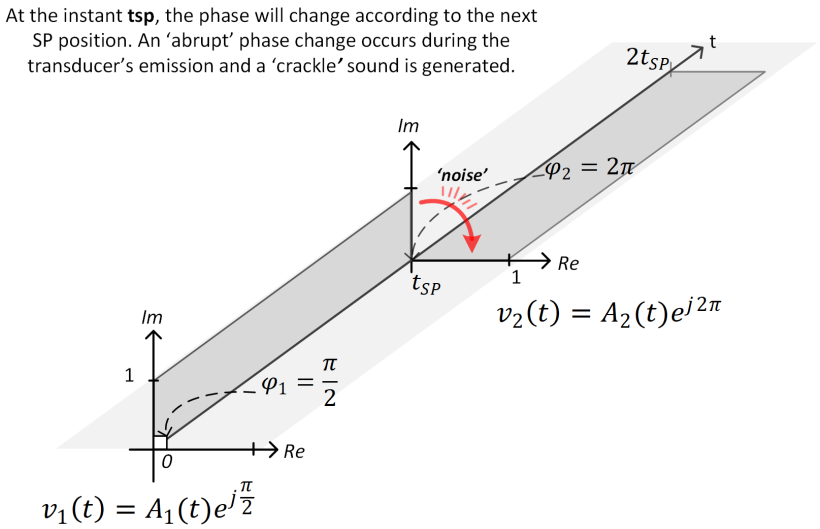

Figure 7.25: Phase discontinuity illustrated in a single transducer STM signal.

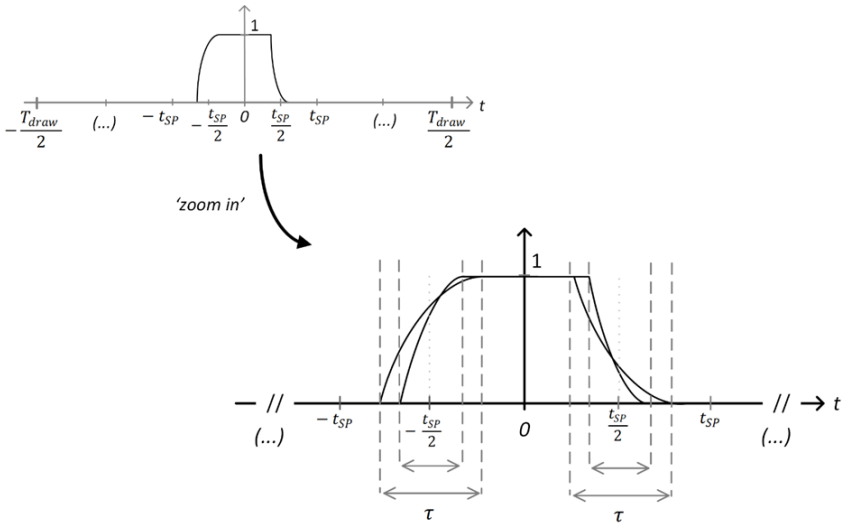

Figure 7.26: Window function used for smoothing phase transitions.

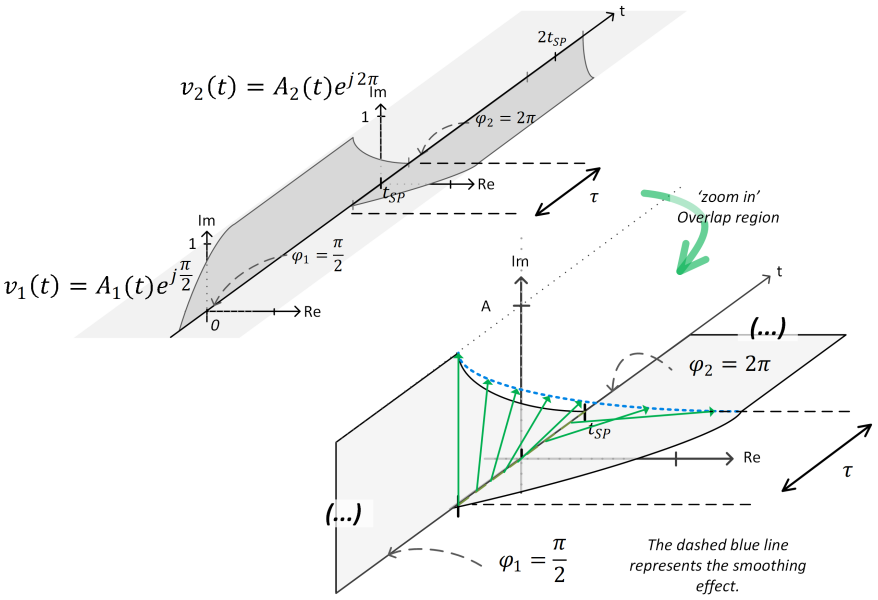

Figure 7.27: Effect of the smoothing window on consecutive SP's signals and their overlaping.

$$f(t) = \begin{cases} 1 - e^{-\tau t}, & -\frac{t_{SP}}{2} - \frac{\tau}{2} \leq t < -\frac{t_{SP}}{2} + \frac{\tau}{2} \\ 1, & -\frac{t_{SP}}{2} + \frac{\tau}{2} \leq t < \frac{t_{SP}}{2} - \frac{\tau}{2} \\ e^{-\tau t}, & \frac{t_{SP}}{2} - \frac{\tau}{2} \leq t < \frac{t_{SP}}{2} + \frac{\tau}{2} \\ 0, & \text{otherwise} \end{cases} \tag{7.4}$$

This window replaces the original rectangular window described in Section 7.3.3 (Figure 7.9). Its wider active region causes overlap between consecutive SP signals, which leads to smoother phase transitions after summation (see Equation 7.3). The degree of smoothing is controlled by τ.

Figure 7.27 illustrates the effect of this approach. The top image shows consecutive SP signals after windowing, while the bottom image highlights the overlapping region of the SP's summation step.

In the overlapping region, the phase transitions gradually between consecutive SPs, as indicated by the phasor arrows. This smooth transition reduces the abrupt phase jumps responsible for 'click' noise.

Although this method has not yet been implemented in practice by the UMAH system, it was validated using the stimulus visualizer (see Section 8.9). It is expected to be a valuable feature for reducing the noise problem in UMAH systems.

It is important to note that this smoothing process affects both phase and amplitude, potentially altering the original haptic sensation. Therefore, a trade-off must be considered, by the UX designer, between the noise reduction problem and sensation fidelity, which can be adjusted via the τ parameter.

7.7 Conclusions

This chapter addressed the module responsible for generating haptic stimuli (i.e., pattern), specifically developed for STM. The chapter begins by reviewing state-of-the-art tools for the creation of UMAH stimuli. It then provides a detailed description of the algorithm used for stimulus generation, along with a discussion of the main challenges encountered during its implementation. In the final part of the chapter, the generation of combined patterns (i.e., stimuli composed of more than one FP) is presented. Lastly, an approach for smoothing transducer phase transitions is described, addressing a common issue of acoustic noise (“clicks”) in UMAH systems.

Simulation Results

8.1 Introduction

In the present chapter, the results corresponding to haptic stimuli (or patterns) created by the haptic stimulus generator module (of Chapter 7) are presented. The visualization of the results was performed using the acoustic simulator discussed in Section 4.2. The goal of this set of results is to demonstrate the main features of the haptic stimulus generator module.

The possibilities for configuring the haptic pattern are virtually limitless. Therefore, the discussion is focused on the most relevant features of the module. These include the ability to create haptic patterns with different sizes, spatial resolutions (i.e., number of SPs), and shapes. Another relevant aspect is the ability to temporally modulate the FP's amplitude. Together, these results encompass the most fundamental features of the haptic stimulus generator module.

It is also relevant to generate multiple FPs (or sensations) simultaneously within the same haptic pattern. In this chapter, combined patterns are also addressed. Moreover, another important feature implemented by the module is phase smoothing, specifically developed to mitigate the "click" noise produced when the FP jumps between different SPs. A set of simulations was developed for this purpose. In the end of the chapter, the acousto optimized haptic sensations are discussed.

The discussion of the simulation results begins with haptic patterns of distinct sizes. For simplicity, circular shape patterns were used to explain most of the implemented features. Nevertheless, an extensive portfolio of pattern shapes can be implemented, as will be shown in the chapter.

8.2 Pressure field computation

As will be seen throughout this chapter, two main techniques were used to display the haptic patterns. For spatial features (such as shape, spatial resolution, or size), the pressure field was computed as a *kind* of "temporal exposure photograph". This approach simulates the real (experimental) acoustic scanning described in Section 5.3.1. Nevertheless, although the haptic stimuli in these results appear static, with multiple FPs created simultaneously, it should be noted that all haptic patterns (with the exception of those with multiple FPs) are sequential in nature, i.e., generated in a temporal order sequence.

For the "temporal exposure" results, the pressure field corresponds to the summation of all the composing SP's fields. The pressure summation is performed in complex form, and the resulting RMS pressure is plotted.

Another important aspect is that the FP was created at 24% of the maximum intensity. This choice ensures consistency with the maximum dynamic range of the microphone (see Section 4.5.1) used in the experimental tests. Whenever a haptic pattern is composed of more than one FP, the acoustic energy is

equally divided among the composing FPs.

The remaining results, namely those that represent the haptic stimulus in a temporal sequential manner (such as in the temporal mosaic representation), display the magnitude of the pressure field in each sub-image.

8.3 Pattern size

The pair of results shown in Figure 8.1 presents two circular patterns: one with a smaller perimeter (left) and another with a larger perimeter (right). Both patterns have identical spatial resolution (i.e., the distance between SPs (i.e., d_{SP}) is equal in both cases). In fact, this spatial resolution is associated with a dynamic pressure rough sensation (see Section 6.4).

To account for the difference in size, the number of SPs used to describe each pattern varies. The smaller circumference is composed of 7 SPs (i.e., $N_{SP} = 7$), whereas the larger one is composed of 10 SPs. There are slight differences in terms of the maximum RMS pressure. These differences arise because, in the smaller pattern, the SPs are located closer to the center of the haptic array and therefore experience higher amplitude.

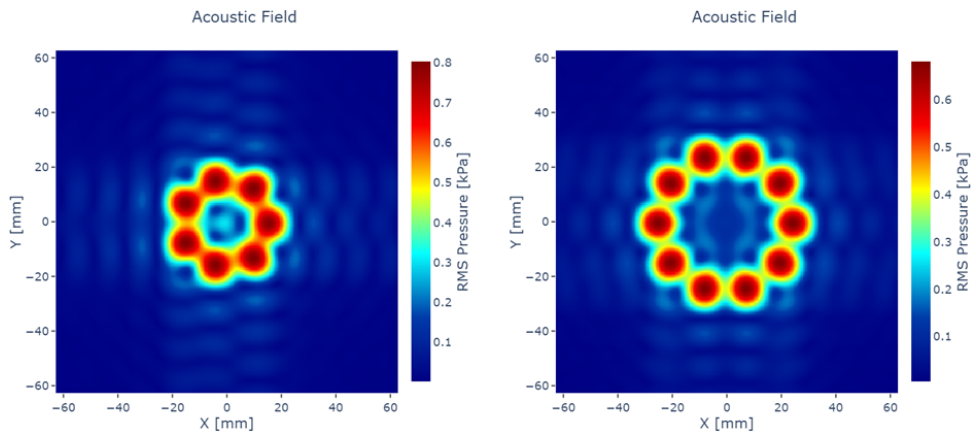

Figure 8.1: Circular patterns with different sizes.(Left) is a 10 cm length pattern ($N_{SP} = 7$). (Right) is a 15.7 cm pattern ($N_{SP} = 10$). Both patterns have the same haptic spatial resolution.

8.4 Pattern spatial resolution

The results shown in Figure 8.2 present haptic patterns with contrasting spatial resolutions (d_{SP}). The spatial resolution of a pattern is related to the number of SPs (N_{SP}) composing it. In the pair of images below, two equally sized patterns are presented (l of 15.7 cm). However, the one on the left is composed of 10 SPs, whereas the pattern on the right has three times more SPs (i.e., 30 points).

Due to the closer proximity between the SPs (as in the right pattern), the individual points merge, appearing as a continuous circumference. This type of spatial resolution is associated with the perception of a dynamic smooth sensation (see Section 6.4).

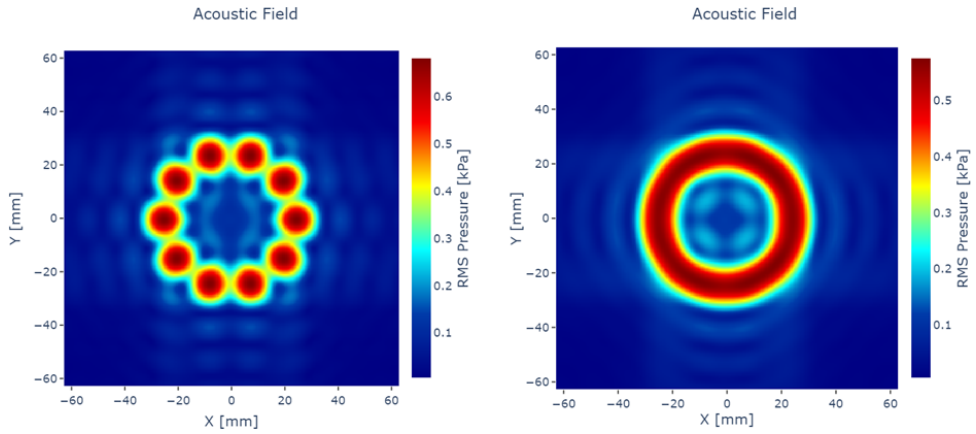

Figure 8.2: Patterns with different haptic spatial resolutions. (Left) is a pattern composed of 10 SPs. (Right) a pattern made of 30 SPs. Both patterns have 15.7 cm in length.

The acoustic field representation of the pair of results shown in Figure 8.2 is very similar to the experimental results measured in Section 5.3.1. This validates the simulation results, as they are coherent with the experimentally obtained ones. Moreover, it also supports the validity of the haptic stimulus generator module in generating the spatio-temporal signals.

8.5 Pattern shape

The mosaic shown in Figure 8.3 presents nine distinct pattern shapes implemented in the haptic stimulus generator module. The UX designer can create any desired shape by implementing the corresponding MATLAB subroutines. The generator module is flexible in that regard, and all shape subroutines are organized within a dedicated pattern shape portfolio sub-folder.

The mosaic includes the following pattern shapes: circle, line, square, triangle, ellipse, spiral, cardioid (i.e., heart shape), rhombus (i.e., diamond shape), and a four-pointed star.

The SP inter-distance (i.e.,d_{SP}) for the circle, line, square, triangle, and rhombus is fixed (i.e., the spatial resolution remains constant throughout the stimulus). On the other hand, the ellipse, spiral, and cardioid shapes exhibit varying spatial resolution. In these cases, the distance between consecutive SPs changes along the pattern.

From a haptic perception standpoint, this is an interesting characteristic. Consider the spiral stimulus as an example. In the outer region of the spiral, the SPs are more widely spaced, which is associated (within

the dynamic sensation) with a rough sensation. As the shape progresses toward the center, the distance between SPs gradually decreases, eventually leading to a smooth perception of the FP's motion. Thus, two distinct dynamic haptic sensations can be achieved within a single pattern stimulus.

Finally, the star shape was drawn with 50 SPs and, for that reason, it appears as a continuous line.

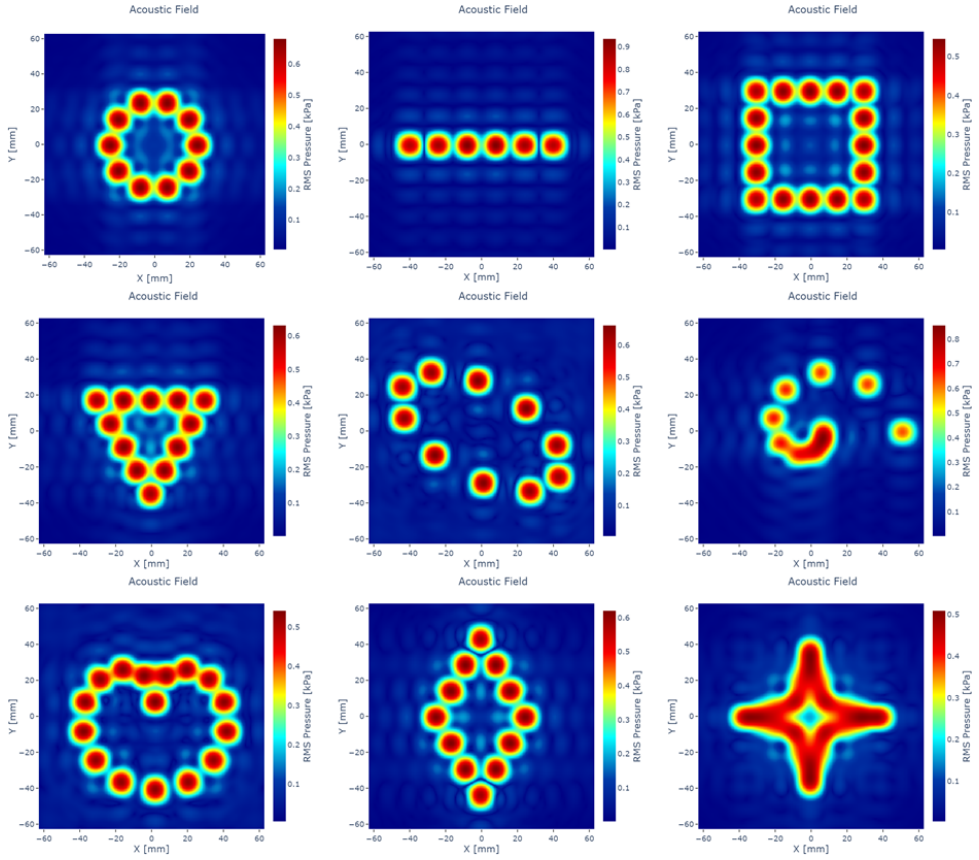

Figure 8.3: Pattern shapes implemented in the haptic stimulus generator module – circle, line, square, triangle, ellipse, spiral, cardioid, rhombus and four-pointed star. Some patterns have constant spatial resolution (e.g., circle, line, square, rhombus), while others exhibit varying spatial resolution (e.g., ellipse, spiral and cardioid).

8.6 Temporal modulation of the Focal Point's amplitude

The previous results demonstrated the versatility of the haptic stimulus generator in creating haptic patterns with diversified spatial characteristics. Moreover, it is also desirable (and possible) to temporally modulate the FP's amplitude, which is an important perceptual aspect, particularly for generating vibrotactile sensations.

Figure 8.4 contains several images (or time frames) intended to illustrate the sinusoidal variation of the FP's amplitude. The several images corresponds to a complete 200 Hz cycle of FP's amplitude modulation

(i.e., a period of 5 ms).

For representation purposes, pairs of images are used in Figure 8.4. The images on the left show the spatial pressure field of the FP, where the FP is colored (e.g., more reddish) according to the amplitude value. The images on the right depict the variation of the FP's amplitude over time. The marker shown in the temporal plot corresponds to the specific time instant represented in the associated pair of images.

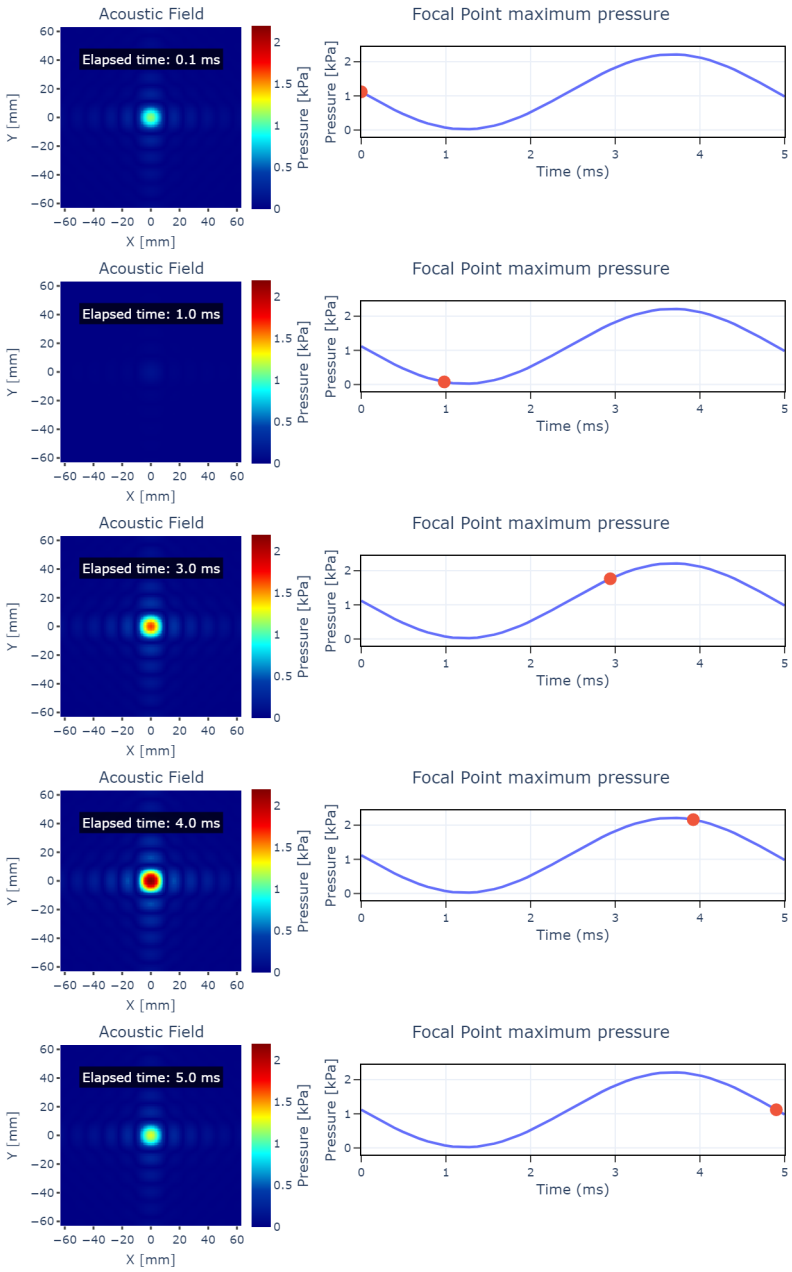

Figure 8.4: Temporal modulation of the FP's amplitude. In this case, the amplitude varies sinusoidally at 200 Hz. The images on the left depict the spatial pressure field of the FP, and the images on the right depict the temporal variation of the FP's amplitude.

As can be easily observed, the FP's amplitude is sinusoidally modulated at 200 Hz. The amplitude modulation can be sustained for the entire duration of the haptic pattern (and not only for a single modulation period, as shown here) in order to confer, for example, a vibrotactile sensation to the haptic pattern. Furthermore, it is possible to modulate the amplitude in ways other than sinusoidal waveform. By implementing the corresponding temporal waveform portfolio, modulation shapes such as sawtooth and triangular waves can be used for the intended purposes. In fact, the optimized dynamic sensation strategies discussed later in this chapter are temporally modulated as pulse trains and square waves.

8.7 Spatial and temporal modulation of the Focal Point

In Figure 8.5, an illustrative example of a FP being temporally modulated (with a sinusoidal variation, as described in the previous section) while describing a circular pattern is shown.

The drawing period (T_{draw}) of the pattern is 10 ms and the FP's amplitude was modulated at an amplitude modulation frequency (f_{am}) of 200 Hz. Note that T_{draw} corresponds to two cycles of the f_{am} equivalent period.

As can be observed (starting from the upper-left corner of Figure 8.5), while the FP moves along the pattern, its amplitude also varies at the same frequency. This is particularly evident at the time instants $t = 5$ ms and $t = 10$ ms, when the FP completes one amplitude modulation cycle and reaches its maximum amplitude repeatedly. The "FP-empty" frames correspond to the moments when the FP amplitude is very low.

8.8 Multiple Focal Points

The haptic stimulus generator module can create haptic patterns containing multiple FPs. This feature is relevant to design new haptic sensations. Haptic stimuli composed of several sensations can be designed in such a way as to take advantage of the selective stimulation of touch (as discussed in Section 2.2.2.3. This can be exploited to create unique haptic sensations.

In this section, three scenarios for haptic stimuli composed of two FPs are presented. Each haptic example is associated with a distinct haptic perception, and the simpler case (i.e., a haptic stimulus composed of two distinct and non-overlapping shapes) is the first one to be discussed. For simplicity, the FP's amplitude is not amplitude modulated (i.e., it is fixed at a constant value).

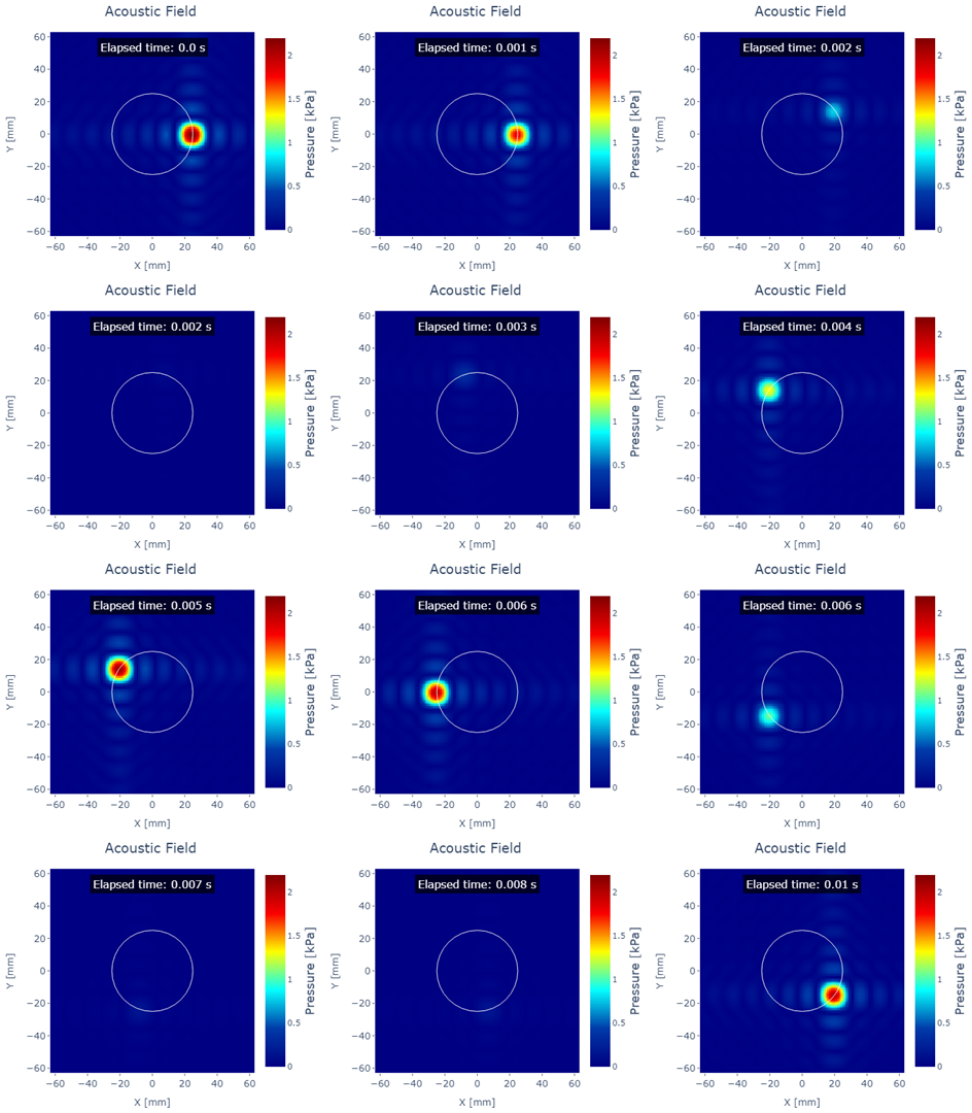

Figure 8.5: The FP being spatially and temporally modulated. For visualization purposes, the drawing period (T_{draw}) is highly exaggerated. It is possible to observe that while the position of the FP is being changed, the FP's amplitude is varying as well ($f_{draw} = 200\ Hz$).

8.8.1 Circle and Square shapes (non-overlapping shapes)

In the example shown in Figure 8.6, the haptic stimulus contains two FPs describing two distinct and non-overlapping pattern shapes. The inner (and smaller) shape is a circle pattern with a length (l) of 10 cm, and the outer (and larger) pattern is a square with a l of 24 cm. In the circular pattern, the FP moves more slowly than in the square pattern. The FP describing the circle takes approximately 640 ms to complete the drawing (T_{draw}), whereas the square takes approximately 530 ms. Both haptic stimuli represent dynamic tactile sensations; however, the square is drawn approximately three times faster than the circle.

Although not visually understandable in Figure 8.6, the circle pattern is composed of 7 SPs, while the

square is composed of 48 SPs. This difference in haptic spatial resolution implies that, at the perceptual level, the two pressure-based dynamic sensations exhibit distinct textures: the circle is associated with a rough *texture*, whereas the square is perceived as smoother *texture*. Thus, the haptic stimulus corresponds to two distinct and simultaneous haptic dynamic sensations (circle: slow and rough; square: fast and smooth).

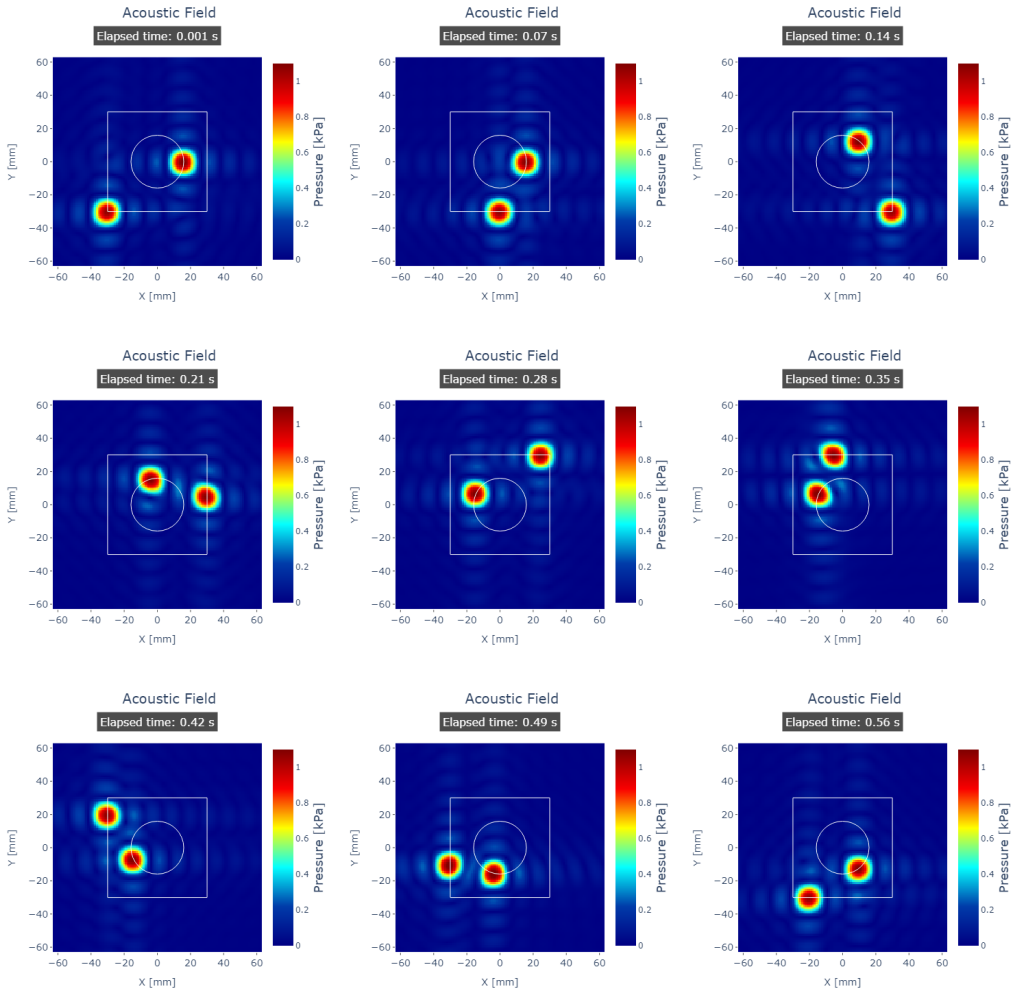

Figure 8.6: Haptic stimulus composed by two FPs. The inner pattern is a circle with 10 cm length. The outer pattern is a square shape with 24 cm in length. The square is drawn about three times faster than the circle. Moreover, the circle is made of 7 SPs (rough texture) and the square is made of 48 SPs (smooth texture).

8.8.2 Two crossing lines (one-point overlapping stimuli)

The haptic stimulus represented in Figure 8.7 contains two identical line shapes oriented in different directions. One line is oriented vertically, and the other is oriented horizontally. Both lines intersect at the center of the image.

Each line has a length of 9.5 cm and is composed of 19 SPs. It takes approximately 211 ms for the FP to travel from one end of the line segment to the other.

In this illustrative haptic stimulus, the FPs overlap at the center of the reference frame. This can be observed in the frame of Figure 8.7 corresponding to the time instant $t = 100$ ms. At that moment, the FP pressures add up (as indicated by the more reddish FP), and the sensation is likely to become sharper or stronger at that instant.

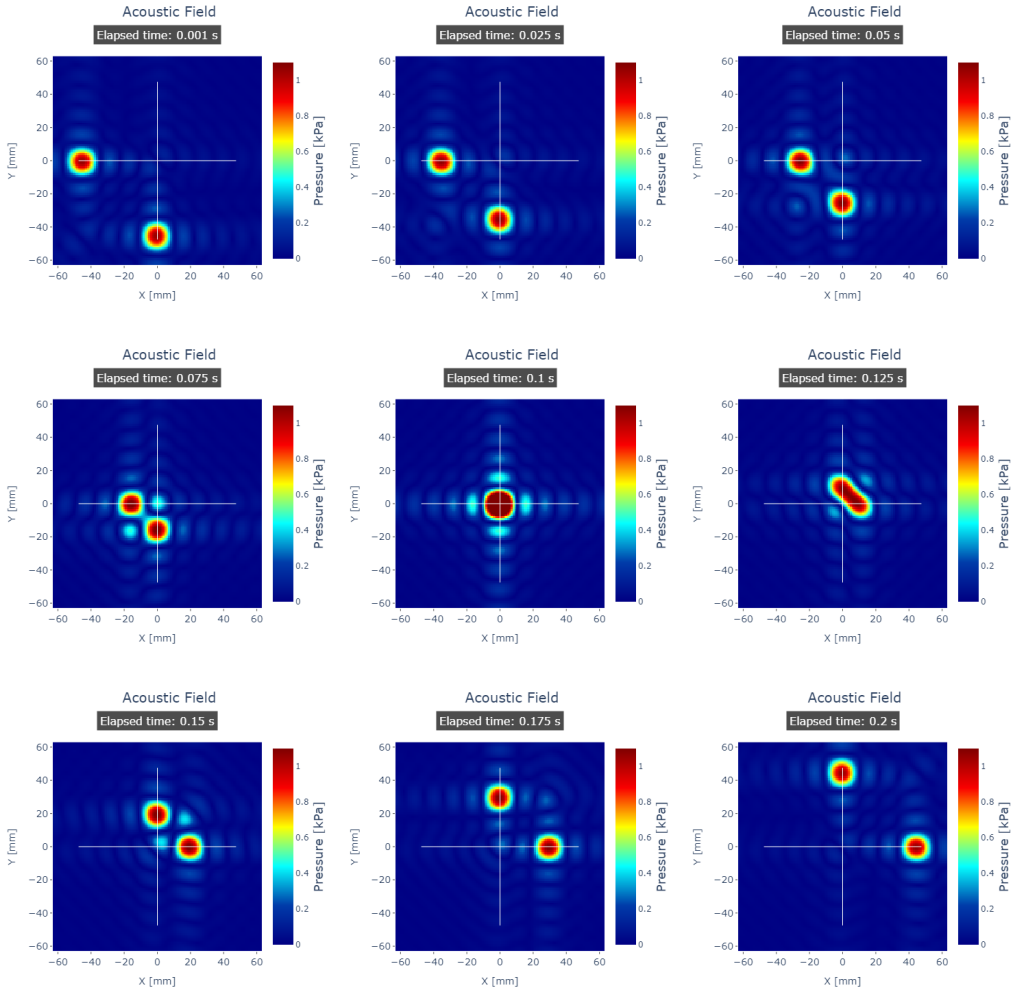

Figure 8.7: Haptic stimulus composed by two FPs. Each FP describes a line segment, but with different orientations. The two lines meet at the center and, in that position, the amplitudes add up and a stronger sensation event occurs.

8.8.3 Haptic Beats (overlapping stimuli)

Audible beats is a well-known phenomenon in acoustics. It occurs when two sounds with slightly different frequencies are played simultaneously. In such case, a gradual increase and decrease in sound volume

is perceived, depending on the frequency difference between the signals (French, 1971).

In Figure 8.8, a haptic beat sensation is illustrated. It is composed of two identical circle shape patterns, but drawn at different speeds (v_{FP}). One FP moves with a v_{FP} of 0.1 m/s, while the other moves at $v_{FP} = 0.5$ m/s. Both correspond to haptic dynamic sensations, but with significantly different FPs' speeds.

Considering Figure 8.8, at the frame corresponding to $t = 1$ ms. Both FPs are at the same position and their pressures add up. Since one FP moves much faster, in the subsequent time instants the two FPs become progressively separated. For example, at $t = 200$ ms they are clearly apart. However, at $t = 400$ ms, the FPs meet again. As the faster FP passes through the position of the slower one, a tactile beat effect occurs. In this particular case, the beat effect is spatially localized and short in duration, due to the speed difference of the FPs.

During half of the traveling cycle of the slower FP, the faster one crosses its position three times (i.e., three haptic beats occur). This half-cycle and the corresponding beats are illustrated in Figure 8.8, at the time instants $t = 1$ ms, $t = 400$ ms, and $t = 785$ ms.

Tactile beats operate in a manner similar to audible beats. The latter are influenced by the difference in sound pitch. In the case of the tactile beat, the v_{FP} difference between the FPs determines the characteristics of the beat. For example, if the v_{FP} difference is large, the beat is spatially concentrated and of short duration. Conversely, if the speeds are closer, the beat becomes more gradual and spatially distributed.

The sensations involved in the example of Figure 8.8 are dynamic haptic sensations. It is also interesting to note that if the haptic sensations involved were, for example, uniform haptic sensations (see Figure 5.8), the beating effect still occurs, but with substantially different sensations. Playing with this effect therefore enables the creation of new haptic sensations.

8.9 Phase smoothing

Phase smoothing is a feature implemented in the haptic stimulus generator module. It is discussed in Section 7.6, and its main purpose is to address a problem associated with the UMAH system. Thus, the haptic stimulus generator module can be used not only to create haptic stimuli, but also to design them in a way that mitigates UMAH system-related issues.

Figure 8.9 shows a circular pattern. For better visualization purposes, the FP position was configured to move between two SPs. The FP remains at the first SP until $t = 100$ ms, at which moment it jumps (instantaneously, in the simulation) to the second SP. It should be noted that, in practice, the FP *jump* is not truly instantaneous due to the inertia of the ultrasonic transducer's membrane. At $t = 100$ ms, a "click" sound is produced as a result of the abrupt phase change of the ultrasonic transducers in the

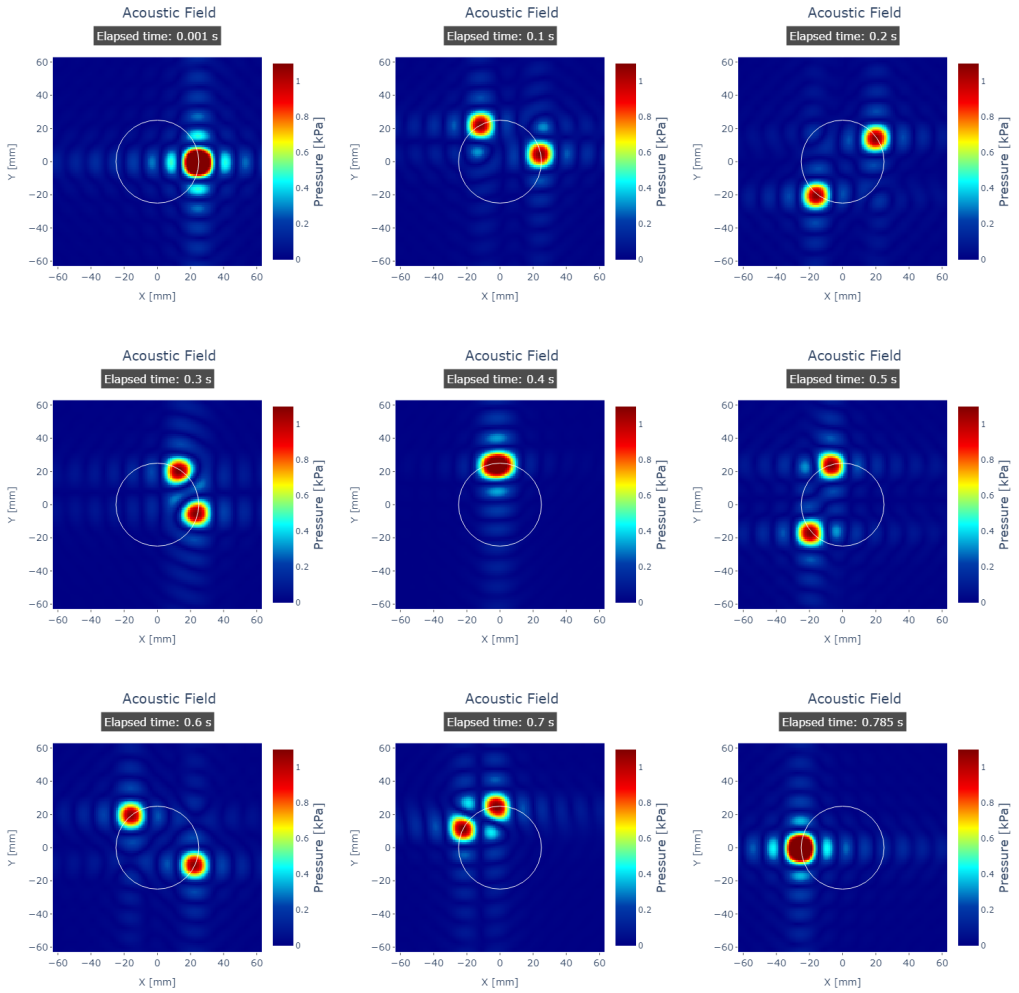

Figure 8.8: Haptic beat sensation. Two FPs travel at different speeds. Thus, the faster FP crosses the slower FP three times (i.e., three beats) per half drawing cycle (of the slower FP). Every time a beat happens, a stronger and localized tactile event occurs.

haptic array.

Figure 8.10 shows the *same* haptic stimulus (as presented in Figure 8.9) but with phase smoothing applied. In this case, the smoothing characteristics were intentionally exaggerated for visualization purposes. The smoothing process takes approximately 20 ms to complete; however, in practice, it should occur much faster — just enough to reduce the "clicking" noise without compromising the intended haptic sensation.

With this in mind, it can be observed that the FP remains at the first SP position until $t = 86$ ms. In the following time frame ($t = 89$ ms), the FP begins to fade, and at $t = 92$ ms it starts to appear at the second SP position. Gradually, the FP's amplitude is re-established in the subsequent time instants. Around $t = 107$ ms, the FP reaches full intensity at the second SP position.

The images in the mosaic of Figure 8.10 display the FP's amplitude being gradually controlled between

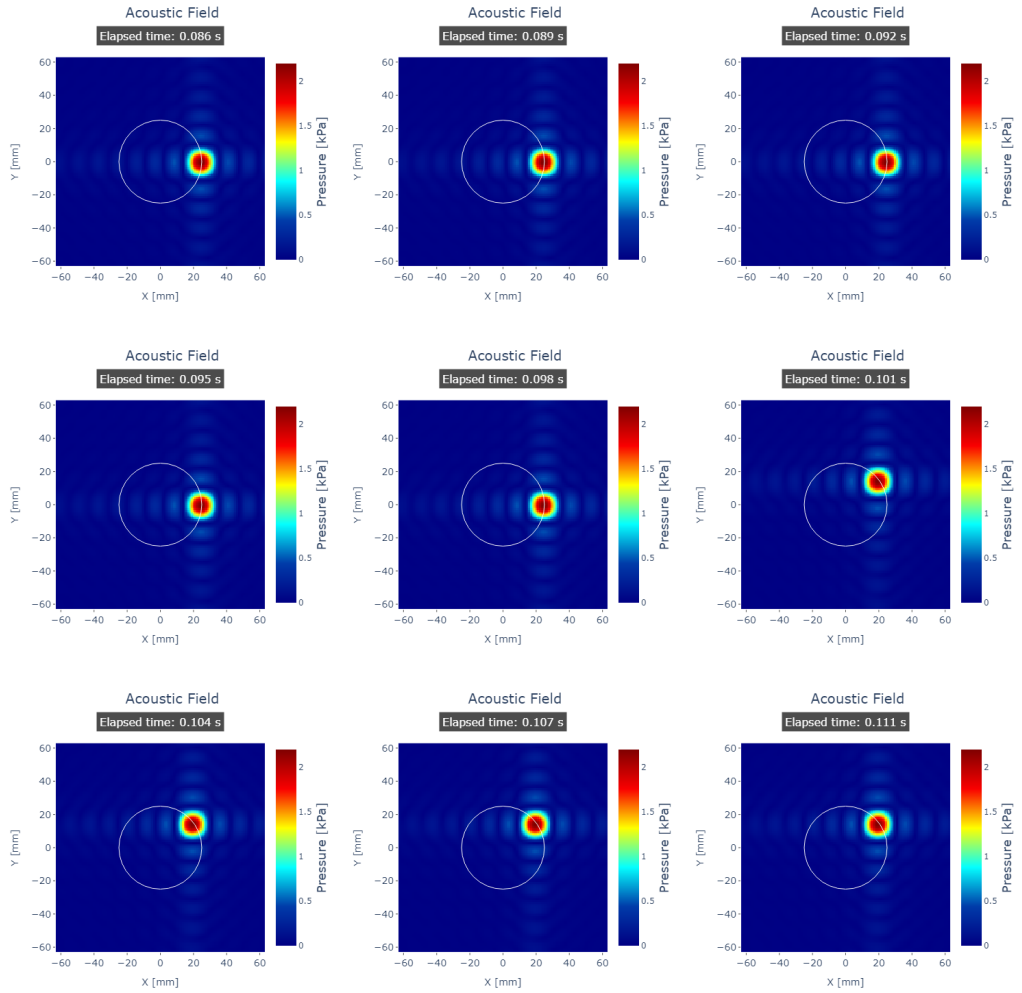

Figure 8.9: Haptics stimulus illustrating the 'noise click' problem. Two SP positions are used for easy explanation. At frame instant $t = 100$ ms, the FP jumps to the new SP and a click noise is created.

the SPs. Nevertheless, the transducers' phases are also gradually adjusted, although this is not visually perceptible in the images. This gradual phase transition is responsible for minimizing the "clicking" noise.

8.10 Optimized dynamic haptic sensations

One of the aims of this PhD thesis was to optimize haptic sensations. In this context, optimization refers to haptic sensations that are less energy (or acoustic) demanding while preserving (or improving) the original haptic sensation.

Optimizations for dynamic sensations were proposed in Section 6.7. In this section, simulations of those optimizations are presented.

For simplicity, only two SPs are presented for the explanations. However, the *optimizations* are repeated

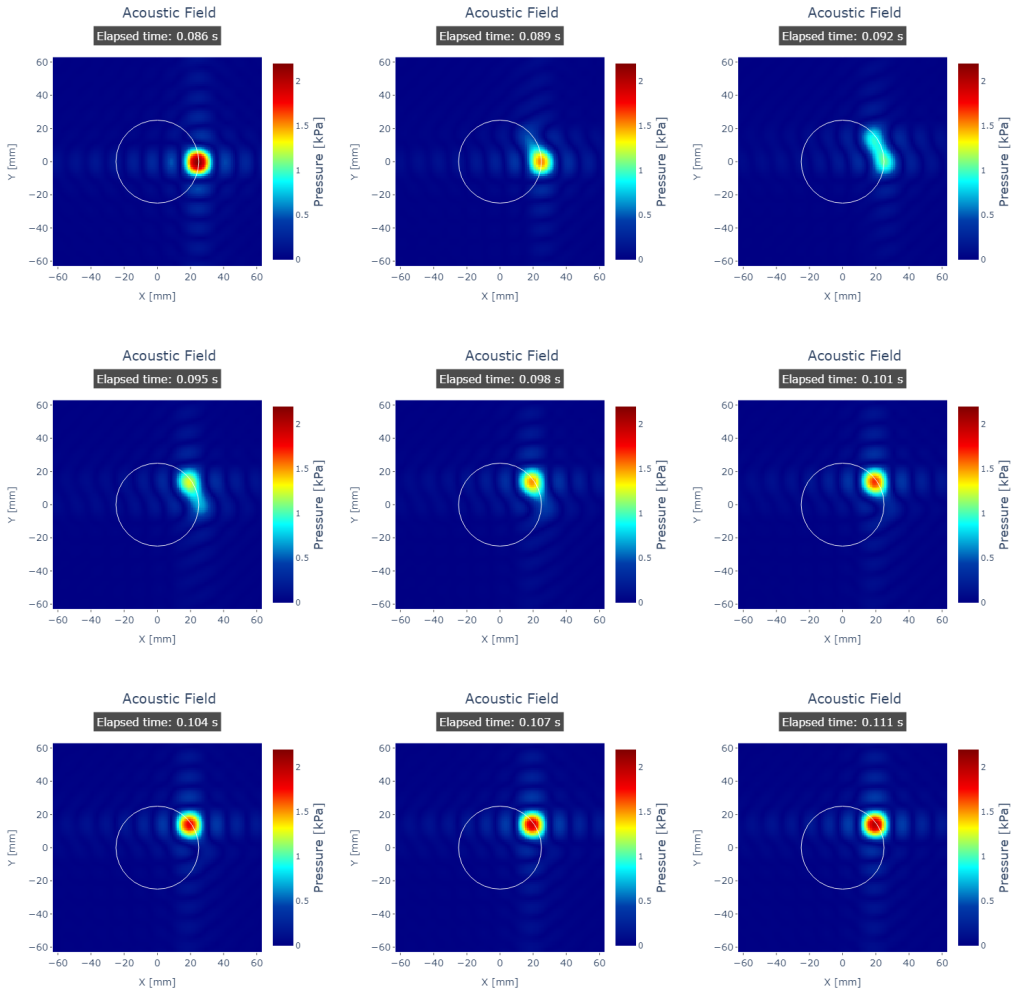

Figure 8.10: Haptic stimulus showing the phase smoothing procedure. In this case, the phase smoothness rate was highly exaggerated for visualization purposes. Two SPs were considered for the demonstration.

and performed for all SPs of the pattern. The explanations consider a circular pattern made of 10 SPs, each one with duration (t_{SP}) of 100 ms.

8.10.1 Optimization Strategy 1

The first optimization to be discussed is optimization strategy 1 (discussed in Section 6.7.1). In short, a long pulse is perceptually similar to two shorter pulses separated by a long inactive interval. This occurs because the perception of longer pulses is mainly associated with their onset and offset.

The haptic sensation corresponds to a dynamic sensation of the pressure type. The SP duration (t_{SP}) in this example is 100 ms. This relatively long pulse duration is required for this optimization. Two shorter pulses were created at the beginning and at the end of the SP (i.e., 18 ms each), while the intermediate duration was set to OFF (i.e., 64 ms).

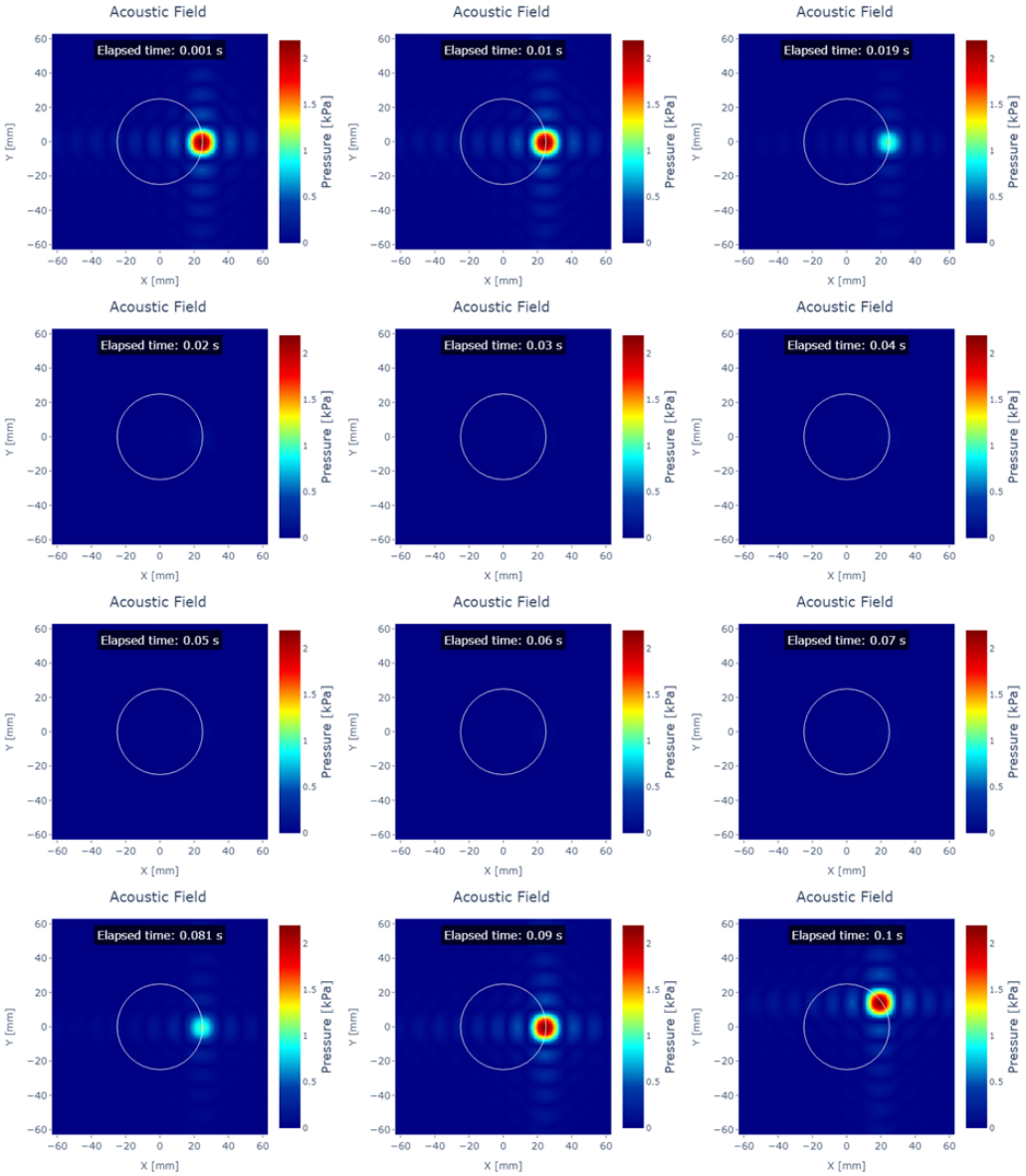

Figure 8.11: Optimization strategy 1 for the dynamic sensation. A long duration pulse (in this case a 100 ms duration SP) is modulated as two short pulses (18 ms each) displayed at the beginning and end of the SP.

The haptic stimulus is shown in Figure 8.11. The FP remains active for 18 ms (corresponding to the first three frame images). It is then turned OFF for approximately 64 ms (as observed in the six consecutive "FP-empty" frames). At $t = 81$ ms, the FP is turned ON again and remains active for 18 ms. At approximately $t = 100$ ms, the FP jumps to the next SP position.

8.10.2 Optimization Strategy 2

The haptic stimulus shown in this subsection represents another possibility for optimizing a dynamic haptic pressure-based sensation. This strategy was detailed in Section 6.7.2. In short, it consists of modulating

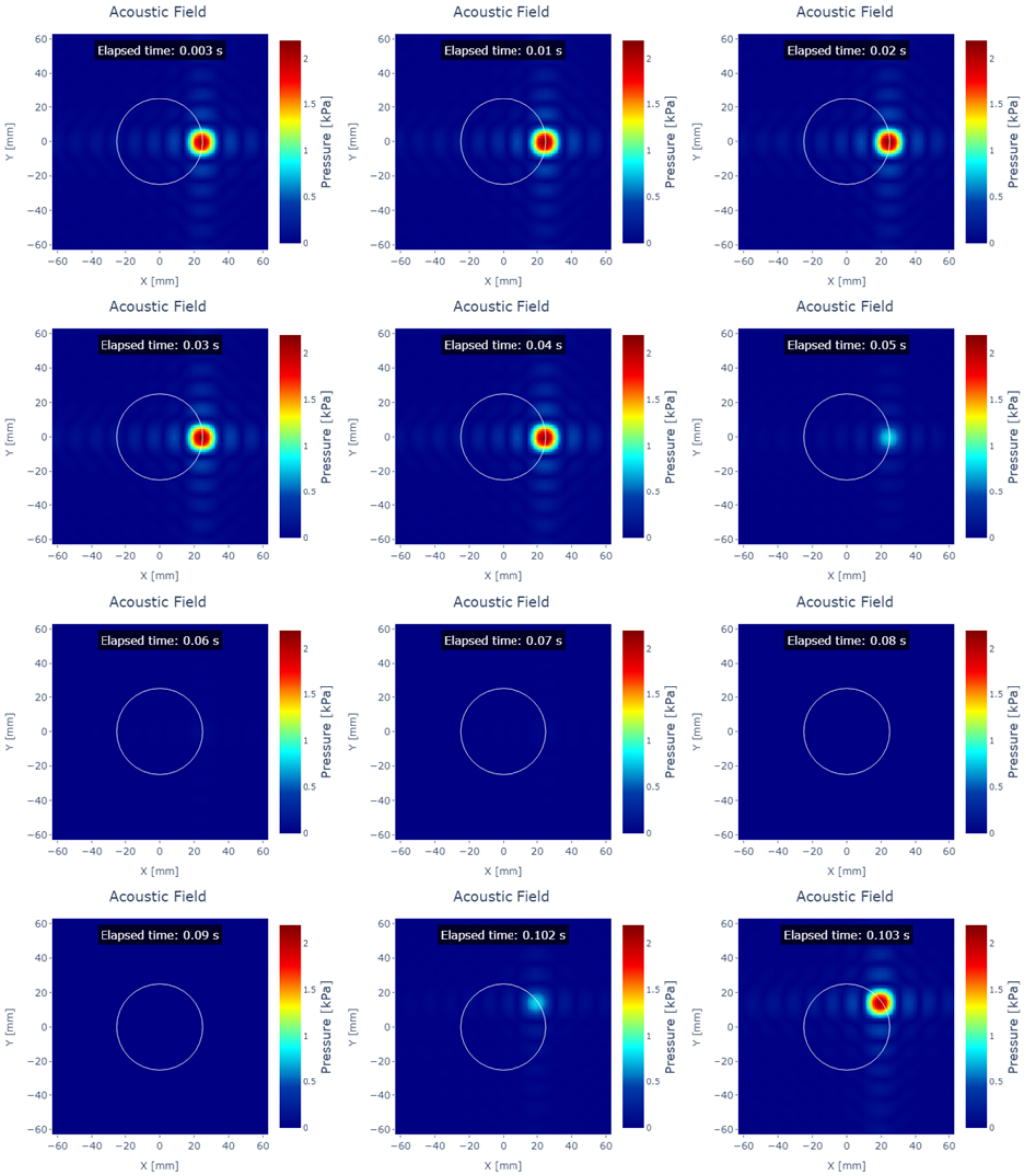

Figure 8.12: Optimization strategy 2 for the dynamic sensation. The FP is kept ON for 50% of the SP's duration and then turned OFF. Only two SPs are represented.

the FP in each SP with, for example, a 50% duty cycle. By modulating the FP's amplitude in this way, the haptic stimulus creates the tactile illusion of the pattern having double the number of SPs (N_{SP}), with the FP's amplitude always active.

The FP's amplitude (at each SP) is modulated with a 50% duty cycle, meaning that it is ON for 50 ms and OFF for the remaining 50 ms. At $t = 100$ ms, the FP jumps to the next SP.

In the context of a dynamic haptic sensation (as explained in Section 6.7.2), this stimulus may be perceptually equivalent to a stimulus with 20 SPs, where the FP has constant amplitude.

8.11 Conclusions

This chapter aims to validate the haptic stimuli generated by the stimuli generation module developed in Chapter 7. To this end, various simulations are presented, demonstrating the module's capability to generate patterns with diverse characteristics. The first part of the chapter focuses on the generation of patterns with different spatial properties, such as shape, size, and spatial resolution of the pattern. This is followed by an analysis of temporal characteristics, including sinusoidal amplitude modulation of the FP. Subsequently, the generation of combined stimuli is presented. The perception of these combined sensations is discussed alongside the obtained results, highlighting their haptic potential. In the final part of the chapter, transducer phase smoothing is demonstrated, and two optimization strategies (explained in Chapter 6) for pressure-based haptic dynamic sensations are implemented.

Conclusions

9.1 Conclusions

As highlighted in Chapter 1, the main limitation of UMAH technology lies in the low intensity of the haptic sensations it produces. In this context, the objective of this PhD is to improve (or optimize) the perceived haptic sensation.

The enhancement of haptic sensations can be achieved in several ways. Increasing the number of ultrasonic transducers, improving the transducers themselves, and/or enhancing the tactile sensation perceived by the human hand by testing different modulation parameterizations. The first approach—namely, increasing the number of ultrasonic transducers in the haptic array—directly increases the intensity of the haptic stimulus. However, this also leads to higher exposure of the user to ultrasonic radiation and results in larger device dimensions, which are unsuitable for automotive applications. The second approach—improving the transducers themselves for haptic applications—is a valid path, as the ultrasonic transducers currently available on the market are not optimized for UMAH applications, representing the main hardware-related challenge in these systems. The third approach—enhancing the tactile sensation perceived by the human hand—was the path chosen for this work.

To address the objectives of this PhD, the research focused on the spatio-temporal modulation (STM) technique. Haptic modulation techniques manipulate the haptic stimulus (in this case, the FP) in order to generate perceptible haptic sensations. STM, a relatively recent technique in the literature, is particularly promising as it produces haptic stimuli with lower tactile perception thresholds and stronger patterns compared to traditional mid-air haptic modulation techniques.

Beyond generating more perceptible stimuli, STM also produces distinct types of haptic sensations. Approaching STM from the perspective of the sensations it generates constitutes the central concept—and main innovation—of this research. A deeper understanding of these sensations enables targeted optimization strategies based on the mechanoreceptors associated with each perceptual response.

At the beginning of this thesis, a complete UMAH demonstrator was developed in collaboration with a research team from ESRG at the University of Minho. This mid-air haptic demonstrator was used in numerous public demonstrations, contributing to the dissemination of UMAH technology in Portugal. The system, presented in Chapter 4, consists of a 16×16 transducer array and generates a FP with a maximum radiation force of 7.8 mN (diameter of approximately 15 mm), at a distance of around 20 cm. An acoustic simulator was also developed (and used throughout the PhD), and a hybrid embedded architecture (CPU + FPGA) was implemented to enable the generation of haptic sensations, forming the basis of the experimental work conducted in this thesis.

The primary objective of the first part of this research (presented in Chapter 5) was to demonstrate that STM produces perceptually distinct haptic sensations. Two user studies were conducted to specify and

validate these sensations. In the first study, modulation parameters—namely the FP velocity (v_{FP}) and the number of points composing the pattern (N_{SP})—were systematically analyzed. This led to the identification of boundary regions between sensations and the definition of three distinct haptic sensations: dynamic, vibratory, and uniform.

The dynamic sensation occurs for $v_{FP} < 0.54$ m/s (10 points), $v_{FP} < 0.79$ m/s (30 points), and $v_{FP} < 0.74$ m/s (50 points). The vibratory sensation occurs within the ranges $1.06 < v_{FP} < 4.9$ m/s (10 points), $1.31 < v_{FP} < 4.6$ m/s (30 points), and $1.26 < v_{FP} < 4.5$ m/s (50 points). The uniform sensation occurs for $v_{FP} > 6.3$ m/s (10 points), $v_{FP} > 6.6$ m/s (30 points), and $v_{FP} > 6.7$ m/s (50 points). These results are illustrated in Figure 5.8.

The second user study aimed to validate participants' ability to identify these sensations. A total of 480 stimuli were generated, including both individual sensations (dynamic, vibratory, and uniform) and combined sensations (dynamic + vibratory, dynamic + uniform, and vibratory + uniform). The results showed identification rates of 92 % for dynamic, 70 % for vibratory, and 82.5 % for uniform sensations, demonstrating that STM-generated sensations are reliably perceivable. Furthermore, the combined dynamic + uniform sensation achieved a 74.4 % identification rate, suggesting that these sensations may originate from distinct physiological mechanisms. The research work that represents the first part of the PhD thesis resulted in a first-quartile publication in the IEEE Transactions on Haptics journal (Mendes et al., 2022).

The second part of the PhD (Chapters 6, 7.3, and 8) focused on the development of a preliminary tool for generating haptic sensations. To the best of our knowledge, no such tool (specifically developed for STM oriented sensations) exists in the literature. Such a tool is essential for simplifying and automating the generation of STM-based sensations. One of its key innovations is a sensation specification layer (introduced in Chapter 6 and based on the findings of Chapter 5), which abstracts the UX designer from the low-level parameterization of the haptic stimulus.

The core of the tool is a novel algorithm for generating haptic stimuli tailored to STM, which is based on mathematical convolution, in both space and time. The stimulus generation module also supports the creation of combined stimuli (i.e., multiple FPs simultaneously) and includes a method for smoothing abrupt phase transitions of the transducers—addressing a well-known limitation in UMAH systems which leads to undesired audible noises ("clicks").

Simulation results (obtained using the acoustic simulator presented in Chapter 4) validate the haptic sensation tool, demonstrating that it enables precise control over the spatial characteristics (e.g., shape, size, and spatial resolution) and temporal characteristics (e.g., modulation frequency and waveform) of the generated haptic pattern. Combined haptic sensations were also generated to show the flexibility of the tool. Finally, two optimization strategies for the dynamic haptic sensation (used as a case study) were proposed in Chapter 6 and implemented in Chapter 7.3, illustrating how perceptually driven optimizations

can be achieved. Based on the findings of this work, the proposed methodology for haptic sensation generation oriented to the human hand tactile perception proved to be an efficient approach to enhance UMAH sensations.

9.2 Future Work

As a primary direction for future work, we highlight the need for a subjective study aimed at evaluating the haptic sensations developed within the scope of this PhD, including the optimized sensations. Such a study would enable the analysis of the newly developed haptic sensations and their comparison with their "original" counterparts.

Currently, a new embedded system architecture is being developed to integrate the UMAH demonstrator with the haptic sensation generation tool. This work is being carried out in the context of the previously mentioned requirement of experimental evaluations.

In this PhD, the specification of the dynamic haptic sensation was addressed (Chapter 6), which was adopted as a case study. However, it is equally important to develop similar specifications for the uniform and vibratory haptic sensations. Additionally, certain haptic phenomena, such as tactile beats (discussed in Chapter 8), deserve further investigation and deeper understanding. Since these create perceptible and new sensations.

UMAH technology has evolved in terms of its application domains over the years. More recently, it has been applied to areas such as acoustic levitation of small particles and multimodal experiences (i.e., visual, auditory, and haptic) (Hirayama et al., 2019). AcoustoFab (AcoustoFab, 2026) is currently a leading company in this domain. The haptic sensations developed in this PhD may be leveraged in such systems to provide more optimized and energy-efficient haptic tactile feedback.

Supplementary Material

A.1 Appendix A

All supplementary materials, including datasets and implementation details, are available on Zenodo (and GitHub) at the following reference link (Mendes, 2026):

https://doi.org/10.5281/zenodo.19858157

This repository includes:

- Code developed for controlling the measurement equipment (described in Chapter 4), required for performing acoustic measurements (acoustic scanning and focal point radiation force estimation).
- A Vivado project developed for the UMAH demonstrator. This project implements the system architecture detailed in Chapter 4 and includes both the PS software (C code) and the PL FPGA implementation.
- Documentation related to the user studies presented in Chapter 5, including ethical approval from the University of Minho, a description of the experimental procedures, and signed participant consent forms.
- User interfaces developed for data acquisition in the user studies described in Chapter 5, as well as code for processing the collected data.
- Project code for the Haptic Sensation Generation Tool. This includes the sensation abstraction layer (for dynamic sensations, discussed in Chapter 6), the haptic stimulus generation module (core component of the tool, discussed in Chapter 7), and the acoustic simulator used for visualizing the generated haptic stimuli (discussed in Chapter 8).
- Additional files, including PCB schematics of the developed UMAH system, as well as images and videos of the haptic stimuli generated by the tool.

Bibliography

Ablart, D., Frier, W., Limerick, H., Georgiou, O., & Obrist, M. (2019). Using ultrasonic mid-air haptic patterns in multi-modal user experiences. *Proceedings of the IEEE International Symposium on Haptic, Audio and Visual Environments and Games (HAVE)*, 1–6. https://doi.org/10.1109/HAVE.2019.8920969 (cit. on pp. 10, 37, 48–51, 79).

AcoustoFab. (2026). *Acoustic levitation for contact-free robotics*. Retrieved 2026-04-20, from https://www.acoustofab.co.uk/ (cit. on p. 158).

AMD. (2026). *Zynq-7000 soc technical reference manual (ug585)*. Retrieved 2026-04-07, from https://docs.amd.com/r/en-US/ug585-zynq-7000-SoC-TRM/Introduction?tocId=Hf6C7Oo5ABvv2hkWRoiihQ (cit. on p. 60).

AudioWell. (2024). *Ultraleap introduces new technology (seen in 2024)*. Retrieved 2024-01-01, from https://www.audiowell.com/industrynews/229.html (cit. on p. 4).

Beattie, D., Frier, W., Georgiou, O., Long, B., & Ablart, D. (2020). Incorporating the perception of visual roughness into the design of mid-air haptic textures. *ACM Symposium on Applied Perception*, 4. https://doi.org/10.1145/3385955.3407927 (cit. on pp. 48, 51).

Billen, M., Ferrer, E. M., Pandian, M. S., Rottenberg, X., & Rochus, V. (2022). Mid-air haptic feedback enabled by aluminum nitride PMUTs. *Proceedings of the IEEE International Conference on Micro Electro Mechanical Systems (MEMS)*, 247–250. https://doi.org/10.1109/MEMS51670.2022.9699528 (cit. on p. 4).

Camelo, A. (2020). *Hardware reconfigurável para interface háptico* [Master dissertation]. University of Minho. https://rep-dspace.uminho.pt/entities/publication/46b44f4f-e574-4e3d-8fbb-58a2cf38e942 (cit. on pp. 6, 17, 21, 73).

Carter, T., Seah, S. A., Long, B., Drinkwater, B. W., & Subramanian, S. (2013). Ultrahaptics: Multi-point mid-air haptic feedback for touch surfaces. *Proceedings of the ACM Symposium on User Interface Software and Technology (UIST)*, 505–514. https://doi.org/10.1145/2501988.2502018 (cit. on p. 6).

Cataldo, A., Frier, W., & Haggard, P. (2023). Quantifying spatial acuity of frequency-resolved mid-air ultrasound vibrotactile stimuli. *Scientific Reports*, *13*(1), 21149. https://doi.org/10.1038/s41598-023-48037-0 (cit. on pp. 24, 77, 109).

Dalecki, D., Child, S. Z., Raeman, C. H., & Carstensen, E. L. (1995). Tactile perception of ultrasound. *The Journal of the Acoustical Society of America*, *97*(5), 3165–3170. https://doi.org/10.1121/1.411877 (cit. on pp. 20, 26, 27, 30, 33, 34, 82).

Denver Instrument. (n.d.). *Summit si-2002 manuals*. Retrieved 2026-04-07, from https://www.manualslib.com/products/Denver-Instrument-Summit-Si-2002-9939970.html (cit. on p. 71).

DS Automobiles. (2021). *Ds aero sport lounge*. Retrieved 2024-01-01, from https://www.dsautomobiles.pt/ds-experience/concept-cars/ds-aero-sport-lounge.html (cit. on p. 2).

French, A. P. (1971). *Vibrations and waves*. W. W. Norton & Company. (Cit. on p. 148).

Frier, W., Abdouni, A., Pittera, D., Georgiou, O., & Malkin, R. (2022). Simulating airborne ultrasound vibrations in human skin for haptic applications. *IEEE Access*, *10*, 15443–15456. https://doi.org/10.1109/ACCESS.2022.3147725 (cit. on pp. 37, 38, 77).

Frier, W., Ablart, D., Chilles, J., Long, B., Giordano, M., Obrist, M., & Subramanian, S. (2018). Using spatiotemporal modulation to draw tactile patterns in mid-air. *Haptics: Science, Technology, and Applications*, 270–281. https://doi.org/10.1007/978-3-319-93445-7_24 (cit. on pp. 6, 9, 37–39, 41, 46–49, 79, 80).

Frier, W., Pittera, D., Ablart, D., Obrist, M., & Subramanian, S. (2019). Sampling strategy for ultrasonic mid-air haptics. *Proceedings of the CHI Conference on Human Factors in Computing Systems*, 1–11. https://doi.org/10.1145/3290605.3300351 (cit. on pp. 6, 9, 10, 37–41, 48–51, 79, 99).

Gavrilov, L. R. (1984). Use of focused ultrasound for stimulation of nerve structures. *Ultrasonics*, *22*(3), 132–138. https://doi.org/10.1016/0041-624X(84)90008-8 (cit. on pp. 19, 27, 29, 30).

Gavrilov, L. R. (2008). The possibility of generating focal regions of complex configurations in application to the problems of stimulation of human receptor structures by focused ultrasound. *Acoustical Physics*, *54*(2), 269–278. https://doi.org/10.1134/S1063771008020152 (cit. on p. 6).

Gavrilov, L. R., Gersuni, G. V., Ilyinski, O. B., Tsirulnikov, E. M., & Shchekanov, E. E. (1977). A study of reception with the use of focused ultrasound. i. effects on the skin and deep receptor structures in man. *Brain Research*, *135*(2), 265–277. https://doi.org/10.1016/0006-8993(77)91030-7 (cit. on pp. 27–30, 109, 110).

Gavrilov, L. R., Gersuni, G. V., Ilyinsky, O. B., Sirotyuk, M. G., Tsirulnikov, E. M., & Shchekanov, E. E. (1976). The effect of focused ultrasound on the skin and deep nerve structures of man and animal. *Progress in Brain Research*, *43*, 279–292. https://doi.org/10.1016/S0079-6123(08)64360-5 (cit. on pp. 19, 26, 27, 29).

Gavrilov, L. R., Hand, J. W., Abel, P., & Cain, C. A. (1997). A method of reducing grating lobes associated with an ultrasound linear phased array intended for transrectal thermotherapy. *IEEE Transactions on Ultrasonics, Ferroelectrics, and Frequency Control*, *44*(5), 1010–1017. https://doi.org/10.1109/58.655626 (cit. on p. 6).

Gavrilov, L. R. (2014). *Use of focused ultrasound for stimulation of various neural structures*. Nova Science Publishers. https://www.researchgate.net/profile/Leonid-Gavrilov/publication/261988313_Us

e_of_Focused_Ultrasound_for_Stimulation_of_Various_Neural_Structures_Nova_Science_Publishers_2014_P182/links/5af6bfdda6fdcc0c030ccdfa/Use-of-Focused-Ultrasound-for-Stimulation-of-Various-Neural-Structures-Nova-Science-Publishers-2014-P182.pdf (cit. on pp. 18, 20, 27–30, 99, 110).

Georgiou, O., Biscione, V., Harwood, A., Griffiths, D., Giordano, M., Long, B., & Carter, T. (2017). Haptic in-vehicle gesture controls. *Proceedings of the International Conference on Automotive User Interfaces and Interactive Vehicular Applications Adjunct*, 233–238. https://doi.org/10.1145/3131726.3132045 (cit. on p. 2).

Georgiou, O., Frier, W., Freeman, E., Pacchierotti, C., & Hoshi, T. (Eds.). (2022). *Ultrasound mid-air haptics for touchless interfaces*. Springer. https://doi.org/10.1007/978-3-031-04043-6 (cit. on pp. 3, 21, 42, 79).

Georgiou, O., Montano, R., Pittera, D., Frier, W., Hughes, S., Haggard, P., Obrist, M., & Cornelio, P. (2026). Mid-air haptics for automotive huds: A sketch anticipation and design fiction study. *Technological Forecasting and Social Change*, *226*. https://doi.org/10.1016/j.techfore.2026.124567 (cit. on p. 2).

Gescheider, G. A. (1967). Auditory and cutaneous temporal resolution of successive brief stimuli. *Journal of Experimental Psychology*, *75*(4), 570–572. https://doi.org/10.1037/h0025113 (cit. on p. 25).

Gescheider, G. A., Bolanowski, S. J., & Chatterton, S. K. (2003). Temporal gap detection in tactile channels. *Somatosensory & Motor Research*, *20*(3-4), 239–247. https://doi.org/10.1080/08990220310001622960 (cit. on pp. 25, 26).

Gescheider, G. A., Güçlü, B., Sexton, J. L., Karalunas, S., & Fontana, A. (2005). Spatial summation in the tactile sensory system: Probability summation and neural integration. *Somatosensory & Motor Research*, *22*(4), 255–268. https://doi.org/10.1080/08990220500420236 (cit. on p. 26).

GRAS. (2026). *Gras 46be 1/4"ccp free-field standard microphone set*. Retrieved 2026-04-07, from https://www.grasacoustics.com/products/measurement-microphone-sets/constant-current-power-ccp/product/143-46be (cit. on p. 70).

Guo, J., Chen, L., Zhang, Y., Yang, K., Li, J., & Gao, X. (2013). Method of ultrasonic phased array imaging based on segment amplitude apodization. *Far East Forum on Nondestructive Evaluation/Testing: New Technology and Application*, 181–188. https://doi.org/10.1109/FENDT.2013.6635552 (cit. on p. 6).

Hajas, D., Pittera, D., Nascé, A., Georgiou, O., & Obrist, M. (2020). Mid-air haptic rendering of 2d geometric shapes with a dynamic tactile pointer. *IEEE Transactions on Haptics*, *13*(4), 806–817. https://doi.org/10.1109/TOH.2020.2966445 (cit. on pp. 79, 80, 106).

Halbach, A., Gijsenbergh, P., Jeong, Y., Devriese, W., Gao, H., Billen, M., Torri, G. B., Chare, C., Cheyns, D., Rottenberg, X., & Rochus, V. (2019). Display compatible PMUT array for mid-air haptic feedback.

Proceedings of the IEEE International Conference on Solid-State Sensors, Actuators and Microsystems (Transducers), 158–161. https://doi.org/10.1109/TRANSDUCERS.2019.8808775 (cit. on p. 4).

Harrington, K., Large, D. R., Burnett, G., & Georgiou, O. (2018). Exploring the use of mid-air ultrasonic feedback to enhance automotive user interfaces. *Proceedings of the International Conference on Automotive User Interfaces and Interactive Vehicular Applications*, 11–20. https://doi.org/10.1145/3239060.3239089 (cit. on p. 2).

Hasegawa, K., & Shinoda, H. (2018). Aerial vibrotactile display based on multiunit ultrasound phased array. *IEEE Transactions on Haptics*, *11*(3), 367–377. https://doi.org/10.1109/TOH.2018.2799220 (cit. on pp. 3, 21, 32–35).

Hirayama, R., Martinez Plasencia, D., Masuda, N., & Subramanian, S. (2019). A volumetric display for visual, tactile and audio presentation using acoustic trapping. *Nature*, *575*(7782), 320–323. https://doi.org/10.1038/s41586-019-1739-5 (cit. on pp. 2, 158).

Hoshi, T. (2016). Mid-air tactile displays. *CHI 2016 Workshop on Mid-Air Haptics*. https://hoshistar81.jp/pdf/2016CHI_MidairWS.pdf (cit. on p. 133).

Hoshi, T., Takahashi, M., Iwamoto, T., & Shinoda, H. (2010). Noncontact tactile display based on radiation pressure of airborne ultrasound. *IEEE Transactions on Haptics*, *3*(3), 155–165. https://doi.org/10.1109/TOH.2010.4 (cit. on pp. 3, 20, 21, 133).

Howard, T., Gallagher, G., Lécuyer, A., Pacchierotti, C., & Marchal, M. (2019). Investigating the recognition of local shapes using mid-air ultrasound haptics. *IEEE World Haptics Conference (WHC)*, 503–508. https://doi.org/10.1109/WHC.2019.8816127 (cit. on p. 37).

Howard, T., Marchal, M., Lécuyer, A., & Pacchierotti, C. (2020). Pumah: Pan-tilt ultrasound mid-air haptics for larger interaction workspace in virtual reality. *IEEE Transactions on Haptics*, *13*(1), 38–44. https://doi.org/10.1109/TOH.2019.2963028 (cit. on p. 2).

Hwang, I., Son, H., & Kim, J. R. (2017). Airpiano: Enhancing music playing experience in virtual reality with mid-air haptic feedback. *Proceedings of the IEEE World Haptics Conference (WHC)*, 213–218. https://doi.org/10.1109/WHC.2017.7989903 (cit. on p. 2).

Iwamoto, T., Tatezono, M., & Shinoda, H. (2008). Non-contact method for producing tactile sensation using airborne ultrasound. *Haptics: Perception, Devices and Scenarios*, 504–513. https://doi.org/10.1007/978-3-540-69057-3_64 (cit. on p. 32).

Johansson, R. S., & Westling, G. (1987). Signals in tactile afferents from the fingers eliciting adaptive motor responses during precision grip. *Experimental Brain Research*, *66*(1), 141–154. https://doi.org/10.1007/BF00236210 (cit. on p. 22).

Johnson, K. O., & Hsiao, S. S. (1992). Neural mechanisms of tactual form and texture perception. *Annual Review of Neuroscience*, *15*, 227–250. https://doi.org/10.1146/annurev.ne.15.030192.001303 (cit. on p. 22).

Johnson, K. O., & Lamb, G. D. (1981). Neural mechanisms of spatial tactile discrimination: Neural patterns evoked by braille-like dot patterns in the monkey. *The Journal of Physiology*, *310*, 117–144. https://doi.org/10.1113/jphysiol.1981.sp013540 (cit. on p. 23).

Kim, D.-G., & Choi, S. (2024). A feasibility study on tactile enhancement of mid-air ultrasonic stimulation by wrist vibration. *Haptics: Science, Technology, and Applications*, 3–14. https://doi.org/10.1007/978-3-031-70061-3_1 (cit. on p. 3).

Kim, M. C., Cho, Y. J., Kim, H. S., & Park, K. K. (2025). Tactile threshold reduction through angle-steered focused ultrasound stimulation using capacitive micromachined ultrasound transducer (CMUT). *Proceedings of the IEEE International Ultrasonics Symposium (IUS)*, 1–4. https://doi.org/10.1109/IUS62464.2025.11201848 (cit. on p. 4).

Kinsler, L. E., Frey, A. R., Coppens, A. B., & Sanders, J. V. (1999). *Fundamentals of acoustics* (4th ed.). John Wiley & Sons. (Cit. on pp. 5, 16, 17, 53).

Lamoré, P. J., Muijser, H., & Keemink, C. J. (1986). Envelope detection of amplitude-modulated high-frequency sinusoidal signals by skin mechanoreceptors. *The Journal of the Acoustical Society of America*, *79*(4), 1082–1085. https://doi.org/10.1121/1.393380 (cit. on pp. 32–34).

Large, D. R., Harrington, K., Burnett, G., & Georgiou, O. (2019). Feel the noise: Mid-air ultrasound haptics as a novel human-vehicle interaction paradigm. *Applied Ergonomics*, *81*, 102909. https://doi.org/10.1016/j.apergo.2019.102909 (cit. on p. 2).

Liebler, M., Kling, C., Gerlach, A., & Koch, C. (2020). Experimental characterization of high-intensity focused airborne ultrasound fields. *The Journal of the Acoustical Society of America*, *148*(3), 1713. https://doi.org/10.1121/10.0001974 (cit. on pp. 3, 20).

Liebler, M., Kling, C., Best, B., Gerlach, A., & Koch, C. (2019). Quantitative characterization of high-intensity focused airborne ultrasonic fields. *Proceedings of the International Congress on Acoustics (ICA)*, 6338–6345. https://doi.org/10.18154/RWTH-CONV-238848 (cit. on p. 3).

Lim, C., Jin, G., Seifi, H., & Park, G. (2025). Designing mid-air ultrasound tactons with spatiotemporal parameters for distinguishable tactile brushes. *IEEE World Haptics Conference (WHC)*, 520–526. https://doi.org/10.1109/WHC64065.2025.11123369 (cit. on p. 37).

Liu, Y.-H., Su, H.-Y., Lin, H.-C., Li, C.-Y., Wang, Y.-H., & Huang, C.-H. (2022). Investigation of achieving ultrasonic haptic feedback using piezoelectric micromachined ultrasonic transducer (pMUT). *Electronics*, *11*(14), 2131. https://doi.org/10.3390/electronics11142131 (cit. on p. 4).

Long, B., Seah, S. A., Carter, T., & Subramanian, S. (2014). Rendering volumetric haptic shapes in mid-air using ultrasound. *ACM Transactions on Graphics*, *33*(6), 181. https://doi.org/10.1145/2661229.2661257 (cit. on p. 6).

Loomis, J. M. (1981). Tactile pattern perception. *Perception*, *10*(1), 5–27. https://doi.org/10.1068/p100005 (cit. on pp. 24, 25).

Marti, P., Parlangeli, O., Recupero, A., Guidi, S., & Sirizzotti, M. (2022). Mid-air haptics for shape recognition of virtual objects. *Ergonomics*, *65*(5), 775–793. https://doi.org/10.1080/00140139.2021.1992019 (cit. on p. 37).

Mendes, E. (2026). *Phd-thesis-umah repository* (Version v1.1-beta). Zenodo. https://doi.org/10.5281/zenodo.19858157 (cit. on p. 159).

Mendes, E., Carvalho, J., Santos, P., Sotgiu, E., & Cabral, J. (2022). Preliminary assessment of combined stimuli with laterally modulated mid-air ultrasound focus. *Proceedings of the IEEE International Symposium on Electrical, Electronics and Information Engineering (ISEEIE)*, 236–239. https://doi.org/10.1109/ISEEIE55684.2022.00048 (cit. on pp. 13, 81, 82, 157).

Mendes, E., Santos, P., Carvalho, J., & Cabral, J. (2024). Spatiotemporal modulation for ultrasonic mid-air haptics: Sensation's specification and validation. *IEEE Transactions on Haptics*, *17*(3), 429–440. https://doi.org/10.1109/TOH.2024.3355187 (cit. on pp. 9, 10, 13, 51, 79, 81).

Microchip Technology. (2026). *Mic4127 mosfet driver*. Retrieved 2026-04-28, from https://www.microchip.com/en-us/product/mic4127 (cit. on p. 58).

Morisaki, T., Fujiwara, M., Makino, Y., & Shinoda, H. (2022). Non-vibratory pressure sensation produced by ultrasound focus moving laterally and repetitively with fine spatial step width. *IEEE Transactions on Haptics*, *15*(2), 441–450. https://doi.org/10.1109/TOH.2021.3125843 (cit. on pp. 10, 37–40, 45, 49, 50, 79, 99, 105, 106).

Mulot, L., Gicquel, G., Zanini, Q., Frier, W., Marchal, M., Pacchierotti, C., & Howard, T. (2021). Dolphin: A framework for the design and perceptual evaluation of ultrasound mid-air haptic stimuli. *ACM Symposium on Applied Perception*, 2. https://doi.org/10.1145/3474451.3476232 (cit. on p. 118).

Murata. (2016). *Ma40s4s/ma40s4r application note*. Retrieved 2025-01-01, from https://www.murata.com/-/media/webrenewal/products/sensor/ultrasonic/open/applinote_maopn.ashx?la=en (cit. on p. 17).

Pashler, H. E. (Ed.). (2002). *Stevens' handbook of experimental psychology: Methodology in experimental psychology*. John Wiley & Sons. (Cit. on pp. 22–24).

Peters, L. C. J. M., Ollearo, R., Verbeek, R. G. F. A., van der Steen, J. L. P. J., Akkerman, H. B., Volker, A. W. F., van Neer, P. L. M. J., & Gelinck, G. H. (2019). Low-cost monolithic processing of large-area ultrasound transducer arrays. *Proceedings of the IEEE International Ultrasonics Symposium (IUS)*, 60–63. https://doi.org/10.1109/ULTSYM.2019.8926238 (cit. on p. 4).

Petrosino, L., & Fucci, D. (1984). Temporal resolution of successive brief stimuli for the tongue and hand. *Bulletin of the Psychonomic Society*, *22*(3), 208–210. https://doi.org/10.3758/BF03333807 (cit. on p. 25).

Price, A., & Long, B. (2018). Fibonacci spiral arranged ultrasound phased array for mid-air haptics. *Proceedings of the IEEE International Ultrasonics Symposium (IUS)*, 1–4. https://doi.org/10.1109/ULTSYM.2018.8580072 (cit. on pp. 5, 6).

Rakkolainen, I., Freeman, E., Sand, A., Raisamo, R., & Brewster, S. (2021). A survey of mid-air ultrasound haptics and its applications. *IEEE Transactions on Haptics*, *14*(1), 2–19. https://doi.org/10.1109/TOH.2020.3018754 (cit. on pp. 3, 6, 42).

Rakkolainen, I., Sand, A., & Raisamo, R. (2019). A survey of mid-air ultrasonic tactile feedback. *IEEE International Symposium on Multimedia (ISM)*, 94–99. https://doi.org/10.1109/ISM46123.2019.00022 (cit. on pp. 3, 42).

Rozenberg, L. D. (Ed.). (1969). *Sources of high-intensity ultrasound*. Springer. https://doi.org/10.1007/978-1-4757-6453-6 (cit. on pp. 18, 19).

Santos, P., Mendes, E., Carvalho, J., Alves, F., Azevedo, J., & Cabral, J. (2024). Hardware accelerated active noise cancellation system using haar wavelets. *Microprocessors and Microsystems*, *107*, 105047. https://doi.org/10.1016/j.micpro.2024.105047 (cit. on p. 13).

Seah, S. A., Drinkwater, B. W., Carter, T., Malkin, R., & Subramanian, S. (2014). Correspondence: Dexterous ultrasonic levitation of millimeter-sized objects in air. *IEEE Transactions on Ultrasonics, Ferroelectrics, and Frequency Control*, *61*(7), 1233–1236. https://doi.org/10.1109/TUFFC.2014.3022 (cit. on p. 2).

Seifi, H., Chew, S., Nascè, A. J., Lowther, W. E., Frier, W., & Hornbæk, K. (2023). Feellustrator: A design tool for ultrasound mid-air haptics. *Proceedings of the CHI Conference on Human Factors in Computing Systems*, Article 266. https://doi.org/10.1145/3544548.3580728 (cit. on pp. 10, 11, 117).

Sekuler, R., & Blake, R. (1994). *Perception*. McGraw-Hill. (Cit. on p. 22).

Shakeri, G., Williamson, J. H., & Brewster, S. (2018). May the force be with you: Ultrasound haptic feedback for mid-air gesture interaction in cars. *Proceedings of the International Conference on Automotive User Interfaces and Interactive Vehicular Applications*, 1–10. https://doi.org/10.1145/3239060.3239081 (cit. on p. 2).

Shinoda, H. (2013). Aerial display of vibrotactile sensation with high spatial-temporal resolution using large-aperture airborne ultrasound phased array. *Proceedings of the IEEE World Haptics Conference (WHC)*. https://doi.org/10.1109/WHC.2013.6548380 (cit. on p. 3).

Takahashi, R., Hasegawa, K., & Shinoda, H. (2020). Tactile stimulation by repetitive lateral movement of mid-air ultrasound focus. *IEEE Transactions on Haptics*, *13*(2), 334–342. https://doi.org/10.1109/TOH.2019.2946136 (cit. on pp. 33, 34, 37, 38, 40, 42–44, 50, 79, 99).

Takahashi, R., Hasegawa, K., & Shinoda, H. (2018). Lateral modulation of midair ultrasound focus for intensified vibrotactile stimuli. *Haptics: Science, Technology, and Applications*, 276–288. https://doi.org/10.1007/978-3-319-93399-3_25 (cit. on pp. 6, 9, 33, 34, 37, 42).

Takahashi, R., Mizutani, S., Hasegawa, K., Fujiwara, M., & Shinoda, H. (2019). Circular lateral modulation in airborne ultrasound tactile display. *Haptic Interaction*, 92–94. https://doi.org/10.1007/978-981-13-3194-7_20 (cit. on pp. 6, 9, 37, 38, 49).

Texas Instruments. (2026). *Sn74avc16t245 16-bit dual-supply bus transceiver*. Retrieved 2026-04-28, from https://www.ti.com/product/SN74AVC16T245 (cit. on p. 58).

Thorlabs. (2026). *Lts300 300 mm translation stage with stepper motor and integrated controller*. Retrieved 2026-04-07, from https://www.thorlabs.com/item/LTS300 (cit. on p. 70).

Tong, J., Mao, O., & Goldreich, D. (2013). Two-point orientation discrimination versus the traditional two-point test for tactile spatial acuity assessment. *Frontiers in Human Neuroscience*, *7*, 579. https://doi.org/10.3389/fnhum.2013.00579 (cit. on p. 24).

Trenz Electronic. (2026a). *System on module with amd zynq-7045*. Retrieved 2026-04-28, from https://www.trenz-electronic.de/en/SoM-with-AMD-Zynq-7045-1C-1-GByte-DDR3L-5.2-x-7.6-cm/TE0745-03-91C31-A (cit. on p. 59).

Trenz Electronic. (2026b). *Te0745 technical reference manual*. Retrieved 2026-04-07, from https://wiki.trenz-electronic.de/display/PD/TE0745+TRM (cit. on p. 59).

Trenz Electronic. (2026c). *Te0790 technical reference manual*. Retrieved 2026-04-28, from https://wiki.trenz-electronic.de/display/PD/TE0790+TRM (cit. on p. 60).

Ultraleap. (2025). *Ultraleap is joining ROLI*. Retrieved 2025-01-01, from https://www.ultraleap.com/ (cit. on p. 4).

Ultraleap. (2026). *Sensation designer documentation*. Retrieved 2026-01-14, from https://docs.ultraleap.com/haptics/sensation-designer.html (cit. on p. 117).

Vallbo, A. B., Olsson, K. A., Westberg, K. G., & Clark, F. J. (1984). Microstimulation of single tactile afferents from the human hand: Sensory attributes related to unit type and properties of receptive fields. *Brain*, *107*(3), 727–749. https://doi.org/10.1093/brain/107.3.727 (cit. on p. 26).

van Neer, P., Volker, A., Berkhoff, A., Schrama, T., Akkerman, H., van Breemen, A., Peeters, L., van der Steen, J.-L., & Gelinck, G. (2019). Development of a flexible large-area array based on printed polymer transducers for mid-air haptic feedback. *Proceedings of Meetings on Acoustics*, *38*(1), 045008. https://doi.org/10.1121/2.0001068 (cit. on p. 4).

Vartanyan, I. A., Gavrilov, L. R., Svetlogorskaya, I. D., & Tsirulnikov, E. M. (1991). Effect of duration of pulses of focused ultrasound on skin sensitivity. *Sensory Systems*, *4*(1), 42–47 (cit. on pp. 27–30).

Verrillo, R. T. (1963). Effect of contactor area on the vibrotactile threshold. *The Journal of the Acoustical Society of America*, *35*(12), 1962–1966. https://doi.org/10.1121/1.1918868 (cit. on pp. 23, 33).

Villa, S., Mayer, S., Hartcher-O'Brien, J., Schmidt, A., & Machulla, T.-K. (2022). Extended mid-air ultrasound haptics for virtual reality. *Proceedings of the ACM on Human-Computer Interaction*, *6*, Article 578. https://doi.org/10.1145/3567731 (cit. on p. 2).

Xilinx, Inc. (2015). *Multiplier v12.0 logicore ip product guide (pg108)*. Retrieved 2026-04-28, from https://docs.amd.com/v/u/en-US/pg108-mult-gen (cit. on p. 67).

Xilinx, Inc. (2021a). *Adder/subtracter v12.0 logicore ip product guide (pg120)*. Retrieved 2026-04-28, from https://docs.amd.com/api/khub/documents/DBKtRd~p6vmy3RuEdGuT4Q/content (cit. on p. 67).

Xilinx, Inc. (2021b). *Cordic v6.0 logicore ip product guide (pg105)*. Retrieved 2026-04-28, from https://docs.amd.com/v/u/en-US/pg105-cordic (cit. on p. 68).

Xilinx, Inc. (2021c). *Divider generator v5.1 logicore ip product guide (pg151)*. Retrieved 2026-04-28, from https://docs.amd.com/v/u/en-US/pg151-div-gen (cit. on p. 68).

Young, G., Milne, H., Griffiths, D., Padfield, E., Blenkinsopp, R., & Georgiou, O. (2020). Designing mid-air haptic gesture controlled user interfaces for cars. *Proceedings of the ACM on Human-Computer Interaction*, *4*, Article 81. https://doi.org/10.1145/3397869 (cit. on p. 2).